MONASH University

COMPUTER-AIDED DESIGN OF BORON-BASED TWO-DIMENSIONAL ELECTROCATALYSTS

CHUANGWEI LIU

DOCTOR OF PHILOSOPHY

SCHOOL OF CHEMISTRY, FACULTY OF SCIENCE

MONASH UNIVERSITY

2019

COMPUTER-AIDED DESIGN OF BORON-BASED TWO-DIMENSIONAL ELECTROCATALYSTS

Chuangwei Liu

M.Sc. Mechanical Engineering

B.Sc. Metallurgical Engineering

A Thesis Submitted for the Degree of Doctor of Philosophy at

School of Chemistry, Faculty of Science, Monash University in 2019

This Thesis is Dedicated to Jing Wu,

Parents, and Annie

CONTENTS

ABSTRACT

The work of this thesis has focused on the design new two-dimensional (2D) electrocatalysts to conversion nitrogen to ammonia by computer-aided under ambient conditions. Especially, our research work associated with the boron-based catalysts. The thesis is divided into the following six Chapters:

➢ Chapter I is a "chapter by review work", it summarizes the electrocatalytic and photocatalytic activity of nitrogen reduction reaction on emerging two-dimensional catalysts.

➢ Chapter II is a "chapter by publication", it describes hydrogen evolution reaction catalytic activity on two-dimensional boron sheets (α and β_{12}) are explored using periodic density functional theory.

➢ Chapter III is a "chapter by publication". It represents two stable two-dimensional boron monolayers (α and β_{12}) as an electrochemical catalyst for nitrogen reduction reaction under ambient conditions.

➢ Chapter IV is a "chapter by publication". It demonstrates single ruthenium atom doped boron sheets exhibited outstanding catalytic activity for ammonia synthesis at ambient conditions through the distal pathway with small activation barrier of 0.42 eV.

➢ Chapter V is a "chapter by publication". It indicates the nitrogen reduction reaction catalytic activity of boron is highly correlated with the degree of charge transfer between the boron atom and the substrate.

➢ Chapter VI contains conclusions and perspectives.

DECLARATION

I hereby declare that this thesis contains no material which has been accepted for the award of any other degree or diploma at any university or equivalent institution and that, to the best of my knowledge and belief, this thesis contains no material previously published or written by another person, except where due reference is made in the text of the thesis.

This thesis includes *four* original papers published in peer reviewed journals. The core theme of the thesis is *boron catalysis*. The ideas, development and writing up of all the papers in the thesis were the principal responsibility of myself, the student, working within the *School of Chemistry* under the supervision of *Prof. Jie Zhang, and Chenghua Sun*.

(The inclusion of co-authors reflects the fact that the work came from active collaboration between researchers and acknowledges input into team-based research.)

In the case of all *Chapters* my contribution to the work involved the following:

Thesis Chapter	Publication Title	Status	Nature and % of student contribution	Co-author name(s) Nature and % of Co-author's contribution*	Co-author(s), Monash student Y/N*
1	*Two-dimensional Electrocatalysts and Photocatalysts for Nitrogen Reduction to Ammonia*	*Not Submitted*	*80%. Writing first draft*	*1)Qinye Li, proof and editing 5% 2) Jie Zhang, proof and editing 5% 3) Yonggang Jin, proof and editing 5% 4) Douglas R. MacFarlane proof and editing 5%*	*Yes No No No*
2	*Two-dimensional Boron Sheets as Metal-Free Catalysts for Hydrogen Evolution Reaction*	*Published*	*80%. Calculate and collect result, writing first draft*	*1)Zhongxu Dai, proof and editing 5% 2) Jie Zhang, proof and editing 5% 3) Yonggang Jin, proof and editing 5% 4) Dongsheng Li proof and editing 5%*	*No No No No*
3	*Theoretical Evaluation of Possible 2D Boron*	*Published*	*80%. Calculate and collect result,*	*1)Qinye Li, proof and editing 5% 2) Jie Zhang,*	*Yes No No*

	Monolayer in N$_2$ Electrochemical Conversion into Ammonia		*writing first draft*	*proof and editing 5% 3) Yonggang Jin, proof and editing 5% 4) Douglas R. MacFarlane proof and editing 5%*	*No*
4	*Conversion of Dinitrogen to Ammonia on Ru Atoms Supported on Boron Sheets: A DFT Study*	*Published*	*80%. Calculate and collect result, writing first draft*	*1)Qinye Li, proof and editing 5% 2) Jie Zhang, proof and editing 5% 3)Yonggang Jin, proof and editing 5% 4) Douglas R. MacFarlane proof and editing 5%*	*Yes No No No*
5	*Single-boron Catalysts for Nitrogen Reduction Reaction*	*Published*	*75%. Calculate and collect result, writing first draft*	*1) Qinye Li, proof and editing 5% 2) Chengzhang Wu proof and editing 5% 3) Jie Zhang, proof and editing 5% 4) Yonggang Jin, proof and editing 5% 5) Douglas R. MacFarlane proof and editing 5%*	*Yes No No No No*

*If no co-authors, leave fields blank

I have not renumbered sections of submitted or published papers in order to generate a consistent presentation within the thesis.

Student Signature: **Date**:

The undersigned hereby certify that the above declaration correctly reflects the nature and extent of the student's and co-authors' contributions to this work. In instances where I am not the responsible author, I have consulted with the responsible author to agree on the respective contributions of the authors.

Main Supervisor Signature: **Date**:

ACKNOWLEDGEMENTS

I would like to take this opportunity to express my deep and sincere gratitude to my supervisor Prof. Chenghua Sun, Prof. Jie Zhang, and Dr. Yonggang Jin for their continuous support and excellent guidance throughout my PhD studies. It is a great honor and pleasure for me to join this group as a PhD candidate, where I have developed my scientific skills. His willingness and patience to provide constant feedback on thesis and manuscript has vastly improved my skills. Besides my advisor, I would like to thank the rest of my advisory panel: Prof. Ekaterina Pas, Prof. San Hoa Thang, Prof. Kellie Tuck, and Dr. David Turner for their insightful encouragement and comment.

I would like to thank Siyao, Xingzhu and Laura for their helps on initiating my PhD projects. And I would also like to thank my current group mates: Tianyi, Guowang, Haikun, and Yuanyuan, for providing a wonderful working environment in our group. I would also like to acknowledge my officemates Xiaoyu.

I would also like to thank Anna and Sarah for their assistance in administrative matters. I am also indebted to the School of Chemistry, Faculty of Science for providing financial support for my PhD studies. Last, I deeply thank the National Computational Infrastructure (NCI), which is supported by the Australian Government, for providing the computational resources

ABBREVIATIONS

2D	Two-dimensional
NH_3	Ammonia
N_2	Nitrogen
CO_2	Carbon Dioxide
HB	Haber-Bosch
H_2	Hydrogen
ATP	Adenosine Triphosphate
ADP	Adenosindi Phosphate
TM	Transition Metal
Ar	Argon
NRR	Nitrogen Reduction Reaction
ORR	Oxygen Reduction Reaction
CRR	Carbon Dioxide Reduction Reaction
HER	Hydrogen Reduction Reaction
FE	Faradaic Efficiency
R	Yield Rate
DFT	Density functional theory
MvK	Mars–van Krevelen Mechanism
$g\text{-}C_3N_4$	Graphitic Carbon Nitride
h-BN	Hexagonal Boron Nitride
BP	Black Phosphorus

TMDs	Transition Metal Dichalcogenides
MXenes	2D Carbides and Nitrides
MOFs	2D Metal-organic Frameworks
LDHs	Layered Double Hydroxides
LUMO	Lowest Unoccupied Molecular Orbital
HUMO	Highest Unoccupied Molecular Orbital
DOS	Density of States
LDOS	Local Density of States
RDS	Rate Determining Steps
SHE	Standard Hydrogen Electrode
RHE	Reversible Hydrogen Electrode
U	Applied Potential
SACs	Single-atom Catalysts
NVs	Nitrogen Vacancies
OVs	Oxygen Vacancies
SVs	Sulfide Vacancies
UV	Ultraviolet
SEM	Scanning Electron Microscopy
TEM	Transmission Electron Microscopy
STEM	Scanning Transmission Electron Microscopy
HRTEM	High-resolution Transmission Electron Microscopy
HAADF-STEM	High-angle Annular Dark-field Imaging-STEM

x

PUBLICATIONS

1. R. Zhao[#], *C. Liu*[#], X. Zhang, X. Zhu, P. Wei, L. Ji, Y. Guo, S. Gao, Y. Luo*, Z. Wang*, X. Sun*, "Ultrasmall Ru_2P Nanoparticles-reduced Graphene Oxide Hybrid: An Efficient Electrocatalyst for NH_3 Synthesis under Ambient Conditions" *J. Mater. Chem. A* (Accepted)

2. Q. Li, *C. Liu*, S. Qiu, F. Zhou, L. He, X. Zhang*, C. Sun*, "Exploration of iron borides as electrochemical catalysts for nitrogen reduction reaction" *J. Mater. Chem. A* 2019, 7, 21507-21513.

3. *C. Liu*, Q. Li, C. Wu, J. Zhang, Y. Jin, D. R. MacFarlane, C. Sun, "Single-Boron Catalysts as Nitrogen Reduction Catalysts". *J. Am. Chem. Soc*. **2019**, *141*, 2884-2888.

4. *C. Liu*, Q. Li, J. Zhang, Y. Jin, D. R. MacFarlane, C. Sun, "Conversion of Dinitrogen to Ammonia on Ru Atom Supported on Boron Sheets: A DFT Study". *J. Mater. Chem. A* 2019, 7, 4771-4776.

5. Q. Li, S. Qiu, *C. Liu*, M. Liu, L. He, X. Zhang, C. Sun, "Computational Design of Single Molybdenum Catalysts for Nitrogen Reduction Reaction". *J. Phys. Chem. C* **2019**, *123*, 2347-2352.

6. *C. Liu*, Q. Li, J. Zhang, Y. Jin, D. R. MacFarlane, C. Sun, "Theoretical Evaluation of Possible 2D Boron Monolayer in N_2 Electrochemical Conversion into Ammonia". *J. Phys. Chem. C* **2018**, *122*, 25268-25273.

7. *C. Liu*, Z. Dai, J. Zhang, Y. Jin, D. Li, C. Sun, "Two-Dimensional Boron Sheets as Metal-Free Catalysts for Hydrogen Evolution Reaction". *J. Phys. Chem. C* **2018**, *122*, 19051-19055.

Chapter I: Two-dimensional Electrocatalysts and Photocatalysts for Nitrogen Reduction to Ammonia

1.1   Introduction

1.2   Categories of 2D Materials

1.2.1 Metal-Free 2D Materials

1.2.2 Transition-Metal Compound

1.2.3   Transition Metals

1.2.4 Transition Metal Chalcogenides

1.2.5 MXenes

1.3   Catalyst Design and Development Protocols

1.3.1 Defect Engineering

1.3.2 Impurity Engineering

1.4   Current Achievements and Challenges

1.1 Introduction

Ammonia (NH_3) is the most essential chemicals in the agriculture world as a fertilizer feedstock and a reagent precursor for productions of other chemicals.[1-3] Especially in the fertilizer area, the need for ammonia production continues to increase in order to support a growing global population, and abundant and low-cost ammonia production is ultimately necessary to provide a stable and affordable food supply.[4,5] Therefore, ammonia is the second most produced chemicals with the production of 172 million tons annually.[6,7] A complete picture of the range of products derived from ammonia is presented in Figure 1.[8,9] In addition, ammonia is also being considered as a significant green energy carrier and an alternative fuel due to high energy density, free carbon dioxide (CO_2) emission.[2,10] It has a high energy density, can be easily stored and transported.[11] Ammonia is already produced in large quantities, and therefore there is already significant infrastructure for its manufacture, and storage.[12] The current industrial production method is the Haber-Bosch (HB), which is known as the greatest invention in the twenty centuries.[13-15] In the process, a mixture of nitrogen (N_2) and hydrogen gas (H_2) molecules, termed synthetic gas, is passed over iron and molybdenum-based in the pressures of 130-170 bar under the temperature about 400-500 ºC to form ammonia according to:[13,16]

$$N_2 + 3H_2 \leftrightarrow 2NH_3 \tag{1}$$

Although the above reaction is exothermic, massive energy and high pressure are required to complete it, due to the facts that nonpolar N_2 has a strong triple bond, high ionization energy, and negative electron affinity.[17] However, the HB method accounts

2

for 1% of the world's yearly natural gas consumption and consumes more than 1.4 % of the global annual energy generation.[18] Inevitably, the HB production process accounts for 1.6% of global CO_2 emissions, owing to the main hydrogen source from natural gas.[6,19]
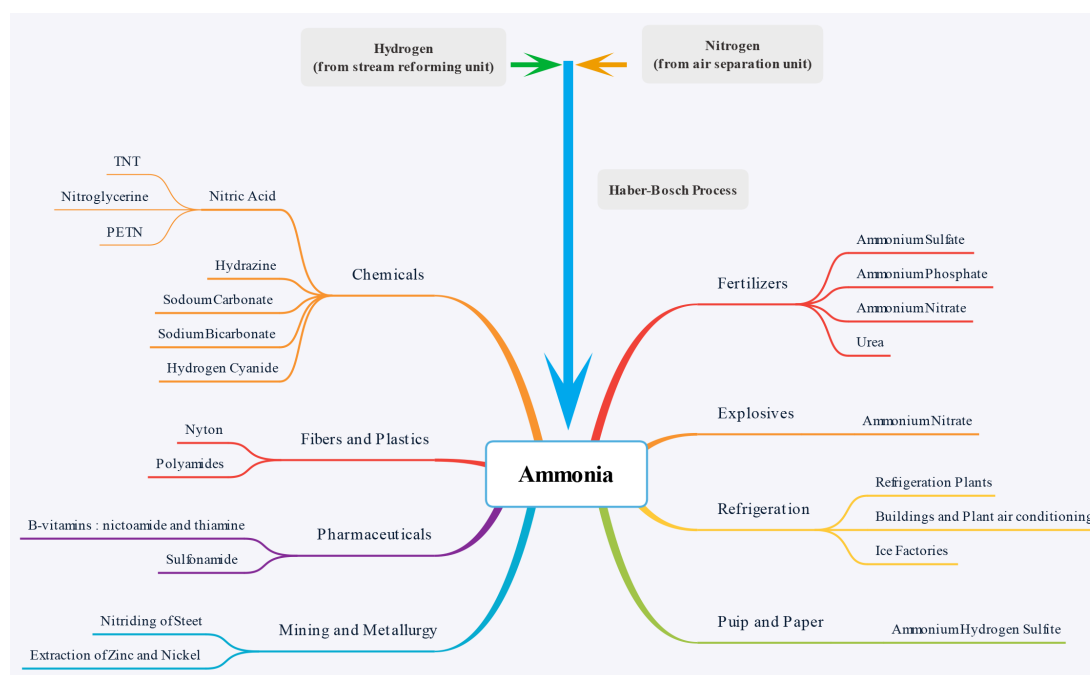
Figure 1. Range of applications of chemically fixed nitrogen in the form of ammonia.[9]

Since the Haber-Bosch was discovered, the process has been improved and optimized by substantially methods. Numerous researchers searched and developed more active catalysts which would allow ammonia synthesis at lower pressures and temperatures.[20-22] Co-containing catalyst is a notable development for the traditional fused iron catalyst.[23,24] The results indicated that cobalt doped iron-based catalysts exhibited beneficial influence on iron for nitrogen chemisorption, and ammonia can be released from catalyst surface at relatively lower temperature.[23] Subsequently, the noble metal with various supports such as SiO_2,[25] Al_2O_3,[26] zeolites,[27] and graphitized carbon were used in many pervious works.[28] Many improved catalysts and drastic reaction

conditions were applied in the HB method, however, the efficiency is still less than 15%.[29]

As opposed to the industrial process which requires elevated pressure and temperature, plants and bacteria can convert gaseous nitrogen into ammonia at ambient conditions.[6,16,21] This process can be achieved by metalloenzymes which are formed by the combination of two proteins. [30] By comparison the disadvantages of HB process, the whole reaction is carbon-free due to the hydrogen generated from renewable sources which can obviate the environment burden.[31] And, the whole enzymatic reaction requires 16 equivalents of ATP coupled with the formation of one equivalent of dihydrogen per turnover of ammonia:[6]

$$N_2 + 8e^- + 16ATP + 8H^+ \rightarrow 2NH_3 + H_2 + 16ADP + 16P_i \qquad (2)$$
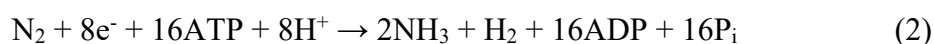
Although extensive effort has been made for the synthesis of NH_3 from coordinated N_2, typically from protonolysis, molecular catalysts for NH_3 synthesis are rarely reported.[32] Since the first transition metal-dinitrogen (TM) complex was discovered in 1965,[33] three different catalysts have been identified (Mo-nitrogenase, MoFe protein, and Fe protein cycle), among which the most optimized formation of ammonia from the reaction of dinitrogen with electron carriers and proton sources is achieved for TM-site where the active site for the coordination, reduction, and protonation of dinitrogen to produce ammonia is identified as the TM-active.[34-36] The most commonly found and best studied nitrogenase is Mo-nitrogenase, reflecting the presence of the element Mo as part of the complex metal cluster that forms the site of N_2 binding and reduction.[30] Then the other two alternative nitrogenases V and Fe-nitrogenase were investigated,

4

with the names reflecting the replacement of Mo by the two metals, respectively.[37]

The MoFe protein is an $\alpha_2\beta_2$ heterotetrametric, with each $\alpha\beta$ dimer constituting a minimal catalytic unit.[38] Each $\alpha\beta$ dimer contains an 8Fe-7S cluster called P cluster and 7Fe-9S-Mo-C-homocitrate cluster called FeMo-cofactor. And the FeMocofactor (also termed FeMo-co) is the site of substrate binding and reduction. The P cluster is proposed to serve as an electron shuttle, delivering electrons to FeMo-cofactor.[39] The Fe protein component is a α_2 homodimer having a single 4Fe-4S cluster that bridges the two subunits. Each subunit of the Fe protein contains an ATP binding site. During the Fe protein transiently associates with the MoFe protein, during which an electron is transferred from the Fe protein to the MoFe protein and the two ATP molecules are hydrolyzed to two ADP and two inorganic phosphate (Pi).[40] The complete catalytic cycle of nitrogenase involves a number of steps in each protein component. The steps in each protein component are intertwined; for convenience the events associated with the Fe protein delivery of electrons are often called the Fe protein cycle, whereas the events associated with the MoFe protein are called the MoFe protein cycle. More than half of the N_2 fixation on Earth is accomplished by microorganisms through the action of the enzyme nitrogenase,[8] however, the poor stability and low yield of ammonia on these catalysts greatly hamper the viability of largescale industrial application.[41]

Table 1. Mechanisms of electrocatalytic NRR with different intermediates

Mechanism routes	Elementary reaction steps
Dissociative	$N_2 + 2^* \rightarrow 2N^*$
	$N^* + e^- + H^+ \rightarrow NH^*$
	$NH^* + e^- + H^+ \rightarrow NH_2^*$
	$NH_2^* + e^- + H^+ \rightarrow NH_3 + {}^*$
Associative distal	$N_2 + {}^* \rightarrow N_2^*$
	$N_2^* + e^- + H^+ \rightarrow NNH^*$
	$NNH^* + e^- + H^+ \rightarrow NNH_2^*$
	$NNH_2^* + e^- + H^+ \rightarrow N^* + NH_3$
	$N^* + e^- + H^+ \rightarrow NH^*$
	$NH^* + e^- + H^+ \rightarrow NH_2^*$
	$NH_2^* + e^- + H^+ \rightarrow NH_3 + {}^*$
Associative alternating	$N_2 + {}^* \rightarrow N_2^*$
Associative enzymatic	$N_2^* + e^- + H^+ \rightarrow NNH^*$
	$NNH^* + e^- + H^+ \rightarrow NHNH^*$
	$NHNH^* + e^- + H^+ \rightarrow NHNH_2^*$
	$NHNH_2^* + e^- + H^+ \rightarrow NH_2NH_2^*$
	$NH_2NH_2^* + e^- + H^+ \rightarrow NH_2^* + NH_3$
	$NH_2^* + e^- + H^+ \rightarrow NH_3 + {}^*$

*Denotes an adsorption site on catalyst surface.

Greatly inspired by the proton and electron transfer in the nitrogenases and molecular catalysts, a number of groups have carried out studies of electrochemical technologies and catalysts.[42] Then, ammonia has been successfully synthesized in the solid electrolyte cell by electrochemical method in 1998.[43] And, a great number of investigations have devoted to the optimization of the electrochemical synthesis of ammonia under low temperature (about 100 °C).[22,44] When the solid-state proton conductor was employed, the Faradaic efficiency (FE) of ammonia can be up to 78%.[43]

6

Compared to the solid conductor, the ionic liquids or molten salts have relatively better performance for ammonia synthesis under low current efficiencies at high temperature.[45,46] Furthermore, numerous proton conducting ceramic membranes have been studied and various materials have been tested as working electrodes in the past decades.[47,48] The synthesized ammonia is easier to separate from mixture gas on the conductor membranes, therefore the ceramic membrane have considerably higher conversion rate of ammonia.[49]

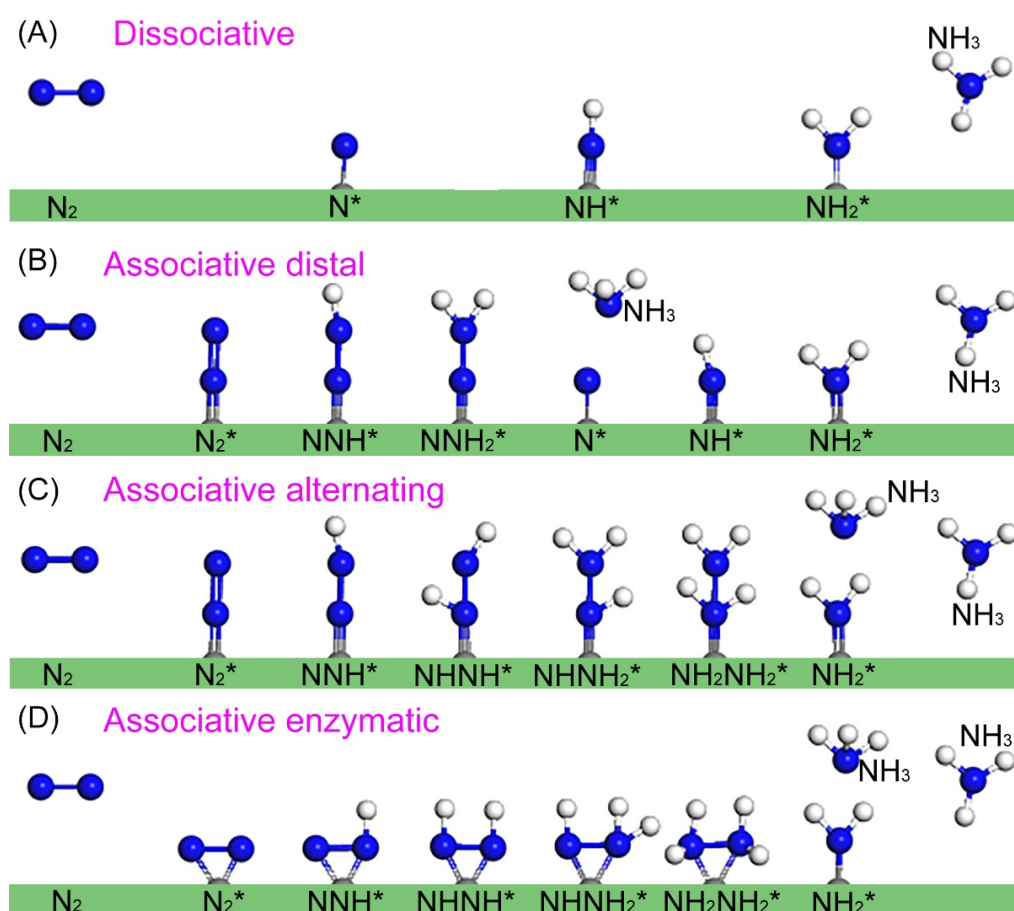**Figure 2.** Nitrogen reduction reaction possible mechanism pathways on catalyst surface: (a) dissociative, (b) associative distal, (c) associative alternating, and (d) associative enzymatic.

Generally, the electrocatalytic nitrogen to ammonia conversion over a heterogenous catalyst is based on two fundamental mechanisms, including dissociative and associative pathways, with different involved intermediates (Table 1).[50] According to

the dissociative mechanism (Figure 2a), the adsorbed N_2 molecules first undergo the cleavage of the triple bond prior to the hydrogenation process with high energy input due to the inertness of nitrogen bond, which can explain why harsh conditions are required for the Haber-Bosch process following the dissociative route. While in the associative pathway, the adsorbed N_2 molecule keeps tow N atoms bound to each other before the formation of the first NH_3 molecule. Considering different sequences of the addition of H to the N atoms, the hydrogenation process in the associative mechanism can proceed via two ways, naming the distal pathway and alternating pathway. In the distal pathway (Figure 2b), the distal N atom far away from the end-on adsorption site preferentially undergoes the hydrogenation process until the release the remote NH_3, and subsequently the remaining N adatoms repeats the same hydrogenation process to produce the second NH_3 molecule.[51] In comparison, the alternating pathway proceeds with the two N atoms hydrogenated in turn accompanied by a proton-coupled electron transfer, and two NH_3 molecules are released sequentially at the final step of the pathway (Figure 2c). In addition, the enzymatic pathway shares a similar hydrogenation process with the alternating pathway, but with both N atoms binding to the catalysts surface following a side-on coordination mode (Figure 2d).

During the past decade, electrochemical and photochemical reduction process using heterogeneous catalysts benefit from clean and renewable energy sources and are promising for achieving ammonia production directly from N_2 and water at ambient conditions.[52] In the aqueous NRR process, the major anodic reaction is the oxidation of water molecules, also known as the oxygen evolution reaction. On the cathode side, N_2

8

gas is supplied as a feed gas steam. The cathodic reaction depends on the type of aqueous electrolyte (acidic or alkaline).[52] In an acidic aqueous electrolyte, the produced protons on the counter electrode are directly transported through a proton exchange membrane toward the cathode, where NH_3 molecules are formed. Thus, the two half reactions in the acidic solution are described as:[53]

| Anodic | $3H_2O \rightarrow 6\,H^+ + 3/2\,O_2 + 6e^-$ | (3) |

| Cathodic | $6H^+ + N_2 + 6e^- \rightarrow 2NH_3$ | (4) |
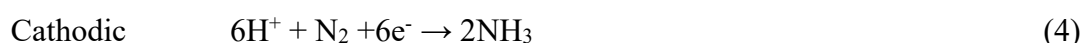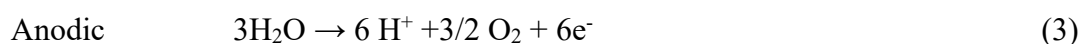
In an alkaline electrolyte, the cathodic half reaction follows another pathway, in which N_2 directly combines with water and electrons to form NH_3. The produced OH^- ions pass through an anion exchange membrane toward the cathode side to be oxidized to O_2, and the reaction of two electrodes are shown as:[54]

| Anodic | $6OH^- \rightarrow 3H_2O + 3/2\,O_2 + 6e^-$ | (5) |

| Cathodic | $6H_2O + N_2 + 6e^- \rightarrow 2NH_3 + 3/2O_2$ | (6) |
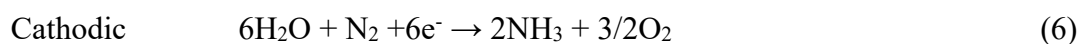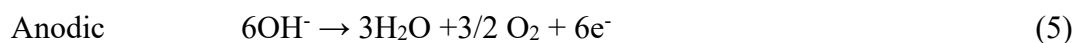
In order to accurately evaluate the catalytic activity of NRR catalysts, it is necessary to establish a reliable detection method for as-produced ammonia. The most common ammonia detection method is the colorimetric method, including Nessler's reagent method and the indophenol blue method, whereas the metallic ions or pH value of the solution might interfere with the NH_3 detection results. Therefore, the combination of colorimetric method and other methods like the ion-selective electrode analysis is essential to make the ammonia detection more reliable. In addition, $^{15}N_2$ isotopic experiments are required to identify the origin of the detected ammonia, especially for those NRR catalysts containing nitrogen species.[55] Also, it is noteworthy that the

contamination might lead to erroneous results of the detected ammonia, especially when the ammonia yield is quite low. Accordingly, it is indispensable to conduct a series of rigorous control experiments, including the electrochemical Ar control experiments and the activity testing, in both Ar and N_2 under an open-circuit condition. With a reasonable combination of multiple ammonia detection methods and a series of control experiments, the NRR performance of catalysts can be reliably evaluated to provide guidance for the future research work.

Except the ammonia detection, the catalytic descriptors of electrocatalyst is also an important standard for NRR. The FE and the NH_3 yield rate (R) are two essential descriptors of the performance of the electrocatalyst. The FE can be defined as the ratio of the charge used for nitrogen reduction to the total charge passed through the circuit, which reflects the selectivity of the electrochemical process for NH_3 synthesis. The ammonia R refers to the NH_3 production per unit time and unit catalyst loading mass or unit electrode surface area, which reflect the NRR reaction rate for NH_3 synthesis. The FE of NRR can be calculated using the equation:

$$FE = \frac{n \cdot F \cdot C \cdot V}{Q} \tag{7}$$

Where n is the number of electrons required for producing one NH_3 molecule (n = 3), F is the Faraday constant (F = 96485.33 C mol^{-1}), C is the measured NH_3 concentration, V is the volume of the electrolyte, and the Q is the total charge passed through the electrodes.

And the R of NRR can be calculated using the following equation:

$$R = \frac{C \cdot V}{t \cdot S} \tag{8}$$

Where C is the measured NH_3 concentration, V is the volume of the electrolyte, t is the reaction time, and S is the catalysts loading mass or the geometric area of the electrode or the electrochemically active surface area of the electrodes.

However, there are two major problems associated with electrochemical N_2 reduction. From a thermodynamic perspective, electrochemical reduction is possible, but all attempts so far have found a large energy consumption and very low selectivity toward nitrogen; most protons and electrons go toward evolving gaseous H_2 molecule. Therefore, the main reaction (NRR) was significantly suppressed by the competing reaction.[56] So far, the focus is to further improve the energy efficiency through smart design of novel catalysts, specifically reducing the overpotential and improving FE during the electrochemical process at mild temperature condition. In addition, the selectivity, activity, and stability at ambient condition of electrocatalyst are ongoing challenges in the current research.

Since the two-dimensional (2D) nanomaterial, graphene, was firstly studied in 2004, their unique properties have been investigated in massive applications, including conventional heterogeneous catalysis, electrocatalysis and photocatalysis.[57-59] Compared to nanowires and nanoparticles catalysis, the 2D nanomaterials have several most important features which are high specific surface area, tunable, uniformly exposed lattice plane and unique electronic state.[60] 2D materials help to obtain a relatively simple type of active site with nearly the same coordination number, while the atomic thickness and ultrahigh specific surface area make the number of their active sites comparable with the total atoms.[61] In addition, the more exposed surface atoms in

the ultrathin two-dimensional sheets can easily escape from the lattice and hence inevitably result in the formation of defect structure, which can strongly affect their electronic structure and hence tune the activity of reactive sites.

The explosive popularity of 2D materials does not only rely on their intrinsic properties but also highly depends on the tunability. With graphene, for example, one can use its edges, defects, or dopants for metal-free catalysis, and the single-atom-layer structure with tunable size allows a higher density of such active sites;[62] the unique electronic structure of graphene can modulate the catalytic behavior of metals anchored on it, and in turn the inert graphene surface can also be activated by the metals underneath graphene through electron penetration effect.[63] Besides above treatment techniques, some 2D materials can achieve a semiconductor-to-metal conversion. Modern technologies and applications require a wide range of excellent performances, which can be hardly realized in a single material. Therefore, 2D materials provide a great platform of tuning their properties toward desired functions, further attracting a great deal of attention and opening up opportunities for a wide range of applications.

Various electrocatalysts based on 2D nanomaterials and their derivatives are simply discussed in the first section of this review. And the physicochemical properties and electrocatalytic performance for NRR of those 2D electromaterials under ambient conditions are also investigated in the following content. In the second part, we described the state-of-the-art advancement for design strategies and synthesis method for electrocatalysts by using the experiments and density functional theory (DFT) calculations results. Then the comprehensive review of the development of 2D

12

electrocatalysts based on an understanding of the reaction mechanisms, catalytic activity trends, and rational design. In addition, the relationship between 2D electrocatalysts and electrocatalytic performance by bridging the fundamental theoretical calculation with electrochemical experiments were discussed, inferring a universal principle for a rational design of new 2D electrocatalysts. Especially highlighted is the significance of merging computational quantum chemistry, surface electrochemistry, materials chemistry, and nanotechnology for electrocatalysis through a range of example covering plenty 2D metal-free, metal, and metal-based compounds materials. Last, the review discusses the remaining reduction challenges and yield quantifications of ammonia in electrocatalysts, moreover, provide the future outlook and principle for designing new 2D electrocatalysts.

1.2 Categories of 2D Materials

Besides graphene, more and more graphene-like 2D materials have been developed over the past decade, such as Graphyne,[64] graphitic carbon nitride (g-C_3N_4),[65] hexagonal boron nitride (h-BN),[66] boron sheet,[67,68] black phosphorus,[69] transition-metal compound,[49] 2D metals,[70] transition metal dichalcogenides (TMDs),[71] 2D Carbides and Nitrides (MXenes),[72] and 2D metal−organic frameworks (MOFs),[73] layered double hydroxides (LDHs).[74] These 2D materials were widely applied in the field of energy storage and catalysis. Catalysis plays an important role in most cases, and the unique geometric and electronic properties of 2D materials make them excellent catalysts for various catalytic processes.[75]

1.2.1 Metal-free based 2D Materials

Since the FeN_3-embedded graphene as the catalyst for nitrogen fixation was reported in the 2016,[63] tremendous 2D metal-free substrate materials have been investigated for conversion of nitrogen to ammonia by using experimental or calculation methods at the ambient conditions. These materials include: carbon-based materials (Figure 3a, b),[63,76] graphitic carbon nitride (Figure 3c, d, and e),[77,78] hexagonal boron nitride (Figure 3f),[79] boron sheet (Figure 3g),[80] black phosphorus (Figure 3h),[80] and boron phosphide (Figure 3i).[80]
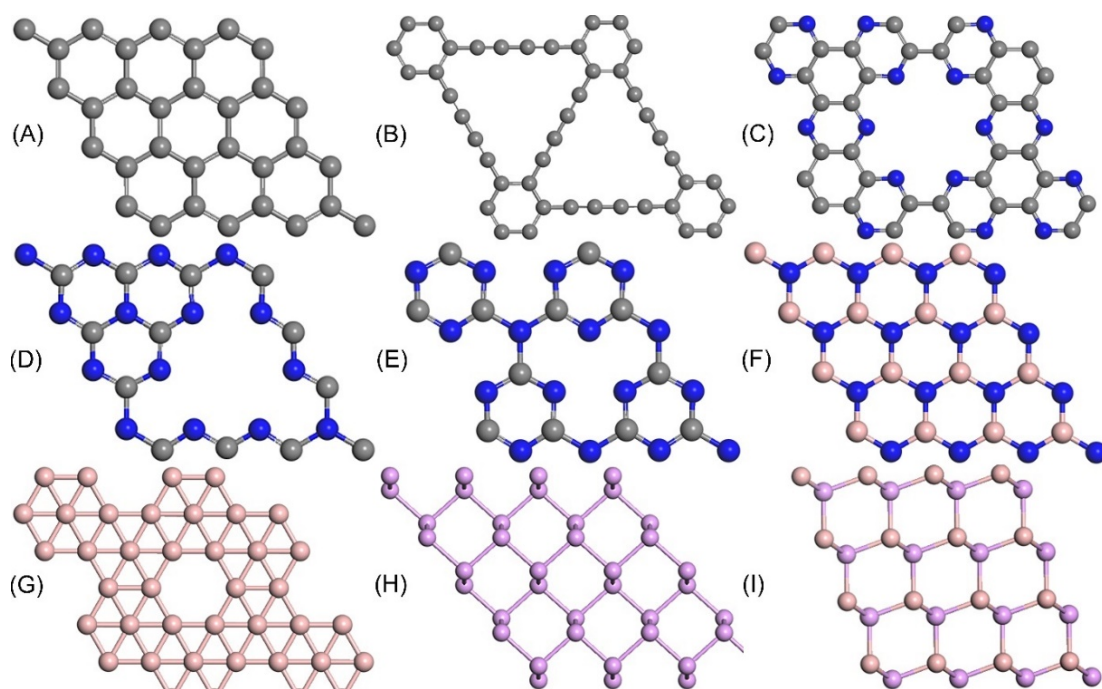
Figure 3. Schematic molecular configurations of (a) graphene, (b) graphdiyne, (c) nitrogenated holey graphene C_2N, (d) s-triazine-constructed g-C_3N_4, (e) tri-s-triazine-constructed g-C_3N_4, (f) hexagonal boron nitride, (g) boron sheet, (h) black phosphorus, (i) boron phosphide

1.2.1.1 2D Carbon-based Materials

In 2009,[81] N-doped carbon nanotubes were discovered to be a promising alternative to Pt catalyst for the oxygen reduction reaction (ORR) in alkaline fuel cells. Since then, this new class of carbon-based catalysts, including carbon nanotubes, graphene, graphdiyne, and carbon dots, have been demonstrated to be efficient for the water splitting, carbon dioxide reduction reaction (CO$_2$RR), NRR, and many other catalytic reactions applications.[82] Thermodynamically, the catalytic activities of carbon-based catalysts have been demonstrated to be induced by doping, including doping with mono/co/tri/multiple heteroatoms, charge-transfer doping, and even defective doping, to modulate the charge distribution of the carbon skeleton with potential synergistic effects.[82,83] Kinetically, the catalytic activities of C-MFCs have been further improved

16

by constructing 2D carbon-based architectures, as the mesoporous 2D framework can provide a large specific surface area to support massive catalytically active sites, a multidimensional conductive network for efficient electron transport, a large space to accommodate the electrolyte/reactant diffusion, and mechanical stability.[84-86]

Table 2. Experiment Activity of NRR on 2D Carbon-based Electrocatalysts.

Catalyst	Yield	FE	U (V)	Synthesis Method	Electrolyte
N/Carbon[87]	23.8 $\mu g\ h^{-1}\ mg^{-1}$	N. A.	-0.9	Carbonization	0.05 M H_2SO_4
$Pd_{0.2}Cu_{0.8}$/Graphene[88]	2.8 $\mu g\ h^{-1}\ mg^{-1}$	N. A.	-0.2	Facile Method	0.1 M KOH
Ru@N/Graphene[89]	120.9 $\mu g\ h^{-1}\ mg^{-1}$	29.6%	-0.2	Pyrolyzing	0.05 M H_2SO_4
TiO_2/Graphene[90]	15.13 $\mu g\ h^{-1}\ mg^{-1}$	3.3%	-0.9	Hydrothermal	0.1 M Na_2SO_4
B/Graphene[91]	9.8 $\mu g\ h^{-1}\ cm^{-2}$	10.8%	-0.5	Carbonization	0.05 M H_2SO_4
Mo_2C/Carbon[92]	11.3 $\mu g\ h^{-1}\ mg^{-1}$	7.8%	-0.3	Molten Salt	0.5 M H_2SO_4
O@N/Carbon[93]	20.15 $\mu g\ h^{-1}\ mg^{-1}$	4.97%	-0.6	Carbonization	0.1 M HCL
Ru/Carbon[94]	3.67 $\mu g\ h^{-1}\ mg^{-1}$	21%	-0.21	Hydrothermal	0.1 M HCL
B@N/Carbon[95]	7.75 $\mu g\ h^{-1}\ mg^{-1}$	13.79%	-0.3	Annealing	0.5 M H_2SO_4
Fe/Carbon[96]	7.48 $\mu g\ h^{-1}\ mg^{-1}$	56.55%	0.19	Carbonization	0.1 M KOH
CuO/Graphene[97]	9.8 $\mu g\ h^{-1}\ cm^{-2}$	3.9%	-0.75	Solvothermal	0.1 M Na_2SO_4
N/Carbon[98]	0.58 $\mu g\ h^{-1}\ cm^{-2}$	10.2%	-0.30	Solvothermal	0.1 M KOH
CoS/Graphene[99]	25.0 $\mu g\ h^{-1}\ mg^{-1}$	25.9%	-0.20	Annealing	0.05 M H_2SO_4

Among those carbon-based catalysts, graphene is single-atom-thick graphite, an allotrope of carbon in the form of 2D structure. It is composed of a hexagonal close-packed carbon network, in which each atom covalently bonds to three neighboring ones through the σ-bond (Figure 3a). For electrocatalytic applications for NRR, graphene presents both challenges and opportunities.[100] Given the delocalized π bonding network of graphene, adsorption dinitrogen molecule of reaction is generally massive endothermic, resulting in low intrinsic activity. Therefore, the basal plane of pristine graphene is normally considered inert for NRR. But its large specific surface area and good electrical conductivity make it very attractive as a substrate for NRR applications. At present, heteroatoms doping and defect engineering which could effectively tune the energy bandgap, spin density and charge density of graphene, regulating the

competition between NRR and HER through synergistic electron transfer interactions between the dopants and surrounding carbon atoms.[101]

Table 3. Calculated Activity of NRR on 2D Carbon-based Electrocatalysts.

Catalyst	GGA	Barrier (eV)	RDS
N/Carbon[87]	PBE	0.7	NHNH$_2$*
B/Graphene[91]	PBE	0.43	NH$_2$*
Mo$_2$C/Carbon[92]	PBE	0.92	NH$_3$*
Ru/Carbon[94]	PBE	0.42	NNH$_2$*
Fe/Carbon[96]	PBE	0.82	NH$_3$
Cuo/Graphene[97]	PBE	0.93	NNH*
Al/Graphene[102]	PBE	0.94	N$_2$H*
Ti@N$_4$/Graphene[103]	RPBE	0.69	NH$_3$*
Mo@N/Graphene[104]	PBE	0.47	NH$_3$
Fe@N$_3$/Graphene[63]	PBE	2.29	NH$_3$
Fe@N$_3$/Graphene[105]	PBE	0.66	N$_2$H*
Ni/Graphene[106]	PBE	1.23	N*
W/Graphene[107]	PBE	0.25	NH$_2$*
W@N/Ggraphdiyne[76]	PBE	0.29	N$_2$H*
B/Graphene[7]	RPBE	0.31	NH*

*Denotes an adsorption site on catalyst surface.

N-graphene is the most widely studied graphene-based electrocatalysts due to its simple synthesis process and relatively good electrocatalytic performance. Nitrogen is of similar atomic size to carbon, but is more electronegative. Therefore, doping with nitrogen can change the electron configuration of graphene while minimizing the lattice mismatch after doping. Being the earliest studied and the most important metal-free electrocatalyst, N-graphene has demonstrated some unique characteristics compared to metal-based electrocatalysts.[108] For example, the first reported N atom doped carbon-based materials electrocatalyst was prepared by carbonization and showed excellent performance for NRR activity.[87] In this work, N-doped carbon materials is reported as a cost-effective electrocatalysts for ammonia synthesis from electrocatalytic N$_2$ reduction under ambient conditions, where its N content and species were tuned to enhance N$_2$ chemical adsorption and nitrogen triple bond cleavage. The resulting

18

catalyst was effective for fixing nitrogen to ammonia with a high production rate of 23.8 $\mu g\ h^{-1}\ mg^{-1}$ in the 0.05 M H_2SO_4 solution. In addition, the material also can exhibit good stability in alkaline conditions owing to its stable chemical structure. At the atomic level, nitrogen doping can significantly enhance the NRR activity of carbon-based material by changing the electronic character of the nearby carbon atoms and by creating defect structures to enable strong nitrogen molecule adsorption. From both experimental and theoretical results, the NRR activity of catalyst is strongly dependent on the carbonization at different temperature. The main reason is the that there are different N contents at different temperature. In general, there are three nitrogen groups in N-carbon: pyridinic-N, pyrrolic-N, and graphitic-N. Pyridinic-N refers to nitrogen atoms at the edge of carbon nanosheet planes, each of which is bonded to two carbon atoms and donates one p-electron to the aromatic π system; pyrrolic-N refers to nitrogen atoms that are bonded to two carbon atoms and contribute to the π system with two p-electrons; and graphitic-N refers to nitrogen atoms that are incorporated into the graphene framework and bonded to three carbon atoms. In J. Zhao et al.'s work, the electrocatalyst of the highest nitrogen content obtained at 750 ℃ carbonization exhibits the best performance, its pyridinic (6.2 atom %), pyrrolic (5.3 atom%), and graphitic N contents (2.1 atom%). Increasing the pyridinic N content of catalyst can promote its ammonia production. Moreover, the above result was confirmed by DFT calculation, indicating that the pyridinic N site has the relatively low energy barrier for ammonia synthesis.

In addition, the NRR mechanism on N-carbon nanosheet has been investigated from both experimental and theoretical perspective in this work. On this catalyst, the NRR performance observed for N catalytic site could be attributed to a charge-transfer effect associated with the nitrogen dopants. More specifically, DFT studies indicate that the doping-induced charge and/or spin redistributions of the active play an important role in the enhancement of NRR activity. However, there is still debate regarding identification of the active site in N atom, mainly to (1) the complexity of nitrogen functionality in N atoms; (2) the difficulty of direct to ensure the origin source of N atom in the NRR catalyst containing nitrogen species.

Besides nitrogen, other p-block elements (e.g., B, O) have been doped into the graphene matrix by physical or chemical approaches,[7, 91, 93] Similar to nitrogen, the differing size and electronegativity of these heteroatoms to carbon can also induce electron modulation, which change the electronic properties of pristine carbon-based 2D materials. These kinds of electrocatalysts can usually be prepared by annealing GO with the appropriate heteroatom-coating precursor at high temperatures (900 °C). Normally, the precursors for B dopant is boron oxide or other boron compounds. It is known that doping graphene with heteroatom of either higher or lower electronegativities than carbon can induce electrocatalytic NRR activity through intramolecular charge transfer in the graphene matrix. Although the macroscopic effects of heteroatom doping are well documented, a microscopic view of the activity trend has not been built. Zheng et al. presented a significant study which linked the experimental NRR performance descriptor on a range of heteroatom-doped graphene

materials with the thermodynamic adsorption energies of series of key reaction intermediates.[91] Boron is an important doping element that induces electron deficiency in graphene, leading to a much improved electrocatalytic activity. Especially, the boron has three valence electrons in the $2s^2 2p^1$ and an empty orbital that is similar to the d orbital of TMs (Figure 4a).[109] In addition, the atom sites can also prohibit the binds of Lewis acid H^+ at those sites (under acidic conditions), which can promote the FE performance.[91] Notably, the authors proposed that boron atoms, confined with a 2D graphene sheet quoted as the BC_3 site, are active sites of nitrogen reduction with no metals involved. Metal-free synthesis of boron-doped graphene was established by thermal reduction of H_3BO_3 with graphene oxide. The concentration of dopants was tuneable in the synthesis and the local chemical environments of the boron dopants could be modified when annealed under different gas environments. Detailed measurement and analysis of X-ray photoelectron spectroscopy unveiled not only the boron contents but also up to four different local environments of boron atoms. The BC_3 structure, in which on boron atom connected with three carbon atoms in a sp^2 conformation, was the predominant configuration with more than 50% abundance when the sample was prepared under a H_2/Ar mixture, whereas its abundance dropped to about 35% when it was annealed in an Ar gas atmosphere. The authors reported encouraging performance of these materials with FE up to 10.8% at -0.5 V versus reversible hydrogen electrode (RHE) (Figure 4b). In order to illustrate the NRR effect of different boron structures, first-principle calculations with DFT showed that the lowest unoccupied molecular orbital (LUMO) (Figure 4c), indicative of the Lewis acid

site for N_2 binding, was perturbed and localized on the introduced boron atom in comparison with the pristine graphene. Concurrently, the binding affinity of proton might not have been promoted on boron, as suggested by the highest occupied molecular orbital (HOMO). The enhanced N_2 binding along with weak proton adsorption on the BC_3 site presumably contributes to the excellent FE, which is the highest among the reported values.
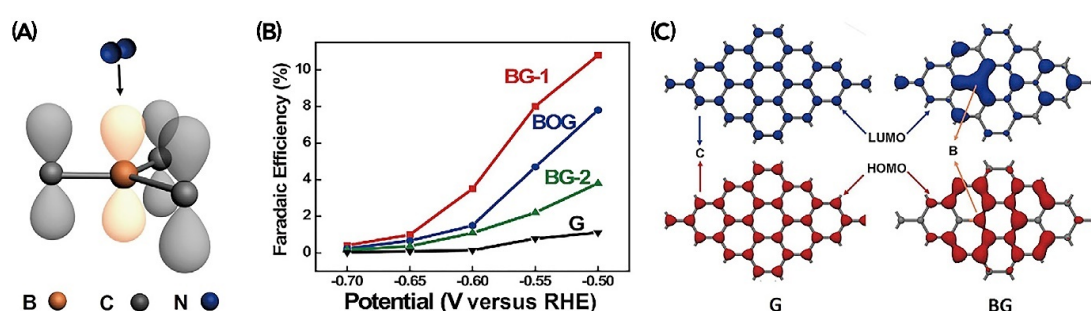
Figure 4. (a) schematic of the atomic orbital of BC_3 for binding N_2. (b) FE of nitrogen fixation at different potentials for boron-doped graphene with varying boron contents of BC_3 sites: pristine graphene, BG-1, 6.2% boron and 63.0% BC_3 sites; BG-2, 3.0% boron and 55.3% BC_3 sites; BOG, 6.4% boron and 35.3% BC_3 sites. (c) Comparison of the calculated LUMOs (blue) and HOMOs (red) between samples G and BG. [109]

Moreover, unlike transition metals, on which the active centres need empty d orbitals to accept the long-pair electrons of the nitrogen molecule, the sp^3 hybrid orbital of the boron atom can form B-to-N π-back bonding. Sun et al. reported that the catalytic activity of boron is highly correlated with the degree of charge transfer between the boron atom and the substrate. Among the 21 concept-catalysts, single boron atoms supported on graphene and substituted into MoS_2 are identified as the most promising NRR catalysts, offering excellent energy efficiency and selectivity against hydrogen evolution reaction.

22

Double P-block atoms doped graphene (O/N,[93] B/N[95]) have also been studied and show significantly enhanced NRR activity compared to their single-doped counterparts. DFT calculations reveal that the origin of this enhancement is the synergistic effect between the two or more different dopant elements. Although direct experimental observation of this synergy within the graphene matrix is difficult, theoretical analysis indicates that dual dopants can tailor the electron-donor properties of nearby carbon atoms to enhance intermediate adsorption. The most widely studied dual pair for carbon materials is B an N atoms. In 2019, wang et al. synthesized B-N pairs enriched defective graphene by three steps. Notably that the potential HER active site of catalytic site is the inner C atom near the NB pair, as the H_2 formation step is quite energetically unfavourable on the edge C site. Due to high selectively for NRR in the work, the FE achieved 9.77% at -0.2 V, exceeding most of the electrocatalysts under ambient conditions. The ammonia concentration was quantified by the indophenol's blue method and the ammonia-selective electrode method to ensure the accuracy of the ammonia yield. Besides the B-N pairs graphene, the O-N carbon nanosheet also synthesized by Sun and co-worker using tannin as the precursor in 2019.[93]

Graphene, with its large specific surface, good stability, and high electrical conductivity, has been considered to be an ideal support for single-atom catalysts (SACs). Atomically dispersing metal catalytic centres on graphene, especially earth-abundant elements could be a promising approach for producing alternative NRR catalysts to conventional catalysts. Luo et al. found the FeN_3 doped on the graphene, transition metal is responsible for the superior N_2 fixation activity for the first time.[63]

Especially, the charge variation of all intermediates was investigated, indicating the catalytic centre serve as the transmitter to transfer electrons and graphene act as an electron reservoir. To get further insight into the interactions between N_2 molecule and Fe catalysts with different N-coordination numbers, the local density of state (LDOS) of all potential catalysts with adsorbed nitrogen molecule was presented in Figure 5 a-f.[105] Generally, Fe 3d-electrons dominate LDOS below the Fermi level, and the comprehensive orbital hybridization with N_2 $2\pi^*$ orbitals, formation of bonding and anti-bonding states below and above the Fermi level. This leads to a significant charge transfer from the substrates to the adsorbed N_2 molecule. Charge transfer from the d band to the bonding state of p-d coupling, which enhances the strength of the chemical bonds between the N_2 adsorbate and the single Fe atom. Moreover, the charge density difference of N_2 adsorption at the Fe site shows a pronounced charge accumulation between Fe and N_2 and the redistribution around Fe and N_2. Such distribution of exchange charges corresponds to the anti-bonding $2p^*$ orbitals of N_2 molecule, which results in repulsive interaction between the two N atoms. As the charge transfer increases, the strong binding between the Fe and the N_2 molecule breaks the N-N triple bond, leading to activated intermediate of adsorbed N_2. By comparing the predicted maximum ΔG values in NRR pathways, we can observe that the rate determining step (RDS) of each substrate is the protonation of N_2* to form a N_2H* species. The applied potential (U) vs. standard hydrogen electrode (SHE) decreases as follows: Fe@G (1.37 V) < Fe@N_1 (1.16 V) < Fe@P_3 (0.92 V) < Fe@N_2 (0.80 V) < Fe@N_3 (0.66 V) (Figure 5i). The U vs. SHE decreases almost linearly with the increase Fe magnetic moment as

24

presented in Figure 5g. These results clearly suggest that Fe magnetic moment is one of important parameters determining the catalytic activity of supported single Fe atom towards N_2 activation. In addition, Bader charge analysis shows that the adsorbed N_2 molecule acts as an electron acceptor, and get about 0.12, 0.26, 0.28, 0.35 and 0.28 eV from the underlying Fe@G, Fe@N_1, Fe@N_2, Fe@N_3 and Fe@P_3 in Figure 5h, respectively. Charge transfer from the d band to the bonding state of p-d coupling, which enhances the strength of the chemical bonds between the N_2 adsorbate and the single Fe atom. Moreover, the charge density difference of N_2 adsorption at the Fe site shows a pronounced charge accumulation between Fe and N_2 and the redistribution around Fe and N_2 molecule. Such distribution of exchange charges corresponds to the antibonding 2p* orbitals of N_2 molecule, which results in repulsive interaction between the two N atoms.

Then the excellent performance for NRR on the Fe doped carbon nanosheet was confirm by some experiment results.[96,110] Emerging cutting-edge operando techniques are considered critical for giving insight into the intrinsic mechanism of catalytic process compared with ex-situ measurements. In-situ X-ray absorption near edge structure with ultra-sensitivity to the electronic properties of the metal was thus conducted under operation conditions to probe if single-atom was the actual active for the NRR. The results shown that the valence state of Fe was decreased during the reaction proceeds. During the reaction process, N_2 molecules are fixed on Fe sites by donating electrons to the unoccupied d orbitals of Fe, thus accounting for the genitive shift of its energy position.
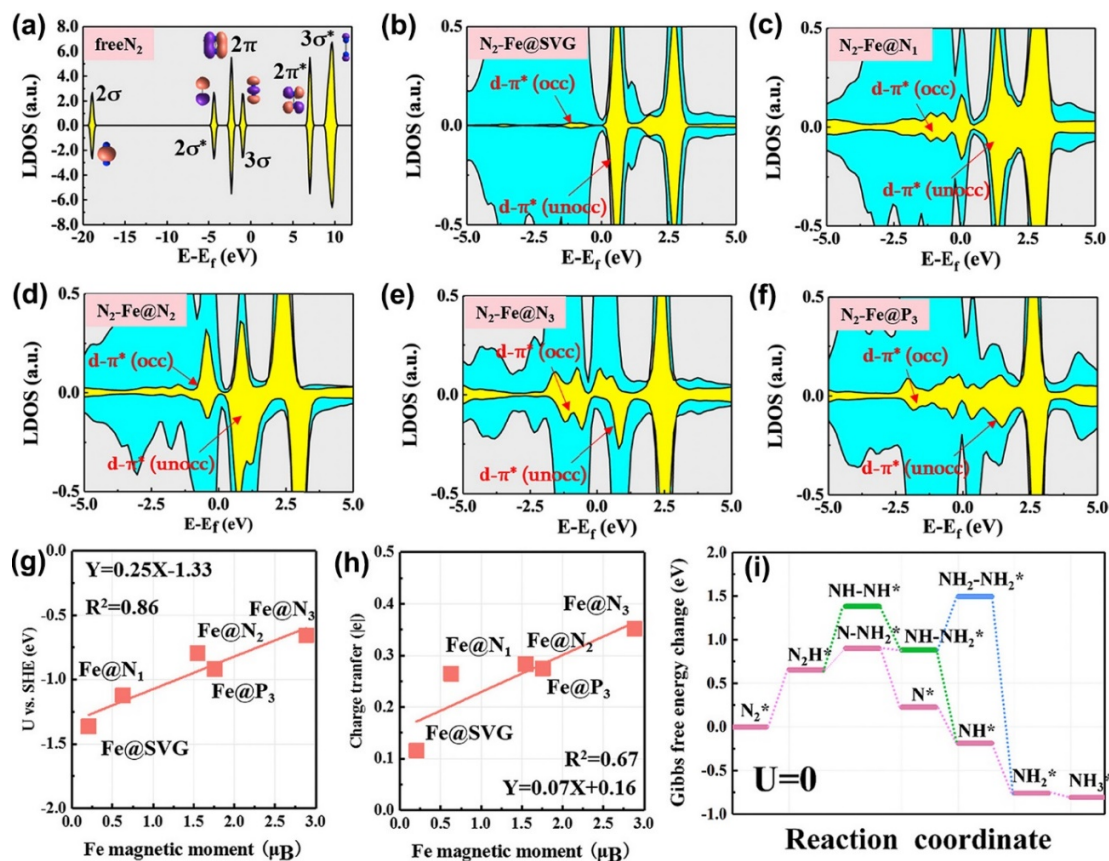
Figure 5. Spin-polarized LDOS of free N_2 molecule, (a) N_2 adsorbed on Fe@G, (b) Fe@N_1, (c) Fe@N_2, (d) Fe@N_3, (e) Fe@P_3, (f) graphene, respectively. The cyan and yellow parts represent Fe-3d and N-2p orbital, respectively. The Fermi level is set to 0 eV. (g) the scaling relations between the U vs. SHE and the Fe magnetic moment, (h) the N_2 molecule charge transfer and the Fe magnetic moment. (i) Correspond to the free energy diagrams for NRR on Fe@N_3 graphene at zero potential.[105]

Except the Fe and Mo, many researchers also studied other transition metal atoms in recent years. Typically, Ru SACs/N-C was prepared via pyrolyzing the Ru-containing derivative of zeolitic imidazolate frameworks (ZIF-8) (Figure 6).[105] Extended X-ray absorption fine structure spectra for samples exhibited only a prominent peak at 2.04 Å, which was attributed to Ru-N bonds. While metallic Ru and oxidized cluster was contributed peak about 2.50 Å, indicating the dispersion of isolated Ru atoms throughout the whole Ru single atoms on nitrogen-doped carbon nanosheet (Ru SACs/N-C) structure. The concentration of NH_4^+ was also quantified via a calibrated

indophenols blue method, which was in good agreement with the result determined by ion chromatography. The production of hydrazine was below the detection limit, indicating the high selectivity for NH_3 over catalysts. Figure 6 shows the Ru SAs/N-C for NH_3 production has the relatively higher partial current density at all applied potential. At -0.2 V versus RHE, Ru SAs/N-C exhibited a FE of 29.6% for ammonia synthesis with the yield rate of 120.9 μg h^{-1} mg^{-1}. Amazingly, the yield rate can be enhanced about thirty times when the above catalyst was prompted by ZrO_2 under a similar applied potential, owing to the promoter which can suppress HER during the NRR.[94]

Due to the excellent NRR performance on the Fe/graphene, two similar works screened all possible transition metal on the graphene with different N coordination.[103,107] Generally, N–G-supported catalysts can be divided into two categories: three-coordinate and four-coordinate configurations by single metal atoms located on single or double C vacancies. As a result, four different types of coordination can be obtained considering the variation of ratio of coordinated N atoms, including M_1C_3, M_1C_4, M_1N_3, and M_1N_4, as shown in Figure 7. Moreover, 30 kinds of TMs with nine different types of coordination and two N_2 adsorption configurations for each SACs are taken into consideration, making 120 initial adsorption systems in total (Figure 7c).
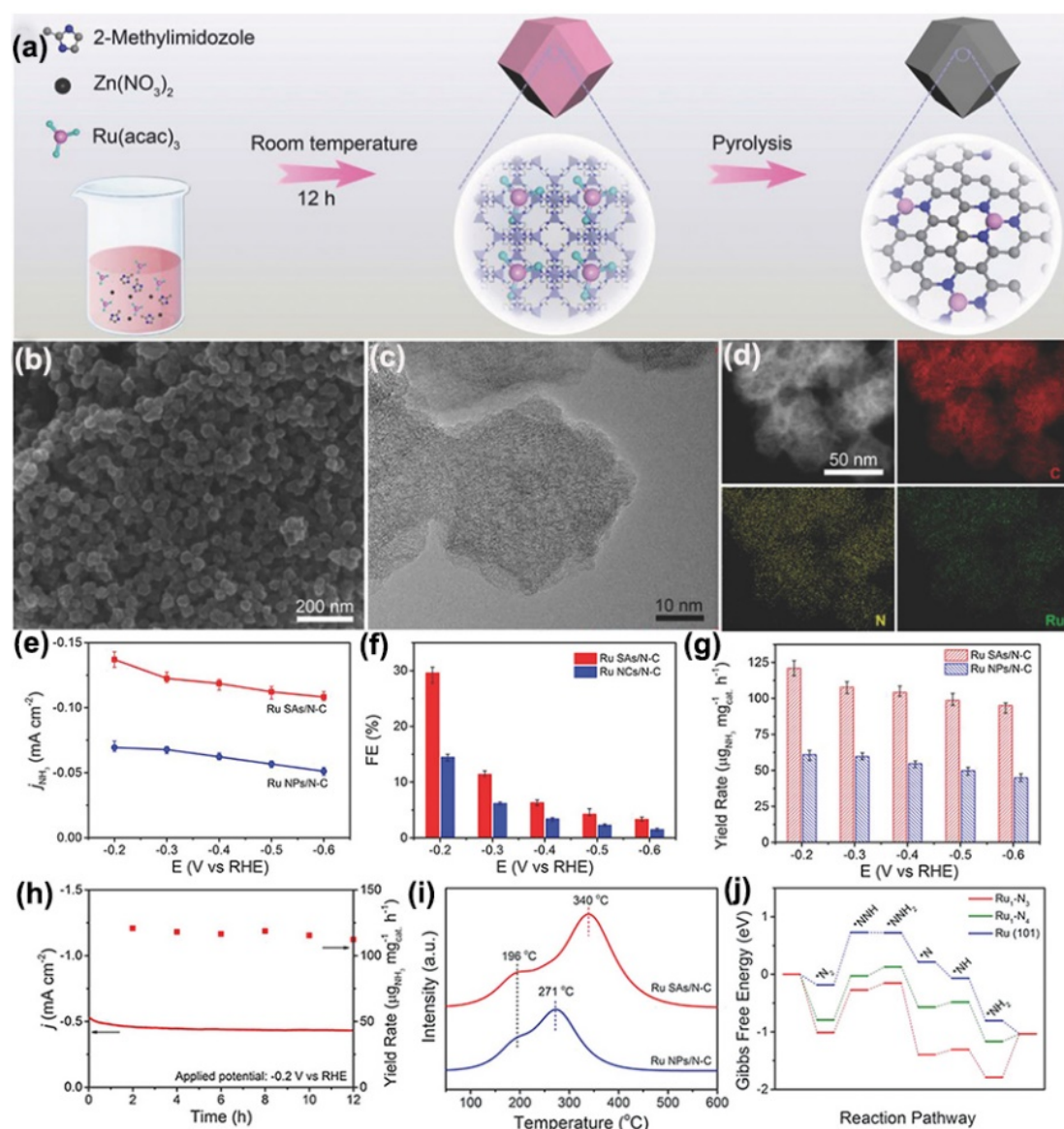
Figure 6. (a) Scheme of the synthetic procedure for Ru SCAs/N-C, (b) typical SEM image, (c) magnified TEM image, (d) HAADF-STEM image and corresponding EDS elemental mapping for Ru SCAs/N-C. (e) Current densities for NH_3 production. (f) FE and (g) yield rate of NH_3 production at different applied potentials on Ru SCAs/N-C and Ru NPs/N-C, h) 12 h durability test for Ru SCAs/N-C toward N_2 electrochemical reduction at −0.2 V versus RHE. (i)The N_2-TPD profiles of Ru SAs/N-C and Ru NPs/N-C. (j) Free energy diagram of the N_2 electrochemical reduction with a distal pathway.[105]

Metal−support interactions are important in heterogeneous catalysis, and especially

so for SACs due to a direct alteration of the electronic structure of the metal atoms.

Diffusion and aggregation of metal can be problematic in catalyst−support systems

since these can reduce catalytic activity and the stability of catalytic cycles. The binding

energy of each metal atom at the defected graphene supports to assess the stability was

28

calculated in this work. Although binding of the metal atom at defect sites is thermodynamically favourable, metal atoms can aggregate on the support. Thus, compared Eb and the cohesive energies of metal of each metal atom in order to determine SACs that prevent both diffusion and aggregation. To find SACs showing an improved catalytic performance compared to the bulk metal catalysts, the work focused on SACs showing $\Delta G_{RDS} \leq 1.0$ eV, corresponding to better or similar catalytic activity than that of Ru (0001) stepped surface (1.08 eV). The ΔG_{RDS}'s of all SACs are shown in Figure 7d.

In addition to suppressed H adsorption on SACs, it investigated NRR selectivity on SACs in more detail by considering $*N_2/*H$ selectivity. If SACs cannot sufficiently bind N_2, it seems difficult to achieve high NRR selectivity although H adsorption is suppressed. As such, the $*N_2/*H$ selectivity is an important indicator to consider in NRR, although in the literature the overpotentials for NRR are in Figure 7e, several SACs are in the $*N_2$ dominant region ($\Delta G(*N_2) < \Delta G(*H)$), showing improved selectivity. For these SACs, N_2 adsorption would be less hindered by H adsorption in the low overpotential region. However, Ir@C_3, Re@C_4, and Os@C_4, known to show low ΔG_{RDS} (Figure 7f), are in the $*H$ dominant region ($\Delta G(*N_2) > \Delta G(*H)$) due to their highly positive $\Delta G(*N_2)$; thus, $*N_2$ activation is expected to be difficult. Consequently, we suggest Mo@C_3, Nb@C_3, V@C_3, Mn@N_3, La@N_3, Sc@N_4, and V@N_4 as satisfying both the superior catalytic activity and $*N_2/*H$ selectivity. Also, V@C_4, Ti@N_3, and Ti@N_4 seem to be promising, which are near the $*N_2/*H$ selectivity borderline ($\Delta G(*N_2) = \Delta G(*H)$) in Figure 7e with significantly low ΔG_{RDS}.

For early TMs such as Sc and Y, their d electrons are mainly donated to graphene to make them stable on the substrate. Thus, these TM atoms lack spare electrons to weaken the nitrogen triple bond, resulting in a very weak binding strength with N_2. On the contrary, late TMs including Cu, Zn, Au, Ag, and so on, have no empty d orbital to accept lone-pair electrons from N_2. Consequently, their binding strengths with N_2 are also weak. For the middle TMs, such as Nb, Mo, and W, they have both unoccupied d orbitals and enough d electrons to ensure the bonding with the substrate and back donation into anti-bonding of N_2. Therefore, the supported metal atoms will present relatively strong binding strength with N_2. Moreover, the third row TMs generally have stronger interaction with N_2 than the second row TMs, followed by the first row TMs, as the areas of red/blue regions increase/decrease gradually with the increase of row number (Figure 7f). This can be ascribed to the distinct electron donating ability of different row TM atoms. The d electrons are more easily to lose and more and more electrons will be donated into anti-bonding orbitals of N_2 with changing elements from top to bottom in the same group. Subsequently, triple bond and TM-N bonds will be gradually weakened and strengthened, respectively. For the same TMs, ΔE_{N2} on metals with high N coordination (such as M_1N_3 and M_1N_4) are usually more negative than that with low N coordination (such as M_1C_3 and M_1C_4). This may be understood by the fact that the coordinated C atoms can retain threefold coordination as that in the sp^2 graphene lattice, leading to more frequently acceptable match with the TM d-states compared to the sp^3-hybridized N atom. As a result, the embedded TM atoms will become more stable with C coordination and thus have a weaker interaction with N_2.
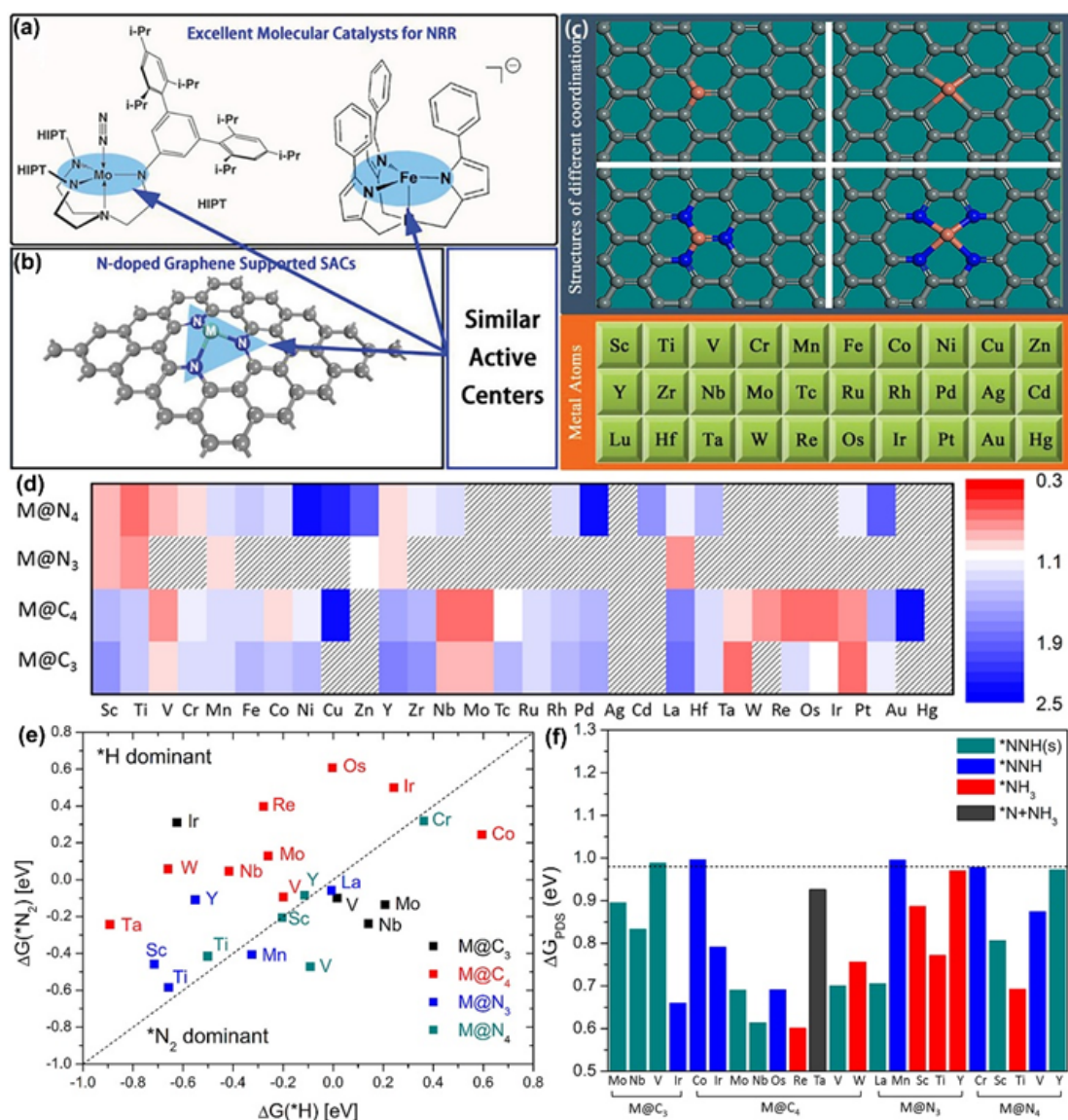
Figure 7. (a) Structures of two excellent molecular catalysts for NRR. (b) Structure of N-doped graphene–supported transition metal, which possess similar active centres to that of the molecular catalysts for NRR. (c) Structures of N–G-supported metal with different coordination.[107] (d) ΔG_{RDS} (eV) on 120 catalysts considered in this work. SACs filled with patterns represent thermodynamically unstable SACs (metal−support anchoring energy less favourable than metal−metal cohesive energy). (e) Calculated $\Delta G(*H)$ and $\Delta G(*N_2)$ on SACs that satisfy $\Delta G_{RDS} \leq 1.0$ eV. Dashed line indicates $\Delta G(*H) = \Delta G(*N_2)$. (f) Reaction free energy change at RDS (ΔG_{RDS}) on SAC candidates. Colour codes represent the product at the RDS of each SAC. Green, blue, red, and black represent that *NNH (s), *NNH, *NH$_3$, and *N+NH$_3$ formations being the RDS, respectively.[103]

And in another work, *N$_2$/*H selectivity was considered by comparing the $\Delta G(*N_2)$ with $\Delta G(*H)$ on promising SACs.[107] The authors proposed several promising

candidates with excellent catalytic performance as efficiently selected out from 540 systems. Especially, WC$_3$/graphene exhibits the most outstanding performance with an extremely low onset potential of 0.25 V. As well, the search criteria also suit for the graphdiyne substrate.[76] Currently, TM-based catalyst complexes are coordination that contain the N atom as a ligand. S is the neighbour of N atom in the periodic table. The strong-coupled CoS@N/graphene were synthesized by an in situ annealing method that enables the uniform growth of cobalt sulphides nanoparticles on a graphene sheet.[99] Notably, the strongly coupled hybrids exhibit an outstanding FE and R, which are superior to some reported TM@N/graphene electrocatalysts. Because the strongly coupled chemical bonds enable control label interfacial effects and can accelerate the reaction kinetics by acting as an electron transport channel.

1.2.1.2 Graphitic Carbon Nitride

Graphitic carbon nitride (g-C$_3$N$_4$) is a 2D crystal with a van der Waals layered structure, and is considered to be the most stable allotrope of all the various carbon nitride materials.[111] Analogous to graphene, the crystal structure of g-C$_3$N$_4$ can be described as a hexagonal carbon framework with N substituted carbon through the sp^2 hybridization of carbon and nitrogen atoms (Figure 2c, d).[112] Three structural isomers of g-C$_3$N$_4$ exist and are synthesized using different precursors and condensation methods. The first one is named C$_2$N-h2D crystal which was successful synthesized through a simple wet chemical reaction (Figure 2b).[113] The second one is constructed by condensed triazine (1,3,5-triazine, C$_3$N$_3$) units with a periodic array of single carbon atom vacancies.[114] The third one is composed of condensed heptazine (1,3,4,6,7,9,9b-

heptaazaphenalene, C_6N_7) subunits connected through planar tertiary amino groups, and has larger periodic vacancies in the lattice.[115] Generally, various nitrogen-rich precursors, such as urea, thiourea, melamine, cyanamide, and Dicyandiamide, can be used for synthesizing g-C_3N_4 via thermal treatment. Like graphene, 2D g-C_3N_4 nanosheets can be obtained from the exfoliation of bulk g-C_3N_4 materials. Corresponding techniques include ultrasonication-assisted liquid exfoliation, liquid ammonia-assisted lithiation, post-thermal oxidation etching, and thermal delamination combined with sonication.[116] To date, heptazine-based g-C_3N_4 has been used as either an active material, support material, or as a metal atom coordinator in various electrocatalytic applications (ORR or NRR).[116,117]

Due to its band gap (~2.7 eV), the semiconducting properties of g-C_3N_4 make it very suitable for visible light.[118] However, the degree of condensation of g-C_3N_4 directly affects its electronic structure and band gap that in turn affects its activity.[119,120] In this regard, bulk g-C_3N_4 suffers from low activity. By contrast, 2D g-C_3N_4 nanosheets have exhibited desirable activity due to the abundant structural defects and surface terminations that play key roles in catalytic activation. Other than band gap, the nitrogen-rich carbon framework of g-C_3N_4 is another important feature for electrocatalysis. Normally, nitrogen or sulphur doping can enhance the electron-donor properties of graphene and other carbon networks, resulting in an improvement to interactions between carbon and intermediates during electrocatalytic processes.[117,121] Therefore, two basic design principles are typically employed for synthesizing g-C_3N_4-based electrocatalysts. These are (1) optimization of material conductivity and (2)

appropriate tuning of active sites. To optimize conductivity, g-C$_3$N$_4$ has been composited with conductive carbon materials. For example, g-C$_3$N4 was incorporated into a mesoporous carbon framework and showed significantly enhanced NRR activity compared to pristine g-C$_3$N$_4$.[122] Active sites can be tuned in various ways but the intention is to favourably modify the adsorption energy of target intermediates. In one example, a g-C$_3$N$_4$ and N-graphene composite achieved NRR performance comparable to that of metallic catalysts.[117] Combined atomic imaging, spectroscopic analysis, and DFT calculations revealed that the interfacial structure of the composite optimized the electronic state and ΔG_{N*} which facilitated electron/charge transfer and enhanced catalytic activity.[7]

Table 4. Experiment Activity of NRR on 2D Graphitic Carbon Nitride Electrocatalysts.

Catalysts	Yield	Synthesis Method	Aqueous
NVs/C$_3$N$_4$[117]	1.24 mmol h^{-1} mg^{-1}	Annealing	20% Methanol
Ga$_2$O$_3$/C$_3$N$_4$[77]	112.5 μmol h^{-1} L^{-1}	Annealing	0.04 mM Methanol
BP/C$_3$N$_4$[119]	347.5 μmol h^{-1} L^{-1}	Photodepostion	5 vol% Methanol
Cyano/C$_3$N$_4$[120]	99.56 μmol h^{-1} L^{-1}	Annealing	10 vol% Methanol
TiO$_2$/C$_3$N$_4$[123]	250.6 μmol h^{-1} L^{-1}	Calcination	0.5 M Na$_2$SO$_4$
Au/C$_3$N$_4$[124]	1305 μg mg^{-1} L^{-1}	Sol-gel	5 mmol L^{-1} H$_2$SO$_4$
Sulfur/C$_3$N$_4$[121]	88.09 μmol h^{-1} L^{-1}	Annealing	4 vol% Methanol
SiW$_{12}$/C$_3$N$_4$[125]	20.77 μmol h^{-1} L^{-1}	Annealing	0.25 M Na$_2$SO$_4$

Photo(electro)catalytic N$_2$ fixation is one of the most interesting and challenging methods for artificial nitrogen under mild conditions because this strategy uses renewable and sufficient solar energy as the driving force. The first study on photocatalytic N$_2$ fixation was reported by Schrauzer and Guth in 1977.[126] Nitrogen was reduced under ultraviolet (UV) light irradiation using iron-doped TiO$_2$ at room conditions. The production rate of ammonia decreases after a few hours of light irradiation because the ammonia produced could be further oxidized by photogenerated

holes. These disadvantages limit the development and practical use of photocatalytic N_2 fixation. Designing new photocatalysts that have a strong ability to selectively photocatalyze N_2 fixation is not only important but also a challenge in the promotion of the development of photocatalytic N_2 conversion.

Table 5. Calculated Activity of NRR on 2D Graphitic Carbon Nitride Electrocatalysts.

Catalysts	GGA	Barrier (eV)	RDS
Mo/C$_2$N[127]	PBE	0.17	NH$_3$
Ti/C$_3$N$_4$[128]	PBE	0.51	NH$_3$*
B/C$_3$N$_4$[129]	PBE	0.20	NH$_3$*
W/C$_3$N$_4$[130]	PBE	0.35	NH$_3$
B/C$_2$N[131]	PBE	0.15	NHNH*
B/C$_2$N[132]	PBE	0.35	NH$_2$NH$_3$*
B/C$_3$N$_4$[7]	RPBE	0.89	NH$_3$
Mo/C$_3$N$_4$[133]	RPBE	0.82	N$_2$H*
Pt/C$_3$N$_4$[134]	PBE	0.24	NHNH*

*Denotes an adsorption site on catalyst surface.

Recently, Li and his coworkers investigated the photocatalytic N_2 fixation on BiOBr nanosheets.[135] They observed that the photocatalytic ammonia synthesis activity of BiOBr could significantly be improved by introducing several oxygen vacancies (OVs). OVs could activate N_2 and excellent improve interfacial electron transfer. Their results give us an inspiration that nitrogen vacancies (NVs) may be more effective for photocatalytic NRR than OVs. First, NVs have the same shape and size as the nitrogen atom in N_2. Thus, a NV-containing material is like a N_2-imprinted polymer. By now, molecular-imprinted polymers are an emerging material for selective recognition. Therefore, NVs may be used as excellent adsorbents and activators for nitrogen molecule.[136] Second, NVs as defects can trap photogenerated electrons to inhibit the recombination of photogenerated carriers.[137]
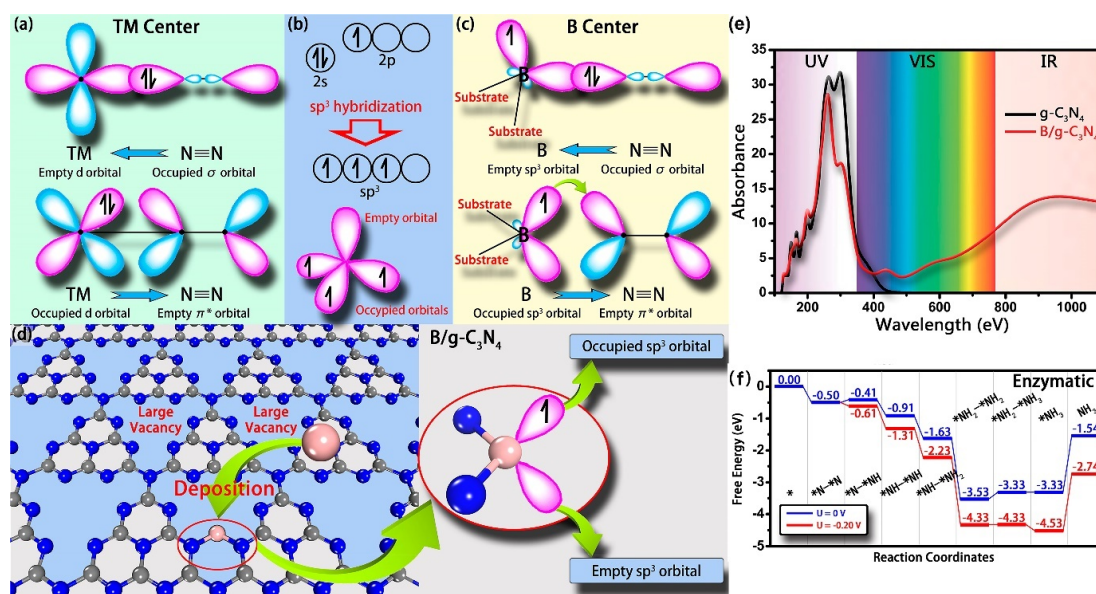
Figure 8. (a) Simplified schematic of N_2 bonding to transition metals. (b) Electronic configuration of pure B atom and B atom with sp^3 hybridization. sp^3 hybridization of B will result in four sp^3 hybrid orbitals, where three of them are half filled and the rest one is empty. (c) N_2 binding motifs to the B atom that is stabilized on the substrate. (d) Design concept of as a photocatalyst for N_2 fixation. Gray, blue, and pink balls represent the C, N, and B atoms, respectively. (e) Optical adsorption spectra of pure g-C_3N_4 and B/g-C_3N_4. (f) Free energy diagrams for NRR by enzymatic mechanisms at different applied potentials.[128]

As mentioned above, g-C_3N_4 is a promising active and stable metal-free photocatalyst and has been applied to various reactions. It is composed of 3-fold-coordinated and 2- fold-coordinated N atoms and 3-fold-coordinated C atoms which are bonded to 3 N atoms (Figure 8d). The 2-foldcoordinated N atoms endow g-C_3N_4 the capacity for the incorporation of extra atom. In Wang's work, two N−B bonds are generated to stabilize the B atom onto g-C_3N_4 and, meanwhile, leaving one occupied sp3 orbital and one empty sp^3 orbital. Therefore, the anchored B atoms will have strong interaction with the gas phase N_2 molecules. Moreover, large periodic vacancies of g-C_3N_4 offer enough space for the adsorption and subsequent reduction of N_2. Generally, the chemisorption of gas phase N_2 onto the surface of the catalysts is the prerequisite

for an efficient NRR process. For transition metal (TM) based catalysts, their strong binding strength with N_2 can be ascribed to their advantageous combination of empty and occupied d orbitals (Figure 8a). On one hand, due to the existence of lone-pair electrons of N_2, TM centres need to have empty d orbitals to accept the lone-pair electrons. On the other hand, to enhance the N−TM bonds, the TM atoms should have separated electrons that can be donated into the antibonding orbital and weaken the nitrogen triple bond. Significant charge transfer between the anchored B atom and N_2 can be observed for both adsorption patterns. Generally, the charge transfer is one-way that from one specie to another depending on their relative electron accepting and donating abilities. Interestingly, charge transfer here is found to be two-way that charge accumulation and depletion can be observed for both N_2 molecule and B atom. This phenomenon is actually in perfect accordance with the "acceptance−donation" process as described above: B atom will accept lone-pair electrons and simultaneously donate electrons into the antibonding orbital of N_2. Therefore, these calculation results, including high binding strength and two-way charge transfer between N_2 and B/g-C_3N_4, strongly support the design concept.

As for photocatalysts, the photoconversion efficiency is very important. However, it is well-known that g-C_3N_4 shows only marginal absorption in the visible light range owing to its relatively large band gap. The improvement of the optical adsorption activity is therefore highly desirable to achieve better photocatalytic performance of g-C_3N_4. Interestingly, the decoration of B on g-C_3N_4 can greatly enhance the visible light and infrared light harvesting. As shown in Figure 8e, the main light adsorption peak of

pure g-C$_3$N$_4$ is located at $\sim$300 nm wavelength, indicative of its strong absorbance of UV light and very limited absorbance of visible light. These results are in good agreement with previous studies. Although the absorbance of ultraviolet light will be slightly weakened, both the visible light and IR light absorbance can be greatly improved for g-C$_3$N4 with the decoration of B. The enhancement of the light absorbance of B/g-C$_3$N$_4$ can be ascribed to the decrease of band gap. With the decoration of B atom, the band gap decreases to 1.12 from 2.7 eV, which endows B/g-C$_3$N$_4$ the ability of capturing the light with longer wavelength (visible and infrared light). Therefore, B/g-C$_3$N$_4$ would possess higher photoconversion efficiency than pure g-C$_3$N$_4$, which can ensure more efficient generation of photoexcited electrons and better photocatalytic performance. Finally, the subsequent N$_2$ reduction process, the computed onset potential is only 0.20 eV through the enzymatic mechanism (Figure 8f). Subsequently, two similar works were published in 2019: the NRR performance on the B doped C$_2$N by using DFT calculation.[130,131] It concluded that the charge transfer between B dopant and the adsorbed N$_2$ molecule on B/C$_2$N similar with variation of B/C$_3$N$_4$. Moreover, they also have the same favorable reaction mechanism.

Phosphorus or sulfur, neighbor of boron, was doped into the C$_3$N$_4$ by a photo-deposition method (Figure 9).[119,121] The visible-light photocatalytic nitrogen fixation activities of BP nanosheets/graphitic carbon nitride nanosheets photocatalyst (BPCNS) are shown in Figure 9g. The nitrogen fixation rates of CN (23.7 μmol h^{-1} L^{-1}), CNS (40.5 μmol h^{-1} L^{-1}), BPCNS (45.3 μmol h^{-1} L^{-1}) and 0.05BPCNS-WC (48.4 μmol h^{-1} L^{-1}) are similar, while BPCNS exhibited a much-improved photocatalytic activity for

nitrogen fixation compared to either BPCNS or CNS. The highest photocatalytic rate for nitrogen fixation is observed on 0.05BPCNS (347.5 μmol h^{-1} L^{-1}), which is even higher than that on 0.05Pt-CNS (337.2 μmol h^{-1} L^{-1}). However, the nitrogen fixation rate decreased to 258.3 μmol h^{-1} L^{-1} when the BP content increased to 10%, it may be attributed to an increase in the recombination of charge carriers owing to the excessive loading of the cocatalyst. Similar results are demonstrated through the photocatalytic reduction of Cr (VI) under visible light irradiation. It can be clearly seen that the reduction activity decreases in the order 0.05BPCNS > 0.1BPCNS > 0.01BPCNS > 0.05Pt-CNS > 0.05BPCNS-WC > CNS > CN (Fig. S4). Both the above experiments prove the high activity of BPCNS for nitrogen fixation as well as pollutant reduction.

Coupling metal nanoparticles with g-C$_3$N$_4$has proven to be an appropriate strategy to improve the photocatalytic activity of g-C$_3$N$_4$. The photogenerated electron transfer between metal and g-C$_3$N$_4$ is different from that of semiconductor modified g-C$_3$N$_4$. When a semiconductor contacts with metal, a contact potential difference will be generated at their interface due to their different work func-tions. This potential difference is called the Schottky barrier, which can induce the direc-tional migration of photogenerated electrons from semiconductor to metal and thereby greatly enhance the charge separation effi-ciency. Moreover, the surface plasmon resonance effect of some noble metals (such as Ag, Au, etc.)[124] and even non-noble metals (e.g., Bi) can enhance light absorp-tion, while the excellent catalytic activity on the surface of some transition metals (e.g., Mo, W, Ti) can accelerate the surface catalytic reactions.[126,127,129,132]
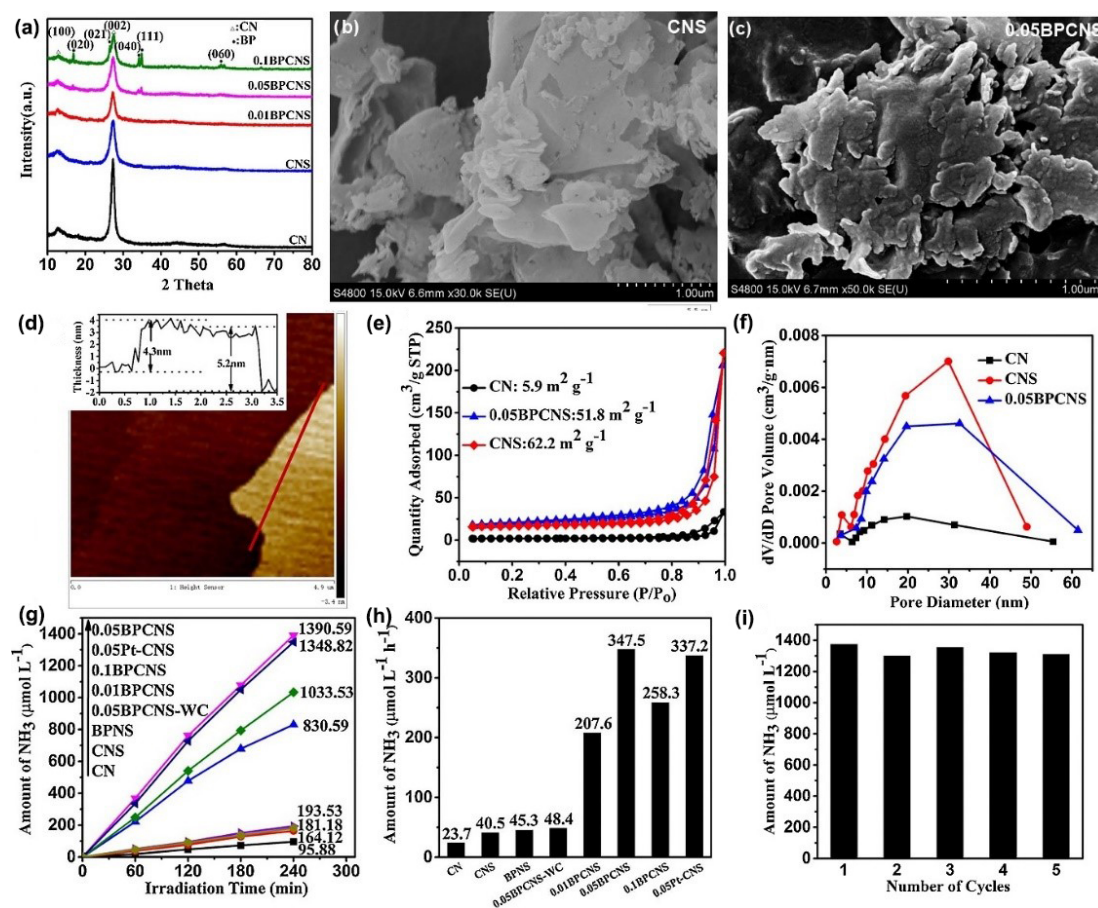
Figure 9. (a) The XRD pattern of CN, CNS, and BPCNS. (b), (c) FESEM images of CNS and 0.05BPCNS, respectively. (d) AFM image of 0.05BPCNS. (e) Nitrogen adsorption-desorption isotherms. (f) Pore size distributions of CN, CNS, and 0.05BPCNS. (g) Time course and (h) 4-h average reaction rate of photocatalytic nitrogen fixation on CN, CNS, BPNS, 0.05 BPCNS-WC and BPCNS. (i) Recycle runs of nitrogen fixation on 0.05BPCNS.[119]

A crucial prerequisite for the application of SACs is to prevent the aggregation of single atoms and guarantee their long-term use; that is to say, the single atom is positioned on a desired position without any apparent migration. Owing to the tunable morphology of the corrugated g-C_3N_4, it is hard to locate the minimum-energy configuration of the SAC using the geometry optimization (Figure 10a).
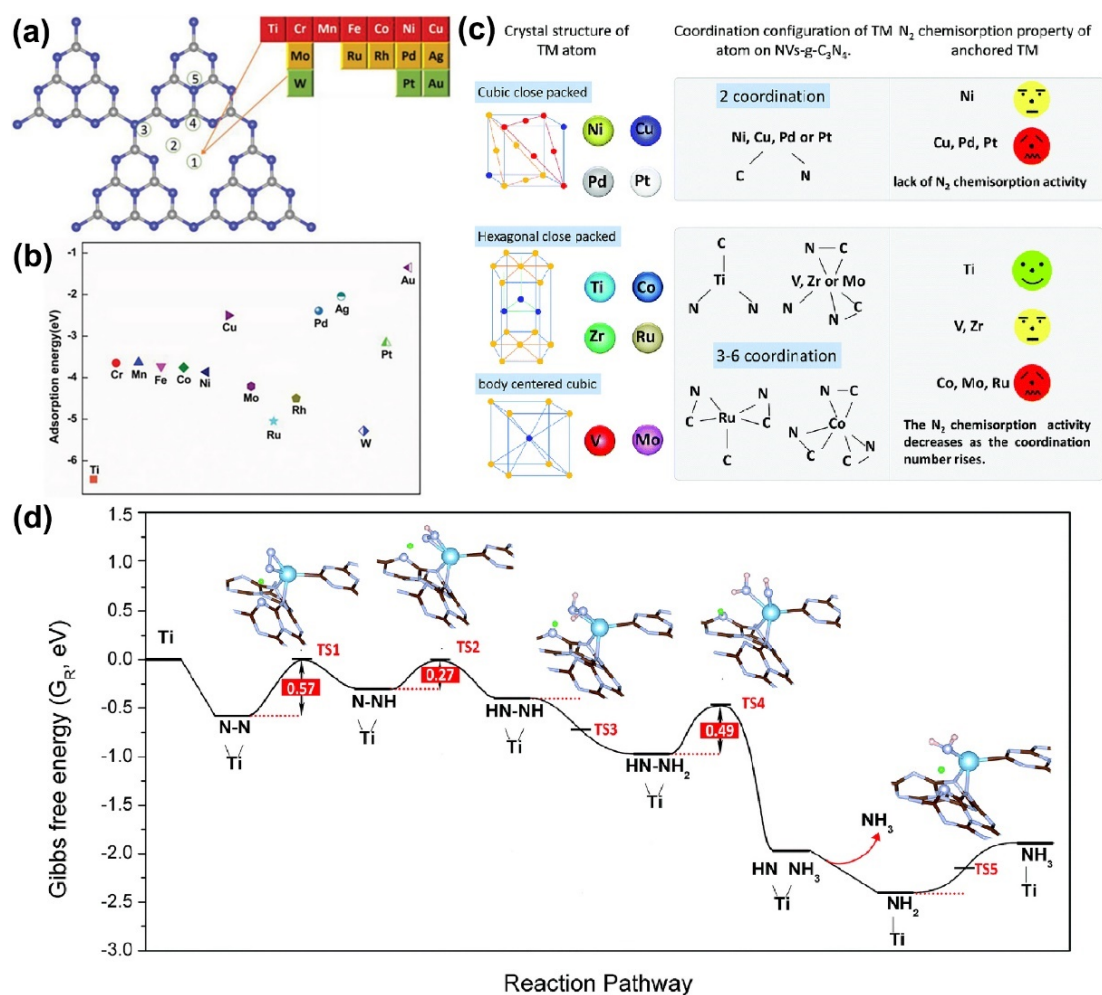
Figure 10. (a) The optimized structure of pristine g-C$_3$N$_4$ monolayer and the possible sites for the single metal atoms to adsorb on the g-C$_3$N$_4$ substrate. (b) The computed adsorption energies of single metal atoms.[107] (c) Illustration of the relationship among the crystal structure of the TM, and the coordination number and the N$_2$ adsorption ability of the single TM atom. (d) The energy barriers along the minimum energy path for NRR on Ti@NVs-g-C$_3$N$_4$.[103]

A rational design of SACs should take the following two factors into account: (1) a stable combination of anchored atoms with anchoring materials and (2) abundant active sites present on the anchored atoms. The different electronegativities may explain the difference in the thermodynamically most favourable anchoring site. The favourable adsorption energies (Figure 10b), especially for Ti, Ru, and W (over -5 eV), indicate that these metal atoms could bind strongly with g-C$_3$N$_4$, and the corresponding SACs are of good thermodynamic stability. The above results are well consistent with

41

previous theoretical studies.[107]. In addition, molecular dynamics calculation is necessary to determine the anchored sites. Firstly, the metal atoms in cubic close-packed structures such as Ni, Pt, Cu and Pd formed only two bonds with the substrate; thus, these metal atoms are dangling in an unstable condition. Even with a low-coordination number, these metal atoms did not perform well in nitrogen adsorption and activation (Figure 10c). On the other hand, hexagonal close-packed and body centered cubic metal atoms can coordinate 3 to 6 atoms on the substrate, among which Co can coordinate with about 6 surrounding atoms. The test implies the failure of the Co atom for N_2 activation. For hexagonal close-packed and body centered cubic metal atoms, it is evident that the N_2 fixation activity predominantly depends on the coordination number of the metal atom.

From the Li et al.'s and above result work,[127] the Ti was selected as the most promising atom in reactive site on substrates, and the RDS of reaction is the first protonation step. Furthermore, in order to comprehend the reaction mechanism in detail, CI-NEB was used to find out the transition states (TS) along the pathway. The energy barriers between every two neighboring intermediates are revealed in Figure 10c. As a supplement of the calculated pathway, the TS suggest the energy barriers even in the spontaneous reactions. The first and maximum energy barrier of 0.66 eV lies in the very first protonation process ($N_2^* + H^+ + e^- / N_2H^*$). Subsequently, it requires an activation energy of 0.40 eV when the second H^+/e^- pair attacks the N_2H^* to produce $N_2H_2^*$ species. A higher barrier of 0.63 eV was found in the hydrogenation of $NHNH_2^*$. If we take the

42

zero-point energy and entropy terms into consideration, the barriers can be further reduced to 0.57 (TS1), 0.27 (TS2) and 0.49 eV (TS4), respectively.
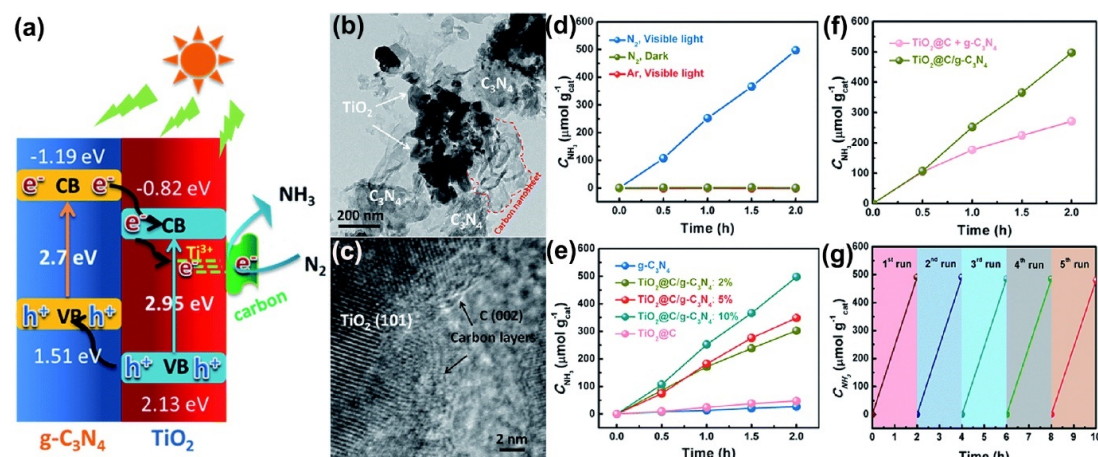
Figure 11. (a) Schematic illustration of the energy band structure and electron–hole separation of $TiO_2@C/g$-C_3N_4. (b) and (c)TEM and HRTEM images of $TiO_2@C/g$-C_3N_4, respectively. (d) Controlled experiments on photocatalytic NH_3 production under different conditions. (e) Photocatalytic activity of the systems of $TiO_2@C/g$-C_3N_4 and $TiO_2@C/g$-C_3N_4 for NH_3 production under visible light irradiation (l > 420 nm). (f) Comparison of the photocatalytic activity of $TiO_2@C/g$-C_3N_4 and physically mixed $TiO_2@C/g$-C_3N_4 for NH_3 production. (g) Cycle runs for photocatalytic NH_3 production over $TiO_2@C/g$-C_3N_4 under visible light irradiation (> 420 nm).[123]

The development of a semiconductor heterojunction by incorporating two different catalysts with appropriate valence band and covalent bond potentials is regarded as one of the effective techniques for promoting charge transfer and separation by taking into account the space charge depletion and accumulation between two semiconductors. Until now, many research groups have developed different types of g-C_3N_4-based semiconductor heterojunctions for applications in environmental remediation and solar energy conversion. Among various metal oxides, TiO_2 has been recognized as a suitable candidate to form heterojunctions with g-C_3N_4.[123] The successful formation of TiO_2/g-C_3N_4 hybrid nanocomposites has been reported to promote the photoactivity for NRR. In the early study, Zhou et al. reported the synthesis of TiO_2 nanosheet array/g-C_3N_4

heterojunction photocatalysts by a facile calcination approach. In another work, wang et al. developed Ga_2O_3/g-C_3N_4 composite materials by a simple thermal process, accompanied by a noticeably enhanced photodegradation of toluene under UV and sunlight-type irradiation.

The work of Jiang et al.[123] showed that TiO_2@C/g-C_3N_4 heterojunctions were prepared via a facile one-step calcination of a mixture of TiC_2 and melamine. Figure 11 illustrates the schematic diagram the energy band structure according to the above estimation and the principle of charge carrier separation in TiO_2@C/g-C_3N_4. Under visible light irradiation, electrons are able to jump from the VB to the CB of g-C_3N_4 and TiO_2, leaving behind holes in the VB (Figure 11a). Due to the more positive potentials of the CB and VB of TiO_2 in comparison with g-C_3N_4, the photoinduced electrons thermodynamically transfer from the CB of g-C_3N_4 to that of TiO_2, while holes transfer from the VB of TiO_2 to that of g-C_3N_4. Figure 11b is the TEM images of the TiO_2@C/g-C_3N_4. They clearly reveal that TiO_2 nanocrystals with a deeper diffractive contrast are effectively anchored on the surfaces (Figure 11b) of the carbon nanosheets, resulting in the TiO_2@C structure, which are hybridized randomly and attached densely to the surface of g-C_3N_4 to form intimate heterojunctions. The high-resolution TEM (HRTEM) image (Figure 11c) indicates the clear lattice fringes of TiO_2 for the (101) planes of anatase phase TiO_2, which is consistent with the results of the corresponding fast Fourier transform (FFT) image, confirming the high crystallinity of the TiO_2 nanocrystals. The HRTEM image further illustrates that few layered carbon nanosheets wrap on the surface of the TiO_2 nanocrystals. Of course, some TiO_2

nanocrystals on carbon nanosheets in the $TiO_2@C/g-C_3N_4$ are actually uncovered or partially covered by graphitic carbon layers, which ensures that these TiO_2 nanocrystals are accessible to reactants and function as active centres for photocatalytic reactions. Then the NRR performance on the $TiO_2@C/g-C_3N_4$ was evaluated under visible light (Figure 11d-g). The $TiO_2@C/g-C_3N_4$ exhibits a significantly enhanced photocurrent density, which is about 1.7 times higher than that of pristine $g-C_3N_4$, indicating the effective separation and longer lifetime of the photogenerated charge carriers. Apart from the photoinduced charge carrier behaviours of irradiated $TiO_2@C/g-C_3N_4$, effective nitrogen adsorption and activation is critical to the efficiency of photocatalytic reduction reaction. Not only the red shift was occurred on the TiO_2 catalysts, but also the $Ga_2O_3/g-C_3N_4$ have extended-light response.[77] The results indicated that the aromatic rings could efficiently promote the separation and transfer of photogenerated charge carriers.

1.2.1.3 Hexagonal Boron Nitride

Hexagonal boron nitride (h-BN) is another analogue of graphite and is also known as "white graphene".[138] Bulk h-BN has a layered structure with lattice constants of 2.50 Å and interlayer distances of 3.33 Å (Figure 3f).[139] Differing from graphene, h-BN is an insulator with a thickness dependent band gap. In electronic and optical devices, h-BN nanosheets have been used as dielectric substrates for graphene and MoS_2-based heterostructures. However, pristine h-BN displays barely no performance for electrocatalysis, limited by its poor conductivity and poor catalytic activity. Therefore, various experiments using physical or chemical methods have been conducted to

activate h-BN. Chen et al. found that the electronic properties of h-BN can be tuned through coupling with Mo nanoparticles. The resultant composite exhibited increased NRR activity which originated from the effective activation of adsorbed N_2 and improved selectivity for the $6e^-$ reduction pathway from nitrogen to ammonia.[79]
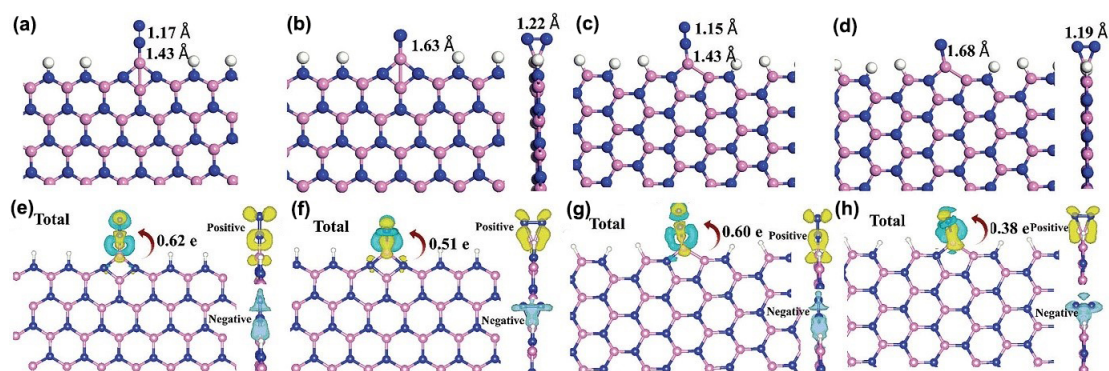
Figure 12. (a–d) Optimised configurations of N_2 bonding to B@ZZBN and B@ACBN edge. (e–h) The charge density difference patterns of N_2 end-on B@ZZBN, side-on B@ZZBN, end-on B@ACBN, and side-on B@ACBN, and the positive and negative charges are shown in yellow and cyan, respectively. Blue, pink, and white balls represent the N, B and H atoms, respectively.[140]

Like for other 2D nanomaterials, heteroatom doping is also an ideal method for activating the catalytic activity of h-BN. Through DFT computations, Du et al. explored the possibility of utilizing boron doped boron nitride edge as NRR electrocatalysts by examining their N_2 adsorption ability and subsequent NRR pathways.[140] In this work, B atoms decorated on BN edges have two different connect sites, including B bonding with double nitrogen atoms of the zigzag edge (B@ZZBN), and bridge sites of BN armchair edges (B@ACBN) (Figure 12). And the zigzag edge of BN was considered as the most stable site for boron doping. And for the armchair edge, B prefers to bond at the hollow site to generate a five-membered ring. For the N_2 reduction reaction on the catalyst, apart from the chemisorption of N_2 molecules onto the catalyst surface, the

46

desorption of NH_3 molecules is another determining factor that may influence the catalytic performance.

It is well recognised that the higher adsorption energy indicates the high surface activity to bond N_2 tightly, however, this may cause a higher bonding strength between NH_3 and active sites as well. Many previous works have shown that although the catalyst shows sufficient catalytic performance for the N_2 reduction process, the NH_3 desorption step is normally hard to proceed due to the high free energy change, which may result in the catalyst poisoning. In our work, the adsorption of N_2 molecules to B@ACBN is as low as -1.97 eV, thus, the desorption of NH_3 at B@ACBN is as high as 0.85 eV, however, at the zigzag edge, the desorption of NH_3 is only 0.35 eV. From their calculations, boron doped h-BN showed promise as an NRR catalyst because it could facilitate the NRR with a lower energy barrier compared to TMs-based catalysts in acidic media. And above DFT results was approved by a similar experimental work.[141] Sun et al. also demonstrated that defect engineering could modify the activity of h-BN for the NRR, whereby its activity was improved by the existence of edge boron atoms energetically favourable for nitrogen adsorption. Therefore, these materials also have potential in NRR applications when appropriate engineering strategies are utilized.

1.2.1.4 Boron Sheet

With A new 2D layered network structure, boron sheet, was firstly predicted by Tang in 2007.[142] In the periodic table, boron is neighbor of carbon with three valence electrons in the 2s and 2p orbitals; thus it is able to form sp^2 hybridization like carbon.[143] The structure of boron sheet composed of triangular and hexagonal motif has been

identified to be energetically more stable than those of only triangular lattices or hexagonal lattices,[67,109,142] that can be viewed as hole-doped triangular lattices and may bring rich chemistry applications (Figure 3g). At present, some more stable structure 2D boron sheets were searched by theoretically method, which including the snub-sheet,[144] α-sheet,[142] β_{12}-sheet,[145] $g_{2/15}$-sheet,[146], struc-1/4, 1/8, 1/10, 1/12-sheet.[147] Among those structures, the α-sheet is confirmed to be the most stable structure,[148] which can be viewed as being directly related to the synthesized BNTs. In additions, β_{12} sheet have been produced on metal surface by direct evaporation of pure boron source.[68] Until now, these boron sheets have demonstrated promising applications in superconductor,[149] hydrogen storage,[150] and oxygen evolution reaction.[151] Remarkably, the 2D sheets have the typically porous characteristic structure due to the "hexagonal hole" involved, which can provide sufficient space to accept the foreign atoms. Especially, the former work indicated that the adsorption of metal atoms on boron sheet is expected to occur more easily than on graphene due to the electron deficiency of boron structure.[152]

Different from other well-known 2D materials, 2D boron is electron-deficient, the sp^3 hybrid orbital of the boron atom can form B-to-N π-back bonding, offering great benefit to N_2 activation, but its use for NRR electrolysis remains unexplored.[153,154] The NRR performance on the 2D boron sheet was firstly studied by using DFT calculation in 2018.[80] The geometrical configuration of the pristine boron sheets were constructed as ideal 2D materials, and the optimized configurations were shown in Figure 13a, b, corresponding to the α-sheet and β_{12}-sheet top views, respectively. Therefore, the two

different boron atoms show the different electronic properties, the hole atom, labelled as 1 in Figure 13, is connected by two 3c-2e bonds and one 4c-2e bonds, while the triangular atom, labelled as 2, is connected by delocalized π-bonds, the 3 in β_{12}-sheet that connect by 3c-2e bonds.

Table 6. Experiment Activity of NRR on 2D Boron-based Electrocatalysts.

Catalysts	Yield	FE	U (V)	Synthesis Method	Electrolyte
Boron Carbide Nanosheet[155]	26.57 μg h^{-1} mg^{-1}	15.95%	-0.75	Ultrasonic	0.5 M H_2SO_4
Boron Sheet[156]	13.22 μg h^{-1} mg^{-1}	4.04%	-0.80	Ultrasonic	0.1 M Na_2SO_4

Table 7. Calculated Activity of NRR on 2D Boron-based Electrocatalysts.

Catalysts	GGA	Barrier (eV)	RDS
Boron Carbide Nanosheet[155]	PBE	0.34	NH_3
Boron Sheet[80]	RPBE	0.77	N_2^*
V/Boron Sheet[157]	PBE	0.28	N_2H^*
Ru/Boron Sheet[41]	RPBE	0.42	N_2H^*
Boron Sheet[156]	PBE	1.30	NH_3

*Denotes an adsorption site on catalyst surface.

And all possible catalytic sites for NRR all were checked in the work. After initial N_2 adsorption, first reduction step has been identified as the rate-determining step. Among these active sites, site-2 of α-sheet monolayer offers the best performance, with $\Delta G_{max} = 0.77$ eV. Although the site-2 of both sheets have the same coordination number, the active site-2 of α-sheet shows the overwhelming performance compared to the β_{12}-sheet (Figure 13e). Transition metals anchored boron sheets with the aim to search some potential catalysts for conversion dinitrogen to ammonia under ambient condition were also investigated.[41,157] Its result indicated that the single Ru (V)-atom-embedded boron monolayers possess outstanding NRR catalytic activity, and the reaction pathway prefer to carry out by distal with a relatively small barrier energy of RDS, with $\Delta G_{max} = 0.42$ and 0.44 eV on both Ru/boron sheets, which are less than half of that for the reported

flat Ru(0001) catalysts (1.08 eV). Therefore, the screening computations suggest that suitable substrate could be improved the catalytic performance of transition metal electrocatalysts for N_2 reduction at ambient condition.
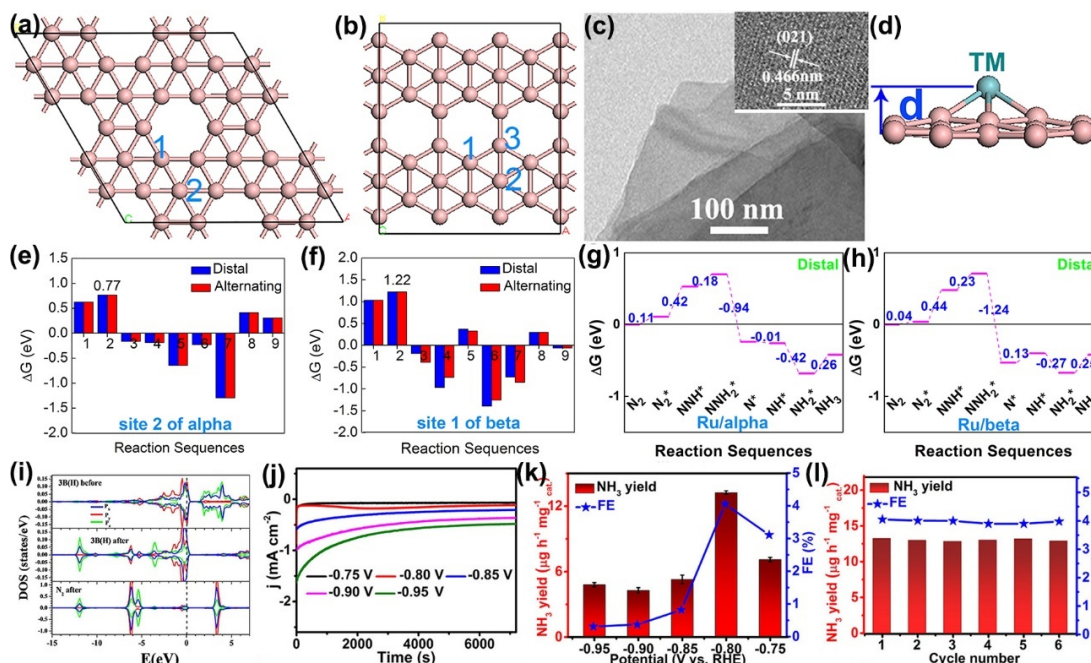
Figure 13. Optimized structure of a boron monolayer: (a) α-sheet and (b) $β_{12}$-sheet. (c) TEM of boron sheet. (d) (c) side view of TM-embedded boron sheet. Calculated reaction free energy ΔG: (e) site-2 of α-sheet, (f) site-1 of $β_{12}$-sheet, (g) Ru/α-sheet, and (h) Ru/$β_{12}$-sheet.[41,80] (i) The DOS of boron atoms site before and after N_2 adsorption. (j) Time-dependent current density curves of boron sheet under various potentials in 0.1 M Na_2SO_4. (k) NH_3 yields and FEs for boron sheet under the corresponding potentials. (l) Recycling tests for boron sheet during NRR at −0.80 V.[156]

Then the ammonia was synthesized on the boron sheet by experimental work in 2019.[156] It discussed the electronic structure before and after N_2 adsorption, and there is an obvious hybridization between the B 2p orbital and the *N_2 2p orbital below the Fermi energy (Figure 13i). This hybridization mainly originates from $B(2p_z) - *N_2(2p_z)$ within the range from −11.5 eV to −12.5 eV and $B(2p_x,2p_y) - *N_2(2p_x,2p_y)$ within the range from −6.0 eV to −7.0 eV, which correspond to σ donation and π back-bonding, respectively. In the NRR experiment, time-dependent current density curves for boron

sheet under different potentials in Na_2SO_4 solution was present in Figure 13j. It is shown that the higher current density was obtained in the N_2-saturated electrolyte, suggesting that boron sheet is catalytically active for N_2 reduction. The calculated results of NH_3 yields and FE are plotted in Figure 13k. Obviously, the material achieves the largest NH_3 yield of 13.22 $\mu g \ h^{-1} \ mg^{-1}$. In sharp contrast, the amount of produced NH_3 for catalyst is 2.64 μg in this experiment research, suggesting that catalyst is highly active for NRR. Such superior NRR performance for can be attributed to the following two reasons: (1) The 2D nature of boron sheet favours the exposure of more active sites, which are advantageous for the NRR process; and (2) The sheet possesses a smaller radius comparing to bulk boron, suggesting that the 2D boron sheet catalyst has a lower charge-transfer resistance. Moreover, the stability of catalyst was tested, indicating that boron sheet possesses stable NRR performance.

1.2.1.5 Black Phosphorus

Black phosphorus (BP) has a 100-year long history as its bulk form was first synthesized in 1914.[158] BP is a layered semiconductor with an orthorhombic crystal structure; one phosphorus atom is covalently bonded with another three to form a puckered honeycomb structure in a single layer (Figure 3h).[159] The three bonds take up all three valence electrons of phosphorus, resulting in a band gap of 2 eV which can be tuned by controlling its thickness. So far, BP has been widely studied in electronic and optical devices. However, only a few works have been reported about its applications in electrocatalysis, which may be due to its low stability under electrocatalytic conditions and poor electrical conductivity.

Recently, it was found that various forms of bulk BP (such as thin films and particles) have electrocatalytic activities for the NRR process comparable to commercial TMs-based catalysts. However, bulk BP has a low density of active sites, which likely limits its electrocatalytic performance. Compared to its bulk form, 2D BP nanosheets synthesized by liquid exfoliation techniques possess increased exposed active sites and surface area.[160] Therefore, the intrinsic benefits of this ultrathin lamellar structure can promote the development of BP for efficient electrocatalysis. As predicted, few-layered BP showed improved NRR performance, achieving a FE and NH_3 production rate for the NRR in an acidic aqueous solution (0.01m HCl) as high as 5.07% and 31.37 μg h^{-1} mg^{-1}, respectively.[161]

Table 8. Experiment Activity of NRR on 2D Phosphorene-based Electrocatalysts.

Catalysts	Yield	FE	U (V)	Electrolyte	GGA	Barrier (eV)	RDS
Fe/Phosphorene[162]	N.A.	N. A.	N. A.	N. A.	PBE	2.34	NH_3
Mo@BC$_2$/Phosphorene[163]	N.A.	N. A.	N. A.	N. A.	RPBE	0.60	N_2H^*
Boron Phosphide[164]	N.A.	N. A.	N. A.	N. A.	PBE	0.12	NH_3^*
Phosphorene[161]	31.37 μg h^{-1} mg^{-1}	5.07%	-0.60	0.01 M HCL	PBE	0.85	N_2H^*

*Denotes an adsorption site on catalyst surface.

BP is attractive as a catalyst for nitrogen reduction because its valence electron structure is similar to that of nitrogen ($3s^23p^3$ and $2s^22p^3$, respectively) and it has an anisotropic lattice structure.[165] In particular, BP is a type of layered crystal (Figure 14a,b) with monolayers stacked together via weak, interlayer van der Waals interactions; these interactions allow BP to be exfoliated into monolayer phosphorene or few-layer black phosphorus, releasing the maximum number of intrinsic active sites.[166] According to the standard curve at λ = 660 nm, the maximum FE of 5.07%for ammonia synthesis on the BP catalyst electrode was achieved at 0.6 V (Figure 13d) and the highest NH_3 yield

rate was 31.37 μg h^{-1} mg^{-1} at 0.7 V, which is significantly higher than that on bulk BP

and powdery BP catalyst electrodes, as well as most nonmetallic and metal-based

catalysts reported at present. Furthermore, no apparent byproduct (N_2H_4) was detected

in the product solutions, which indicates that the BP has a good selectivity for N_2

electroreduction into NH_3. To verify the source of ammonia, some necessary

comparative experiments were carried out at the optimal potential of 0.6 V, including

using Ar instead of nitrogen as the feed gas, BP as the working electrode, and $^{15}N_2$ as

the feed gas. Specifically, no apparent NH_4^+ was detected in the electrolyte after two

hours of electrolysis when Ar replaced N_2. By contrast, typical $^{15}NH_4^+$ signal was

detected in the presence of continuous $^{15}N_2$ bubbling (based on the 1HNMR spectra,

Figure 14e). Moreover, the corresponding 1HNMR spectra had only a double peak of

$^{15}NH_4^+$, which confirms that the formation of NH_3 was completely derived from the

electrochemical reduction of N_2 in the presence of FL-BP NSs catalyst. Furthermore,

to identify the intrinsic nitrogen adsorption active sites and understand the possibility

reaction pathway of nitrogen reduction, and it performed DFT calculations for the

molecular orbitals of FL-BP NSs (Figure 14f), which due to the electron distribution in

the molecular orbital of the catalyst is the key factor to determine the active sites for

nitrogen fixation. The results shown that the lowest unoccupied molecular orbital

(LUMO, yellow) and the highest occupied molecular orbital (HOMO, blue) present a

nonlocalized, asymmetric electron distribution. The electron densities of the HOMO

and LUMO are obviously concentrated on the zigzag and diff-zigzag edges, and at the

edges, the active orbitals are beneficial for adsorbing N_2 and boosting the NRR

performance. For the alternating hydrogenation pathway in an association mechanism

is the plausible low-energy NRR pathway.
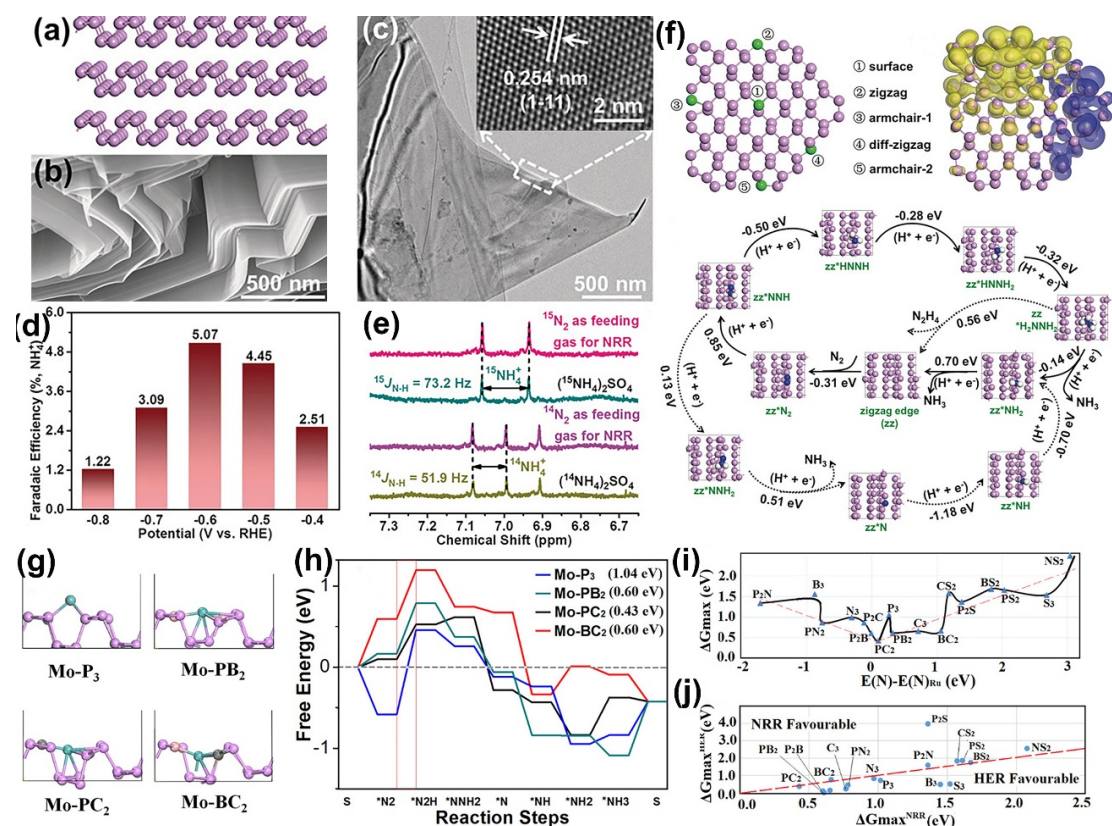
Figure 14. (a) Optimized structure of BP. (b) SEM image of bulk BP. (c) TEM images of BP nanosheet. (d) FE of BP at various potentials. (e) ^{1}HNMR spectra (600 MHz) of both $^{14}NH_4^+$ and $^{15}NH_4^+$ produced from the NRR reaction (at 0.6 V) using $^{14}N_2$ or $^{15}N_2$ as the N_2 source. (f) Structure of ideal FL-BP NSs. The green balls represent five active sites (surface, zigzag, armchair-1, diff-zigzag, and armchair-2 edge); LUMO and HOMO (blue) of FL-BP NSs; The possible reaction mechanisms at the zigzag edge.[161] (g) Optimized geometries of all potential catalysts with different ligands. (h) Calculated NRR profile. Computational screening of ligands combinations: (i) ΔG_{max} vs E(N)−E(N)$_{Ru}$, (j) $\Delta G_{max(HER)}$ vs $\Delta G_{max(NRR)}$. Mo, P, N, and H are shown as cyan, purple, blue, and white spheres, respectively.[163]

In 2017, Mo mediated by PNP-type pincer ligands even set a new record of 415 equiv of NH_3 per Mo. These achievements vividly demonstrated the importance of ligand optimization in the design of NRR catalysts.[167] N_2 adsorption on a single Mo atom adsorbed on BP with three potential geometries was analyzed, including end-on, side-on, and tilt end-on adsorption geometries (Figure 14). And the Bader charge

54

variations were present, indicating nitrogen molecule was activated by Mo atom. Following the above analysis, a series of model catalysts starting from the Mo$-$P$_3$ configuration were screened with p-block ligands, including B, C, N, S, and P. The optimized geometries for these 17 catalysts are shown in Figure 14g. For NRR, the adsorption energy of a single nitrogen, labeled as E(N*), has been widely employed as an indicator to search for potential catalysts and a volcano curve has often been obtained.[168] A reversed volcano plot between ΔG_{max} and E(N*)$-$E(N*)$_{Ru}$ has been plotted, confirming the validity of the E(N*) indicator. It is worth noting that such validity origins from the linear relationship between the adsorption energies of intermediates; therefore, scattering or deviation from the linear is often seen, particularly when the RDS comes from N$_2$ adsorption, NH$_3$ release, or surface reconstruction during the reaction. In additional, HER is a competition reaction for NRR, leading to low FE when HER is more favorable than NRR. Therefore, the catalyst reaction is another indicator for NRR (Figure 14i). But there are no outstanding improved when the Fe doped phosphorene for NRR, due to the energy barrier is over 2.0 eV on the Fe catalytic site which similar with the Fe@N$_3$/graphene.[162]

1.2.2   Transition Metal Compound

1.2.2.1 Oxides

Transition-metal oxides (TMOs) have been employed for almost all electrocatalytic processes due to their low cost, high stability, and tunable activity. The layered class consists of metal trioxides (e.g., MoO$_3$, TiO$_2$, and CuO$_3$) can be synthesized by hydrothermal and calcination methods. However, most pristine TMOs exhibit

unsatisfactory performance compared to benchmark electrocatalysts due to their low activity and poor conductivity. Many recent studies have shown that the electrocatalytic activity of TMOs can be improved by reducing their thickness. Thus, 2D TMOs have become promising candidate electrocatalysts for NRR. However, 2D TMOs are significantly limited by their weak electron transfer abilities. Therefore, optimizing their electrical conductivity is an ideal way to improve their catalytic performance. For example, plasmonic gold nanocrystals on 2D TiO_2 nanosheets exhibited efficient NRR performance due to their highly exposed surface area, enhanced electrical conductivity, and vacancy introduced active sites.[169] Furthermore, the catalytic performance of 2D TMOs can be improved using defect engineering or doping. For example, MoS_2/ZnO nanosheets with doped catalyst showed a significantly improving yield rate, which is 9.3 times higher than that of pristine ZnO.[170]

Table 9. Experiment Activity of NRR on Transition Metal Oxides-based Electrocatalysts.

Catalysts	Yield	FE	U (V)	Synthesis Method	Electrolyte
Au/TiO$_2$[169]	2.22 $\mu g^{-1} h^{-1} mg^{-1}$	N.A.	N.A.	Hydrothermal	0.1 M Na$_2$SO$_4$
TiO$_2$[171]	5.61 $\mu g^{-1} h^{-1} cm^{-2}$	2.5%	-0.70	Hydrothermal	0.1 M Na$_2$SO$_4$
MoO$_3$[172]	29.43 $\mu g^{-1} h^{-1} mg^{-1}$	1.9%	-0.50	Hydrothermal	0.1 M HCl
MoS$_2$/ZnO[170]	4.18 $\mu g^{-1} h^{-1} mg^{-1}$	N.A.	N.A.	Calcination	Ethanol
Pd-Co/CuO[173]	10.04 $\mu g^{-1} h^{-1} mg^{-1}$	2.16%	-0.20	Hydrothermal	0.1 M KOH
La$_2$O$_3$[174]	17.04 $\mu g^{-1} h^{-1} mg^{-1}$	4.76%	-0.80	Hydrothermal	0.1 M Na$_2$SO$_4$
AgCl/Bi$_2$O$_3$[175]	10.3 $\mu g^{-1} h^{-1} mg^{-1}$	N.A.	N.A.	Hydrothermal	Water
Ru/TiO$_2$[176]	2.11 $\mu g^{-1} h^{-1} cm^{-2}$	0.72%	-0.10	Hydrothermal	0.1 M KOH
MoO$_2$[177]	12.20 $\mu g^{-1} h^{-1} mg^{-1}$	8.2%	-0.15	Calcination	0.1 M HCl
TiO$_2$[178]	0.03 $\mu g^{-1} h^{-1} mg^{-1}$	N.A.	N.A.	Hydrothermal	Water

Table 10. Calculated Activity of NRR on Transition Metal Oxides-based Electrocatalysts.

Catalysts	GGA	Barrier (eV)	RDS
MoO$_3$[172]	PBE	2.25	N*
La$_2$O$_3$[174]	PBE	0.76	N$_2$H*
Ru/TiO$_2$[176]	PBE	0.21	NH*
MoO$_2$[177]	PBE	0.69	NHNH*

*Denotes an adsorption site on catalyst surface.

The excellent performance of the photolysis of water on TiO$_2$ created great awareness of the application of TiO$_2$-based nitrogen photofixation catalysts.[179] Bourgeois et al. reported that unmodified TiO$_2$ exhibited N$_2$ photocatalytic activity after annealing in air because the thermal pretreatment generated surface defects which introduced defect or impurity states in the band gap of the semiconductor.[180] Most recently, Zhang el al. reported that tuning oxygen vacancies in ultrathin TiO$_2$ nanosheets to boost photocatalytic nitrogen fixation up to 700 nm.[178] It demonstrated that the concentration of VOs in ultrathin TiO$_2$ nanosheets can be precisely controlled by doping with copper ions (Figure 15b), leading to greatly improved N$_2$ photofixation performance under visible-light irradiation and near ambient conditions. Efficient light absorption and charge separation are key requirements for efficient photocatalytic performance. The UV–vis diffuse reflectance spectra of Bulk-TiO$_2$ and the doped-TiO$_2$ nanosheets were shown in the Figure 15. Bulk-TiO$_2$ showed only absorption below 400 nm due to charge transfer process from valence band O 2p orbitals to conduction band Ti 3d orbitals. The 0% doped-TiO$_2$ nanosheets showed an additional feature from 400 nm to longer wavelengths due to V$_O$ which lead to the formation of colored Ti^{3+} centers.[181] With several transformations of surficial Ti from Ti^{3+} to Ti^{4+}, the electrons were naturally injected into N$_2$.[182] Meanwhile, Ti^{3+} could be regenerated under UV irradiation. With increasing copper doping, the color of the samples transformed from white to dark green (the inset of Figure 15d), with the features above 400 nm becoming progressively stronger with Cu doping up to 6%, evidence for increased VOs defect states in the TiO$_2$ crystal lattice. Furthermore, the absorption edges for the X%-TiO$_2$

nanosheets red shifted from 400 to 700 nm as X increased, which is explained by the presence of VOs.

Defect-rich TiO_2 nanosheets containing 6 mol% Cu (denoted herein as 6%-TiO_2 nanosheets) exhibited remarkable and stable performance toward photofixation of N_2 to NH_3 in water under UV–vis and visible light (Figure 15e), with the activity extending up to 700 nm (yield rates were 1.54 μmol h^{-1} g^{-1} at 600 nm, and 0.72 μmol h^{-1} g^{-1} at 700 nm with corresponding quantum yields of 0.08% and 0.05%, respectively). The DFT results shown that the excellent activity to be attributed to Jahn–Teller distortions and around the Cu dopant which create abundant V_O and introduce compressive strain into the TiO_2 nanosheets, which act synergistically to promote N_2 adsorption and activation while facilitating fast charge separation under UV–vis or visible irradiation. The paper described that bulk doping of TiO_2 with Cu ions offers a new pathway for optimizing the concentration of VOs for efficient dinitrogen photoreduction to ammonia. And the photocatalytic performance of 6%-TiO_2 was investigated under monochromatic light at 600 and 700 nm. Ion chromatography (Figure 15f) was used to quantify NH_3 evolution and establish the structure–activity relationship. Under 600 and 700 nm irradiation, no NH_3 was formed in the absence of N_2, whereas under a N_2 flow the concentration of NH_3 increased linearly with irradiation time. NH_3 evolution rates for 6%-TiO_2 were 1.54 μmol h^{-1} g^{-1} under 600 nm, and 0.72 μmol h^{-1} g^{-1} under 700 nm irradiation, respectively
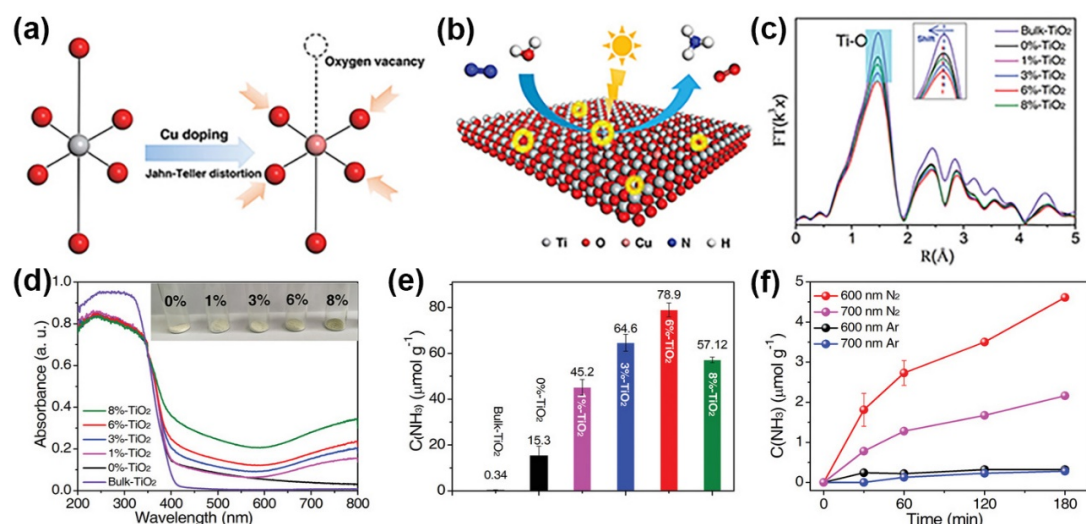
Figure 15. (a) Polyhedral representation of a TiO_6 octahedron and a defective octahedron with V_O resulting from copper doping at a Ti site. b) Photocatalytic N_2 fixation process on the surface of ultrathin TiO_2 nanosheets with OVs and engineered strain (OV marked with yellow circles). (c) Magnitude of k^2-weighted Fourier transforms of Ti K-edge EXAFS spectra for X%-TiO_2 (X = 0, 1, 3, 6, 8) and Bulk-TiO_2 nanosheets. (d) UV-DRS of X%-TiO_2 nanosheets (X = 0, 1, 3, 6, 8) and Bulk-TiO_2. (e) Yield of NH_3 detected by Nessler's reagent for different samples under UV–vis illumination after 1 h with water as the proton source. (f) Time course of NH_3 evolution for 6%-TiO_2 detected by ion chromatography under 600 and 700 nm irradiation.[178]

And Sun et al. utilized the hydrothermal technique to prepare defect TiO_2 nanosheet array on the Ti plate.[171] An improved NH_3 production rate was gained, due to the enhanced adsorption and activation of N_2 by OVs in situ generated by electrochemical tests. And they result suggested the resulting OVs favors more effective N_2 adsorption and activation of the nitrogen triple bond, leading to superior electrocatalytic NRR performance.[183,184] It is worthy to note that surface OVs not only serve as N_2 absorption sites, but also promote charge-carrier transportation to the adsorbed nitrogen while bulk-vacancies act as recombination centers to trap the photo-excited electrons and holes.

Except the defected TiO_2 nanosheets, further research corroborated that the loading of Ru or Au particles would enhanced the yield of NH_3 because these particles can be

applied into the active sites for NRR performance.[169,176] According to literature reports, the effect of metal atom facilitated the transformation of the crystallinity of TiO_2, which noticeably affected the photocatalytic efficiency. Notably, the incorporation of Ru accelerated the phase transformation of anatase into rutile and also promoted grain growth during synthesized. In this regard, the ratio of anatase to rutile played a prevailing role in the efficiency of the catalysts by maintaining a constant particle size of Ru. From the DFT calculation, the partial DOS of N_2 adsorption presents an effectively overlap between Ru-4d and N-2p orbitals in the vicinity of the Fermi level. The N-2p orbitals slightly shift to lower energy on the Ru/TiO_2. And the Au doped atom can inject in the conduction band of TiO_2, leading to the temporary accumulation of electrons in the conduction band of TiO_2 and holes in the Au nanoparticles.[185,186] And the injected hot electrons were trapped by the OVs-induced defect states, which can be activated nitrogen. Hot holes are mainly generated and consumed by the hole scavenger, methanol, on the plasmonic Au nanoparticles.

Apart from TiO_2, many unremitting efforts have been devoted to the study of other metal oxides, including MoO_3, La_2O_3, MoO_2, ZnO, CuO, and Bi_2O_3.[170,172-175,177] These results provided unprecedented ideas and vistas for investigations toward the application of metal oxides in N_2 photo(electro)reduction. It is worth noting that molybdenum is useful in the Haber–Bosch process and also functions similarly to a nitrogen enzyme because of its good interaction with dinitrogen. Much attention has been focused on developing Mo-based molecular or single metal atom catalysts for N_2 reduction.[79,104] However, these catalysts suffer from limited stability under strictly

condition and it is challenging to effectively graft them onto electrodes. Then two molybdenum oxides were synthesized by hydrothermal and calcination, respectively.[172,177] As expected, these studies have proven that molybdenum oxides are capable of conversion nitrogen to ammonia under ambient conditions. The mechanism of activate nitrogen is similar to the TiO_2, owing to the VOs of molybdenum oxides. In their work, surface vacancies with different concentrations were regulated on layered molybdenum oxides under reduction atmosphere, with efforts to increases NRR efficiency and insight into the role of VOs underlying N_2 reduction reaction. Especially, the suitable introduction of vacancies not only boost chemical-adsorption toward N_2 via electron donation on Mo^{3+} ions, but lowered activation energy barrier via effective stabilization of N_2H^* species and destabilizing $N_2H_2^*$ in the process.

Moreover, Fu and co-workers designed $AgCl/Bi_2O_3$ with a low valent Bi^{3+} for N_2 photocatalysis by using a facile hydrothermal synthesis method.[175] The valent Bi^{3+} possesses empty 6d orbitals, which can accept electrons from N_2 molecules and provide excellent N_2 chemisorption and activation. Similar to Fe-doped TiO_2, their range of oxidation states gives ferric and Bi^{2+} the ability to donate and accept electrons, which can continuously activate N_2 during the catalysis process. However, for CuO and ZnO the introduction of noble metals onto the surface is vital for active site construction. He et al. found that highest NH_3 production on the optimal 1% MoS_2/C-ZnO–300 which is 9.3 and 4.0 times higher than that of ZnO and C-ZnO.[170] Shen and co-workers synthesized Pt-Co nanoalloys nested on CuO nanosheets with a suitable band position for N_2 activation, thus exhibiting N_2 fixation activity at room condition.[173] It pointed

that the NH_3 yield increased with increasing Pd/Co ration, and the yield will decrease when the ratio reached 3:1. This is attributed to the hydrogen poisoning of Pd active site, as reported previously.[187]

1.2.2.2 Nitrides and Carbides

Under the circumstance of comprehensive DFT investigations on a range of transition metal nitrides (TMN) for catalyzing electrochemical nitrogen reduction to produce ammonia, metal nitrides are believed more active toward NRR than toward HER compared with pure metal catalysts.[51,188-190] Abghoui et al. proposed that nitrogen electroreduction to ammonia on the TMN surface followed a favorable Mars–van Krevelen mechanism (MvK), in which a surface N atom of TMN can in principle be reduced to NH_3, and the created N vacancy is then replenished by N_2 molecule to endure the catalytic cycle.[190]

Table 11. Experiment Activity of NRR on Transition Metal Nitrides or Carbides-based Electrocatalysts.

Catalysts	Yield	FE	U (V)	Synthesis Method	Electrolyte
VN[191]	5.14 μg $^{-1}$ h^{-1} cm $^{-2}$	2.25%	-0.50	Hydrothermal	0.1 M HCl
MoN[192]	18.42 μg $^{-1}$ h^{-1} cm $^{-2}$	1.15%	-0.30	Hydrothermal	0.1 M HCl

Table 12. Calculated Activity of NRR on Transition Metal Nitrides or Carbides-based Electrocatalysts.

Catalysts	GGA	Barrier (eV)	RDS
MoN[193]	PBE	0.70	NH_2^*
RuN[194]	RPBE	0.41	NH_3
VN[188]	RPBE	0.51	N_2H^*
VN[189]	RPBE	0.50	N_2H^*
CrN[190]	RPBE	0.68	N_2H^*
CoN[51]	RPBE	0.23	N_2H^*
Fe/MoN$_2$[195]	RPBE	0.47	N_2H^*
MoC$_6$[196]	PBE	0.54	N_2H^*
MoC[197]	PBE	0.28	N_2H^*
Mo$_2$C[198]	PBE	1.02	N_2H^*

*Denotes an adsorption site on catalyst surface.

Based on the MvK mechanism, a series of DFT calculations were carried out to compare the catalytic activity and stability of various TMN when considering the possibility of N vacancy poisoning and the likelihood of catalyst decomposition and regeneration.[199] The most promising nitride candidates were found to be ZrN, NbN, CrN, and VN with the (100) facets of rocksalt structure, which were expected to catalyze electrochemical ammonia synthesis at smaller overpotentials of around -0.5 to -0.8 V (Figure 16a). Most of the nitrides exhibit relatively high activity towards ammonia formation, with the exception of ScN, YN and HfN, which have $\Delta G_{RDS} > 1.5$ eV. All of the nitrides with $\Delta G_{RDS} < 1.5$ eV are considered potentially active and are retained for a more detailed mechanistic study.[188] An interesting point to note is that there is no clear trend in the nature of the RDS; for some nitrides the addition of the first proton is rate-limiting, while for others the addition of the third, fourth, or fifth proton is rate-limiting while for some it is the release of the ammonia molecule which is the RDS. This is in contrast to the case of electrochemical ammonia formation on pure metals, for which primarily only two different RDS exist across the whole series of pure transition metal surfaces. That results in a volcano-shaped activity curve when plotted against a common descriptor. Besides the energy barrier of TMN, the current efficiency is calculated 6/n × 100% (6 being minimum number of H^+/e^- pairs) and is presented in Figure 16b which along with the onset potential for ammonia production. It is assumed here that the H adatoms that do not form NH_3 will contribute to H_2 formation from the surfaces and thus offer a lower bound to the current efficiency. catalysts.[188] The current efficiency is high in most cases for these metal nitrides.

Although a range of metal nitrides were proven to be promising NRR catalysts through theoretical analyses, only Mo and V-based nitrides have been experimentally proven to show good catalytic activity toward NRR, in which the identification of nitrogen source of produced ammonia and the validation of reaction mechanism are extremely vital.[193] Sun et al. conducted investigations on the NRR performance of vanadium nitride (VN) and molybdenum nitride (MoN) nanosheet electrocatalysts in 0.1 M HCl under ambient conditions.[191,192] Ammonia yield rate of 5.14 $\mu g^{-1} h^{-1} cm^{-2}$ and 18.42 $\mu g^{-1} h^{-1} cm^{-2}$ were obtained on the VN and MoN, respectively (Figure 16). The recycling experiment was also carried out. NRR experiment was repeatedly conducted at −0.5 V for 3 h for 10 times using VN/TM catalyst. Fresh electrolyte was used in each cycle, suggesting its excellent stability for NRR after 10 times recycling stability tests.[191] While another work reported that no ammonia could be detected after 1h on VN nanoparticles catalyst at applied potentials.[200] Furthermore, $^{15}N_2$ isotopic experiments showed that both $^{14}NH_3$ and $^{15}NH_3$ were detected with the feed of $^{15}N_2$ indicating that the reaction process followed the MvK mechanism. On the basis of the DFT calculations, reactivity experiments, and characterization results, it was hypothesized that only the surface N atoms adjacent to a surface vacancy serve as active sites for catalyzing NRR and more negative potentials would lead to the replacement of unstable surface vacancy by N atoms from N_2 feed, resulting in the formation of inactive VN phase accompanied by the deactivation of catalyst.

(a) Free energy change (ΔG_{RDS}, eV) of the rate-determining step of NH₃ formation... [figure]

(b)	RS(100)	RS(111)	ZB(100)	ZB(110)
ZrN	75% CE of NH₃ U = -0.76 V	60% CE of NH₃ U = -1.42 V	-	40% CE of NH₃ U = -1.02 V
NbN	75% CE of NH₃ U = -0.65 V	75% CE of NH₃ U = -1.12 V	-	Decomposition U = -0.59 V
CrN	100% CE of NH₃ U = -0.76 V	Decomposition U = -0.58 V	Non-catalytic U = -1.11 V	86% CE of NH₃ U = -0.54 V
VN	100% CE of NH₃ U = -0.51 V	Decomposition U = -0.85 V	Decomposition U = -0.97 V	Decomposition U = -1.06 V

Figure 16. (a) Free energy change (ΔG_{RDS}, eV) of the rate-determining step of NH₃ formation on transition metal nitride catalysts.[188] (b) Most promising facets of the nitride candidates (green background) and corresponding potential window and current efficiency for N₂ electroreduction to NH₃ via a MvK mechanism.[189] (c) and (d) SEM and TEM image of VN nanosheets, respectively. (e) Average NH₃ yields and FEs for VN at different potentials. (f) Proposed pathway for the NH₃ electrosynthesis using VN. (g) Amperometric i−t curves of VN/TM for NRR at a series of potentials in 0.1 M HCl. (h) Recycling test of VN at a potential of −0.50 V. (blue, purple, and gray balls represent H, N, and V atoms, respectively).[191]

In terms of transition metal carbides, DFT calculation investigated that the viability of cubic molybdenum carbide (MoC) as NRR electrocatalyst.[196-198] The comparison between the N atoms and H atoms adsorption energies of various crystallographic surfaces of cubic MoC revealed that the nitrogen reduction in MoC (1 1 1) surface could proceed at small negative potentials of -0.3 V vs. SHE due to the stronger N atoms adsorption. Besides, the hydrogen evolution could be suppressed via introducing carbon vacancies to prevent the accumulation of H-adatoms.[198] The NRR catalytic activity of transition metal carbides was further confirmed by Wang's group via developing molybdenum carbide nanodots embedded in ultrathin carbon nanosheets (Mo₂C/C) as

65

a highly efficient catalyst for electrochemical N_2 fixation.[92] The obtained Mo_2C/C

nanosheets exhibited excellent NRR catalytic performance with a high NH_3 production

rate of 11.3 $\mu g\, h^{-1}\, mg^{-1}$ due to the abundant active sites of Mo_2C nanodots for favourable

N_2 adsorption and unique electronic structure beneficial for the activation of nitrogen

triple bond and catalytic hydrogenation. Importantly, the influence of hydrogen

evolution on the catalytic activity of Mo_2C/C nanosheets toward NRR was investigated

by controlling the availability of protons. The NRR performance control experiments

between proton-enriched condition and proton suppressed condition revealed that the

suppressed proton supply could significantly enhance the FE but at the expense of

decreased NH_3 yield rate, indicating that excessive suppression of hydrogen evolution

might deteriorate the NRR performance of catalysts. Under this circumstance, the

Mo_2C/C nanosheets were capable of catalyzing NRR process under ambient conditions

even though accompanied with hydrogen evolution.

1.2.3   Transition Metals

Transition metals are a class of materials with a long history in electrocatalysis, and

for decades, fundamental studies for electrocatalysis were all based on metals

surface.[201,202] And Nørskov et al. proposed a basic model for the ammonia production

for an electrochemical reduction process.[56,168,203] To date, ΔG_{max} of 1.08 eV for the

precious flat ruthenium (Ru) (0001) was used as a reference for the NRR activity.[50,204]

Their calculation results indicated that, in the associative pathway, the addition of the

first proton to the adsorbed dinitrogen atoms is the limiting step on a flat surface of

transition metal.

66

Table 13. Experiment Activity of NRR on Transition Metal-based Electrocatalysts.

Catalysts	Yield	FE	U (V)	Synthesis Method	Electrolyte
Mo Nanosheet[205]	1.89 $\mu g^{-1} h^{-1} cm^{-2}$	0.72%	-0.49	Anodization Reduction	0.5 M H_2SO_4
Rhodium Nanosheet[206]	23.88 $\mu g\ h^{-1}\ mg^{-1}$	0.22%	-0.20	Hydrothermal	0.1 M KOH
Ag Nanosheet[207]	2.83 $\mu g\ h^{-1}\ cm^{-2}$	4.8%	-0.60	Sol-gel	0.1 M HCl

On a stepped surface, the reaction may proceed via a dissociative pathway. As the *NNH is stable, the addition of a second proton coupled with electron transfer is considered to be the potential determining step. A volcano plot relating the theoretical limiting potential to the adsorption energies of nitrogen species on different metal surfaces is illustrated in Figure 17a, with Fe and Mo to be the most active surfaces for ammonia formation. In the figure, the metals on the right sides with both stepped and flat surfaces exhibit similar reaction mechanisms: addition of the first proton as the limiting step in the associative pathway, while cleavage of the triple bond of dinitrogen is the determining step in the dissociative pathway. The metals on the left side share the identical RDS for both the associative and dissociative pathways. Moreover, there is a lack of available sites for N_2 adsorption and large overpotentials are requested to activate N_2 on the meal, such as Rh, Ru, Ir, Co, Ni and Pt, which mainly leads to HER instead of NRR on most surfaces. In the contrast, the flat metal surfaces of some early transition metals such as Sc, Y, Ti, and Zr are expected to bind N-adatoms more strongly than H-adatoms, allowing for the reduction of N_2 to NH_3 at a theoretical applied bias about −1.0 to −1.5 V vs NHE.[208]

The volcano shape of the plot implies that there is an optimum for the nitrogen adsorption energy (Figure 17b).[209] This optimum reflects a compromise between two mutually opposing ways of achieving a high activity: a small activation barrier for N_2 dissociation and a surface with low coverage of adsorbed atomic nitrogen during

ammonia synthesis.[208] This requires a strong and a weak N-surface interaction, respectively. Therefore, they designed the bimetallic catalyst to adjust the suitable interaction, and combination of Mo (which binds N too strongly) with Co (which binds N too weakly) was selected by the design concept A Co-Mo catalyst was developed using this principle, and it had an ammonia synthesis activity much better than that of the constituents and even better than those of both Fe and Ru at low NH_3 concentrations. The electrochemical reduction of N_2 to NH_3 on transition metal surfaces is severely limited by the linear scaling between the energetics of two key intermediates (Figure 17c, d).[168,210] It is reasonably supposed that selectively stabilizing N_2H^* and destabilizing NH_2^* could reduce the overpotential to an optimal region. However, taking the competitive hydrogen evolution reaction (HER) into consideration, many potentially active metals have a less negative HER limiting-potential requirements than that of NRR. So, the N* binding energy was chosen for both NRR and HER because the N and H adsorption energy scales.
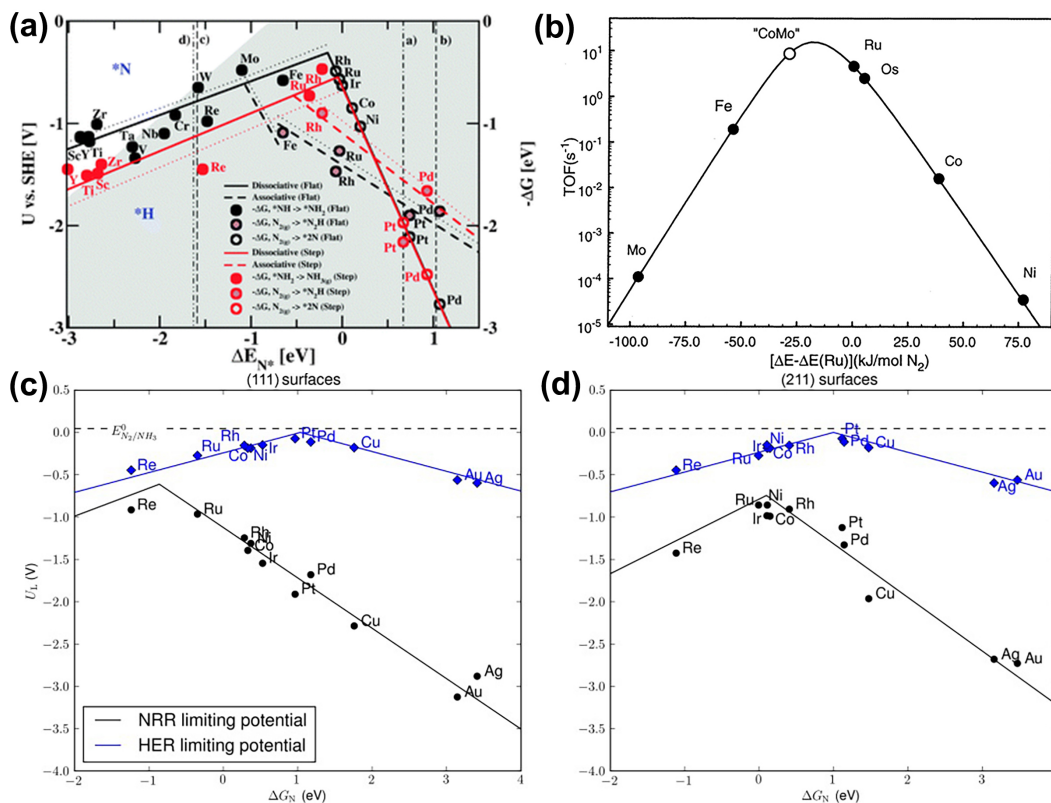
Figure 17. (a) Combined volcano diagrams (lines) for the flat (black) and stepped (red) transition metal surfaces for reduction of nitrogen with a Heyrovsky type reaction, without (solid lines) and with (dotted lines) H-bonds effect.[50] (b) Calculated turnover frequencies for ammonia synthesis as a function of the adsorption energy of nitrogen. The synthesis conditions are 400 °C, 50 bar, gas composition $H_2:N_2 = 3:1$ containing 5% NH_3.[209] (c and d) Comparison of HER and NRR limiting-potential volcanoes. The HER and NRR overpotentials as a function of the *N binding-energy descriptor are shown in blue and black, respectively, and individual metal points are labelled for (111) and (211) surfaces. Note that the HER limiting potentials are consistently less negative than those for NRR. The difference between the limiting potentials of HER and NRR is less severe on (111) facets, although none of the metals shown have a difference less than 0.4 V, which suggests that the selectivity should consistently favour HER.[168]

Depend on the extensive library of electroactive metal nanosheets were predicted by the DFT calculation, several metal-based electrocatalysts have been developed for ammonia synthesis by experiment, including Mo, Rh, Ag, and Au.[205-207,211] As we know, the precious metal nanoparticles were an ideal electrocatalyst not only for the NRR but also for the HER. Especially, the metals hold the high selected activity for HER, which resulted in the extremely low FE for NRR. Due to the 2D structure, ultrathin precious

metal nanosheets, nearly many metal atoms on nanosheets with atomic thickness existed on the outer surface, which not only provided abundant low-coordinate defective atoms but also maximized the utilization of active metals. For example, the Rhodium (Rh) nanosheets, previous work indicated that the Rh–Rh coordination number in the atomically thick Rh nanosheets was lower than that in the conventional Rh nanocrystals. The detailed morphology and crystallographic texture of Rh nanosheets were further investigated by SEM, TEM, and AFM. TEM images showed that the flower-like 2D materials consisted of numerous nanosheets (Figure 18 a-d). The characterization results shown that the thickness of Rh nanosheets was only ca. 1.0–1.1 nm, and the enormous low coordination Rh atoms would facilitate the electrocatalytic activity of Rh NNs for the NRR performance. The electrocatalytic performance of Rh NNs for the NRR was first investigated by LSV in N_2-saturated and Ar-saturated 0.1 M KOH electrolyte at ambient temperature and pressure. Every chronoamperometric curve of Rh NNs for the NRR at different applied potentials showed that the cathode currents almost remain constant, indicating the excellent stability of Rh nanosheets (Figure 18e). For the NRR at all potentials, no hydrazine was detected, indicating the excellent selectivity of Rh NN catalyst for the NRR. The average yields of NH_3 and faradaic efficiencies at different potentials were plotted and listed (Figure 18f). As observed, the average yield of NH_3 increased with decreasing the potential until -0.2 V vs. RHE. Beyond this potential, the average yields of NH_3 decreased significantly, which would be attributed to the competitive adsorption of N_2 and H species on the precious metal surface.
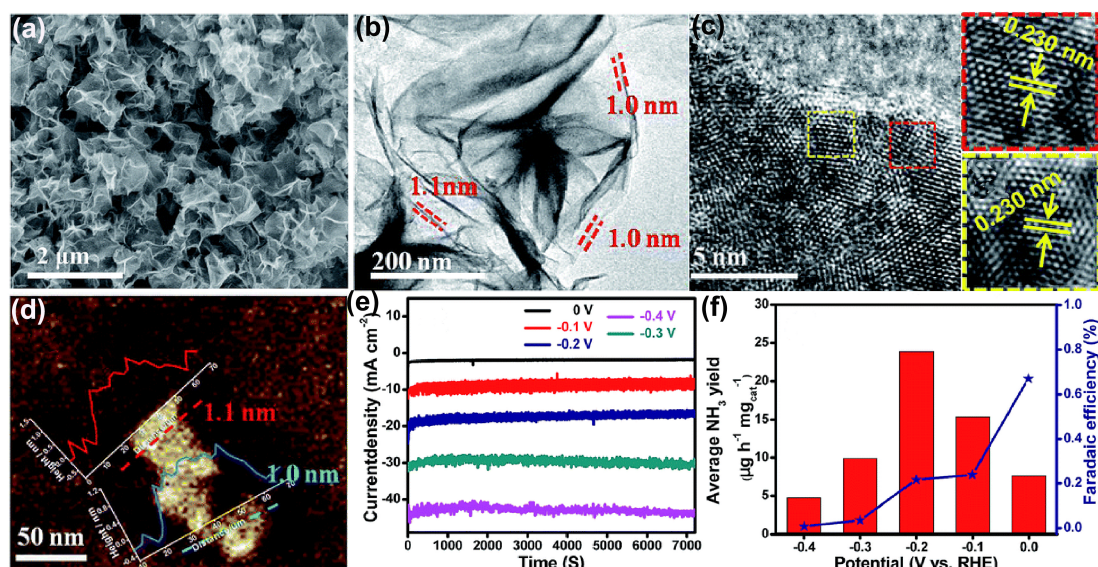
Figure 18. (a) SEM, (b) HRTEM, (c) Enlarged HRTEM, and (d) AFM images of Rhodium nanosheets. (e) chronoamperometric curves of Rh NNs in a N_2-saturated 0.1 M KOH electrolyte at different applied potentials, (f) yield rate of NH_3 (red) formation and FE (blue) at each given potential.[206]

Recently, in situ surface-enhanced infrared absorption spectroscopy has provided a detailed mechanistic description of the surface chemistry responsible for the electrochemical reduction of N_2 to NH_3, N_2H_4, and H_2 on a gold electrode in a 0.1 M KOH electrolyte.[211] The detection of vibrational modes diagnostic of NH_2 bending at 1,453 cm^{-1} and 1,298 cm^{-1}, together with N=N stretching at 1,109 cm^{-1} served to identify surface reaction intermediates N_2H_y ($1 < y < 4$). The observation of these fingerprint modes favours an associative reaction pathway, whereby adsorbed N_2 on Au is protonated and reduced to N_2H_y ($1 < y < 4$) via a four-electron transfer process to N_2H_4 and/or a six-electron one to NH_3.

1.2.4 Transition Metal Chalcogenides

Ultrathin two-dimensional nanosheets of layered transition metal dichalcogenides (TMDs) are fundamentally and technologically intriguing. In contrast to the graphene sheet, they are chemically versatile. Mono- or few-layered TMDs were obtained

either through exfoliation of bulk materials or bottom-up syntheses are direct-gap

semiconductors whose bandgap energy, as well as carrier type (n- or p-type), varies

between compounds depending on their composition, dimensionality, and

structure.[212]
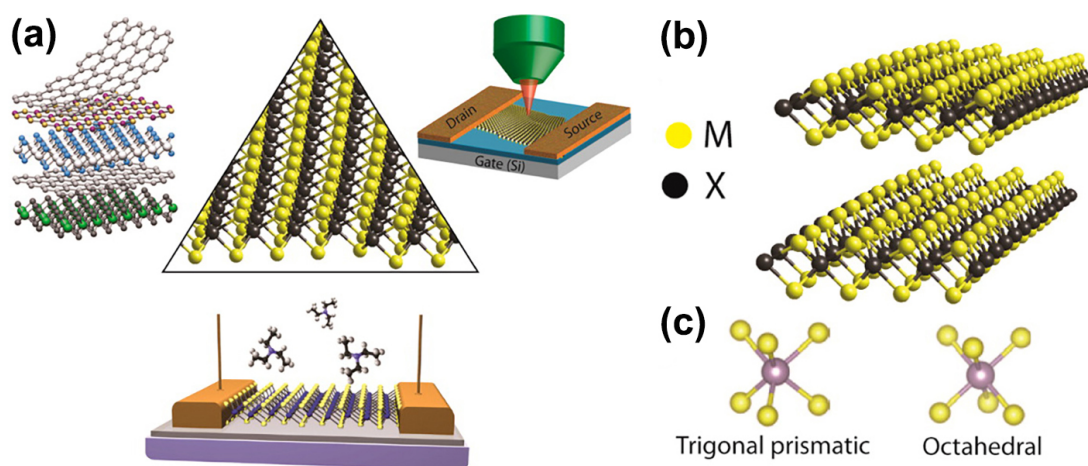
Figure 19. (a) Illustration of layered transition metal dichalcogenides. (b) Chemical structure of two layers of a TMDC where M is a transition element and X is a chalcogen. (c) Two polytypes of single-layer TMDCs: trigonal prismatic (1H) and octahedral (1T).[212]

As shown in Figure 19, layered TMDs can be described with the general chemical

formula MX_2 (M is a transition-metal element and X is a chalcogen such as S or

Se).[212,213] Bulk TMDs consist of monolayers stacked by van der Waals forces whereas

the general crystal structure of a TMD monolayer can be described as a sandwich

structure where one layer of transition metal is situated between two layers of chalcogen

(i.e., X-M-X). A unique feature of 2D TMDs is their multi-crystal structures.[214] For

example, 2H (hexagonal), 1T (trigonal), and 3R (rhombohedral) are the three common

crystal structures of molybdenum disulfide (MoS_2) which are dependent on the different

coordination models between Mo and S-atoms and the staking order between layers.

The band gaps of bulk and monolayer MoS_2 are also different due to the strong changes

72

in electronic structure.[215] The different crystal types and band gaps among the various TMDs lead to different surface properties and hence varied catalytic activities.

For electrocatalytic applications, the M sites at the layer edges or X vacancies, rather than the perfectly basal plane, have been identified as the catalytically active sites by both DFT calculations and experiments.[216,217] Inspired by this finding, various methods have been developed to expose more active edge sites (such as lateral size control, defect engineering etc.) and further improve the electrocatalytic performance of TMDs.[218] Additionally, either the M or X sites located in the basal plane can be activated using heteroatom doping.[219,220] Experiments and DFT calculations indicate that metallic atom (Fe, V, Li) doping are both effective for improving the NRR activity of TMDs. Such as, MacFarlane et al. identified that the edge sites of MoS_2 to be active for the NRR due to the high density of d electrons in Fe-doped, indicating the electrons from N_2 can fill the unoccupied t_2 orbital of the Fe center.[220,221]

Table 14. Experiment Activity of NRR on Transition Metal Chalcogenides-based Electrocatalysts.

Catalysts	Yield	FE	U (V)	Synthesis Method	Electrolyte
MoS_2[216]	5.53 µg h^{-1}mg^{-1}	N.A.	-0.35	Sonicated	0.1 M Ethanol
MoS_2[217]	4.94 µg h^{-1}cm^{-1}	1.17%	-0.50	Hydrothermal	0.1 M Na_2SO4
Li-S/MoS_2[219]	43.4 µg h^{-1} mg^{-1}	9.81 %	-0.20	Hydrothermal	0.1 M Li_2SO4
MoS_2[218]	6.98 µg h^{-1} cm^{-1}	17.6%	-0.15	Hydrothermal	0.01 M HCL
Fe_3S_4[222]	75.4 µg h^{-1}mg^{-1}	6.45%	-0.40	Eutectic-Solvothermal	0.1 M HCL

Table 15. Calculated Activity of NRR on Transition Metal Chalcogenides-based Electrocatalysts.

Catalysts	GGA	Barrier (eV)	RDS
MoS_2[217]	PBE	0.68	N_2H^*
Li-S/MoS_2[219]	PBE	0.42	N_2H^*
MoS_2[218]	RPBE	0.64	N_2H^*
Fe/MoS_2[220]	PBE	1.02	N_2H^*
Mo/MoS_2[223]	PBE	0.53	N_2H^*
V/MoP[221]	PBE	0.69	N_2H^*
Mo/MoSSe[224]	PBE	0.49	N_2H^*

*Denotes an adsorption site on catalyst surface.

In 2018, the MoS_2 is first utilized to catalyze the N_2 reduction reaction under room conditions.[217] As we know, the MoS_2 was considered as the good catalytic activity for HER, which is a significant suppression for the NRR process. But Mo ion at the edge possess atomic charge of +0.93 e according to the isosurface calculated, indicating the positively charged Mo-edge plays the key role to polarize and activate the N_2 molecules. And the DFT result described that the potential-determining step is the reductive protonation of adsorbed N_2, with a barrier of 0.68 eV without external potential (Figure 20g). As a proof-of concept experiment, MoS_2 nanosheet array was hydrothermally grown on carbon cloth (MoS_2/CC). High-resolution transmission electron microscopy (HRTEM) image (Figure 20a) take from the MoS_2 nanosheet (G) shows lattice fringe with an interplanar distance of 6.15 Å indexed to the (002) plane of MoS_2 phase. The XPS survey spectrum is mainly dominated by the characteristic Mo and S peaks. In Mo 3d region (Figure 20b), the peaks at 232.2 and 229.1 eV are assigned to the binding energies of Mo $3d_{3/2}$ and Mo $3d_{5/2}$, respectively. The S 2s peak at 226.7 eV is also visible in the Mo region. And the average NH_3 yields and corresponding FE under different potentials are plotted in (Figure 20d), The NH_3 yield rate and FE increased with increasing negative potential, but the two values decreased when the potential over than -0.5V, which is ascribed to the competitive adsorption of nitrogen and hydrogen species on the electrode surface. Besides the catalytic activity of nanosheet in the Na_2SO_4 electrolyte, the NRR performance of MoS_2/CC in acidic media (0.1 m HCl) was also studied (Figure 20f). It is shown that the NH_3 yield can reach the best value of 4.94 μg h^{-1} cm^{-1} with a FE of 0.096% at potential of −0.5 V.
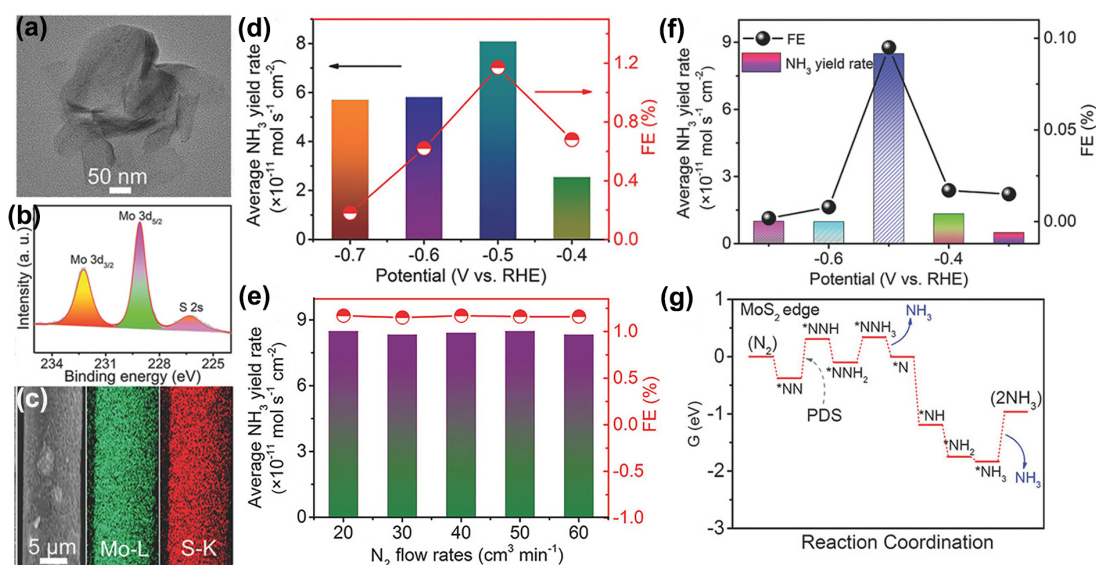
Figure 20. (a) TEM image of MoS_2 nanosheets. (c) XPS spectra of MoS_2 in the Mo 3d. (c) SEM image and EDX elemental mapping images of Mo and S in MoS_2/CC. (d) Average NH_3 yields and FEs of MoS_2/CC at different potentials in the 0.1 M Na_2SO_4. (e) Recycling test of MoS_2/CC at the potential of −0.5 V. (f) Average NH_3 yields and FEs of MoS_2/CC at different potentials in 0.1 m HCl. (g) Free-energy profile for NRR at MoS_2 edge site.[217]

As with graphene, doping heteroatoms at the edge or in the basal plane of TMDs can modify their electronic structures and consequently increase the number of active sites. Therefore, the identification of heteroatom doping sites in TMDs is crucial for revealing the effect that doping has on NRR activity. Recently, some metals, like Fe, Ru, Mo, Li, have doped into MoS_2 nanosheet and change both the geometric parameters and the intrinsic activity of MoS_2.[218-220,223] Further, Cai et al, employed DFT computations to reveal the effect of Mo doping the S-edge of MoS_2 for NRR activity. The results showed that for pristine MoS_2 nanosheet, $\Delta G_{max} = 0.98$ eV for Mo-edges. Incorporating Mo dopants at the S-edge decreased ΔG_{max} to 0.53 eV, indicating the presence of Mo can improved the NRR activity on the MoS_2.
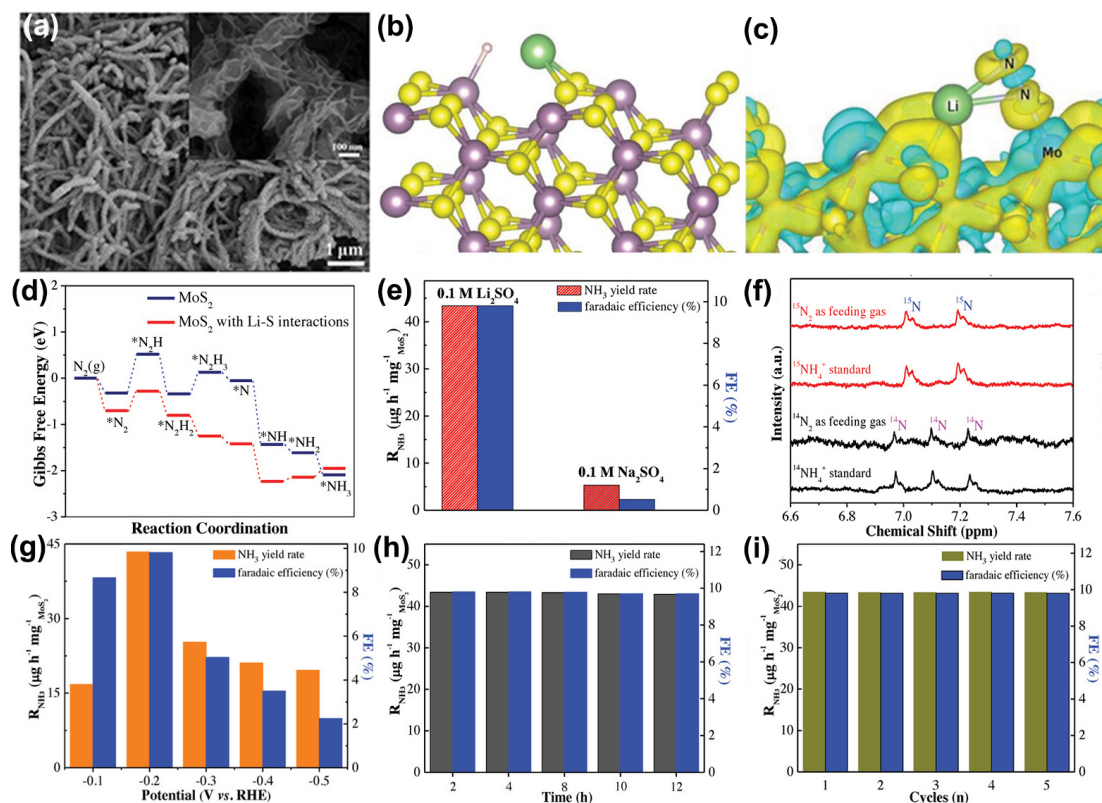
Figure 21. (a) SEM image of the as-synthesized MoS$_2$. (b) H* adsorption on the Mo-edge site of MoS$_2$ (Mo: purple, S: yellow, Li: green, and H: pink). (c) Deformation charge density of *N$_2$ at MoS$_2$ edge with Li–S interactions (yellow and blue represent charge accumulation and loss, respectively). (d) Free-energy diagrams of NRR at the edges of MoS$_2$ with and without Li–S interactions. (e) Yield rate and FE of MoS$_2$/BCCF obtained from N$_2$-saturated 0.1 m Li$_2$SO$_4$ and 0.1 m Na$_2$SO$_4$ electrolytes at −0.2 V (vs RHE) with a reaction time of 2 h. (f) 1H NMR spectra of the yielded ^{14}NH$_4^+$ and ^{15}NH$_4^+$ from ^{14}N$_2$ and ^{15}N$_2$ feeding gases, and corresponding standards (all standard concentration of 25 µg mL^{-1}). (g) NRR performance of MoS$_2$/BCCF in N$_2$-saturated 0.1 m Li$_2$SO$_4$ solution at −0.2 V (vs RHE). a) Influence of the applied potential on yield rate and FE for 2 h reaction. (h) Rate and FE during 12 h NRR process. (i) Reusability test with 2 h for each cycle.[219]

Recently, Zhang and co-workers purposely designed and synthesized an NRR electrocatalyst using MoS$_2$ nanosheet to incorporate Li$^+$. Their theoretical and experimental studies revealed that Li$^+$ association with sulphur functional groups in MoS$_2$ can retard the HER process and create a larger potential window to enable a highly selective NRR process through an alternative "[S–Li$^+$] · N$_2$–H$_x$" hydrogenation. The DFT result confirmed that without Li–S interactions on S-edge sites, the hydrogen

(H*) adsorption free energies (ΔG_{H*}) of 0.03 and 0.09 eV can be respectively obtained on S-edge and Mo-edge sites, suggesting S-edge sites are more favourable for HER. In strong contrast, with Li–S interactions, the ΔG_{H*} changes dramatically to 0.47 eV on S-edge sites (Figure a) and -0.72 eV on Mo-edge sites (Figure b). Such Li–S interactions induced changes, on one hand, make the S-edge sites thermodynamically unfavourable for HER, on the other hand, make the produced active H* firmly adsorbed on Mo-edge sites that is unfavourable for HER due to the suppressed H$_2$ formation mode. Moreover, the Li–S interactions induced charge redistributions lead to a change in Gibbs adsorption free energy of nitrogen molecule on Mo-edge site from -0.32 eV (without Li–S interaction) to -0.70 eV (with Li–S interaction) in the Figure 21C.

This means that the Li–S interactions can significantly enhance N$_2$ adsorption on Mo-edge sites. As a result, the calculated maximum energy barrier of 0.42 eV for N$_2$H formation at the Li-incorporated MoS$_2$ edges sites is much lower than that at the MoS$_2$ edge site without Li-S interactions (0.84 eV). The calculated result was confirmed by experiment that the in-operando created strong Li–S interactions to empower the S-rich MoS$_2$ nanosheets with superior NRR catalytic activity. In the Figure 21e, when the 0.1 m Na$_2$SO$_4$ electrolyte was used in the experiment, MoS$_2$ shows a poor NRR electrocatalytic performance, achieving an ammonia yield rate of 5.35 µg h^{-1} mg^{-1} and FE of 0.53%. While the rate and FE were up to 43.4 µg h^{-1} mg^{-1} and FE of 9.81% under the Li$_2$SO$_4$ electrolyte. The ^{14}NH$_4^+$ and ^{15}NH$_4^+$ concentrations of 2.84 and 2.85 µg mL^{-1} for these samples were also obtained from the indophenol blue method (Figure2f). The almost identical yielded ^{14}NH$_4^+$ and ^{15}NH$_4^+$ concentrations determined by both methods

categorically confirm that the yielded NH_3 is exclusively resulted from the MoS_2 catalyzed NRR. From the electrochemistry test standards (Figure 21g-i), the in-operando created Li–S interactions on MoS_2 electrocatalyst have excellent NRR catalytic activity, stability and HER suppression ability. The Li^+ interactions with S-edge sites of MoS_2 can effectively suppress hydrogen evolution reaction by reducing H* adsorption free energy from 0.03 to 0.47 eV, and enhance electrocatalytic N_2 reduction activity by decreasing the activation energy barrier. Except the MoS_2 can be applied to the NRR activity, Fe_3S_4 catalyst can be used in this reaction.[222] Compared to other TMDs, the catalyst exhibits a relatively higher ammonia yield rate (75.4 $\mu g\ h^{-1}$ mg^{-1}).

1.2.5   MXenes

The term MXenes refers to 2D layered materials derived from transition metal carbides, nitrides, or carbonitrides, such as Ti_3C_2.[72] Unlike graphene and phosphorene, which respectively have graphite and BP natural 3D bulk precursors, MXenes do not have a straightforward 3D precursor in nature. Instead, MXenes multilayer flakes are usually produced by the selective removal of the A layers in MAX phases, e.g., the removal of Al from Ti_3AlC_2. Thus, upon delamination using intercalation agents such as dimethyl sulfoxide and LiF, few-layer MXenes nanosheets can be readily created. MXenes were first experimentally used in lithium-ion batteries for energy storage, and research rapidly expanded to the prediction of new MXenes family members with the assistance of theoretical computational chemistry.[225]

MAX and $M_{n+1}AX_n$ phases refer to hexagonal layered transition metal carbides and nitrides.[226] The variable n can be assigned three different integers, n = 1, 2, and 3, while the MAX phases are classified as three types, 211, 312, and 413 structures. M represents an early transition metal element, such as Ti; A represents an element from group 13 or 14 (formerly groups 3A and 4A), such as Al or Si; and X refers to C, N, or their blends. For example, the simplest crystal structure of Ti_2AlC comprises a MAX phase with periodic stacking of four atom layers, Ti–C–Ti–Al, along its cross section. The Ti bilayers consist of two layers of close-packed atoms. The C monolayer is composed of C atoms occupying the octahedral sites between two Ti atomic layers, while the Al monolayer interleaves two periodic units of the Ti–C–Ti trilayer. The Ti_6C octahedral structure is analogous to rock salt, while the Al atoms occupy the centers of trigonal prisms.

Although MXenes exhibit an inherent metallic character, they can act as semiconductors when it covered by some terminates (OH, O, H).[227] Among a variety of properties, MXenes are notable for their similar conductivity to multilayer graphene, excellent stabilities, as well as hydrophilic properties.[228] During past decades, MXenes were applied to many applications, including electrode applications in Li-ion, and Na-ion batteries or electrochemical supercapacitors, MXenes have also been tested as catalytic and electro-catalytic materials for water splitting.[228-230] Owing to it have high specific areas, good electrical conductivities, stability, and hydrophilic behaviors. chemistry.[225]

Table 16. Experiment Activity of NRR on 2D MXenes-based Electrocatalysts.

Catalysts	Yield	FE	U (V)	Synthesis Method	Electrolyte
$Ti_3C_2\ T_x$[231]	20.4 μg h^{-1} mg^{-1}	9.3 %	-0.40	Etching	0.5 M Na_2SO_4
$Ti_3C_2T_x$[232]	4.72 μg h^{-1} cm^{-1}	5.78%	-0.20	Etching	0.5 M Li_2SO_4
TiO_2/ $Ti_3C_2T_x$[233]	31.17 μg h^{-1} mg^{-1}	16.07%	-0.45	Ethanol-thermal	0.1 M HCL
TiO_2/ $Ti_3C_2T_x$[234]	26.32 μg h^{-1} mg^{-1}	8.42%	-0.60	Hydrothermal	0.1 M HCL
$Ti_3C_2T_x$[235]	36.9 μg h^{-1} mg^{-1}	9.1%	-0.30	Etching	0.1 M HCL

Table 17. Calcualted Activity of NRR on 2D MXenes-based Electrocatalysts.

Catalysts	GGA	Barrier (eV)	RDS
V_3C_2[227]	PBE	0.32	NH_3
Mo_2TiC_2[236]	PBE	0.26	NH_3^*
$Mo/Ti_3C_2O_2$[237]	PBE	0.68	N_2H^*
Mo_2C[238]	PBE	N.A.	NH_2^*
$Ti_3C_2\ T_x$[231]	PBE	1.06	NH_3
$Ti_3C_2T_x$[232]	PBE	0.64	N_2H^*
TiO_2/ $Ti_3C_2T_x$[233]	PBE	0.40	$N_2H_2^*$

*Denotes an adsorption site on catalyst surface.

From the DFT calculations firstly revealed that V_3C_2 and Nb_3C_2 can activate the adsorbed N_2 and promote the conversion of N_2 into NH_3 under ambient condition.[227] The mechanism of electrocatalytic ammonia synthesis on others MXenes were investigated by DFT or experiment, including Mo_2TiC_2, Mo_2C, and $Ti_3C_2T_x$.[231-233,236-238] In the work of Sun et al., they compared the reaction energies and TS on two potential materials, indicating the distal pathway is the favourable route for conversion nitrogen to ammonia. Moreover, the effect of kinetic factors via an investigation of the TS was investigated in the paper. And DFT+D3 calculations have also identified the TSs and their structures and energies. The results, also shown in Figure 22, indicate activation barriers of 0.64 (V_3C_2, RDS) and 0.85 eV (Nb_3C_2) for the TS1 ($N_2 + H^*$) that connects N_2 and N_2H^*. While second hydrogenation step (0.90 eV) for Nb_3C_2, which is the RDS of Nb_3C_2.
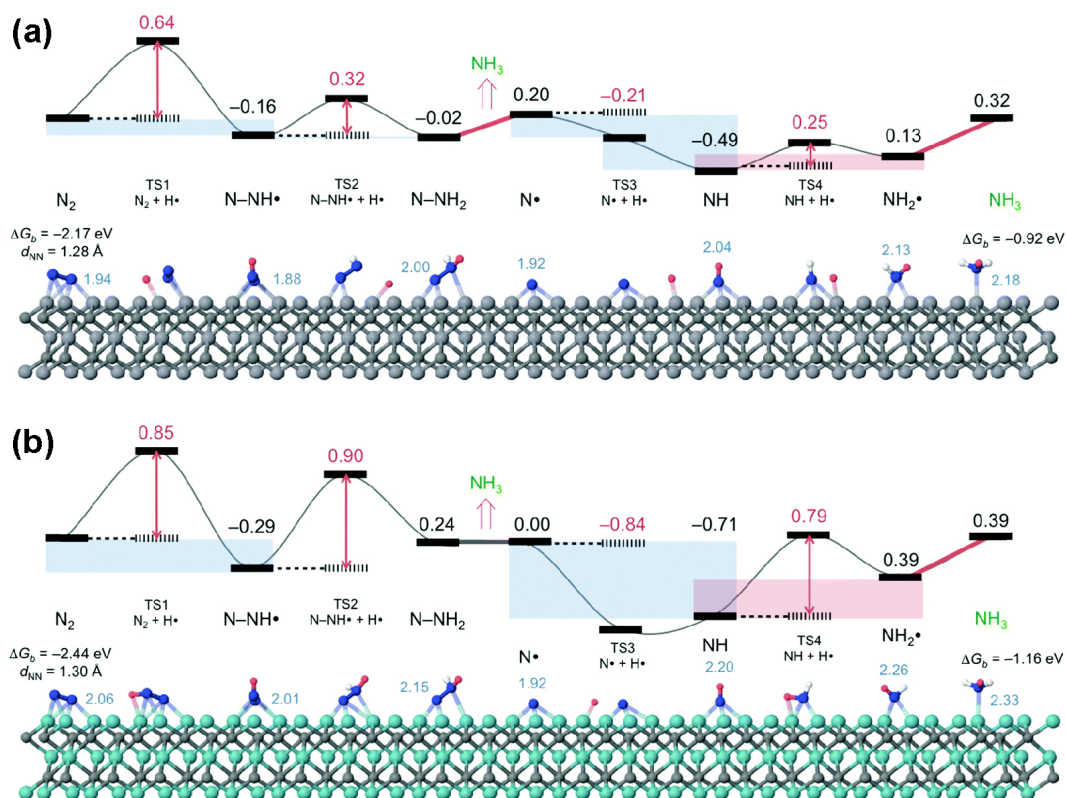
Figure 22. Minimum energy path for the N_2 conversion into NH_3 catalysed by V_3C_2 (a) and Nb_3C_2 (b) MXenes, and structures and energies of the intermediates and transition states (TS) all indicated. Selected d_{MN} distances are shown in Å. Shading indicates spontaneous (blue) versus non-spontaneous (red) steps.[227]

Recently $Ti_3C_2T_x$ nanosheets can achieve a high FE of the NRR at an ultralow potential for NH_3 electrosynthesis was studied by Wang et al.[232] $Ti_3C_2T_x$ with a single-layered, T–Ti–C– Ti–C–Ti–T sandwich structure (Figure 23) possesses various atomic sites, including C, O, lateral Ti, and middle Ti. Detailed characterizations including X-ray diffraction, atomic force microscopy, and transmission electron microscopy revealed the highly crystalline $Ti_3C_2T_x$ structure assembled by a 1.5-nm-thick nanosheet morphology. Raman analysis and Fourier transform infrared spectroscopy showed the abundant surface-terminating –O and –OH groups on the basal planes. The authors then performed an electrocatalytic N_2 fixation experiment by loading MXenes on parallel stainless-steel mesh as the working electrode, which produced results in

accordance with the predicted N_2 reduction ability of MXenes from their calculations. Specifically, the MXenes provided a maximum FE (4.62%) at -0.1 V versus the RHE for the NRR. When the applied potential was below -0.1 V (versus RHE), the FE of the NRR decreased dramatically as a result of the domination of the HER side reaction.
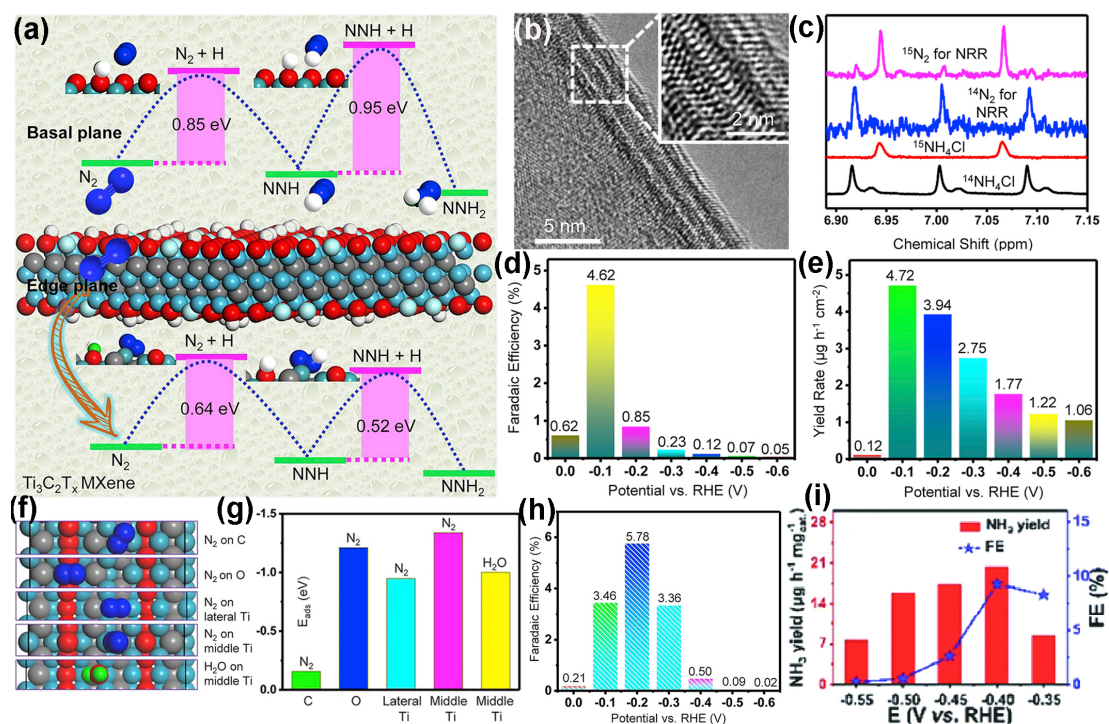
Figure 23. (a) Transition states path for ammonia formation catalysed by basal plane and edge sites of $Ti_3C_2T_x$ MXenes. (b) TEM images of an MXenes nanosheet. (c) ^{1}H NMR spectra (600 MHz) of standard samples of $^{14}NH_4^+$ and $^{15}NH_4^+$, and the electrolyte produced from the NRR reaction using $^{14}N_2$ and $^{15}N_2$ as the isotopic N_2 source. (d, e) FE and NH_3 yield rate of MXenes at various potentials. (f) Possible catalytic actives for N_2. (g) adsorption energy for N_2 on various atomic sites of MXenes and H_2O on the middle Ti atomic site. (h) FE of MXenes/FeOOH at various potentials.[232] (i) FE of MXenes/carbon at various potentials.[231] (C: gray, O: red, H: white Ti: sky blue, F: bluish white, and N: blue).

Then the authors conducted DFT calculations to investigate the favourable route and catalytic site on MXenes (Figure 23a). It inferred that the NRR performance of the edge planes of MXenes with exposed middle Ti sites should be better than that of basal planes with terminal O. After identifying and comparing the active sites on the basal

plane and edge plane with DFT calculations. Especially the catalyst has poor HER

activity by introducing the metal host in this experiment, having improved FE (5.78%).

At first, the experiment confirmed that NH_3 is generated from N_2 reduction by using

$^{15}N_2$ isotopic source (Figure 23c). Then the FE of NH_3 production is highly dependent

on the applied potential (Figure 23d), and MXenes achieves a maximum FE of 4.62%

at -0.1 V versus RHE, surpassing the efficiency of most of the reported water-based

approaches under ambient conditions. This achievement could be ascribed to the

limited HER at a low applied potential. Similarly, the NH_3 yield rates (Figure 23e) also

have a negative relation with the applied potential, and the maximum NH_3 yield rate of

4.72 mg h^{-1} cm^{-2} at the same applied potential. And it also studied the N_2 chemisorption

on different active sites of MXenes, which is an important factor affecting the catalytic

performance (Figure 23f). It concluded that the most active site for N_2 adsorption in

the MXenes structure is the middle Ti atom, due to it has the biggest adsorption energy

(-1.34 eV, Figure 23g). Thus, the ability of the basal planes of MXenes with terminal

oxygens to carry out the NRR should be lower than that of the edge planes with exposed

middle Ti sites. In the following work, the work synthesized vertically aligned metal

hosts (FeOOH nanosheets) to support the MXenes to overcome thermodynamic

obstacles. The FE of MXenes/FeOOH can reach a value of 5.78% under -0.2 V (versus

RHE), about 1.25 times higher than the maximum value of MXenes (Figure 23h). This

achievement can be mainly ascribed to two factors: a greater number of exposed active

edge sites on MXenes when hosted on vertically aligned FeOOH results in stronger

adsorption of N_2, and the HER activity of MXenes/FeOOH is relatively poor because

of the sluggish nature of FeOOH toward HER based on a comparison of the linear

sweep voltammograms and electrochemical impedance spectra of MXene/FeOOH and

MXene/SSM. Similarly, the MXenes performance was improved when the catalyst

loaded on the carbon nanosheets (Figure 23i).[231]

As we know, the marginal titanium atoms on the $Ti_3C_2T_X$ MXenes surface are

thermodynamically metastable, which could act as nucleating sites to enable the

generation of relatively stable foreign doped atoms, such as single transition metal, or

TiO_2. Xu and Yao reported that TiO_2/Ti_3C_2Tx electrocatalyst for NRR was synthesized

by one-step thermal treatment of the Ti_3C_2Tx nanosheets.[233,234] The as-prepared

electrocatalysts exhibit an NH_3 yield of 31.17 µg h^{-1} mg^{-1} and 26.32 µg h^{-1} mg^{-1} in two

work, respectively, which results all higher than the yield of pristine $Ti_3C_2T_X$ (20.4 µg

h^{-1} mg^{-1}). In the paper of Xu, they found that large number of VOs (33%) were

generated on $TiO_2/Ti_3C_2T_X$ during the ethanol-thermal process by using ESR spectra.

And the VO$_s$ act as the active sites for the NRR catalytic process. The morphologies

and structures of the $Ti_3C_2T_X$ and $TiO_2/Ti_3C_2T_X$ were characterized by the transmission

electron microscopy. The average NH_3 yields and the corresponding FEs at a series of

potentials for $TiO_2/Ti_3C_2T_X$ and $Ti_3C_2T_X$ were measured and compared. As indicated,

the $TiO_2/Ti_3C_2T_X$ can achieve a high NH_3 yield (32.17 µg h^{-1} mg^{-1}) at −0.55 V and FE

(16.07%) at −0.45 V, which were both higher than those of $Ti_3C_2T_X$.

The improvement of NH_3 yield and FE of $TiO_2/ Ti_3C_2T_X$ as electrochemical NRR

catalyst could be attributed to its hierarchical architecture that the TiO_2 using the

untreated $Ti_3C_2T_X$ nanosheets as supporting platform. Due to the supporting effect, the

self-aggregation of the TiO_2 can be efficiently avoided. In addition, the intrinsically good conductivity of the $Ti_3C_2T_X$ nanosheets could facilitate the electron transport in the NRR process. Meanwhile, the increased surface of the $TiO_2/ Ti_3C_2T_X$ upon the ethanol-thermal treatment was also favourable for the NRR performance. In addition, the charge exchange and transfer mainly occurred between the Ti atoms and N_2. The synergistic effect between $Ti_3C_2T_x$ nanosheets and TiO_2 could promote the charge exchange and transfer. Meanwhile, the electrons on adjacent Ti atoms can be easily retransferred to the adsorbed N_2 due to the synergistic effect. Furthermore, the charge transfer and electrons injection took place more strongly in the V_O. The adsorbed N_2 molecule could be significantly weakened and endowed with high activity for the subsequent hydrogenation procedures resulting from the injected electrons.

1.3 Catalyst Design and Development Protocols

Although many nanostructured materials have been successfully applied in a variety of catalytic N_2 fixation routes, until now, the efficiency of catalytic N_2 fixation is still low and is far from practical for the industrial production of NH_3 and remains a big challenge. There are two main reasons that limit the efficiency of this kind of reaction, the first of which is the strong nonpolar bond of the N_2 molecule, which has a considerably high activation barrier. This property is inherent to the N_2 molecule, which cannot be changed. However, the other limitation is the restriction of catalytic capability, which can be significantly increased after modification. With the high demand for N_2 fixation catalysts, many efforts have been devoted to developing several strategies for designing catalysts. In this section, the strategies for efficiently designing nanostructured N_2 fixation catalysts based on recent works are summarized below, such as enlarging the active surface area, constructing single atoms, stabilizing vacancies, and developing biomimetic devise. Although some strategies are not unique to the N_2 fixation reaction, these high-frequency reporting strategies are still widely recognized as having potential for breaking through the limitation of low efficiency N_2 fixation.

1.3.1 Defect Engineering

The advanced catalyst syntheses are always accompanied by the introduction of intrinsic defects and impurities phase. Defect engineering is an effective strategy for tuning and controlling the nature of materials such as their electronic and chemical properties. Generally, engineered defects are classified into three main categories based

on the dimensions of defects: point, line planar, and volume defects. Depending on the catalytic purposes, different types of defects have been employed. In this section, the positive and negative impacts of defects are discussed.

Defective materials usually show remarkable activities compared to defect-free materials. Massive studies revealed that the "induced" intrinsic defects in 2D electrocatalysts help to reduce these limitations and enhance photo(electro)activity. Above improvements might be contributed by the following aspects. First, the engineered-defects such as anion vacancies and dopants induced impurity phases can act as trapping centers to capture electrons or holes, inhibiting charge recombination as well as promoting their separation. Additionally, point defects such as VOs play a role as active sites which facilitate the adsorption and activation of reactant molecules. Third, creating defects leads to narrow down band gap energy, resulting in increasing of light absorption ability. It is worth noting that a number of generated electron hole would be greater if a semiconductor can absorb light in the longer wavelength region.

In addition to the desired effects on the catalytic activity of the semiconductors, intrinsic defects also have negative effects on catalytic materials. Recent studies reported that only the surface defects support the enhanced photoactivity performance, whereas the bulk defects suppress electron–hole separation and inhibit the photogenerated charges migration.[183] For example, Gurylev et al fabricated OVs supported amorphous Titania thin film by atomic layer-by-layer deposition.[239] Dong et al are one of the first pioneers to introduce nitrogen vacancies as defects in graphitic carbon nitride photocatalysts for ammonia production.[117] And the sulfur vacancies as

88

efficient catalysts for NRR also was developed after the above two vacancies.[216] The

photoexcited electrons may be relaxed at the defect states formed in band gap energy.

Therefore, only the electrons that can absorb high photon energy and overcome the

defect level are valuable to N_2 reduction. So far, in order to control desired defects

formation, various synthesis approaches have been devoted towards controlling the

surface and bulk defects. Several recent approaches were developed for controlling the

defect formation, such as high temperature treatment at reducing or inert atmosphere,

chemical reduction, vacuum activation, ultraviolet irradiation, phase transformation via

fast heating, ball milling, plasma etching, and lithium-induced conversion.[240]

1.3.1.1 Oxygen Vacancies

OVs are a type of defect introduced into the surface of photocatalysts to facilitate

adsorption of nitrogen on the active site and assist in activation of the nitrogen

molecules. The OVs induce mid-gap states within the bandgap structure, facilitating the

separations of photogenerated electrons and holes.[241,242]

Li et al. demonstrated that bismuth oxybromide (BiOBr) nanosheets (BOB 001-OVs)

photocatalysts with induced OVs on the (001) exposed facet could elongate the triple

bonds of nitrogen, which is an evidence of nitrogen activation.[135,243] The induced OVs

on the BiOBr nanosheets aid photocatalytic ammonia synthesis process by allowing the

system to operate without an introduction of organic scavengers or precious metal

cocatalysts. As theoretically depicted in Figure 3a, the OVs-induced defects states could

act as an initial charge carriers acceptor, inhibiting electron/hole recombination while

promoting the interfacial charge transfer from the excited BiOBr nanosheets to activate

N_2.[135] The results of the study have shown that OVs-induced on BiOBr nanosheets also lowers the N_2 activation energy required for the system. BiOBr belongs to the family of bismuth oxyhalides, which are a class of V–VI–VII ternary semiconductor materials. Within this family of materials, Li et al. also reported bismuth oxychloride (BiOCl) nanosheets with induced OVs for ammonia synthesis.[243] Bismuth oxyhalides have high concentrations of oxygen atoms which allows easy generations of OVs on the surface of the material.

Two models can be used to describe the nitrogen adsorption on the OVs of BiOCl nanosheets. BiOCl with (001) facets favors the terminal end-on adsorption of N_2, which follows an asymmetric distal mode and selectively generating NH_3. Meanwhile, BiOCl with (010) facets favors the side-on bridging adsorption structure of N_2, which follows a symmetric alternating mode to produce N_2H_4 as the primary intermediate. The engineered oxygen vacancies also contribute to the widening of the adsorption edges of BiOCl and BiOBr.[244] Li et al. also developed layered bismuth oxyhalide with induced OVs. The layered structures of bismuth oxyhalides enable natural generations of surface OVs due to strain differences between interlayers and intralayer of the structures. The layered structures also stimulate an internal electric field, which assist in efficient separation of electrons, thus facilitate more electrons to reach the active sites.

1.3.1.2 Nitrogen Vacancies

According to the discussions above, OVs can activate N_2 and significantly enhance interfacial electron transfer to bring high NRR performance. These results enlighten researchers to assume that nitrogen vacancies (NVs) can also be effective for NRR

processes. For the reason that NVs showed the same situation with the nitrogen atom in N_2, the NVs sites may have enhanced ability to activate N_2. In addition, NVs can also affect the electronic and band structure of the nanomaterials. Many kinds of transition metal nitride were studied by computational studies.[51,188-190,194] The results showed that VN, CrN, ZrN, and NbN have a low onset potential for NRR. Moreover, NVs play the key role in adsorbing and activating nitrogen, which would further improve their performance. Except for the theory processes, many experimental-based achievements have been reported. Recently, Yu and co-workers reported a defect engineering strategy to induce NVs in the metal free carbon nitrides to realize active electrocatalytic NRR performance.[245] To further study the effect of the NVs on N_2 activation, the theoretical calculation was conducted to conform the feasibility of N_2 activation on the material to NVs. The calculation results show the pristine material have a weak N_2 adsorption, while after introducing an NV at active site, N_2 can adsorb on in the form of binuclear end-on coordinated mode. Some novels work systematically studied the effect of nitrogen vacancies in carbon nitrides on the electrochemical NRR. It can guide other researchers to design various other catalysts with enhanced performance by inducing nitrogen vacancies to generate more active sites to activate N_2. The positive effect of nitrogen vacancies can also be expanded to the photocatalytic area. Graphitic carbon nitride (g-C_3N_4) was commonly chosen as photocatalyst for various reactions and many different strategies were developed to engineer its properties to enhance performance. For example, Wang and co-workers have designed various kinds of g-C_3N_4, which showed excellent performance in pthotocatalytic HER or some organic reactions.[246] It

is believed that inducing nitrogen vacancies in g-C$_3$N$_4$ would generate N$_2$ activation sites and enhance its photocatalytic NRR activity.

Recently, Wang and co-workers synthesized g-C$_3$N$_4$ with NVs by annealing it in nitrogen gas.[117] After inducing the NVs, the NV sites can selectively adsorb and activate N$_2$ molecule. Also, the nitrogen vacancies can enhance the separation efficiency of photogenerated electron and the carriers transfer from g-C$_3$N$_4$ to adsorbed N$_2$. Therefore, the g-C$_3$N$_4$ with nitrogen vacancies could photoreduce N$_2$ to NH$_3$ at ambient condition even with the air gas. It can conclude that nitrogen vacancies sites in the catalysts can effectively induce extra sites for N$_2$ activation and adsorption to enhance both electrocatalytic and photocatalytic NRR performance. Many other nitrides showed great potential in the catalytic fields and the researchers should try to search ideal nitrides for NRR according to the DFT results. Then they can further induce the NVs in the nitrides to enhance their NRR performance by various defects engineering strategies, such as plasma etching, electrochemical corrosion, and so on. The researchers should pay more attention to study the nitrogen vacancies effect on the NRR process with both experimental and computational strategies to insight under the effect clearly.

1.3.1.3 Sulfur Vacancies

Learning from the nature, the biological nitrogen fixation can give the researchers some inspiration to design ideal catalysts to accelerate the NRR process. And according to the component elements of nitrogenases, the Mo and S elements play significant roles in NRR.[247] Recently, transitional metal dichalcogenides (TMDs) have received much

attention in the catalytic field due to their inherent advantages for various reactions. Therefore, these TMDs are expected to exhibit good NRR catalytic performance. Sun and co-workers recently used DFT calculations to study the electrochemical NRR process of MoS_2 on different sites.[217] The theoretical result indicated that the positively charged Mo edge was the active site to activate and polarize the N_2 molecules. In their work, the RDS is the reductive protonation of adsorbed N_2, with only a barrier of 0.68 eV without external potential, which is much lower than the limiting barriers for some other flat metal surfaces. In addition, MoS_2 also showed good NRR activity in acid solution where obvious hydrogen evolution occurred. This work not only provided us an attractive high active electrocatalyst for N_2 reduction under ambient conditions but also guide other researchers to explore transition metal sulfides-based materials as NRR catalysts. Moreover, the oxygen and sulfur elements have very similar chemical properties according to previous literatures. Therefore, the sulfur vacancies (SVs) formed can engineer the band structure and electronic structure of the TMDs and affect their electrocatalytic/photocatalytic NRR performance by inducing extra sites for N_2 activation and adsorption. Thus, we hypothesize that SVs formed by various defect-engineering strategies in metal sulfide may have a similar effect on nitrogen photoreduction because oxygen and sulfur atom have the similar chemical properties. Hu and co-workers designed a novel ternary metal sulfide catalyst with excellent nitrogen photoreduction performance under visible light. They studied the positive effect of the sulfur vacancies on their photofixation activities. The obtained catalyst shows an enhanced NRR performance since the SVs can not only serve as active sites

to adsorb and activate N_2 molecules but also promote the interfacial charge transfer from catalysts to N_2 molecules. The author also compared several different sulfides samples and this vacancies effect was useful in all of the prepared samples.

And according to many published research results, the TMDs can contain large amount of vacancy defects by reducing its layers to the atomic thickness or ultrathin form.[248] Recently, Wang and co-workers designed ultrathin MoS_2 nanosheets by sonicating the prepared MoS_2 nanosheets in water for different time. For its ultrathin structure and the treatment of sonication, the prepared MoS_2 was expected to have many vacancies. The inductively coupled plasma result told the stoichiometry ratio of Mo:S in the ultrathin MoS_2 is 1:1.75, which was much smaller than 1:2, indicating many S vacancies existed in the nanosheets. They result showed the NRR photoreduction and ammonia production efficiency of the different samples and conditions. As we can see that the ultrathin MoS_2 nanosheets showed much better NRR performance (0.83 μg mL^{-1}) than both that of the bulk MoS_2 and hydrothermal prepared MoS_2 (0.35 μg mL^{-1}), indicating the advantages of the SVs in photocatalytic NRR process. Also, in the acidic condition, the samples would show better NRR performance, resulting from the decreased kinetic barrier for NRR.

This result would guide other researchers to pay more attention to preparing various transition metal sulfides and developing different strategies to induce sulfur vacancies to increase the active sites for NRR. In summary, the anion vacancies (oxygen, nitrogen, and sulfur) can efficiently regulate the electronic structure and the band gap of the nanomaterials, which would in turn increase the number of active sites for NRR

processes and enhance the catalytic performance. Apart from anion vacancies, making the cation vacancy is also an effective strategy to tailor the electronic structure variation of the various nanomaterials result in attractive properties. To date, there are some experimental results to systematically study the effect of cation vacancy on the NRR process at ambient conditions. Then, the effect of the anion vacancies and the cation vacancies should be further compared and discussed to illuminate the process of NRR by the defect sites.

1.3.2 Impurity Engineering

As mentioned in previous sections, most pristine 2D nanomaterials are inert for electrocatalysis due to their low adsorption energy, limited number of active sites, and low conductivity. Therefore, preparation of high-performance 2D catalysts with favorable composition, thickness, defects, and surface properties is extremely important for their practical application. To this end, various methods such as heteroatom doping, defect engineering, interfacial structure engineering, etc. have been utilized to tailor the catalytic activity of 2D nanomaterials. Chemical doping with heteroatoms is an effective method for tailoring electronic properties, manipulating surface chemistry, and modifying the elemental composition of 2D nanomaterials to improve the NRR performance. To date, heteroatom doping has demonstrated its ability to impart catalytic activity for various 2D nanomaterials. In this section, we briefly summarize catalyst design protocols for wide variety 2D catalysts. The advantages and limitations of each protocol are systematically discussed together with some featured examples of electrocatalytic applications.

1.3.2.1 Metal-Atom Doping

The heteroatom doping has also been recognized as an effective approach to adjust the chemical or physical properties of materials for their electronegativity difference with intrinsic atoms. Therefore, inducing metal or nonmetal elements into metal compounds or metal-free nanomaterials can effectively turn their surface properties (metal valence, coordination, and so on) even doping at a very low level. The doping effect has been widely researched in other NRR electrocatalytic reactions.

Recently, both the theoretical and experimental results of NRR have been made at ambient conditions by defect engineering of doping. For example, R. MacFarlane and co-workers recently used DFT to study the NRR performance of Fe-doped MoS_2 nanosheets. As we know, the basal planes of MoS_2 show nearly no catalytic activities.[220] Therefore, doping other transition metals into the basal plane of MoS_2 would result in the charge re-distribution, which can effectively adjust its electronic structure and increase the active sites number. The DFT results showed that the absolutely inactive MoS_2 become active for NRR when single Fe atoms are doped on. From their DFT results we can see that the Fe center yields electron charge to MoS_2 resulting in the formation of the very rare and reactive species. The catalyst can achieve NRR process under mild conditions and the limiting step is regard as the first H^+/e^- pair transfer, which has an activation barrier of 1.02 eV. Also, the binding energy between the catalyst and the NH_3 product was much lower than that of N_2 adsorption, indicating that it can be used as an ideal catalyst for its successful electroreduction cycles. Apart from the theoretic results, many meaningful and successful experimental results were also

96

reported. For example, Xiong and co-workers induced the defects states in $W_{18}O_{49}$ ultrathin nanowires to increase the NRR active sites by doping metal element Mo.

1.3.2.2 Non-Metal-Atom Doping

Apart from the metal-based catalysts, the carbon-based materials or analogue also play very important role in the catalytic fields. Various kinds of the carbon-based materials were developed and showed highly efficient catalytic performance, such as CRR and ORR. According to the published results, the heteroatom (N, P, S, etc.) doping can induce more defects served as the active sites for catalytic reaction. [97] The heteroatom doping can induce the charge redistribution, which can change the chemisorption mode of the reaction gas, enhancing the O_2 or CO_2 reduction reactions. The heteroatom dopants can effectively change the electron properties of the neighboring carbon atoms for their different atom sizes and electronegativities of the carbon atom. Inspired by this understanding and the effect of doping, the researchers have the reasons to believe that the ideal doped carbon materials can also show high NRR activities. The doped carbon materials are expected to promote the chemical adsorption of N_2 and further fast the dissociation of the N_2 at the defect sites.

Recently, many researchers reported the doped carbon materials as NRR electrocatalysts. However, different groups may report different NRR performances even though they designed nearly the same catalysts. Because there was no recognized experimental standard and detection means until now. Recently, Quan's group developed an N-doped porous carbon as NRR electrocatalyst under ambient conditions, which can achieve high ammonia production rate of 23.8 $\mu g\ h^{-1}\ mg^{-1}$ (-0.9 V vs RHE)

in the solution of 0.05 m H_2SO_4. And the best current efficiency can reach 1.42%, which was higher than most other reported electrocatalysts. The material was prepared by pyrolyzing from a zeolite imidazolate framework, which have high N contents and the type of the N species can be controlled. The author compared the N-doped porous carbon samples prepared at different temperature and the sample prepared at the temperature of 750 °C showed the best NRR activity. They also carried out the control experiment under the Ar atmosphere to make sure the nitrogen source of ammonia was from the N_2. And the stability test showed its excellent durability, since there was no obvious deterioration after 10 consecutive cycles. To exclude the effects of the Zn impurity from the precursor, they use the inductively coupled plasma atomic emission spectroscopy to analyze the content of the Zn, which was only around 0.08 wt%. They further prepared the samples with different Zn contents to study the effect of Zn. The results told that their NRR activities were nearly the same, indicating that the trace Zn has nearly no effect on NRR. Their XPS results showed that the pyridine N benefit to the NRR activity and the DFT calculation also confirmed that, which guide others to further improve the NRR performance of carbon-based catalysts by increasing the pyridine N content. Moreover, chose the KOH as the solution to suppress the HER process because the HER is more dominant in acids than that in the alkaline electrolytes. Also, they carried out the stability test and the NRR in the Ar atmosphere to prove the formation NH_3 came from N_2. In addition, they systematically studied the effect of Fe doping on the NH_3 formation. The results demonstrated that the negative effect of Fe doping on the NRR since the increasing Fe doping content would induce the decreased

production rate of NH$_3$, which may result from the enhancement of the HER. Interestingly, they found that both the types and the concentration of the electrolytes have great effects on the NRR process.

1.4 Current Achievements and Challenges

In the past decades, suitable catalysts were developed in the industrial world by using trial-and error traditional approaches because of the complex structures of supported catalysts and the limited in situ characterization technologies. Recently, computational modelling provides a more rational way to design catalysts. Using density functional theory and other theoretical methods, reaction mechanisms at the molecular level can be determined. Concurrently, the discovery of scaling relationships between properties of catalytic materials and the stability of the reactive intermediates have furthered knowledge of the catalytic process. More specifically, computational chemistry has investigated the electronic structure of the catalyst, the binding strength of intermediates on the surface and a range of geometric properties. These scaling relationships reveal the factors that influence the catalytic trends of different materials. Based on the scaling relationships, researchers can choose one or a few properties, termed reactivity descriptors, to correlate surface reaction energies and activation barriers. In this way, a high dimensional kinetic model based on the activation and reaction energies of all elementary reaction steps is reduced to a few dimensions described by a series of reactivity descriptors, which can predict trends in catalytic performance.

Based on thermodynamics, it is possible to synthesize ammonia by an electrochemical NRR process. Electrocatalytic artificial nitrogen fixation have drawn rising research interest owing to the following merits: (i) the NH_3 synthesis can be realized by using abundant N_2 and H_2O as raw materials under mild conditions, leading to the lower cost;

(ii) the NRR process without carbon dioxide emission can efficiently alleviate environmental, and (iii) it can provide a potential route to store clean and renewable solar energy and electricity in the form of a hydrogen carrier and carbon-free fuel. Until now, all efforts have found that such a method has two major problems: low rates and low selectivity associated with the reaction. In addition, the ammonia production is normally accompanied by the simultaneous generation of hydrogen and hydrazine, resulting in a very low selectivity towards NH_3. More importantly, current understanding on the fundamental mechanisms of N_2 photo-reduction and electro-reduction is still very limited due to the considerably complicated reaction process. To promote the development of heterogeneous nitrogen fixation under ambient conditions, there are some perspective suggest to further improve the performance of electrocatalytic NRR systems. Firstly, the design of more efficient, cost-effective, environment friendly and robust catalysts is very desirable. It is essential to develop novel technologies for nanomaterial synthesis, because the variant compositions and morphologies of nanostructured materials play an important role in enhancing the catalytic nitrogen fixation performance. The interface control, surface engineering, chemical modification and so on are promising methods for the optimization of catalyst performance. Especially, defective catalyst surface has an enormous impact on the catalytic performance. Compared to the flat bulk surfaces, the roughened surfaces with rich defects and doped heteroatoms possess larger catalytic active surface area and considerably more low-coordination sites (such as vacancies, corners, edges and steps), which have greatly enhanced intrinsic catalytic activity. Some works demonstrated that

102

the introduction of NVs could endow g-C$_3$N$_4$ with excellent photocatalytic NRR activity. In contrast, the photocatalytic activity was greatly inhibited when the NVs were occupied by Pd nanoparticles.[117] In addition, the electronic and geometric effects induced by chemical modification can give rise to the appropriate variation and adjustment of binding strengths of reaction intermediates on catalyst surface, giving better catalytic properties. The construction of heterogeneous SAC is another inviting approach for promoting the NRR performance due to the high activities of single metal atoms. For example, Ru-single atoms were used for NRR and exhibited improved ammonia yield and selectivity.[231] The good news is SACs could be conveniently synthesized from metal-organic frameworks or metal-organic complexes.

Secondly, to understand the obscure fundamental mechanisms of heterogeneous NRR processes is important. N$_2$ reduction is regarded as a considerably complicated multi-step reaction, and many details still remain unclear. The DFT method has been utilized as a powerful tool to predict the possible active sites, the rate-determining step and the intermediates of the reaction. The effective combination of theoretical analysis and experimental results is advantageous to reveal the reaction mechanisms of NRR at molecular scale. Especially, more attention should be paid to building reasonable models closer to the actual reaction systems. Meanwhile the theoretical computation based on materials genome method and more approaches could provide a feasible way to design novel catalysts.

Thirdly, advanced characterization techniques, such as spherical aberration corrected transmission electron microscopy, in-situ synchrotron radiation techniques,

in-situ X-ray photoelectron spectroscopy, in-situ diffuse reflectance Fourier transform infrared spectroscopy, and in-situ electron paramagnetic resonance spectroscopy are suggested to be used for the precise investigation of the active sites as well as the intermediates structure during the reaction processes. Moreover, isotope labelling is an effective and direct method for detecting the source and pathway of reaction products. In-situ FTIR has also be utilized to monitor the time-dependent change of the functional groups on catalyst surfaces, which is helpful to confirm the ammonia formation process.

1.5 References

(1) Erisman, J. W.; Sutton, M. A.; Galloway, J.; Klimont, Z.; Winiwarter, W. How a Century of Ammonia Synthesis Changed the World. *Nat. Geosci.* **2008,** *1*, 636.

(2) Foster, S. L.; Bakovic, S. I. P.; Duda, R. D.; Maheshwari, S.; Milton, R. D.; Minteer, S. D.; Janik, M. J.; Renner, J. N.; Greenlee, L. F. Catalysts for Nitrogen Reduction to Ammonia. *Nat. Catal.* **2018,** *1*, 490-500.

(3) Hoffman, B. M.; Lukoyanov, D.; Yang, Z.-Y.; Dean, D. R.; Seefeldt, L. C. Mechanism of Nitrogen Fixation by Nitrogenase: The Next Stage. *Chem. Rev.* **2014,** *114*, 4041-4062.

(4) MacKay, B. A.; Fryzuk, M. D. Dinitrogen Coordination Chemistry: On the Biomimetic Borderlands. *Chem. Rev.* **2004,** *104*, 385-402.

(5) Liu, J.; Ma, K.; Ciais, P.; Polasky, S. Reducing Human Nitrogen Use for Food Production. *Sci. Rep.* **2016,** *6*, 30104-30104.

(6) Van der Ham, C. J. M.; Koper, M. T. M.; Hetterscheid, D. G. H. Challenges in Reduction of Dinitrogen by Proton and Electron Transfer. *Chem. Soc. Rev.* **2014,** *43*, 5183-5191.

(7) Liu, C.; Li, Q.; Wu, C.; Zhang, J.; Jin, Y.; MacFarlane, D. R.; Sun, C. Single-Boron Catalysts for Nitrogen Reduction Reaction. *J. Am. Chem. Soc.* **2019,** *141*, 2884-2888.

(8) Patil, B.; Hessel, V.; Seefeldt, L. C.; Dean, D, R.; Hoffman, B. M.; *In Ullmann's Encyclopedia of Industrial Chemistry,* **2017**, 1st.

(9) Patil, B. S.; Wang, Q.; Hessel, V.; Lang, J. Plasma N_2-fixation: 1900–2014. *Catal. Today* **2015,** *256*, 49-66.

(10) Klerke, A.; Christensen, C. H.; Nørskov, J. K.; Vegge, T. Ammonia for Hydrogen Storage: Challenges and Opportunities. *J. Mater. Chem.* **2008,** *18*, 2304-2310.

(11) Guo, J.; Chen, P. Catalyst: NH_3 as an Energy Carrier. *Chem* **2017,** *3*, 709-712.

(12) Deng, J.; Iñiguez, J. A.; Liu, C. Electrocatalytic Nitrogen Reduction at Low Temperature. *Joule* **2018,** *2*, 846-856.

(13) Haber, F. Bemerkung zu vorstehender Notiz. *Naturwissenschaften* **1923,** *11*, 339-340.

(14) Haber, F. Neue Arbeitsweisen. *Naturwissenschaften* **1923,** *11*, 753-756.

(15) Über die Bildung von Ammoniak den Elementen. *Zeitschrift für Anorganische Chemie* **1905,** *44*, 341-378.

(16) Rod, T. H.; Logadottir, A.; Nørskov, J. K. Ammonia Synthesis at Low Temperatures. *J. Chem. Phys.* **2000,** *112*, 5343-5347.

(17) Zhan, C.-G.; Nichols, J. A.; Dixon, D. A. Ionization Potential, Electron Affinity, Electronegativity, Hardness, and Electron Excitation Energy: Molecular Properties from Density Functional Theory Orbital Energies. *J. Phys. Chem. A* **2003,** *107*, 4184-4195.

(18) Patil, B.; Hessel, V.; Seefeldt, L. C.; Dean, D, R.; Hoffman, B. M.; *In Ullmann's Encyclopedia of Industrial Chemistry,* **2017**, 2nd.

(19) Tanabe, Y.; Nishibayashi, Y. Developing more Sustainable Processes for Ammonia Synthesis. *Coord. Chem. Rev.* **2013,** *257*, 2551-2564.

(20) Giddey, S.; Badwal, S. P. S.; Kulkarni, A. Review of Electrochemical Ammonia Production Technologies and Materials. *Int. J. Hydrog. Energy* **2013,** *38*, 14576-14594.

(21) Montoya, J. H.; Tsai, C.; Vojvodic, A.; Nørskov, J. K. The Challenge of Electrochemical Ammonia Synthesis: A New Perspective on the Role of Nitrogen Scaling Relations. *ChemSusChem* **2015,** *8*, 2180-2186.

(22) Amar, I. A.; Lan, R.; Petit, C. T. G.; Tao, S. Solid-state Electrochemical Synthesis of Ammonia: A Review. *J. Solid State Electrochem.* **2011,** *15*, 1845-1860.

(23) Taylor, D. W.; Smith, P. J.; Dowden, D. A.; Kemball, C.; Whan, D. A. Ammonia Synthesis and Related Reactions over Iron-cobalt and Iron-nickel Alloy Catalysts. Part I. Catalysts Reduced at 853 K. *Appl. Catal.* **1982,** *3*, 161-176.

(24) J., K. R. Study on the Properties of Iron–cobalt Alumina Supported Catalyst for Ammonia. *J. Chem. Technol. Biotechnol.* **1994,** *59*, 73-81.

(25) López, T.; Bosch, P.; Gómez, R. Non-conventional Preparation of Ru/SiO$_2$ Catalysts. *React. Kinet. Catal. Lett.* **1990,** *41*, 217-221.

(26) Kadowaki, Y.; Aika, K. i. Promoter Effect of Sm$_2$O$_3$on Ru/Al$_2$O$_3$ in Ammonia Synthesis. *J. Catal.* **1996,** *161*, 178-185.

(27) Siporin, S. E.; McClaine, B. C.; Anderson, S. L.; Davis, R. J. Lanthanum Promotion of Ru/Zeolite X Catalysts for Ammonia Synthesis. *Catal. Lett.* **2002,** *81*, 265-269.

(28) Kowalczyk, Z.; Jodzis, S.; Sentek, J. Studies on Kinetics of Ammonia Synthesis over Ruthenium Catalyst Supported on Active Carbon. *Appl. Catal., A* **1996,** *138*, 83-91.

(29) Schlögl, R. Catalytic Synthesis of Ammonia—A "Never-Ending Story"? *Angew. Chem. Int. Ed.* **2003,** *42*, 2004-2008.

(30) Burgess, B. K.; Lowe, D. J. Mechanism of Molybdenum Nitrogenase. *Chem. Rev.* **1996,** *96*, 2983-3012.

(31) Hoffman, B. M.; Lukoyanov, D.; Dean, D. R.; Seefeldt, L. C. Nitrogenase: A Draft Mechanism. *Acc. Chem. Res.* **2013,** *46*, 587-595.

(32) Schrock, R. R. Catalytic Reduction of Dinitrogen to Ammonia at a Single Molybdenum Center. *Acc. Chem. Res.* **2005,** *38*, 955-962.

(33) Allen, A. D.; Senoff, C. V. Nitrogenopentammineruthenium(II) Complexes. *Chem. Commun.* **1965**, *24*, 621-625.

(34) Einsle, O.; Tezcan, F. A.; Andrade, S. L. A.; Schmid, B.; Yoshida, M.; Howard, J. B.; Rees, D. C. Nitrogenase MoFe-Protein at 1.16 Å Resolution: A Central Ligand in the FeMo-Cofactor. *Science* **2002,** *297*, 1696-1700.

(35) Spatzal, T.; Aksoyoglu, M.; Zhang, L.; Andrade, S. L. A.; Schleicher, E.; Weber, S.; Rees, D. C.; Einsle, O. Evidence for Interstitial Carbon in Nitrogenase FeMo Cofactor. *Science* **2011,** *334*, 940-940.

(36) Lancaster, K. M.; Roemelt, M.; Ettenhuber, P.; Hu, Y.; Ribbe, M. W.; Neese, F.; Bergmann, U.; DeBeer, S. X-ray Emission Spectroscopy Evidences a Central Carbon in the Nitrogenase Iron-Molybdenum Cofactor. *Science* **2011,** *334*, 974-977.

(37) Eady, R. R. Structure−function Relationships of Alternative Nitrogenases. *Chem. Rev.* **1996,** *96*, 3013-3030.

(38) Kim, J.; Rees, D. Structural Models for the Metal Centers in the Nitrogenase Molybdenum-iron Protein. *Science* **1992,** *257*, 1677-1682.

(39) Chan, J. M.; Christiansen, J.; Dean, D. R.; Seefeldt, L. C. Spectroscopic Evidence for Changes in the Redox State of the Nitrogenase P-Cluster during Turnover. *Biochemistry* **1999,** *38*, 5779-5785.

(40) Duval, S.; Danyal, K.; Shaw, S.; Lytle, A. K.; Dean, D. R.; Hoffman, B. M.; Antony, E.; Seefeldt, L. C. Electron Transfer Precedes ATP Hydrolysis during Nitrogenase Catalysis. *Proc. Natl. Acad. Sci. U.S.A.* **2013,** *110*, 16414-16419.

(41) Liu, C.; Li, Q.; Zhang, J.; Jin, Y.; MacFarlane, D. R.; Sun, C. Conversion of Dinitrogen to Ammonia on Ru Atoms Supported on Boron Sheets: A DFT Study. *J. Mater. Chem. A* **2019,** *7*, 4771-4776.

(42) Rosca, V.; Duca, M.; de Groot, M. T.; Koper, M. T. M. Nitrogen Cycle Electrocatalysis. *Chem. Rev.* **2009,** *109*, 2209-2244.

(43) Marnellos, G.; Stoukides, M. Ammonia Synthesis at Atmospheric Pressure. *Science* **1998,** *282*, 98-100.

(44) Kyriakou, V.; Garagounis, I.; Vasileiou, E.; Vourros, A.; Stoukides, M. Progress in the Electrochemical Synthesis of Ammonia. *Catal. Today*, **2017,** *286*, 2-13.

(45) Murakami, T.; Nishikiori, T.; Nohira, T.; Ito, Y. Electrolytic Synthesis of Ammonia in Molten Salts under Atmospheric Pressure. *J. Am. Chem. Soc.* **2003,** *125*, 334-335.

(46) Zhou, F.; Azofra, L. M.; Ali, M.; Kar, M.; Simonov, A. N.; McDonnell-Worth, C.; Sun, C.; Zhang, X.; MacFarlane, D. R. Electro-synthesis of Ammonia from Nitrogen at Ambient Temperature and Pressure in Ionic Liquids. *Energy Environ. Sci.* **2017,** *10*, 2516-2520.

(47) Li, Z.; Liu, R.; Xie, Y.; Feng, S.; Wang, J. A Novel Method for Preparation of Doped $Ba_3(Ca_{1.18}Nb_{1.82})O_{9-\delta}$: Application to Ammonia Synthesis at Atmospheric Pressure. *Solid State Ion.* **2005,** *176*, 1063-1066.

(48) Kordali, V.; Kyriacou, G.; Lambrou, C. Electrochemical Synthesis of Ammonia at Atmospheric Pressure and Low Temperature in a Solid Polymer Electrolyte Cell. *Chem. Commun.* **2000**, 1673-1674.

(49) Abghoui, Y.; Garden, A. L.; Hlynsson, V. F.; Bjorgvinsdottir, S.; Olafsdottir, H.; Skulason, E. Enabling Electrochemical Reduction of Nitrogen to Ammonia at Ambient Conditions through Rational Catalyst Design. *Phys. Chem. Chem. Phys.* **2015,** *17*, 4909-4918.

(50) Skúlason, E.; Bligaard, T.; Gudmundsdóttir, S.; Studt, F.; Rossmeisl, J.; Abild-Pedersen, F.; Vegge, T.; Jónsson, H.; Nørskov, J. K. A Theoretical Evaluation of Possible Transition Metal Electro-catalysts for N_2 Reduction. *Phys. Chem. Chem. Phys.* **2012,** *14*, 1235-1245.

(51) Abghoui, Y.; Skúlason, E. Computational Predictions of Catalytic Activity of Zincblende (110) Surfaces of Metal Nitrides for Electrochemical Ammonia Synthesis. *J. Phys. Chem. C* **2017,** *121*, 6141-6151.

(52) Cao, N.; Zheng, G. Aqueous Electrocatalytic N_2 Reduction under Ambient Conditions. *Nano Res.* **2018,** *11*, 2992-3008.

(53) Chen, G.; Cao, X.; Wu, S.; Zeng, X.; Ding, L.; Zhu, M.; Wang, H. Ammonia Electrosynthesis with High Selectivity under Ambient Conditions via a Li^+ Incorporation Strategy. *J. Am. Chem. Soc.* **2017,** *139*, 9771-9774.

(54) Bao, D.; Zhang, Q.; Meng, F.; Zhong, H.; Shi, M.; Zhang, Y.; Yan, J.; Jiang, Q.; Zhang, X. Electrochemical Reduction of N_2 under Ambient Conditions for Artificial N_2 Fixation and Renewable Energy Storage Using N_2/NH_3 Cycle. *Adv. Mater.* **2017,** *29*, 1604799.

(55) Rittle, J.; Peters, J. C. An Fe-N_2 Complex That Generates Hydrazine and Ammonia via Fe=NNH_2: Demonstrating a Hybrid Distal-to-Alternating Pathway for N_2 Reduction. *J. Am. Chem. Soc.* **2016,** *138*, 4243-4248.

(56) Singh, A. R.; Rohr, B. A.; Schwalbe, J. A.; Cargnello, M.; Chan, K.; Jaramillo, T. F.; Chorkendorff, I.; Nørskov, J. K. Electrochemical Ammonia Synthesis—The Selectivity Challenge. *ACS Catal.* **2017,** *7*, 706-709.

(57) Novoselov, K. S.; Geim, A. K.; Morozov, S. V.; Jiang, D.; Zhang, Y.; Dubonos, S. V.; Grigorieva, I. V.; Firsov, A. A. Electric Field Effect in Atomically Thin Carbon Films. *Science* **2004,** *306*, 666-669.

(58) Tan, C.; Cao, X.; Wu, X.-J.; He, Q.; Yang, J.; Zhang, X.; Chen, J.; Zhao, W.; Han, S.; Nam, G.-H.et al. Recent Advances in Ultrathin Two-dimensional Nanomaterials. *Chem. Rev.* **2017,** *117*, 6225-6331.

(59) Geim, A. K.; Novoselov, K. S. The Rise of Graphene. *Nat. Mater.* **2007,** *6*, 183-191.

(60) Sun, Y.; Gao, S.; Lei, F.; Xie, Y. Atomically-thin Two-dimensional Sheets for Understanding Active Sites in Catalysis. *Chem. Soc. Rev.* **2015,** *44*, 623-636.

(61) Sun, Y.; Liu, Q.; Gao, S.; Cheng, H.; Lei, F.; Sun, Z.; Jiang, Y.; Su, H.; Wei, S.; Xie, Y. Pits confined in Ultrathin Cerium(IV) Oxide for Studying Catalytic Centers in Carbon Monoxide Oxidation. *Nat. Commun.* **2013,** *4*, 2899.

(62) Deng, D.; Yu, L.; Pan, X.; Wang, S.; Chen, X.; Hu, P.; Sun, L.; Bao, X. Size Effect of Graphene on Electrocatalytic Activation of Oxygen. *Chem. Commun.* **2011,** *47*, 10016-10018.

(63) Li, X.-F.; Li, Q.-K.; Cheng, J.; Liu, L.; Yan, Q.; Wu, Y.; Zhang, X.-H.; Wang, Z.-Y.; Qiu, Q.; Luo, Y. Conversion of Dinitrogen to Ammonia by FeN_3-embedded Graphene. *J. Am. Chem. Soc.* **2016,** *138*, 8706-8709.

(64) Li, G.; Li, Y.; Liu, H.; Guo, Y.; Li, Y.; Zhu, D. Architecture of Graphdiyne Nanoscale Films. *Chem. Commun.* **2010,** *46*, 3256-3258.

(65) Liu, J.; Liu, Y.; Liu, N.; Han, Y.; Zhang, X.; Huang, H.; Lifshitz, Y.; Lee, S.; Zhong, J.; Kang, Z. Metal-free Efficient Photocatalyst for Stable Visible Water Splitting via a Two-electron Pathway. *Science* **2015,** *347*, 970-974.

(66) Golberg, D.; Bando, Y.; Huang, Y.; Terao, T.; Mitome, M.; Tang, C.; Zhi, C. Boron Nitride Nanotubes and Nanosheets. *ACS Nano* **2010,** *4*, 2979-2993.

(67) Wu, X.; Dai, J.; Zhao, Y.; Zhuo, Z.; Yang, J.; Zeng, X. C. Two-dimensional Boron Monolayer Sheets. *ACS Nano* **2012,** *6*, 7443-7453.

(68) Feng, B.; Zhang, J.; Zhong, Q.; Li, W.; Li, S.; Li, H.; Cheng, P.; Meng, S.; Chen, L.; Wu, K. Experimental Realization of Two-dimensional Boron Sheets. *Nat. Chem.* **2016,** *8*, 563-568.

108

(69) Favron, A.; Gaufrès, E.; Fossard, F.; Phaneuf-L'Heureux, A.; Tang, N. Y. W.; Lévesque, P. L.; Loiseau, A.; Leonelli, R.; Francoeur, S.; Martel, R. Photooxidation and Quantum Confinement Effects in Exfoliated Black Phosphorus. *Nat. Mater.* **2015,** *14*, 826-832.

(70) Honkala, K.; Hellman, A.; Remediakis, I. N.; Logadottir, A.; Carlsson, A.; Dahl, S.; Christensen, C. H.; Nørskov, J. K. Ammonia Synthesis from First-principles Calculations. *Science* **2005,** *307*, 555-558.

(71) Splendiani, A.; Sun, L.; Zhang, Y.; Li, T.; Kim, J.; Chim, C.; Galli, G.; Wang, F. Emerging Photoluminescence in Monolayer MoS_2. *Nano Lett.* **2010,** *10*, 1271-1275.

(72) Naguib, M.; Mochalin, V. N.; Barsoum, M. W.; Gogotsi, Y. 25th Anniversary Article: MXenes: A New Family of Two-dimensional Materials. *Adv. Mater.* **2014,** *26*, 992-1005.

(73) Furukawa, H.; Cordova, K. E.; O'Keeffe, M.; Yaghi, O. M. The Chemistry and Applications of Metal-Organic Frameworks. *Science* **2013,** *341*, 1230444.

(74) Fan, G.; Li, F.; Evans, D. G.; Duan, X. Catalytic Applications of Layered Double Hydroxides: Recent Advances and Perspectives. *Chem. Soc. Rev.* **2014,** *43*, 7040-7066.

(75) Deng, D.; Novoselov, K. S.; Fu, Q.; Zheng, N.; Tian, Z.; Bao, X. Catalysis with Two-dimensional Materials and Their Heterostructures. *Nat. Nanotech.* **2016,** *11*, 218-233.

(76) He, T.; Matta, S. K.; Du, A. Single Tungsten Atom Supported on N-doped Graphyne as a High-Performance Electrocatalyst for Nitrogen Fixation under Ambient Conditions. *Phys. Chem. Chem. Phys.* **2019,** *21*, 1546-1551.

(77) Cao, S.; Zhou, N.; Gao, F.; Chen, H.; Jiang, F. All-solid-state Z-scheme 3,4-dihydroxybenzaldehyde-functionalized Ga_2O_3/Graphitic Carbon Nitride Photocatalyst with Aromatic Rings as Electron Mediators for Visible-light Photocatalytic Nitrogen Fixation. *Appl. Catal. B* **2017,** *218*, 600-610.

(78) Zhang, X.; Chen, A.; Zhang, Z.; Zhou, Z. Double-atom Catalysts: Transition Metal Dimer-anchored C_2N Monolayers as N_2 Fixation Electrocatalysts. *J. Mater. Chem. A* **2018,** *6*, 18599-18604.

(79) Zhao, J.; Chen, Z. Single Mo Atom Supported on Defective Boron Nitride Monolayer as an Efficient Electrocatalyst for Nitrogen Fixation: A Computational Study. *J. Am. Chem. Soc.* **2017,** *139* , 12480-12487.

(80) Liu, C.; Li, Q.; Zhang, J.; Jin, Y.; MacFarlane, D. R.; Sun, C. Theoretical Evaluation of Possible 2D Boron Monolayer in N_2 Electrochemical Conversion into Ammonia. *J. Phys. Chem. C* **2018,** *122*, 25268-25273.

(81) Gong, K.; Du, F.; Xia, Z.; Durstock, M.; Dai, L. Nitrogen-Doped Carbon Nanotube Arrays with High Electrocatalytic Activity for Oxygen Reduction. *Science* **2009,** *323*, 760-764.

(82) Hu, C.; Dai, L. Carbon-Based Metal-Free Catalysts for Electrocatalysis Beyond the ORR. *Angew. Chem. Int. Ed.* **2016,** *55*, 11736-11758.

(83) Mao, J.; Iocozzia, J.; Huang, J.; Meng, K.; Lai, Y.; Lin, Z. Graphene Aerogels for Efficient Energy Storage and Conversion. *Energy Environ. Sci.* **2018,** *11*, 772-799.

(84) Wang, H.; Li, X.; Gao, L.; Wu, H.; Yang, J.; Cai, L.; Ma, T.; Tung, C.; Wu, L.; Yu, G. Three-Dimensional Graphene Networks with Abundant Sharp Edge Sites for

Efficient Electrocatalytic Hydrogen Evolution. *Angew. Chem. Int. Ed.* **2018,** *130*, 198-203.

(85) Qiu, B.; Xing, M.; Zhang, J. Recent Advances in Three-dimensional Graphene Based Materials for Catalysis Applications. *Chem. Soc. Rev.* **2018,** *47*, 2165-2216.

(86) Li, X.; Zhi, L. Graphene Hybridization for Energy Storage Applications. *Chem. Soc. Rev.* **2018,** *47*, 3189-3216.

(87) Liu, Y.; Su, Y.; Quan, X.; Fan, X.; Chen, S.; Yu, H.; Zhao, H.; Zhang, Y.; Zhao, J. Facile Ammonia Synthesis from Electrocatalytic N_2 Reduction under Ambient Conditions on N-Doped Porous Carbon. *ACS Catal.* **2018,** *8*, 1186-1191.

(88) Shi, M.-M.; Bao, D.; Li, S.; Wulan, B.; Yan, J.; Jiang, Q. Anchoring PdCu Amorphous Nanocluster on Graphene for Electrochemical Reduction of N_2 to NH_3 under Ambient Conditions in Aqueous Solution. *Adv. Energy Mater.* **2018,** *8*, 1800124.

(89) Geng, Z.; Liu, Y.; Kong, X.; Li, P.; Li, K.; Liu, Z.; Du, J.; Shu, M.; Si, R.; Zeng, J. Achieving a Record-high Yield Rate of 120.9 for N_2 Electrochemical Reduction over Ru Single-atom Catalysts. *Adv. Mater*. **2018,** *30*, 1803498.

(90) Zhang, X.; Liu, Q.; Shi, X.; Asiri, A. M.; Luo, Y.; Sun, X.; Li, T. TiO_2 Nanoparticles–reduced Graphene Oxide Hybrid: an Efficient and Durable Electrocatalyst Toward Artificial N_2 fixation to NH_3 under Ambient Conditions. *J. Mater. Chem. A* **2018,** *6*, 17303-17306.

(91) Yu, X.; Han, P.; Wei, Z.; Huang, L.; Gu, Z.; Peng, S.; Ma, J.; Zheng, G. Boron-Doped Graphene for Electrocatalytic N_2 Reduction. *Joule* **2018,** *2*, 1610-1622.

(92) Cheng, H.; Ding, L.; Chen, G.; Zhang, L.; Xue, J.; Wang, H. Molybdenum Carbide Nanodots Enable Efficient Electrocatalytic Nitrogen Fixation under Ambient Conditions. *Adv. Mater.* **2018,** *30*, 1803694.

(93) Huang, H.; Xia, L.; Cao, R.; Niu, Z.; Chen, H.; Liu, Q.; Li, T.; Shi, X.; Asiri, A. M.; Sun, X. A Biomass-Derived Carbon-Based Electrocatalyst for Efficient N_2 Fixation to NH_3 under Ambient Conditions. *Chem.: Eur. J.* **2019,** *25*, 1914-1917.

(94) Tao, H.; Choi, C.; Ding, L.; Jiang, Z.; Han, Z.; Jia, M.; Fan, Q.; Gao, Y.; Wang, H.; Robertson, A. W.et al. Nitrogen Fixation by Ru Single-Atom Electrocatalytic Reduction. *Chem* **2019,** *5*, 204-214.

(95) Chen, C.; Yan, D.; Wang, Y.; Zhou, Y.; Zou, Y.; Li, Y.; Wang, S. B N Pairs Enriched Defective Carbon Nanosheets for Ammonia Synthesis with High Efficiency. *Small* **2019,** *15*, 1805029.

(96) Wang, M.; Liu, S.; Qian, T.; Liu, J.; Zhou, J.; Ji, H.; Xiong, J.; Zhong, J.; Yan, C. Over 56.55% Faradaic Efficiency of Ambient Ammonia Synthesis Enabled by Positively Shifting the Reaction Potential. *Nat. Commun.* **2019,** *10*, 341.

(97) Wang, F.; Liu, Y.; Zhang, H.; Chu, K. CuO/Graphene Nanocomposite for Nitrogen Reduction Reaction. *ChemCatChem* **2019,** *11*, 1441-1447.

(98) Mukherjee, S.; Cullen, D. A.; Karakalos, S.; Liu, K.; Zhang, H.; Zhao, S.; Xu, H.; More, K. L.; Wang, G.; Wu, G. Metal-organic Framework-derived Nitrogen-doped Highly Disordered Carbon for Electrochemical Ammonia Synthesis using N_2 and H_2O in Alkaline Electrolytes. *Nano Energy* **2018,** *48*, 217-226.

(99) Chen, P.; Zhang, N.; Wang, S.; Zhou, T.; Tong, Y.; Ao, C.; Yan, W.; Zhang, L.; Chu, W.; Wu, C.et al. Interfacial Engineering of Cobalt Sulfide/Graphene Hybrids for

Highly Efficient Ammonia Electrosynthesis. *Proc. Natl. Acad. Sci. U.S.A.* **2019,** *116*, 6635-6640.

(100) Jin, H.; Guo, C.; Liu, X.; Liu, J.; Vasileff, A.; Jiao, Y.; Zheng, Y.; Qiao, S. Emerging Two-Dimensional Nanomaterials for Electrocatalysis. *Chem. Rev.* **2018,** *118*, 6337-6408.

(101) Zhao, S.; Lu, X.; Wang, L.; Gale, J.; Amal, R. Carbon-Based Metal-free Catalysts for Electrocatalytic Reduction of Nitrogen for Synthesis of Ammonia at Ambient Conditions. *Adv. Mater.* **2019,** *31*, 1805367.

(102) Tian, Y.; Hu, S.; Sheng, X.; Duan, Y.; Jakowski, J.; Sumpter, B. G.; Huang, J. Non-Transition-Metal Catalytic System for N_2 Reduction to NH_3: A Density Functional Theory Study of Al-doped Graphene. *J. Phys. Chem. Lett.* **2018,** *9*, 570-576.

(103) Choi, C.; Back, S.; Kim, N.; Lim, J.; Kim, Y.; Jung, Y. Suppression of Hydrogen Evolution Reaction in Electrochemical N_2 Reduction Using Single-atom Catalysts: A Computational Guideline. *ACS Catal.* **2018,** *8*, 7517-7525.

(104) Ling, C.; Bai, X.; Ouyang, Y.; Du, A.; Wang, J. Single Molybdenum Atom Anchored on N-Doped Carbon as a Promising Electrocatalyst for Nitrogen Reduction into Ammonia at Ambient Conditions. *J. Phys. Chem. C* **2018,** *122*, 16842-16847.

(105) Guo, X.; Huang, S. Tuning Nitrogen ReductionRreaction Activity via Controllable Fe Magnetic Moment: A Computational Study of Single Fe Atom Supported on Defective Graphene. *Electrochim. Acta* **2018,** *284*, 392-399.

(106) Yang, T.; Tang, S.; Li, X.; Sharman, E.; Jiang, J.; Luo, Y. Graphene Oxide-Supported Transition Metal Catalysts for Dinitrogen Reduction. *J. Phys. Chem. C* **2018,** *122*, 25441-25446.

(107) Ling, C.; Ouyang, Y.; Li, Q.; Bai, X.; Mao, X.; Du, A.; Wang, J. A General Two-step Strategy–based High-throughput Screening of Single Atom Catalysts for Nitrogen Fixation. *Small Methods 2018*, 1800376.

(108) Dai, L.; Xue, Y.; Qu, L.; Choi, H.; Baek, J.. Metal-free Catalysts for Oxygen Reduction Reaction. *Chem. Rev.* **2015,** *115*, 4823-4892.

(109) Ma, F.; Jiao, Y.; Gao, G.; Gu, Y.; Bilic, A.; Chen, Z.; Du, A. Graphene-like Two-dimensional Ionic Boron with Double Dirac Cones at Ambient Condition. *Nano Lett.* **2016,** *16*, 3022-3028.

(110) Lu, Y.; Yang, Y.; Zhang, T.; Ge, Z.; Chang, H.; Xiao, P.; Xie, Y.; Hua, L.; Li, Q.; Li, H.et al. Photoprompted Hot Electrons from Bulk Cross-linked Graphene Materials and Their Efficient Catalysis for Atmospheric Ammonia Synthesis. *ACS Nano* **2016,** *10*, 10507-10515.

(111) Ong, W.; Tan, L.; Ng, Y. H.; Yong, S.; Chai, S. Graphitic Carbon Nitride (g-C_3N_4)-based Photocatalysts for Artificial Photosynthesis and Environmental Remediation: Are We a Step Closer To Achieving Sustainability? *Chem. Rev.* **2016,** *116*, 7159-7329.

(112) Zheng, Y.; Liu, J.; Liang, J.; Jaroniec, M.; Qiao, S. Z. Graphitic Carbon Nitride Materials: Controllable Synthesis and Applications in Fuel Cells and Photocatalysis. *Energy Environ. Sci.* **2012,** *5*, 6717-6731.

(113) Mahmood, J.; Lee, E. K.; Jung, M.; Shin, D.; Jeon, I.; Jung, S.; Choi, H.; Seo, J.; Bae, S.; Sohn, S.et al. Nitrogenated Holey Two-dimensional Structures. *Nat. Commun.* **2015,** *6*, 6486.

(114) Zhao, Y.; Zhang, J.; Qu, L. Graphitic Carbon Nitride/Graphene Hybrids as New Active Materials for Energy Conversion and Storage. *ChemNanoMat* **2015,** *1*, 298-318.

(115) Zambon, A.; Mouesca, J. M.; Gheorghiu, C.; Bayle, P. A.; Pécaut, J.; Claeys-Bruno, M.; Gambarelli, S.; Dubois, L. s-Heptazine Oligomers: Promising Structural Models for Graphitic Carbon Nitride. *Chem. Sci.* **2016,** *7*, 945-950.

(116) Yang, S.; Gong, Y.; Zhang, J.; Zhan, L.; Ma, L.; Fang, Z.; Vajtai, R.; Wang, X.; Ajayan, P. M. Exfoliated Graphitic Carbon Nitride Nanosheets as Efficient Catalysts for Hydrogen Evolution Under Visible Light. *Adv. Mater*. **2013,** *25*, 2452-2456.

(117) Dong, G.; Ho, W.; Wang, C. Selective Photocatalytic N_2 Fixation Dependent on g-C_3N_4 Induced by Nitrogen Vacancies. *J. Mater. Chem. A* **2015,** *3*, 23435-16301.

(118) Su, F.; Mathew, S. C.; Lipner, G.; Fu, X.; Antonietti, M.; Blechert, S.; Wang, X. mpg-C_3N_4-Catalyzed Selective Oxidation of Alcohols Using O_2 and Visible Light. *J. Am. Chem. Soc.* **2010,** *132*, 16299-16301.

(119) Qiu, P.; Xu, C.; Zhou, N.; Chen, H.; Jiang, F. Metal-free Black Phosphorus Nanosheets-decorated Graphitic Carbon Nitride Nanosheets with CP Bonds for Excellent Photocatalytic Nitrogen Fixation. *Appl. Catal. B Environ.* **2018,** *221*, 27-35.

(120) Zhou, N.; Qiu, P.; Chen, H.; Jiang, F. KOH Etching Graphitic Carbon Nitride for Simulated Sunlight Photocatalytic Nitrogen Fixation with Cyano Groups as Defects. *J. Taiwan Inst. Chem. Eng.* **2018,** *83*, 99-106.

(121) Wang, K.; Li, Q.; Liu, B.; Cheng, B.; Ho, W.; Yu, J. Sulfur-doped g-C_3N_4 with Enhanced Photocatalytic CO_2-reduction Performance. *Appl. Catal. B Environ.* **2015,** *176-177*, 44-52.

(122) Zheng, Y.; Jiao, Y.; Chen, J.; Liu, J.; Liang, J.; Du, A.; Zhang, W.; Zhu, Z.; Smith, S. C.; Jaroniec, M.et al. Nanoporous Graphitic-C_3N_4@Carbon Metal-Free Electrocatalysts for Highly Efficient Oxygen Reduction. *J. Am. Chem. Soc.* **2011,** *133*, 20116-20119.

(123) Liu, Q.; Ai, L.; Jiang, J. MXene-derived TiO_2@C/g-C_3N_4 Heterojunctions for Highly Efficient Nitrogen Photofixation. *J. Mater. Chem. A* **2018,** *6*, 4102-4110.

(124) Wang, X.; Wang, W.; Qiao, M.; Wu, G.; Chen, W.; Yuan, T.; Xu, Q.; Chen, M.; Zhang, Y.; Wang, X.et al. Atomically Dispersed Au1 Catalyst Towards Efficient Electrochemical Synthesis of Ammonia. *Sci. Bull.* **2018,** *63*, 1246-1253.

(125) Xiao, C.; Zhang, L.; Wang, K.; Wang, H.; Zhou, Y.; Wang, W. A New Approach to Enhance Photocatalytic Nitrogen Fixation Performance via Phosphate-bridge: A Case Study of SiW_{12}/K-C_3N_4. *Appl. Catal. B Environ.* **2018,** *239*, 260-267.

(136) Frank, S. N.; Bard, A. J. Heterogeneous Photocatalytic Oxidation of Cyanide Ion in Aqueous Solutions at Titanium Dioxide Powder. *J. Am. Chem. Soc.* **1977,** *99*, 303-304.

(127) Wang, Z.; Yu, Z.; Zhao, J. Computational Screening of A Single Transition Metal Atom Supported on the C_2N Monolayer for Electrochemical Ammonia Synthesis. *Phys. Chem. Chem. Phys.* **2018,** *20*, 12835-12844.

112

(128) Chen, X.; Zhao, X.; Kong, Z.; Ong, W.-J.; Li, N. Unravelling the Electrochemical Mechanisms for Nitrogen Fixation on Single Transition Metal Atoms Embedded in Defective Graphitic Carbon Nitride. *J. Mater. Chem. A* **2018,** *6*, 21941-21948.

(129) Ling, C.; Niu, X.; Li, Q.; Du, A.; Wang, J. Metal-free Single Atom Catalyst for N_2 Fixation Driven by Visible Light. *J. Am. Chem. Soc.* **2018,** *140*, 14161-14168.

(130) Chen, Z.; Zhao, J.; Cabrera, C. R.; Chen, Z. Computational Screening of Efficient Single-Atom Catalysts Based on Graphitic Carbon Nitride (g-C_3N_4) for Nitrogen Electroreduction. *Small Methods 2018*, 1800368.

(131) Ji, S.; Wang, Z.; Zhao, J. A Boron-interstitial Doped C_2N Layer as a Metal-free Electrocatalyst for N_2 Fixation: A Computational Study. *J. Mater. Chem. A* **2019,** *7*, 2392-2399.

(132) Yongyong, C.; Shengwei, D.; Qiaojun, F.; Xiang, S.; Chenxia, Z.; Jingnan, Z.; Yijing, G.; Han, Z.; Yuejin, L.; zihao, Y.et al. Single and Double Boron Atoms Doped Nanoporous C_2N−h2D Electrocatalysts for Highly Efficient N_2 Reduction Reaction: A Density Functional Theory Study. *Nanotechnology* **2019,** *30*, 335403.

(133) Zhang, L.; Zhao, W.; Zhang, W.; Chen, J.; Hu, Z. Gt-C_3N_4 Coordinated Single Atom as an Efficient Electrocatalyst for Nitrogen Reduction Reaction. *Nano Res.* **2019,** *12*, 1181-1186.

(134) Yin, H.; Li, S.; Gan, L.; Wang, P. Pt-embedded in Monolayer g-C_3N_4 as a Promising Single-atom Electrocatalyst for Ammonia Synthesis. *J. Mater. Chem. A* **2019,** *7*, 11908-11914.

 (135) Li, H.; Shang, J.; Ai, Z.; Zhang, L. Efficient Visible Light Nitrogen Fixation with BiOBr Nanosheets of Oxygen Vacancies on the Exposed {001} Facets. *J. Am. Chem. Soc.* **2015,** *137*, 6393-6399.

(136) Subat, M.; Borovik, A. S.; König, B. Synthetic Creatinine Receptor: Imprinting of a Lewis Acidic Zinc(II)cyclen Binding Site to Shape Its Molecular Recognition Selectivity. *J. Am. Chem. Soc.* **2004,** *126*, 3185-3190.

(137) Tay, Q.; Kanhere, P.; Ng, C. F.; Chen, S.; Chakraborty, S.; Huan, A. C. H.; Sum, T. C.; Ahuja, R.; Chen, Z. Defect Engineered g-C_3N_4 for Efficient Visible Light Photocatalytic Hydrogen Production. *Chem. Mater.* **2015,** *27*, 4930-4933.

(138) Li, L. H.; Chen, Y. Atomically Thin Boron Nitride: Unique Properties and Applications. *Adv. Funct. Mater.* **2016,** *26*, 2594-2608.

(139) Geick, R.; Perry, C. H.; Rupprecht, G. Normal Modes in Hexagonal Boron Nitride. *Phys. Rev.* **1966,** *146*, 543-547.

(140) Mao, X.; Zhou, S.; Yan, C.; Zhu, Z.; Du, A. A Single Boron Atom Doped Boron Nitride Edge as a Metal-free Catalyst for N_2 Fixation. *Phys. Chem. Chem. Phys.* **2019,** *21*, 1110-1116.

(141) Zhang, Y.; Du, H.; Ma, Y.; Ji, L.; Guo, H.; Tian, Z.; Chen, H.; Huang, H.; Cui, G.; Asiri, A. M.et al. Hexagonal Boron Nitride Nanosheet for Effective Ambient N_2 Fixation to NH_3. *Nano Res.* **2019,** *12*, 919-924.

(142) Tang, H.; Ismail-Beigi, S. Novel Precursors for Boron Nanotubes: The Competition of Two-center and Three-center Bonding in Boron Sheets. *Phys. Rev. Lett.* **2007,** *99*, 115501.

(143) Liu, H.; Gao, J.; Zhao, J. From Boron Cluster to Two-dimensional Boron Sheet on Cu(111) Surface: Growth Mechanism and Hole Formation. *Sci Rep* **2013,** *3*, 3238.

(144) Zope, R. R.; Baruah, T. Snub Boron Nanostructures: Chiral Fullerenes, Nanotubes and Planar Sheet. *Chem. Phys. Lett.* **2011,** *501*, 193-196.

(145) Tang, H.; Ismail-Beigi, S. Self-doping in Boron Sheets from First Principles: A Route to Structural Design of Metal Boride Nanostructures. *Phys. Rev. B* **2009,** *80*, 134113.

(146) Penev, E. S.; Bhowmick, S.; Sadrzadeh, A.; Yakobson, B. I. Polymorphism of Two-dimensional Boron. *Nano Lett.* **2012,** *12*, 2441-2445.

(147) Yu, X.; Li, L.; Xu, X.; Tang, C. Prediction of Two-dimensional Boron Sheets by Particle Swarm Optimization Algorithm. *J. Phys. Chem. C* **2012,** *116*, 20075-20079.

(148) Oganov, A. R.; Chen, J.; Gatti, C.; Ma, Y.; Ma, Y.; Glass, C. W.; Liu, Z.; Yu, T.; Kurakevych, O. O.; Solozhenko, V. L. Ionic High-pressure Form of Elemental Boron. *Nature* **2009,** *457*, 863-867.

(149) Wu, C.; Wang, H.; Zhang, J.; Gou, G.; Pan, B.; Li, J. Lithium–Boron (Li–B) Monolayers: First-principles Cluster Expansion and Possible Two-dimensional Superconductivity. *ACS Appl. Mater. Interfaces* **2016,** *8*, 2526-2532.

(150) Li, J.; Zhang, H.; Yang, G. Ultrahigh-capacity Molecular Hydrogen Storage of a Lithium-Decorated Boron Monolayer. *J. Phys. Chem. C* **2015,** *119*, 19681-19688.

(151) Mir, S. H.; Chakraborty, S.; Jha, P. C.; Wärnå, J.; Soni, H.; Jha, P. K.; Ahuja, R. Two-dimensional Boron: Lightest Catalyst for Hydrogen and Oxygen Evolution Reaction. *Appl. Phys. Lett.* **2016,** *109*, 053903.

(152) Er, S.; de Wijs, G. A.; Brocks, G. DFT Study of Planar Boron Sheets: A New Template for Hydrogen Storage. *J. Phys. Chem. C* **2009,** *113*, 18962-18967.

(153) Qiu, W.; Xie, X.; Qiu, J.; Fang, W.; Liang, R.; Ren, X.; Ji, X.; Cui, G.; Asiri, A. M.; Cui, G.et al. High-performance Artificial Nitrogen Fixation at Ambient Conditions Using a Metal-free Electrocatalyst. *Nat. Commun.* **2018,** *9*, 3485.

(154) Zhang, X.; Wu, T.; Wang, H.; Zhao, R.; Chen, H.; Wang, T.; Wei, P.; Luo, Y.; Zhang, Y.; Sun, X. Boron Nanosheet: An Elemental Two-dimensional (2D) Material for Ambient Electrocatalytic N_2-to-NH_3 Fixation in Neutral Media. *ACS Catal.* **2019,** *9*, 4609-4615.

(155) Zhu, H.; Hu, Y.; Wei, S.; Hua, D. Single-Metal Atom Anchored on Boron Monolayer (β_{12}) as an Electrocatalyst for Nitrogen Reduction into Ammonia at Ambient Conditions: A First-Principles Study. *J. Phys. Chem. C* **2019,** *123*, 4274-4281.

(156) Sun, X.; Liu, X.; Yin, J.; Yu, J.; Li, Y.; Hang, Y.; Zhou, X.; Yu, M.; Li, J.; Tai, G.et al. Two-Dimensional Boron Crystals: Structural Stability, Tunable Properties, Fabrications and Applications. *Adv. Funct. Mater.* **2017,** *27*, 1603300.

(157) Lu, J.; Ma, X.; Wang, J.; Liu, J.; Xiao, H.; Li, J. Efficient Nitrogen Fixation via a Redox-flexible Single-Iron Site with Reverse-Dative Iron→Boron σ Bonding. *J. Phys. Chem. A* **2018,** *122*, 4530-4537.

(160) Bridgman, P. W. Further Note on Black Phosphorus. *J. Am. Chem. Soc.* **1916,** *38*, 609-612.

(161) Sajedi-Moghaddam, A.; Mayorga-Martinez, C. C.; Sofer, Z.; Bouša, D.; Saievar-Iranizad, E.; Pumera, M. Black Phosphorus Nanoflakes/Polyaniline Hybrid Material for High-performance Pseudocapacitors. *J. Phys. Chem. C* **2017,** *121*, 20532-20538.

(162) Ren, X.; Zhou, J.; Qi, X.; Liu, Y.; Huang, Z.; Li, Z.; Ge, Y.; Dhanabalan, S. C.; Ponraj, J. S.; Wang, S.et al. Few-layer Black Phosphorus Nanosheets as Electrocatalysts for Highly Efficient Oxygen Evolution Reaction. *Adv. Energy Mater.* **2017,** *7*, 1700396.

(163) Zhang, L.; Ding, L.; Chen, G.; Yang, X.; Wang, H. Ammonia Synthesis under Ambient Conditions: Selective Electroreduction of Dinitrogen to Ammonia on Black Phosphorus Nanosheets. *Angew. Chem. Int. Ed.* **2019,** *58*, 2612-2616.

(164) Wei, Z.; Zhang, Y.; Wang, S.; Wang, C.; Ma, J. Fe-doped Phosphorene for the Nitrogen Reduction Reaction. *J. Mater. Chem. A* **2018,** *6*, 13790-13795.

(165) Li, Q.; Qiu, S.; Liu, C.; Liu, M.; He, L.; Zhang, X.; Sun, C. Computational Design of Single-molybdenum Catalysts for the Nitrogen Reduction Reaction. *J. Phys. Chem. C* **2019,** *123*, 2347-2352.

(166) Chen, Z.; Zhao, J.; Yin, L.; Chen, Z. B-terminated (111) Polar Surfaces of BP and BAs: Promising Metal-free Electrocatalysts with Large Reaction Regions for Nitrogen Fixation. *J. Mater. Chem. A* **2019**, *7*, 13284-13292.

(167) Boukhvalov, D. W. The Atomic and Electronic Structure of Nitrogen- and Boron-doped Phosphorene. *Phys. Chem. Chem. Phys.* **2015,** *17*, 27210-27216.

(168) Wang, J.; Liu, D.; Huang, H.; Yang, N.; Yu, B.; Wen, M.; Wang, X.; Chu, P. K.; Yu, X. In-Plane Black Phosphorus/Dicobalt Phosphide Heterostructure for Efficient Electrocatalysis. *Angew. Chem. Int. Ed.* **2018,** *130*, 2630-2634.

(169) Eizawa, A.; Arashiba, K.; Tanaka, H.; Kuriyama, S.; Matsuo, Y.; Nakajima, K.; Yoshizawa, K.; Nishibayashi, Y. Remarkable Catalytic Activity of Dinitrogen-bridged Dimolybdenum Complexes bearing NHC-based PCP-pincer Ligands toward Nitrogen Fixation. *Nat. Commun.* **2017,** *8*, 14874.

(170) Yang, J.; Guo, Y.; Jiang, R.; Qin, F.; Zhang, H.; Lu, W.; Wang, J.; Yu, J. C. High-Efficiency "Working-in-Tandem" Nitrogen Photofixation Achieved by Assembling Plasmonic Gold Nanocrystals on Ultrathin Titania Nanosheets. *J. Am. Chem. Soc.* **2018,** *140*, 8497-8508.

(171) Xing, P.; Chen, P.; Chen, Z.; Hu, X.; Lin, H.; Wu, Y.; Zhao, L.; He, Y. Novel Ternary MoS_2/C-ZnO Composite with Efficient Performance in Photocatalytic NH_3 Synthesis under Simulated Sunlight. *ACS Sustain. Chem. Eng.* **2018,** *6*, 14866-14879.

(172) Zhang, R.; Ren, X.; Shi, X.; Xie, F.; Zheng, B.; Guo, X.; Sun, X. Enabling Effective Electrocatalytic N_2 Conversion to NH_3 by the TiO_2 Nanosheets Array under Ambient Conditions. *ACS Appl. Mater. Interfaces* **2018,** *10*, 28251-28255.

(173) Han, J.; Ji, X.; Ren, X.; Cui, G.; Li, L.; Xie, F.; Wang, H.; Li, B.; Sun, X. MoO_3 Nanosheets for Efficient Electrocatalytic N_2 Fixation to NH_3. *J. Mater. Chem. A* **2018,** *6*, 12974-12977.

(174) Fu, W.; Cao, Y.; Feng, Q.; Smith, W. R.; Dong, P.; Ye, M.; Shen, J. Pd–Co Nanoalloys Nested on CuO Nanosheets for Efficient Electrocatalytic N_2 Reduction and Room-temperature Suzuki–Miyaura Coupling Reaction. *Nanoscale* **2019,** *11*, 1379-1385.

(175) Xu, B.; Liu, Z.; Qiu, W.; Liu, Q.; Sun, X.; Cui, G.; Wu, Y.; Xiong, X. La$_2$O$_3$ Nanoplate: An Efficient Electrocatalyst for Artificial N$_2$ Fixation to NH$_3$ with Excellent Selectivity at Ambient Condition. *Electrochim. Acta* **2019**, *298*, 106-111.

(176) Gao, X.; Shang, Y.; Liu, L.; Fu, F. Chemisorption-enhanced Photocatalytic Nitrogen Fixation via 2D Ultrathin p–n Heterojunction AgCl/δ-Bi$_2$O$_3$ Nanosheets. *J. Catal.* **2019**, *371*, 71-80.

(177) Cheng, S.; Gao, Y.; Yan, Y.; Gao, X.; Zhang, S.; Zhuang, G.; Deng, S.; Wei, Z.; Zhong, X.; Wang, J. Oxygen Vacancy Enhancing Mechanism of Nitrogen Reduction Reaction Property in Ru/TiO$_2$. *J. Energy Chem.* **2019**, *39*, 144-151.

(178) Zhang, G.; Ji, Q.; Zhang, K.; Chen, Y.; Li, Z.; Liu, H.; Li, J.; Qu, J. Triggering Surface Oxygen Vacancies on Atomic Layered Molybdenum Dioxide for a low Energy Consumption Path toward Nitrogen Fixation. *Nano Energy* **2019**, *59*, 10-16.

(179) Zhao, Y.; Zhao, Y.; Shi, R.; Wang, B.; Waterhouse, G. I. N.; Wu, L.; Tung, C; Zhang, T. Tuning Oxygen Vacancies in Ultrathin TiO$_2$ Nanosheets to Boost Photocatalytic Nitrogen Fixation up to 700 nm. *Adv. Mater.* **2019**, *31*, 1806482.

(180) Fujishima, A.; Honda, K. Electrochemical Photolysis of Water at a Semiconductor Electrode. *Nature* **1972**, *238*, 37-38.

(181) Bourgeois, S.; Diakite, D.; Perdereau, M. A Study of TiO$_2$ Powders as a Support for the Photochemical Synthesis of Ammonia. *React. Solids* **1988**, *6*, 95-104.

(182) Liu, G.; Zhao, Y.; Sun, C.; Li, F.; Lu, G. Q.; Cheng, H. Synergistic Effects of B/N Doping on the Visible-light Photocatalytic Activity of Mesoporous TiO$_2$. *Angew. Chem. Int. Ed.* **2008**, *47*, 4516-4520.

(183) Chen, X.; Li, N.; Kong, Z.; Ong, W.; Zhao, X. Photocatalytic Fixation of Nitrogen to Ammonia: State-of-the-art Advancements and Future Prospects. *Mater. Horiz.* **2018**, *5*, 9-27.

(184) Li, C.; Wang, T.; Zhao, Z.; Yang, W.; Li, J.; Li, A.; Yang, Z.; Ozin, G. A.; Gong, J. Promoted Fixation of Molecular Nitrogen with Surface Oxygen Vacancies on Plasmon-enhanced TiO$_2$ Photoelectrodes. *Angew. Chem. Int. Ed.* **2018**, *57*, 5278-5282.

(185) Zhao, Y.; Zhao, Y.; Waterhouse, G. I. N.; Zheng, L.; Cao, X.; Teng, F.; Wu, L; Tung, C.; O'Hare, D.; Zhang, T. Layered-Double-Hydroxide Nanosheets as Efficient Visible-light-driven Photocatalysts for Dinitrogen Fixation. *Adv. Mater.* **2017**, *29*, 1703828.

(186) Tian, Y.; Tatsuma, T. Mechanisms and Applications of Plasmon-induced Charge Separation at TiO$_2$ Films Loaded with Gold Nanoparticles. *J. Am. Chem. Soc.* **2005**, *127*, 7632-7637.

(187) Varcoe, J. R.; Atanassov, P.; Dekel, D. R.; Herring, A. M.; Hickner, M. A.; Kohl, P. A.; Kucernak, A. R.; Mustain, W. E.; Nijmeijer, K.; Scott, K.et al. Anion-Exchange Membranes in Electrochemical Energy Systems. *Energy Environ. Sci.* **2014**, *7*, 3135-3191.

(188) Morales-Guio, C. G.; Stern, L.; Hu, X. Nanostructured Hydrotreating Catalysts for Electrochemical Hydrogen Evolution. *Chem. Soc. Rev.* **2014**, *43*, 6555-6569.

(189) Abghoui, Y.; Garden, A. L.; Howalt, J. G.; Vegge, T.; Skúlason, E. Electroreduction of N$_2$ to Ammonia at Ambient Conditions on Mononitrides of Zr, Nb, Cr, and V: A DFT Guide for Experiments. *ACS Catal.* **2016**, *6*, 635-646.

(190) Abghoui, Y.; Skúlason, E. Onset potentials for Different Reaction Mechanisms of Nitrogen Activation to Ammonia on Transition Metal Nitride Electro-catalysts. *Catal. Today* **2017,** *286*, 69-77.

(191) Abghoui, Y.; Skúlason, E. Electrochemical Synthesis of Ammonia via Mars-van Krevelen Mechanism on the (111) Facets of Group III–VII Transition Metal Mononitrides. *Catal. Today* **2017,** *286*, 78-84.

(192) Zhang, R.; Zhang, Y.; Ren, X.; Cui, G.; Asiri, A. M.; Zheng, B.; Sun, X. High-efficiency Electrosynthesis of Ammonia with High Selectivity under Ambient Conditions Enabled by VN Nanosheet Array. *ACS Sustain. Chem. Eng.* **2018,** *6*, 9545-9549.

(193) Zhang, L.; Ji, X.; Ren, X.; Luo, Y.; Shi, X.; Asiri, A. M.; Zheng, B.; Sun, X. Efficient Electrochemical N_2 Reduction to NH_3 on MoN Nanosheets Array under Ambient Conditions. *ACS Sustain. Chem. Eng.* **2018,** *6*, 9550-9554.

(194) Matanović, I.; Garzon, F. H.; Henson, N. J. Electro-reduction of Nitrogen on Molybdenum Nitride: Structure, Energetics, and Vibrational Spectra from DFT. *Phys. Chem. Chem. Phys.* **2014,** *16*, 3014-3026.

(195) Abghoui, Y.; Skúlasson, E. Transition Metal Nitride Catalysts for Electrochemical Reduction of Nitrogen to Ammonia at Ambient Conditions. *Proced. Comput. Sci.* **2015,** *51*, 18971906.

(196) Li, Q.; He, L.; Sun, C.; Zhang, X. Computational Study of MoN_2 Monolayer as Electrochemical Catalysts for Nitrogen Reduction. *J. Phys. Chem. C* **2017,** *121*, 27563-27568.

(197) Chen, Z. W.; Lang, X. Y.; Jiang, Q. Discovery of Cobweb-like MoC6 and its Application for Nitrogen Fixation. *J. Mater. Chem. A* **2018,** *6*, 9623-9628.

(198) Matanovic, I.; Garzon, F. H. Nitrogen Electroreduction and Hydrogen Evolution on Cubic Molybdenum Carbide: A Density Functional Study. *Phys. Chem. Chem. Phys.* **2018,** *20*, 14679-14687.

(199) Li, Q.; Qiu, S.; He, L.; Zhang, X.; Sun, C. Impact of H-termination on the Nitrogen Reduction Reaction of Molybdenum Carbide as an Electrochemical Catalyst. *Phys. Chem. Chem. Phys.* **2018,** *20*, 23338-23343.

(200) Yang, X.; Nash, J.; Anibal, J.; Dunwell, M.; Kattel, S.; Stavitski, E.; Attenkofer, K.; Chen, J. G.; Yan, Y.; Xu, B. Mechanistic Insights into Electrochemical Nitrogen Reduction Reaction on Vanadium Nitride Nanoparticles. *J. Am. Chem. Soc.* **2018,** *140*, 13387-13391.

(201) Kang, Y.; Yang, P.; Markovic, N. M.; Stamenkovic, V. R. Shaping Electrocatalysis through Tailored Nanomaterials. *Nano Today* **2016,** *11*, 587-600.

(202) Seh, Z. W.; Fredrickson, K. D.; Anasori, B.; Kibsgaard, J.; Strickler, A. L.; Lukatskaya, M. R.; Gogotsi, Y.; Jaramillo, T. F.; Vojvodic, A. Two-dimensional Molybdenum Carbide (MXene) as an Efficient Electrocatalyst for Hydrogen Evolution. *ACS Energy Lett.* **2016,** *1*, 589-594.

(203) Howalt, J. G.; Bligaard, T.; Rossmeisl, J.; Vegge, T. DFT based study of Transition Metal Nano-clusters for Electrochemical NH_3 Production. *Phys. Chem. Chem. Phys.* **2013,** *15*, 7785-7795.

(204) Garden, A. L.; Skúlason, E. The Mechanism of Industrial Ammonia Synthesis Revisited: Calculations of the Role of the Associative Mechanism. *J. Phys. Chem. C* **2015,** *119*, 26554-26559.

(205) Singh, A. R.; Montoya, J. H.; Rohr, B. A.; Tsai, C.; Vojvodic, A.; Nørskov, J. K. Computational Design of Active Site Structures with Improved Transition-State Scaling for Ammonia Synthesis. *ACS Catal.* **2018,** *8*, 4017-4024.

(206) Jacobsen, C. J. H.; Dahl, S.; Clausen, B. S.; Bahn, S.; Logadottir, A.; Nørskov, J. K. Catalyst Design by Interpolation in the Periodic Table: Bimetallic Ammonia Synthesis Catalysts. *J. Am. Chem. Soc.* **2001,** *123*, 8404-8405.

(207) Hellman, A.; Baerends, E. J.; Biczysko, M.; Bligaard, T.; Christensen, C. H.; Clary, D. C.; Dahl, S.; van Harrevelt, R.; Honkala, K.; Jonsson, H.et al. Predicting Catalysis: Understanding Ammonia Synthesis from First-principles Calculations. *J. Phys. Chem. B* **2006,** *110*, 17719-17735.

(208) Yang, D.; Chen, T.; Wang, Z. Electrochemical Reduction of Aqueous Nitrogen (N_2) at a Low Overpotential on (110)-oriented Mo Nanofilm. *J. Mater. Chem. A* **2017,** *5*, 18967-18971.

(209) Liu, H.; Han, S.; Zhao, Y.; Zhu, Y.; Tian, X.; Zeng, J.; Jiang, J.; Xia, B. Y.; Chen, Y. Surfactant-free Atomically Ultrathin Rhodium Nanosheet Nanoassemblies for Efficient Nitrogen Electroreduction. *J. Mater. Chem. A* **2018,** *6*, 3211-3217.

(210) Huang, H.; Xia, L.; Shi, X.; Asiri, A. M.; Sun, X. Ag Nanosheets for Efficient Electrocatalytic N_2 Fixation to NH_3 under Ambient Conditions. *Chem. Commun.* **2018,** *54*, 11427-11430.

(211) Yao, Y.; Zhu, S.; Wang, H.; Li, H.; Shao, M. A Spectroscopic Study on the Nitrogen Electrochemical Reduction Reaction on Gold and Platinum Surfaces. *J. Am. Chem. Soc.* **2018,** *140*, 1496-1501.

(212) Jariwala, D.; Sangwan, V. K.; Lauhon, L. J.; Marks, T. J.; Hersam, M. C. Emerging Device Applications for Semiconducting Two-dimensional Transition Metal Dichalcogenides. *ACS Nano* **2014,** *8*, 1102-1120.

(213) Podberezskaya, N. V.; Magarill, S. A.; Pervukhina, N. V.; Borisov, S. V. Crystal Chemistry of Dichalcogenides MX_2. *J. Struct. Chem.* **2001,** *42*, 654-681.

(214) Voiry, D.; Mohite, A.; Chhowalla, M. Phase Engineering of Transition Metal Dichalcogenides. *Chem. Soc. Rev.* **2015,** *44*, 2702-2712.

(215) Xiao, D.; Liu, G.-B.; Feng, W.; Xu, X.; Yao, W. Coupled Spin and Valley Physics in Monolayers of MoS_2 and Other Group-VI Dichalcogenides. *Phys. Rev. Lett.* **2012,** *108*, 196802.

(216) Sun, S.; Li, X.; Wang, W.; Zhang, L.; Sun, X. Photocatalytic Robust Solar Energy Reduction of Dinitrogen to Ammonia on Ultrathin MoS_2. *Appl. Catal. B Environ.* **2017,** *200*, 323-329.

(217) Zhang, L.; Ji, X.; Ren, X.; Ma, Y.; Shi, X.; Tian, Z.; Asiri, A. M.; Chen, L.; Tang, B.; Sun, X. Electrochemical Ammonia Synthesis via Nitrogen Reduction Reaction on a MoS_2 Catalyst: Theoretical and Experimental Studies. *Adv. Mater.* **2018,** *30*, 1800191.

(218) Suryanto, B. H. R.; Wang, D.; Azofra, L. M.; Harb, M.; Cavallo, L.; Jalili, R.; Mitchell, D. R. G.; Chatti, M.; MacFarlane, D. R. MoS_2 Polymorphic Engineering

118

Enhances Selectivity in the Electrochemical Reduction of Nitrogen to Ammonia. *ACS Energy Lett.* **2019,** *4*, 430-435.

(219) Liu, Y.; Han, M.; Xiong, Q.; Zhang, S.; Zhao, C.; Gong, W.; Wang, G.; Zhang, H.; Zhao, H. Dramatically Enhanced Ambient Ammonia Electrosynthesis Performance by In-Operando Created Li–S Interactions on MoS_2 Electrocatalyst. *Adv. Energy Mater.* **2019,** *9*, 1803935.

(220) Azofra, L. M.; Sun, C.; Cavallo, L.; MacFarlane, D. R. Feasibility of N_2 Binding and Reduction to Ammonia on Fe-Deposited MoS_2 2D Sheets: A DFT Study. *Chem. Eur. J.* **2017,** *23*, 8275-8279.

(221) Han, M.; Wang, G.; Zhang, H.; Zhao, H. Theoretical Study of Single Transition Metal Atom Modified MoP as a Nitrogen Reduction Electrocatalyst. *Phys. Chem. Chem. Phys.* **2019,** *21*, 5950-5955.

(222) Zhao, X.; Lan, X.; Yu, D.; Fu, H.; Liu, Z.; Mu, T. Deep Eutectic-solvothermal Synthesis of Nanostructured Fe_3S_4 for Electrochemical N_2 Fixation under Ambient Conditions. *Chem. Commun.* **2018,** *54*, 13010-13013.

(223) Zhao, J.; Zhao, J.; Cai, Q. Single Transition Metal Atom Embedded into A MoS_2 Nanosheet as a Promising Catalyst for Electrochemical Ammonia Synthesis. *Phys. Chem. Chem. Phys.* **2018,** *20*, 9248-9255.

(224) Li, L.; Li, B.; Guo, Q.; Li, B. Theoretical Screening of Single-atom-embedded MoSSe Nanosheets for Electrocatalytic N_2 Fixation. *J. Phys. Chem. C* **2019,** *123*, 14501-14507.

(225) Pang, J.; Mendes, R. G.; Bachmatiuk, A.; Zhao, L.; Ta, H. Q.; Gemming, T.; Liu, H.; Liu, Z.; Rummeli, M. H. Applications of 2D MXenes in Energy Conversion and Storage Systems. *Chem. Soc. Rev.* **2019,** *48*, 72-133.

(226) Naguib, M.; Gogotsi, Y. Synthesis of Two-dimensional Materials by Selective Extraction. *Acc. Chem. Res.* **2015,** *48*, 128-135.

(227) Azofra, L. M.; Li, N.; MacFarlane, D. R.; Sun, C. Promising Prospects for 2D d^2–d^4 M_3C_2 Transition Metal Carbides (MXenes) in N_2 Capture and Conversion into Ammonia. *Energy Environ. Sci.* **2016,** *9*, 2545-2549.

(228) Naguib, M.; Mashtalir, O.; Carle, J.; Presser, V.; Lu, J.; Hultman, L.; Gogotsi, Y.; Barsoum, M. W. Two-dimensional Transition Metal Carbides. *ACS Nano* **2012,** *6*, 1322-1331.

(229) Er, D.; Li, J.; Naguib, M.; Gogotsi, Y.; Shenoy, V. B. Ti_3C_2 MXene as a High Capacity Electrode Material for Metal (Li, Na, K, Ca) Ion Batteries. *ACS Appl. Mater. Interfaces* **2014,** *6*, 11173-11179.

(230) Chen, W. F.; Wang, C. H.; Sasaki, K.; Marinkovic, N.; Xu, W.; Muckerman, J. T.; Zhu, Y.; Adzic, R. R. Highly Active and Durable Nanostructured Molybdenum Carbide Electrocatalysts for Hydrogen Production. *Energy Environ. Sci.* **2013,** *6*, 943-951.

(231) Zhao, J.; Zhang, L.; Xie, X.; Li, X.; Ma, Y.; Liu, Q.; Fang, W.; Shi, X.; Cui, G.; Sun, X. $Ti_3C_2T_x$ (T = F, OH) MXene Nanosheets: Conductive 2D Catalysts for Ambient Electrohydrogenation of N_2 to NH_3. *J. Mater. Chem. A* **2018,** *6*, 24031-24035.

(232) Luo, Y.; Chen, G.; Ding, L.; Chen, X.; Ding, L.; Wang, H. Efficient Electrocatalytic N_2 Fixation with MXene under Ambient Conditions. *Joule* **2019**, *3*, 279-289.

(233) Fang, Y.; Liu, Z.; Han, J.; Jin, Z.; Han, Y.; Wang, F.; Niu, Y.; Wu, Y.; Xu, Y. High-Performance Electrocatalytic Conversion of N_2 to NH_3 Using Oxygen-Vacancy-Rich TiO_2 In Situ Grown on Ti_3C_2Tx MXene. *Adv. Energy Mater.* **2019**, *9*, 1803406.

(234) Zhang, J.; Yang, L.; Wang, H.; Zhu, G.; Wen, H.; Feng, H.; Sun, X.; Guan, X.; Wen, J.; Yao, Y. In Situ Hydrothermal Growth of TiO_2 Nanoparticles on a Conductive $Ti_3C_2T_x$ MXene Nanosheet: A Synergistically Active Ti-based Nanohybrid Electrocatalyst for Enhanced N_2 Reduction to NH_3 at Ambient Conditions. *Inorg. Chemistry* **2019**, *58*, 5414-5418.

(235) Li, T.; Yan, X.; Huang, l.; Li, J.; Yao, L.; Zhu, Q.; Wang, W.; Abbas, W.; Naz, R.; Gu, J.et al. Fluorine-Free $Ti_3C_2T_x$ (T= O, OH) Nanosheets (~50-100 nm) for Nitrogen Fixation under Ambient Conditions. *J. Mater. Chem. A* **2019**, *7,* 14462-14465

(236) Gao, Y.; Cao, Y.; Zhuo, H.; Sun, X.; Gu, Y.; Zhuang, G.; Deng, S.; Zhong, X.; Wei, Z.; Li, X.et al. Mo_2TiC_2 MXene: A Promising Catalyst for Electrocatalytic Ammonia Synthesis. *Catal. Today* **2018**, doi.org/10.1016/j.cattod.2018.12.029

(237) Gao, Y.; Zhuo, H.; Cao, Y.; Sun, X.; Zhuang, G.; Deng, S.; Zhong, X.; Wei, Z.; Wang, J. A Theoretical Study of Electrocatalytic Ammonia Synthesis on Single Metal Atom/MXene. *Chin. J. Catal.* **2019**, *40*, 152-159.

(238) Shao, M.; Shao, Y.; Chen, W.; Ao, K. L.; Tong, R.; Zhu, Q.; Chan, I. N.; Ip, W. F.; Shi, X.; Pan, H. Efficient Nitrogen Fixation to Ammonia on MXenes. *Phys. Chem. Chem. Phys.* **2018**, *20*, 14504-14512.

(239) Gurylev, V.; Mishra, M.; Su, C.; Perng, T. Enabling Higher Photo-electrochemical Efficiency of TiO_2 via Controlled Formation of a Disordered Shell: an Alternative to the Hydrogenation Process. *Chem. Commun.* **2016**, *52*, 7604-7607.

(240) Xiong, J.; Di, J.; Xia, J.; Zhu, W.; Li, H. Surface Defect Engineering in 2D Nanomaterials for Photocatalysis. *Adv. Funct. Mater.* **2018**, *28*, 1801983.

(241) Cai, J.; Wu, M.; Wang, Y.; Zhang, H.; Meng, M.; Tian, Y.; Li, X.; Zhang, J.; Zheng, L.; Gong, J. Synergetic Enhancement of Light Harvesting and Charge Separation over Surface-disorder-engineered TiO_2 Photonic Crystals. *Chem* **2017**, *2*, 877-892.

(242) Cai, J.; Wang, Y.; Zhu, Y.; Wu, M.; Zhang, H.; Li, X.; Jiang, Z.; Meng, M. In Situ Formation of Disorder-Engineered TiO_2(B)-anatase Heterophase Junction for Enhanced Photocatalytic Hydrogen Evolution. *ACS Appl. Mater. Interfaces* **2015**, *7*, 24987-24992.

(243) Li, H.; Shang, J.; Shi, J.; Zhao, K.; Zhang, L. Facet-dependent Solar Ammonia Synthesis of BiOCl Nanosheets via a Proton-assisted Electron Transfer Pathway. *Nanoscale* **2016**, *8*, 1986-1993.

(244) Li, J.; Li, H.; Zhan, G.; Zhang, L. Solar Water Splitting and Nitrogen Fixation with Layered Bismuth Oxyhalides. *Acc. Chem. Res.* **2017**, *50*, 112-121.

(245) Lv, C.; Qian, Y.; Yan, C.; Ding, Y.; Liu, Y.; Chen, G.; Yu, G. Defect Engineering Metal-Free Polymeric Carbon Nitride Electrocatalyst for Effective Nitrogen Fixation under Ambient Conditions. *Angew. Chem. Int. Ed.* **2018**, *57*, 10246-10250.

(246) Ou, H.; Lin, L.; Zheng, Y.; Yang, P.; Fang, Y.; Wang, X. Tri-s-triazine-Based Crystalline Carbon Nitride Nanosheets for an Improved Hydrogen Evolution. *Adv. Mater*. **2017,** *29*, 1700008.

(247) Lee, C. C.; Hu, Y.; Ribbe, M. W. ATP-independent Formation of Hydrocarbons Catalyzed by Isolated Nitrogenase Cofactors. *Angew. Chem. Int. Ed.* **2012,** *51*, 1947-1949.

(248) Xie, J.; Zhang, H.; Li, S.; Wang, R.; Sun, X.; Zhou, M.; Zhou, J.; Lou, X. W.; Xie, Y. Defect-Rich MoS_2 Ultrathin Nanosheets with Additional Active Edge Sites for Enhanced Electrocatalytic Hydrogen Evolution. *Adv. Mater*. **2013,** *25*, 5807-5813.

122

Chapter II. Two-Dimensional Boron Sheets as Metal-Free Catalysts for Hydrogen Evolution Reaction

This Chapter describes HER catalytic activity on two-dimensional (2D) boron sheets (α and β_{12}) are explored using periodic density functional theory. Using the binding free energy of H (ΔG_{H*}) as the descriptor, we found that both α and β_{12} sheets present superior activity, with ΔG_{H*} being close to zero. It is expected that 2D boron sheets would be a promising metal-free catalyst in the electrolysis of water and may offer novel thoughts for the design of new catalysts for other reactions.
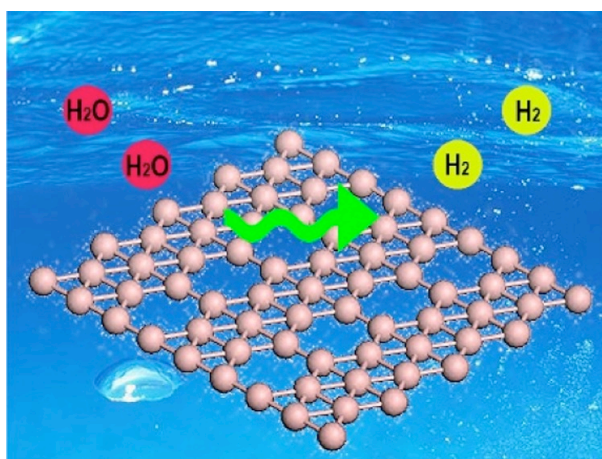
Scheme 2.1 Electrochemical water splitting on two-dimensional boron sheets.

This Chapter consists of two sections: (1) published paper, and (2) Supporting Information. The Supporting Information involves the computational details, the Gibbs free energies, geometries at different H-coverages.

2.1 Published Paper

Two-Dimensional Boron Sheets as Metal-Free Catalysts for Hydrogen Evolution Reaction

Chuangwei Liu,[†] Zhongxu Dai,[‡] Jie Zhang,[†] Yonggang Jin,[§] Dongsheng Li,[‡] and Chenghua Sun*,[‖]

[†]School of Chemistry, Faculty of Science, Monash University, Clayton, Victoria 3800, Australia

[‡]Key Laboratory of Inorganic Nonmetallic Crystalline and Energy Conversion Materials, College of Materials and Chemical Engineering, China Three Gorges University, Yichang 443002, China

[§]CSIRO Energy, 1 Technology Court, Pullenvale, Queensland 4069, Australia

[‖]Department of Chemistry and Biotechnology, Faculty of Science, Engineering & Technology, Swinburne University of Technology, Hawthorn, Victoria 3122, Australia

S *Supporting Information*

ABSTRACT: Current metal-free catalysts for hydrogen evolution reaction (HER) are mainly carbon-based. In this work, HER catalytic activity on two-dimensional (2D) boron sheets (α and β_{12}) are explored using periodic density functional theory. Using the binding free energy of H (ΔG_{H*}) as the descriptor, we found that both α and β_{12} sheets present superior activity, with ΔG_{H*} being close to zero. It is expected that 2D boron sheets would be a promising metal-free catalyst in the electrolysis of water and may offer novel thoughts for the design of new catalysts for other reactions.
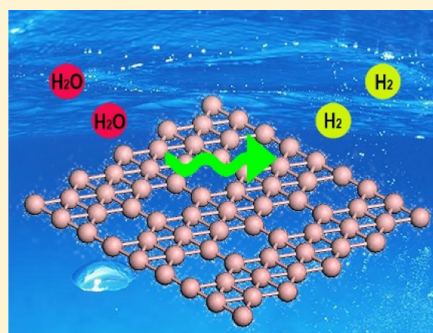
Favorable catalysts play an important role in the electrochemical water-splitting reaction for hydrogen production.[1,2] So far, noble metal materials have been regarded as the most efficient electrocatalysts owing to their excellent thermodynamics and kinetics in the electrocatalytic hydrogen evolution reaction (HER).[3−5] However, the limited resources and the high cost of noble metals have hampered the viability of large-scale commercialization.[6] In addition, noble metals also face other problems, such as migration, loss of active surface area, and detrimental environmental effects.[7] Therefore, Pt-comparable catalysts, particularly two-dimensional (2D) structures, have been extensively explored, including carbides,[8−10] transition metal dichalcogenides,[11−13] metal organic frameworks (MOFs),[14] carbon nanotubes,[15] and doped and defective graphene.[16,17] Although these 2D structures offer large surface areas, the catalytic sites often originate from the edges, defects, or embedded dopants or metal, rather than the inherent basal planes; as a result, the loading of active sites over specific weight is often low.[9,12] External strain energy can be helpful to improve it without introducing new components,[18] but the catalysis performance is sensitive to the degree of deformation and can be hardly durable if the strain energy cannot be accurately controlled and maintained.

Recently, 2D boron monolayer has been theoretically predicted and experimentally synthesized on single-crystal Ag(111)[19] and Cu(111)[20] substrates under ultrahigh vacuum conditions, gaining widespread attention because of their potentially low cost, large surface area, and unique catalytic activities,[21] together with excellent mechanical,[22] thermal,[23] and electrical properties.[23−25] Similar to carbon, the neighboring boron element also exhibits honeycomb-like 2D structures, but differently, the unit cell of the boron sheet composed of triangular and hexagonal motifs has been identified to be energetically more stable than those of only triangular lattices or hexagonal lattices,[26−28] which can be viewed as hole-doped triangular lattices and may bring rich chemistry. Among many predicted structures, the α-sheet was confirmed to be the most stable structure,[29] and β_{12} sheet can be produced readily on an Ag surface by direct evaporation of a pure boron source.[19] Both sheets have a typically porous characteristic structure that can provide sufficient surface space and active atoms. Until now, these boron sheets have demonstrated promising applications in superconductors,[30] hydrogen storage,[31] and oxygen evolution reaction.[21] In our work, we perform first-principles calculations to investigate boron sheets as catalysts for HER activity. As demonstrated below, boron sheets can offer excellent HER catalysis performance, being comparable or even better than those reported for noble metal and metal-free catalysts.
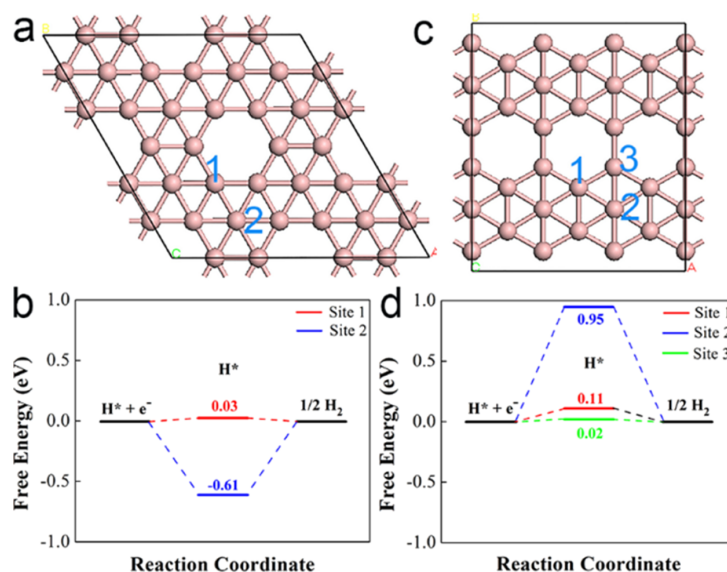
Figure 1. Models and calculated HER performance: (a) α-sheet supercell and (c) β_{12} sheet supercell. The calculated free-energy diagram for the formation of single H$_2$ at equilibrium on the different sites: (b) α-sheet and (d) β_{12} sheet.
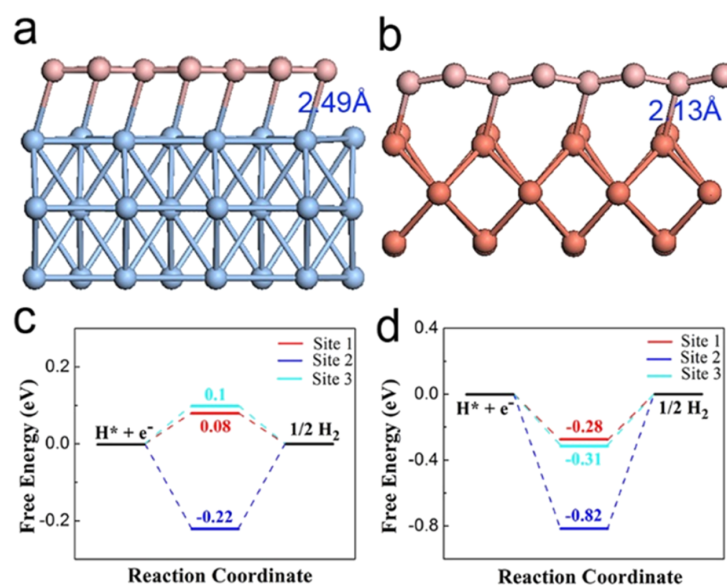
Figure 2. Effect of metal substrate. Optimized geometries of β_{12} sheet on (a) Ag(111) and (b) Cu(111) and calculated ΔG_{H*} for (c) β_{12}-Ag(111) and (d) β_{12}-Cu(111).

Our calculations start from the early studies of boron sheets;[28,32] $2 \times 2 \times 1$ supercell for α and $3 \times 2 \times 1$ supercell for β_{12} have been employed consisting of 32 and 30 boron atoms, respectively. All structures are fully optimized under the scheme of density functional theory, as described in the Supporting Information. Optimized structures are shown in Figure 1a,c, which clearly keep perfect monolayer structural characteristics. The triangular and hexagonal motifs and the resulting porous structural characteristic of this "hexagonal hole" could provide lowly coordinated sites for HER. Because of the difference in the coordination numbers, boron atoms have been classified into different types, labelled in Figure 1. Following early studies,[13] the Gibbs free energy of H-

adsorption, ΔG_{H*} (see Table S1), has been employed to evaluate the catalysis performance of different sites. Using a standard hydrogen electrode as the energy reference, HER catalysts with $\Delta G_{H*} \approx 0$ eV has been targeted in terms of energy efficiency.[9] More positive ΔG_{H*} suggests that the catalyst exhibits relatively weak stabilization for the protons bonded, whereas the hydrogen release will be slow under a bigger negative ΔG_{H*}. The calculated ΔG_{H*} for different sites has been presented in Figure 1b,d, according to which both site-2 of α and β_{12} show poor HER performance, whereas site-1 in α and site-1&3 in β_{12} offer nearly zero ΔG_{H*}, indicating superior HER activity. Apparently, such high performance originates from the unsaturated nature of boron, as site 1 (in

128
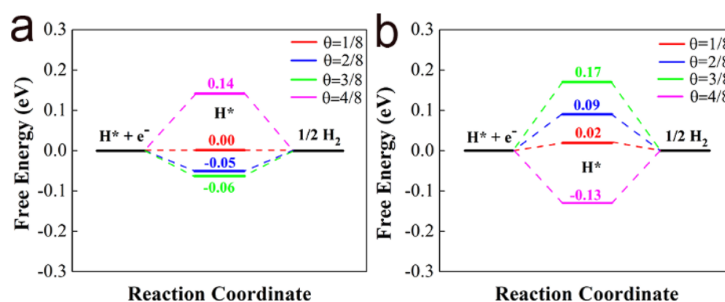
Figure 3. Free-energy diagram for hydrogen evolution over two boron sheets: (a) site 1 of α-sheet and (b) site 3 of β_{12} sheet.

both cases) and site 3 are five- and four-coordinated, whereas poorly performed site-2 is fully coordinated. Therefore, lowly coordinated boron has be identified as active sites for HER, similar as edge sites of MoS$_2$ monolayers.[11]

Although there are a large variety of planar 2D boron structures with competitive cohesive energy, the experimental realization of 2D boron sheets remains a challenge. This problem may hamper the further large-scale application of these technologies. Currently, boron sheets are synthesized on specific metal surfaces, such as Ag and Cu.[19,20] In our case, the as-grown β_{12} sheet on metal substrates has been modelled with β_{12} on Ag(111) and Cu(111), and the optimized geometries are shown in Figure 2a,b, respectively, according to which the boron−metal substrate distance is around 2.49 and 2.13 Å. The B−metal distance is comparable to that in the known B−metal alloys and suggests moderate covalent bonding interaction between boron and metal atoms.[33] HER over three sites have been further investigated, as shown in Figure 2c,d. With respect to free-standing boron sheets (see Figure 1c), the Ag substrate can slightly improve the performance for site 1 ($|\Delta G| = 0.11$ eV changing to 0.08 eV) and worsen site 3 ($|\Delta G| = 0.02$−0.10 eV), but remarkably improve site 2 ($|\Delta G| = 0.95$−0.22 eV) (see Table S2).

The above results indicate that the Ag(111) substrate does not bring negative effect on the HER performance for the boron sheet. In Figure 2d, we can find that all activity sites of the boron sheet were deteriorated when the β_{12} sheet grows on Cu(111), and all free energy changes from a positive to negative value, indicating stronger interaction between hydrogen and boron. This should be related to the strong electron coupling between the boron sheet and metals, as strong electron transfer from metals to boron sheet will strengthen H-adsorption, increasing the difficulty for H$_2$ release and thus resulting in higher HER overpotential. Therefore, transferring boron sheets to a proper substrate (such as Ag) may be an option to further optimize their HER performance.

Now, we turn to the investigation of the durability of those active sites. One of the key issues is whether the calculated performance will lose if more hydrogen atoms are introduced to the sheet. Figure 3 shows the calculated ΔG_{H*} versus the H-coverages (see Table S3) in the absence of water and a bias potential. The adsorption geometries at different H-coverages are provided in the Supporting Information (see Figures S1 and S2). As revealed by the calculated ΔG_{H*}, both α and β_{12} still show excellent HER performance at all these coverages with a maximum value of $\Delta G_{H*} = 0.14$ eV for α and 0.17 eV for β_{12}, being close to MoS$_2$-edges.[11]

To verify the calculated HER activity of two boron sheets, we have cited the data that were carefully selected from the

representative literature for several benchmark catalysts, including Pt,[5] MoS$_2$ S-edge,[11] and Co−MOF.[14] The volcano plot was made using the average Gibbs free energy of hydrogen atoms adsorbed on the boron sheet surface as the same hydrogen coverages ($\theta = 1/4$) as the above work in Figure 4.
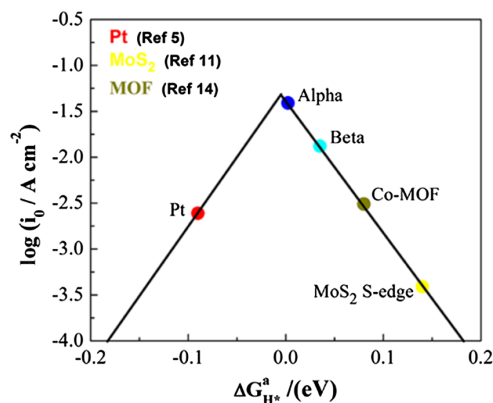
Figure 4. Volcano curve of exchange current (i_0) as a function of the average Gibbs free energy of hydrogen adsorption (ΔG_{H*}^a).

The theoretical exchange current i_0 was calculated using averaged ΔG_{H*}, labelled as ΔG_{H*}^a. In this curve, the position of log i_0 and ΔG_{H*}^a in the volcano plot are usually used for the evaluation of HER performance. More specifically, the closer to the curve peak, the better catalytic activity on the boron sheet.[9] From Figure 4, we can find that the value of Pt is located in the left leg of the volcano curve, whereas several 2D materials are located in the right leg of the plot. The value of ΔG_{H*}^a and log i_0 of Pt are −0.09 eV and −2.61 A/cm^{-2}, respectively. Whereas a relatively large positive ΔG_{H*}^a of Co−MOF and MoS$_2$ have comparatively low exchange currents, which are −2.45 and −3.44 A/cm^{-2}, respectively. In our work, the positions of two boron sheets are closer to the peak than Pt, Co−MOF, and MoS$_2$, indicating that they can offer higher exchange current, which is favorable for hydrogen adsorption and release in the HER. Specifically, the calculated ΔG_{H*}^a and log i_0 of the β_{12} sheet are 0.04 eV and −1.79 A/cm^{-2}, whereas α-sheet even performs better, with $\Delta G_{H*}^a \approx 0.00$ eV (exactly 0.0023 eV) and log $i_0 = -1.41$ A/cm^{-2}, respectively. Therefore, the two boron sheets display excellent HER performance according to our results, especially for the α-sheet.

As HER catalysts need to collect electrons from the electrode and simultaneously attract proton from the solution to generate H*, the coexistence of unpaired electrons and empty states is believed to be beneficial for HER.[34]

Unsaturated boron (site-1 in α and site-1&3 in β_{12}) along the hole of boron sheets offers such an electronic feature, which can also explain the poor performance of site-2 in these sheets. It is also worth to point out that those active sites are stable, as evidenced by the high cohesive energy. In addition, B-sheets present a high density of such active sites, with atomic ratio as high as 3/4 and 4/5 for α and site-1&3 in β_{12}, respectively, which is hardly obtainable for MoS_2 and MOF. Currently, the synthesis of boron sheets needs the mediation of metal support, such as Cu, Ag, and Au.[35] As presented in Figure 2, the Ag substrate can promote HER performance of the boron sheet, whereas the Cu substrate may deteriorate it, indicating a potential approach to further optimize the performance through properly choosing the substrate.

In summary, HER performance of α and β_{12} sheets has been explored by density functional theory calculations. As indicated by ΔG_{H*}, both α and β_{12} sheets offer an ultralow overpotential for HER, and such performance can keep well at different H-coverages. Because of the coexistence of unpaired electron and empty states, unsaturated boron atoms along the hexagon holes are the active sites, with loading as high as 3/4 and 4/5 in terms of atomic ratio. Given that the boron nanosheets are excellent conductors, metal-free, and have been synthesized readily, they are promising candidates for HER.

■ ASSOCIATED CONTENT

Ⓢ Supporting Information

The Supporting Information is available free of charge on the ACS Publications website at DOI: 10.1021/acs.jpcc.8b05859.

Computational details and optimized structures (PDF)

■ AUTHOR INFORMATION

Corresponding Author
*E-mail: chenghuasun@swin.edu.au.

ORCID ⊚
Jie Zhang: 0000-0003-2493-5209
Dongsheng Li: 0000-0003-1283-6334
Chenghua Sun: 0000-0001-7654-669X

Notes
The authors declare no competing financial interest.

■ ACKNOWLEDGMENTS

■ REFERENCES

(1) Borup, R.; Meyers, J.; Pivovar, B.; Kim, Y. S.; Mukundan, R.; Garland, N.; Myers, D.; Wilson, M.; Garzon, F.; Wood, D. Scientific Aspects of Polymer Electrolyte Fuel Cell Durability and Degradation. *Chem. Rev.* **2007**, *107*, 3904−3951.

(2) Fosdick, S. E.; Berglund, S. P.; Mullins, C. B.; Crooks, R. M. Evaluating Electrocatalysts for the Hydrogen Evolution Reaction Using Bipolar Electrode Arrays: Bi- and Trimetallic Combinations of Co, Fe, Ni, Mo, and W. *ACS Catal.* **2014**, *4*, 1332−1339.

(3) Skúlason, E.; Karlberg, G. S.; Rossmeisl, J.; Bligaard, T.; Greeley, J.; Jónsson, H.; Nørskov, J. K. Density Functional Theory Calculations for the Hydrogen Evolution Reaction in an Electro-chemical Double Layer on the Pt(111) Electrode. *Phys. Chem. Chem. Phys.* **2007**, *9*, 3241−3250.

(4) Subbaraman, R.; Tripkovic, D.; Strmcnik, D.; Chang, K.-C.; Uchimura, M.; Paulikas, A. P.; Stamenkovic, V.; Markovic, N. M. Enhancing Hydrogen Evolution Activity in Water Splitting by Tailoring Li+-Ni(OH)2-Pt Interfaces. *Science* **2011**, *334*, 1256−1260.

(5) Nørskov, J. K.; Bligaard, T.; Logadottir, A.; Kitchin, J. R.; Chen, J. G.; Pandelov, S.; Stimming, U. Trends in the Exchange Current for Hydrogen Evolution. *J. Electrochem. Soc.* **2005**, *152*, J23.

(6) Bai, S.; Wang, C.; Deng, M.; Gong, M.; Bai, Y.; Jiang, J.; Xiong, Y. Surface Polarization Matters: Enhancing the Hydrogen-Evolution Reaction by Shrinking Pt Shells in Pt-Pd-Graphene Stack Structures. *Angew. Chem., Int. Ed.* **2014**, *53*, 12120−12124.

(7) Sealy, C. The problem with platinum. *Mater. Today* **2008**, *11*, 65−68.

(8) Wan, C.; Regmi, Y. N.; Leonard, B. M. Multiple Phases of Molybdenum Carbide as Electrocatalysts for the Hydrogen Evolution Reaction. *Angew. Chem., Int. Ed.* **2014**, *53*, 6407−6410.

(9) Gao, G.; O'Mullane, A. P.; Du, A. 2D MXenes: A New Family of Promising Catalysts for the Hydrogen Evolution Reaction. *ACS Catal.* **2017**, *7*, 494−500.

(10) Zheng, Y.; Jiao, Y.; Chen, J.; Liu, J.; Liang, J.; Du, A.; Zhang, W.; Zhu, Z.; Smith, S. C.; Jaroniec, M.; et al. Nanoporous Graphitic-C3N4@Carbon Metal-Free Electrocatalysts for Highly Efficient Oxygen Reduction. *J. Am. Chem. Soc.* **2011**, *133*, 20116−20119.

(11) Tsai, C.; Abild-Pedersen, F.; Nørskov, J. K. Tuning the MoS2 Edge-Site Activity for Hydrogen Evolution via Support Interactions. *Nano Lett.* **2014**, *14*, 1381−1387.

(12) Qu, Y.; Shao, M.; Shao, Y.; Yang, M.; Xu, J.; Kwok, C. T.; Shi, X.; Lu, Z.; Pan, H. Ultra-high electrocatalytic activity of VS2 nanoflowers for efficient hydrogen evolution reaction. *J. Mater. Chem. A* **2017**, *5*, 15080−15086.

(13) Tang, Q.; Jiang, D.-e. Mechanism of Hydrogen Evolution Reaction on 1T-MoS2 from First Principles. *ACS Catal.* **2016**, *6*, 4953−4961.

(14) Wu, Y.-P.; Zhou, W.; Zhao, J.; Dong, W.-W.; Lan, Y.-Q.; Li, D.-S.; Sun, C.; Bu, X. Surfactant-Assisted Phase-Selective Synthesis of New Cobalt MOFs and Their Efficient Electrocatalytic Hydrogen Evolution Reaction. *Angew. Chem., Int. Ed.* **2017**, *56*, 13001−13005.

(15) Das, R. K.; Wang, Y.; Vasilyeva, S. V.; Donoghue, E.; Pucher, I.; Kamenov, G.; Cheng, H.-P.; Rinzler, A. G. Extraordinary Hydrogen Evolution and Oxidation Reaction Activity from Carbon Nanotubes and Graphitic Carbons. *ACS Nano* **2014**, *8*, 8447−8456.

(16) Sathe, B. R.; Zou, X.; Asefa, T. Metal-free B-doped Graphene with Efficient Electrocatalytic Activity for Hydrogen Evolution Reaction. *Catal. Sci. Technol.* **2014**, *4*, 2023−2030.

(17) Duan, J.; Chen, S.; Jaroniec, M.; Qiao, S. Z. Porous C3N4 nanolayers@N-graphene films as Catalyst Electrodes for Highly Efficient Hydrogen Evolution. *ACS Nano* **2015**, *9*, 931−940.

(18) Li, H.; Tsai, C.; Koh, A. L.; Cai, L.; Contryman, A. W.; Fragapane, A. H.; Zhao, J.; Han, H. S.; Manoharan, H. C.; Abild-Pedersen, F.; et al. Activating and optimizing MoS2 basal planes for hydrogen evolution through the formation of strained sulphur vacancies. *Nat. Mater.* **2015**, *15*, 48−53.

(19) Feng, B.; Zhang, J.; Zhong, Q.; Li, W.; Li, S.; Li, H.; Cheng, P.; Meng, S.; Chen, L.; Wu, K. Experimental Realization of Two-dimensional Boron Sheets. *Nat. Chem.* **2016**, *8*, 563−568.

(20) Liu, Y.; Penev, E. S.; Yakobson, B. I. Probing the Synthesis of Two-Dimensional Boron by First-Principles Computations. *Sci. Rep.* **2013**, *125*, 3238−3241.

(21) Mir, S. H.; Chakraborty, S.; Jha, P. C.; Wärnå, J.; Soni, H.; Jha, P. K.; Ahuja, R. Two-Dimensional Boron: Lightest Catalyst for Hydrogen and Oxygen Evolution Reaction. *Appl. Phys. Lett.* **2016**, *109*, 053903.

(22) Jiao, Y.; Ma, F.; Bell, J.; Bilic, A.; Du, A. Two-Dimensional Boron Hydride Sheets: High Stability, Massless Dirac Fermions, and Excellent Mechanical Properties. *Angew. Chem., Int. Ed.* **2016**, *55*, 10292−10295.

130

(23) Tsafack, T.; Yakobson, B. I. Thermomechanical Analysis of Two-dimensional Boron Monolayers. *Phys. Rev. B* **2016**, *93*, 165434.

(24) Penev, E. S.; Kutana, A.; Yakobson, B. I. Can Two-Dimensional Boron Superconduct? *Nano Lett.* **2016**, *16*, 2522−2526.

(25) Penev, E. S.; Bhowmick, S.; Sadrzadeh, A.; Yakobson, B. I. Polymorphism of Two-Dimensional Boron. *Nano Lett.* **2012**, *12*, 2441−2445.

(26) Tang, H.; Ismail-Beigi, S. Novel Precursors for Boron Nanotubes: The Competition of Two-Center and Three-Center Bonding in Boron Sheets. *Phys. Rev. Lett.* **2007**, *99*, 115501.

(27) Wu, X.; Dai, J.; Zhao, Y.; Zhuo, Z.; Yang, J.; Zeng, X. C. Two-dimensional Boron Monolayer Sheets. *ACS Nano* **2012**, *6*, 7443−7453.

(28) Ma, F.; Jiao, Y.; Gao, G.; Gu, Y.; Bilic, A.; Chen, Z.; Du, A. Graphene-like Two-Dimensional Ionic Boron with Double Dirac Cones at Ambient Condition. *Nano Lett.* **2016**, *16*, 3022−3028.

(29) Oganov, A. R.; Chen, J.; Gatti, C.; Ma, Y.; Ma, Y.; Glass, C. W.; Liu, Z.; Yu, T.; Kurakevych, O. O.; Solozhenko, V. L. Ionic High-pressure Form of Elemental Boron. *Nature* **2009**, *457*, 863−867.

(30) Wu, C.; Wang, H.; Zhang, J.; Gou, G.; Pan, B.; Li, J. Lithium-Boron (Li-B) Monolayers: First-Principles Cluster Expansion and Possible Two-Dimensional Superconductivity. *ACS Appl. Mater. Interfaces* **2016**, *8*, 2526−2532.

(31) Li, J.; Zhang, H.; Yang, G. Ultrahigh-Capacity Molecular Hydrogen Storage of a Lithium-Decorated Boron Monolayer. *J. Phys. Chem. C* **2015**, *119*, 19681−19688.

(32) Yu, X.; Li, L.; Xu, X.-W.; Tang, C.-C. Prediction of Two-Dimensional Boron Sheets by Particle Swarm Optimization Algorithm. *J. Phys. Chem. C* **2012**, *116*, 20075−20079.

(33) Andersson, S.; Callmer, B. The solubilities of copper and manganese in *β*-rhombohedral boron as determined in CuB∼28 and MnB∼23 by single-crystal diffractometry. *J. Solid State Chem.* **1974**, *10*, 219−231.

(34) Zhao, S.; Wang, Y.; Dong, J.; He, C.-T.; Yin, H.; An, P.; Zhao, K.; Zhang, X.; Gao, C.; Zhang, L.; et al. Ultrathin Metal−organic Framework Nanosheets for Electrocatalytic Oxygen Evolution. *Nat. Energy* **2016**, *1*, 16184.

(35) Zhang, Z.; Yang, Y.; Gao, G.; Yakobson, B. I. Two-Dimensional Boron Monolayers Mediated by Metal Substrates. *Angew. Chem., Int. Ed.* **2015**, *54*, 13022−13026.

131

132

2.1 Supporting Information

Supporting Information

Two-Dimensional Boron Sheets as Metal-Free

Catalysts for Hydrogen Evolution Reaction

Chuangwei Liu,[†] Zhongxu Dai,[‡] Jie Zhang,[†] Yonggang Jin,[T̄] Dongsheng Li,[‡] Chenghua Sun*,[⊥]

† School of Chemistry, Faculty of Science, Monash University, Clayton, VIC 3800, Australia

‡ Key Laboratory of Inorganic Nonmetallic Crystalline and Energy Conversion Materials, College of Materials and Chemical Engineering, China Three Gorges University, Yichang 443002, China

T̄ CSIRO Energy Flagship, PO BOX 883, Kenmore, QLD 4069, Australia

⊥ Department of Chemistry and Biotechnology, Faculty of Science, Engineering & Technology, Swinburne University of Technology, Hawthorn, VIC 3122, Australia

Email: chenghuasun@swin.edu.au

COMPUTATIONAL DETAILS

First-principle calculations were performed with the frame work of density functional theory (DFT) as implemented in the plane wave set Vienna ab initio Simulation Package (VASP, version 5.43) incorporating the projector augmented wave (PAW) scheme.[1,2] All electron exchange-correlation calculations were performed with the functional of revised Perdew-Burke-Ernzerhof (RPBE) of generalized gradient approximation (GGA).[1] A cutoff energy of 380 eV was used throughout the computations. The Brillouin zone was sample using $3 \times 3 \times 1$ k-point grid generated with the Monkhorst-Pack scheme and thermal and zero point energy (ZPE) corrections were calculated over Γ points. The calculations were completed on the $2 \times 2 \times 1$ and $3 \times 2 \times 1$ supercells consisting of 32 and 30 boron atoms in α-sheet and β_{12}-sheet, respectively. The structures were optimized using energy and force convergence limits equal to 10^{-4} eV/atom and 0.01 eV/Å, respectively. To avoid interaction between two monolayers in neighboring supercells, a vacuum distance of 20 Å was imposed between different layers. For the HER performance on the boron sheets with the metal substrates, the same DFT calculation was applied, and the supercells consisting of 48 metal atoms and 40 boron atoms, respectively.

The free energy of the adsorption atomic hydrogen (ΔG_{H*}) can be calculated by

$$\Delta G_{H*} = \Delta E_{H*} + \Delta E_{ZPE} - T\Delta S_{H*} \tag{1}$$

Where the ΔE_H is describes the energy needed to increase the coverage by one hydrogen atom. And in the individual catalytic process, the ΔE_{H*} is described as

$$\Delta E_{H*} = E_{nH*} - E_{(n-1)H*} - \frac{1}{2}E_{H_2} \tag{2}$$

Where the asterisk denotes the catalyst. And the ΔE_{ZPE} is the zero point energy difference between the adsorbed and the free hydrogen, ΔS_{H*} is their entropy difference.

136

In the volcano curve, the integral average adsorption energy of hydrogen adsorption on the both monolayers with the surface coverage of $\theta = 1/4$ is defined by

$$\Delta E_{H*}^a = \frac{1}{n} (E_{nH*} - E_{cat} - \frac{n}{2} E_{H_2})$$

Where n is the number of H atoms in the calculation.

$$\Delta G_{H*}^a = \Delta E_{H*}^a + \Delta E_{ZPE} - T\Delta S_{H*} \tag{4}$$

From the Norskov's previous work,[3] the exchange current can be described the following equation at PH 0.

$$i_0 = -ek_0 \frac{1}{1+\exp(|\Delta G_{H*}^a|/kT)} \tag{5}$$

where k_0 is an rate constant, should be set it to 1 follow the previous paper.[4]

GIBBS FREE ENERGIES

The energies of proton and electron ($E(H^+)$ and $E(e^-)$) were achieved, when the reaction working at standard hydrogen electrode (SHE) conditions which defined to be in equilibrium at zero voltage, at all values of pH, at all temperatures, and with H_2 at 101 kPa pressure. Therefore, in the SHE, the chemical potential of a proton-electron pair, $\mu(H^+) + \mu(e^-)$ is equal to half of the chemical potential of gaseous hydrogen ($1/2\ \mu(H_2)$) at a potential of 0 V. In this way, the chemical potential of the proton-electron pair can be calculated simply by calculating the chemical potential of gas-phase H_2, the value is 3.55eV.

Table S1. Gibbs free energies at 298.15 K (ZPE and D3 corrections applied), in eV, corresponding to the chemisorbed one hydrogen atom on the different active sites of both boron sheets surfaces.

Active sites	α-sheet	β_{12}-sheet
clean surface	-196.25	-182.83
site 1	-199.77	-186.27
site 2	-200.41	-185.43
site 3		-186.36

Table S2. Gibbs free energies at 298.15 K (ZPE and D3 corrections applied), in eV, corresponding to the chemisorbed one hydrogen atom on the different active sites of β_{12}-sheet on Ag(111) and Cu(111) surfaces.

Active sites	Ag(111)	Cu(111)
clean surface	-391.49	-424.41
site 1	-394.96	-428.24
site 2	-395.26	-428.78
site 3	-394.94	-428.26

Table S3. Gibbs free energies at 298.15 K (ZPE and D3 corrections applied), in eV, corresponding to the chemisorbed different H-coverages on the site 1 of α-sheet, and site 3 of β_{12} sheet.

Different H-coverages	α-sheet	β_{12}-sheet
1/8	-199.77	-186.36
2/8	-206.86	-189.82
3/8	-213.26	-193.20
4/8	-219.34	-196.88

GEOMETRIES AT DIFFERENT H-COVERAGES

1/8   2/8   3/8   4/8
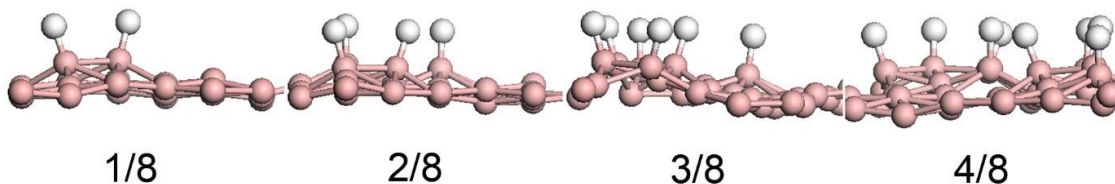
Figure S1. The optimized structures of different H-coverages on α-sheet.

1/8   2/8   3/8   4/8
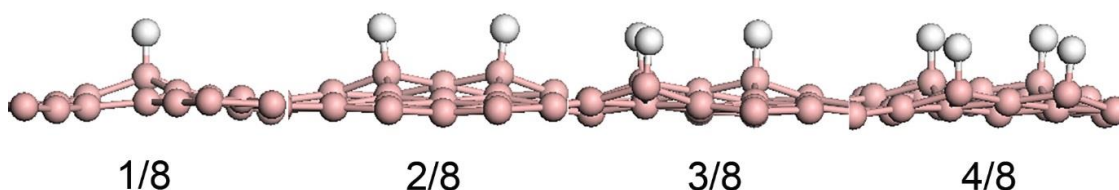
Figure S2. The optimized structures of different H-coverages on β_{12}--sheet.

138

REFERENCES

(1)Hammer, B.; Hansen, L. B.; Nørskov, J. K. Improved Adsorption Energetics Within Density-Functional Theory Using Revised Perdew-Burke-Ernzerhof Functionals. *Phys. Rev. B* **1999**, *59*, 7413-7421.

(2) Blöchl, P. E. Projector Augmented-wave Method. *Phys. Rev. B* **1994**, *50*, 17953-17979.

(3) Nørskov, J. K.; Bligaard, T.; Logadottir, A.; Kitchin, J. R.; Chen, J. G.; Pandelov, S.; Stimming, U. Trends in the Exchange Current for Hydrogen Evolution. *J. Electrochem. Soc.* **2005**, *152*, 23-26.

(4) Gao, G.; O'Mullane, A. P.; Du, A. 2D MXenes: A New Family of Promising Catalysts for the Hydrogen Evolution Reaction. *ACS Catal.* **2017**, *7*, 494-500.

Chapter III. Theoretical Evaluation of Possible 2D Boron Monolayer in N₂ Electrochemical Conversion into Ammonia

This Chapter demonstrates two stable boron 2D monolayers (α and β_{12}) as electrochemical catalysts for nitrogen reduction reaction (NRR). Our results revealed that the rate-determining step for nitrogen reduction to ammonia over two-dimensional boron structures is the first reduction step. Hexagonal triangular boron atoms in the α-sheet exhibit the best catalytic performance in all possible positions on the boron monolayer sheet surface, with a maximum energy input of 0.77 eV vs SHE.
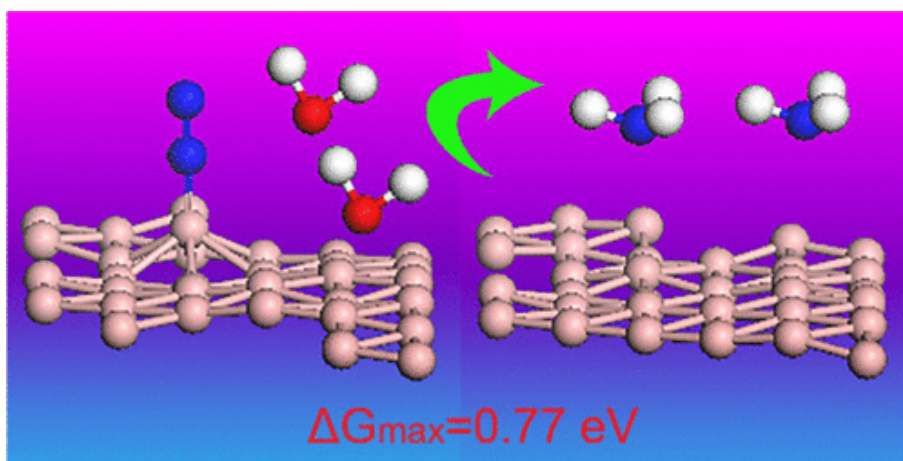
Scheme 3.1 Electrochemical nitrogen reduction reaction on 2D boron sheets.

This Chapter consists of two sections: (1) Published Paper, and (2) Supporting Information. The supporting information involves the computational details, the Gibbs free energies, geometries at different intermediates during reduction reaction.

3.1 Published Paper

Theoretical Evaluation of Possible 2D Boron Monolayer in N$_2$ Electrochemical Conversion into Ammonia

Chuangwei Liu,[†,§] Qinye Li,[‡] Jie Zhang,[†] Yonggang Jin,[∥] Douglas R. MacFarlane,[†] and Chenghua Sun*[,§,⊥]

[†]School of Chemistry, Faculty of Science and [‡]School of Chemical Engineering, Monash University, Clayton, Victoria 3800, Australia

[§]Science & Technology Innovation Institute, Dongguan University of Technology, Dongguan 511700, China

[∥]CSIRO Energy, 1 Technology Court, Pullenvale, Queensland 4069, Australia

[⊥]Department of Chemistry and Biotechnology, Faculty of Science, Engineering & Technology, Swinburne University of Technology, Hawthorn, Victoria 3122, Australia

Ⓢ *Supporting Information*

ABSTRACT: This work aims to explore inorganic boron as an electrochemical catalyst for nitrogen reduction reaction (NRR). The density functional theory approach has been employed to evaluate the free-energy profile for NRR on two stable boron monolayer types (α and β_{12}). Our results revealed that the rate-determining step for nitrogen reduction to ammonia over two-dimensional boron structures is the first reduction step. Hexagonal triangular boron atoms in the α-sheet exhibit the best catalytic performance in all possible positions on the boron monolayer sheet surface, with a maximum energy input of 0.77 eV vs stand hydrogen electrode.

ΔG$_{max}$=0.77 eV
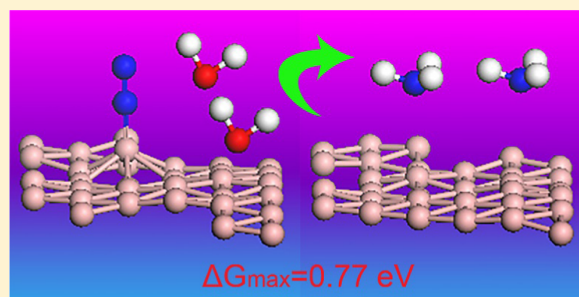
INTRODUCTION

Ammonia (NH$_3$) is one of the most widely produced chemicals, because it is not only a major fertilizer but also an important energy carrier.[1] For the past century, ammonia has been successfully synthesized by the Haber−Bosch method in the chemical industry.[2] In this process, nitrogen and hydrogen gas molecules are dissociated as N- and H-adatoms over Fe-based catalysts at pressures of 130−170 bar and temperatures around 400−500 °C to form ammonia according to[1,3]

$$N_2 + 3H_2 \rightarrow 2NH_3 \quad \Delta H^0 = -91.8 \text{ kJ}$$
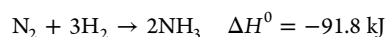
Even though the above reaction is exothermic, substantial energy input is required to complete the reaction, essentially for breaking the strong triple bond of nitrogen in the first stage.[4] In addition, the synthesis of ammonia is accompanied by CO$_2$ emission associated with the hydrogen production from methane reforming, which further increases the environment burden.[5] In the past decades, extensive efforts have been made with an ambition to synthesize ammonia through electrochemical methods at ambient temperature using various electrode materials and electrolytes to alleviate the thermodynamic requirements and optimize the ammonia formation rate.[6−10]

With advancements in the field of computations and modeling, theoretical investigations have provided a deeper insight into catalysis, especially the different active sites and mechanisms of reactions.[11−13] For instance, transition metal (TM) carbides and nitrides are investigated for electrochemical formation of ammonia at ambient temperature.[6,14−16] These materials are known as MXenes, which exhibit a unique combination of ceramic and metal properties.[14] The results indicated that the largest reaction energies for Nb$_3$C$_2$ and V$_3$C$_2$ materials are only 0.39 and 0.32 eV vs the standard hydrogen electrode as calculated with the Perdew−Burke−Ernzerhof functional, respectively.[16] Imitating the biological process, transition metal−nitrogen complexes can serve as an effective catalyst for conversion of dinitrogen to ammonia under ambient conditions, such as Fe−N$_3$[17] and Mo−N$_3$.[18] In the catalytic center of TM−N$_3$, the d-electrons of TM could promote the binding and activation of the N$_2$ ligands.[19] Therefore, the main catalytic site is the TM, whereas the nitrogen atoms only serve as the ligands to transfer electrons. Subsequently, single-atom catalysts were proved to be effective for nitrogen fixation. In these heterogeneous catalysts, single metal atoms can be distributed separately into the substrate, such as Al-doped graphene,[20] Fe-doped MoS$_2$,[21] and Fe-doped MoN$_2$.[22]

145
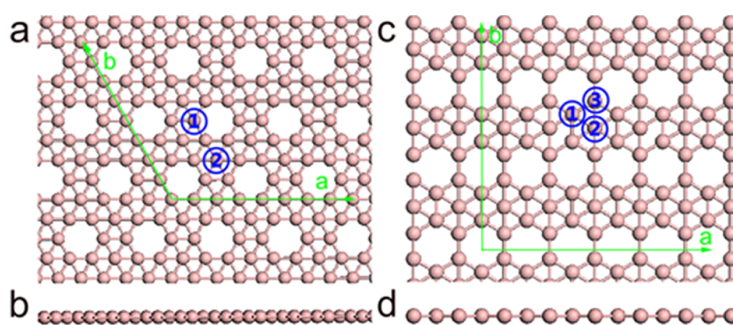
Figure 1. Top and side optimized structure of a boron monolayer: (a, b) α-sheet and (c, d) β_{12}-sheet.

Currently, most of the catalysts for nitrogen fixation and functionalization are based on metals under ambient conditions. Recently, two pioneering works proposed that nitrogen could be fixed and reduced by boron atom, providing a new approach for ammonia synthesis by metal-free catalysts.[23,24] Boron is an electron deficiency atom with three valence electrons in the 2s and 2p orbitals, leading to a notably different bonding characteristic compared with carbon.[25] A new class of two-dimensional (2D) crystalline monolayer structures of boron have been theoretically predicted from first principles-based electronic structure calculations.[26,27] Due to the electron deficiency, the boron monolayer composed of triangular and hexagonal motifs was identified to be energetically more stable than those of only triangular lattices or hexagonal lattices.[27,28] So far, structures of 2D boron materials with the hexagon hole density value η of 0, 1/4, 1/5, 1/6, 1/7, 1/8, and 1/9 were published by Yakobson and other researchers.[28−30] Among them, the unit cell of α-sheet (η = 1/9) was predicted to be the most stable structure,[31] and the β_{12}-sheet (η = 1/6) has been synthesized on a single-crystal Ag and Cu surface by direct evaporation of a pure boron source.[32] Although many theoretical investigations indicated that most boron sheets should be metallic, Wu et al. proposed that the α-sheet is a semiconductor with an indirect band gap of 1.4 eV.[27] In this work, ammonia synthesis on 2D boron materials (α-sheet and β_{12}-sheet), metal free materials, at ambient conditions were first investigated. Density functional theory (DFT) calculations of ammonia formations on potential active sites were carried out. The favorable reaction path was identified by calculating the Gibbs free reaction energies for all elementary steps.

COMPUTATIONAL METHODS

All calculations were performed using standard DFT through the generalized gradient approximation with the revised Perdew−Burke−Ernzerhof functional using a plane-wave cutoff energy of 380 eV.[33,34] The α-sheet and β_{12}-sheet boron monolayers were modeled using 2 × 2 × 1 and 3 × 2 × 1 supercells consisting of 32 and 30 boron atoms, respectively. The structures were optimized using energy and force convergence limits equal to 10^{-4} eV/atom and 0.01 eV/Å, respectively. In all calculations, spin polarization of the valence state has been taken into account. For the analysis of structural and electronic properties of the defects, the Brillouin zone was sampled using a 3 × 3 × 1 k-point grid generated within the Monkhorst−Pack. Thermal and zero-point energy corrections were calculated over Γ points. All calculations were performed using the Vienna ab initio simulation package.[35,36] The van der Waals interaction has been considered using the DFT-D$_3$ scheme.[37]

RESULTS AND DISCUSSION

The geometrical configuration of the pristine boron sheets were constructed as ideal 2D materials, and the optimized configurations are shown in Figure 1, corresponding to the α-sheet and β_{12}-sheet top and side views, respectively. As shown in Figure 1, the equilibrium configuration of freestanding boron sheets retains perfect monolayer structural characteristics and agrees with previous reports.[27] The α-sheet atoms are aggregated and well-regulated to be triangular and hexagonal motifs by forming B−B bonds, with the bond lengths distributed from 1.68 to 1.70 Å, and the average value of 1.69 Å. The special structural feature of the α-sheet was that every center-occupied hexagon is isolated from each other, and the angle of zigzag was 120°. The coordination number (CN) of boron atoms in the boron sheet has been used to label different sites in boron sheets. In the case of α-sheets, CN5 and CN6 can be found. In addition, the triangular and hexagonal motifs have the resulting porous structural characteristics of a "hexagonal hole atom" and "hexagonal triangular atom",[38] which correspond to CN5 and CN6, respectively. The adaptive natural density partitioning method was used to analyze the chemical bonding of the boron sheet.[29] The results show that there are six three-center-two-electron (3c−2e) σ-bonds, three 4c−2e σ-bonds, and delocalized π-bonds in the unit cell of the α-sheet. Therefore, the two different boron atoms show different electronic properties: the hole atom, labeled as 1 in Figure 1a,c, is connected by two 3c−2e bonds and one 4c−2e bond, whereas the triangular atom, labeled as 2, is connected by delocalized π-bonds, the three in β_{12}-sheet that connect by 3c−2e bonds.

In this work, we considered three possible ways to investigate the N$_2$ adsorbed on the α-sheet, including two end-on and one tilt end-on configurations, and the full relaxation structures are shown in Figure 2a−c. For the end-on configuration, the B−N bond lengths in site-1 and site-2 are about 1.52 and 1.47 Å, respectively. The N−N bond lengths of two ways are about 1.12 and 1.13 Å, which are close to the length of an individual N$_2$ molecule (1.10 Å). For the tilt end-on way, two B−N bonds with a length of 1.56 Å are formed as shown in Figure 2c and the N−N bond length increases to 1.45 Å, indicating that N ≡ N bond has been activated remarkably in this way. The N$_2$ adsorption energies in the three configurations are about 1.17, 0.63, and 2.89 eV, respectively. Therefore, the tilt end-on way is not eligible for
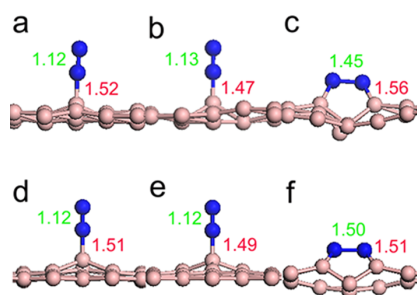
Figure 2. Optimized structures of N_2 adsorption on two 2D boron sheets: (a) site-1 of α-sheet, (b) site-2 of α-sheet, (c) tilt end-on of α-sheet, (d) site-1 of β_{12} sheet, (e) site-3 of β_{12} sheet, and (f) tilt end-on of β_{12} sheet. The B−N and N−N lengths (Å) are also given.

N_2 fixation as such an adsorption results in heavy distortion and requires a large energy input (Table S1).

Similar to the α-sheet, the β_{12}-sheet monolayer is also composed of triangular and hexagonal motifs and the equilibrium configuration retains perfect monolayer structural characteristics as shown in Figure 1. However, the B−B bond lengths in the β_{12}-sheet monolayer are slightly dispersed, with the value distributed from 1.65 to 1.72 Å and the average value of 1.68 Å. Moreover, the β_{12}-sheet structure is characterized by hexagonal hole chains separated by hexagonal triangular boron. As reported earlier, it revealed that the unit cell of a β_{12}-sheet is rectangular, with lattice constants of 3.0 and 5.0 Å in the two directions.[32] Based on the coordination, three sites, labeled as 1, 2, and 3 in Figure 1b, have been identified, corresponding to CN = 5, 6, and 4, respectively. The CN5 atom, named as site-1, has two 3c−2e bonds and one 4c−2e bond; CN6, named as site-2, has delocalized π-bonds; and CN4, named as site-3, has three 3c−2e bonds. In the primary results, site-2 is not fit for N_2 fixation because the B−N bond reached 3.49 Å, which is too far for effective activation. Based on the above analysis, three configurations for N_2 adsorption have been considered, as shown in Figure 2d−f. The B−N bond lengths with N_2 adsorbed over 1 and 3 are about 1.51, and 1.49 Å, respectively, together with the N−N bond length of 1.12 Å; with the tilt end-on adsorption (Figure 2f), the N−N bond length is increased to 1.5 Å. The N_2 adsorption energies in the three structures are about 1.03, 0.91, and 3.29 eV on the β_{12}-sheet, respectively.

Starting from N_2-adsorption, DFT calculations were used to estimate the free energy of each elementary step. For both α- and β_{12}-sheets, tilt end-on adsorptions result in heavy local distortions, indicating that such an adsorption is not energetically favorable. In fact, the calculated adsorption energies are as large as 2.89 and 3.29 eV in the two boron sheets, respectively, confirming that N_2 can hardly adsorb in this way. Therefore, two reaction pathways on the basis of end-on adsorption have been investigated, namely distal and alternating mechanisms. To obtain details of the conversion of the activated N_2 to NH_3 on the boron monolayer, we calculated the key reaction steps and products during the conversion based on the distal and alternating mechanisms.[17,39] Hydrogen atoms are added one by one to the adsorbed species and DFT calculations are used to find the minimum energy configuration, as shown in Figure 3. For each path, full N_2 reduction is incorporated with six pairs of electrons and protons. For the distal pathway, the consecutive protonation occurs first at the distal N and then at the
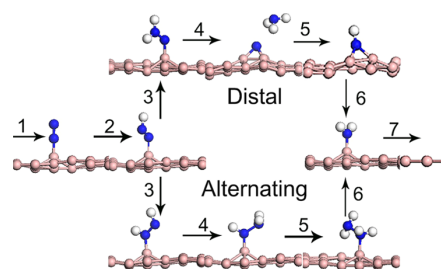
Figure 3. Optimized geometric structures of various intermediates along the two reaction paths of nitrogen reduction reaction (NRR) on boron.

proximal N. The following steps result in the full scission of the N−N bond and release of an NH_3, whereas the second NH_3 is released in the subsequent parts. For the alternating pathway, the protonation alternates between the two N atoms, making the first NH_3 release at the sixth step.

For the α-sheet, N_2 reduction over sites 1 and 2 has been studied and the calculated values of ΔG for each step have been shown in Figure 4a,b, respectively. In terms of initial N_2
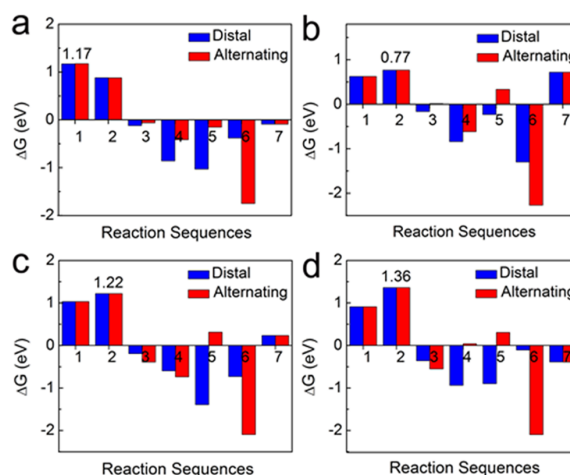
Figure 4. Calculated reaction free energy ΔG: (a) site-1 of α-sheet, (b) site-2 of α-sheet, (c) site-1 of β_{12}-sheet, and (d) site-3 of β_{12}-sheet. Step numbers for the reaction sequences are defined in Figure 3.

adsorption, site-2 is the favorable site with $\Delta G = 0.63$ eV, whereas it is 1.17 eV on site-1. A positive ΔG indicates that boron sheets do not offer a strong capacity to adsorb N_2. For the following reduction steps, the first protonation is the most energy-consuming step for the conversion from N_2^* to N_2H^* intermediate state, with an energy request of 0.88 eV for site-1 (Table S2) and 0.77 eV for site-2. With N_2H^*, the lengths of both B−N and N−N were slightly elongated to 1.50 and 1.26 Å from 1.47 and 1.13 Å, respectively, on site-2 (Table S3); meanwhile, the N−H length was 1.03 Å during this process. As we know, N_2 activation is very hard to complete: once the first protonation is completed, all of the subsequent steps are exothermic on site-1 under ambient conditions, whereas most steps are exothermic except the second NH_3 release, which needs a small energy input (0.31 eV) for site-2. Regarding the selectivity, the distal mechanism is favorable for both site-1 and site-2; moreover, step 2 ($N_2^* \rightarrow N_2H^*$), has been identified as

147

the rate-determining step for both site-1 and site-2. Overall, the most possible path will be the distal mechanism over site-2, with a maximum energy request of 0.77 eV using the standard hydrogen electrode as the energy reference. From the above results, it is clear that the boron atoms of hexagonal triangular are more active than the atoms of the hexagonal hole in the α-sheet monolayer (Table S6).

Similar to the α-sheet, the activation and conversion of N_2 on the β_{12}-sheet surface also have two reaction pathways and seven steps. The calculated profiles for reaction free energies have been shown in Figure 4c,d, according to which the initial N_2 adsorption and activation are quite difficult. Specifically, an intact N_2 molecule binds on the β_{12}-sheet boron monolayer surface, leading to $\Delta G = 1.03$ and 0.91 eV on site-1 (Table S4) and site-3 (Table S5), respectively. The addition of the first hydrogen atom is uphill, as high as 1.22 and 1.36 eV, respectively, which is also the maximum energy request for the whole reactions, suggesting that this step is the determining step in the reduction to form ammonia on the β_{12}-sheet (Table S7). The successive five steps result in the full scission of the N—N bonds and the release of two NH_3 molecules, most of them being exothermic. The nearly linear variation of N—N bond lengths suggested that the stretching effect of adsorption is comparable to that of the hydrogenation (see the Supporting Information), indicating the considerable ability of the boron sheet to activate nitrogen. In terms of reaction paths, the distal mechanism is slightly favorable, which needs only a small amount of energy input to release the second NH_3. As to the active sites, site-1 exhibits a relatively higher activity toward ammonia formation, with $\Delta G_{max} = 1.22$ eV, whereas 1.36 eV is requested for site-3. Overall, the two boron sheets show the potential capacity to activate N_2 and convert it into NH_3 under ambient conditions, with site-2 in α-sheet being the best candidate with $\Delta G_{max} = 0.77$ eV.

As we know, the hydrogen evolution reaction (HER) is a major competing reaction for NRR in the electrochemical reaction. Thus, the free energy change for the adsorption of single hydrogen was calculated on different active sites of two boron sheets, according to which the maximum free energy of HER has been given in Table 1 with or without an applied

Table 1. Calculated Free Energy of HER and ΔG_{max} for NRR with and without an Applied Voltage $(U)^a$

		α-sheet		β_{12}-sheet	
		site 1	site 2	site 1	site 3
free energy of HER (eV)	$U = 0$	0.03	−0.61	0.11	0.02
	$U = U_A$	−0.74	−1.38	−1.11	−1.20
ΔG_{max} of NRR (eV)	$U = 0$	1.17	0.77	1.22	1.36
	$U = U_A$	0.40	0.00	0.00	0.14

^{a}For α- and β_{12}-sheets, the minimum applied voltage (U_A) is −0.77 and −1.22 V, respectively, as determined by the calculated ΔG_{max} (Figure 4).

potential U. The optimum value of U is determined by the calculated ΔG_{max}(NRR) in Figure 4, as 0.77 and 1.22 V for α- and β_{12}-sheets, respectively. When $U = 0$ V, HER is favorable on both α- and β_{12}-sheets, with free energy as low as 0.03 and 0.11 eV, respectively. However, when the minimum potential U has been applied toward NRR, the step for the formation of H* is so favorable that the release of H_2 from H* becomes difficult, with a large free energy. In this case, NRR becomes favorable, and it is worth to note site 2 of the α-sheet is the

most active site for NRR, and the worst site for HER. Therefore, site 2 of the α-sheet can still hold the NRR activity.

To further understand the catalytic property of 2D boron sheets, the Bader charge has been calculated, as shown in Figure 5. For the α-sheet, electron transfer associated with N_2
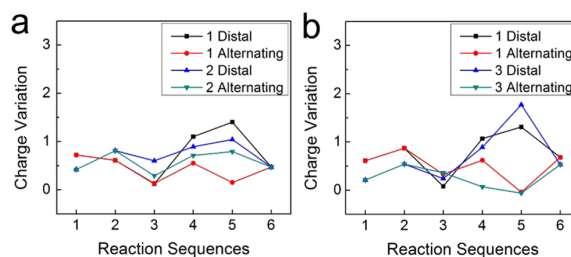
Figure 5. Charge variation of the adsorbed N_xH_y species for the (a) α-sheet and (b) β_{12}-sheet. The numbers (1, 2, 3) in the insets indicate active sites. Reaction sequences are defined in Figure 3.

adsorption is 0.72e and 0.42e from site-1 and site-2, respectively. It is very interesting that N_2 adsorption is achieved through electron transfer from boron to N_2 (empty π^* state). Such a charge transfer is essential for N_2 fixation, but apparently destabilizes boron sheets as indicated by the positive ΔG, which is not surprising because a freestanding boron nanosheet is highly electron deficient. Experimentally, metal substrates have been widely employed in boron synthesis, which can inject electrons to the boron sheet, which can remarkably stabilize the B-sheet and may be helpful to balance this effect, as confirmed below. For the following hydrogenation steps, calculated charges located on N_xH_y species are shown in Figure 5a, which vividly shows the obvious charge fluctuation for the intermediate species. Therefore, the boron sheet serves as an electron reservoir. Given that the initial N_2 adsorption and first H-adding are the most energy-consuming steps, proper functionalization to improve boron-to-N_2 electron transfer should be helpful. Similar results have been found for the β_{12}-sheet, including net electron transfer from boron to N_2 (0.61e for site-1 and 0.21e for site-3), as shown in Figure 5b. For the subsequent reduction process, almost all NH_x species gain electrons from the boron sheet with a similar trend, except the fifth step, during which about 0.05e has been transferred from $NH_2NH_2^*$ to the boron sheet in the two sites during the alternating pathways.

To further evaluate the potential of the boron sheet as an electrocatalyst for the conversion of N_2 to NH_3, the catalytic performance of site-1 of the β_{12}-sheet boron deposited on Ag and Cu surfaces was investigated in this work, which is also the real case so far obtained in the lab.[17,39] In this part, we add the influence of an applied electric potential U. At $U = 0.00$ V, the calculated ΔG for N_2 adsorption on boron mediated by Ag(111) and Cu(111) reduces from 1.03 to 0.91 and 0.66 eV, respectively, confirming that a metal substrate can improve the NRR performance. Moreover, the calculated ΔG for the first hydrogenation $N_2^* \rightarrow N_2H^*$ decreases from 1.22 to 0.93 and 0.94 eV surface, respectively. By applying an electric potential that raises the free energy of the electrons in the metal electrode and hence drives protons from the electrolyte toward the metal surface, the uphill reaction steps can be eliminated. There, the potential of $U = -0.93$ or -0.94 V suffices to make the reaction downhill in free energy at each step, as shown in

Figure 6. Therefore, metal substrates introduced during the synthesis of boron sheets are beneficial for NRR. Based on the
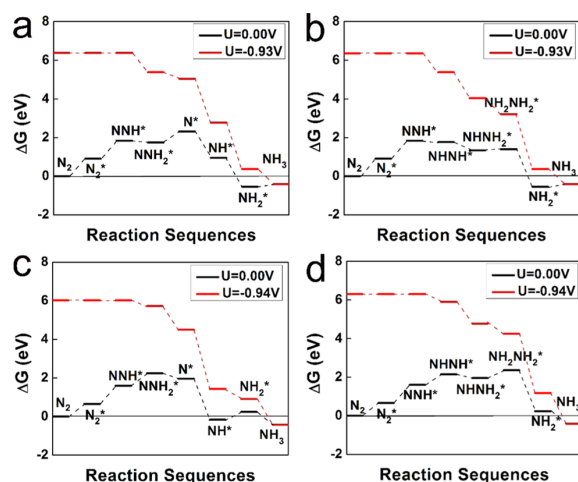
Figure 6. Free energy for the associative mechanism at a step on the β_{12}-sheet deposited on Ag(111) and Cu(111) substrates at zero and applied potential: (a) distal path of Ag, (b) alternating path of Ag, (d) distal path of Cu, and (d) alternating path of Cu (d).

above calculated data, it is expected that metal-mediated α-sheets, as synthesized readily in the lab, can offer better performance.

CONCLUSIONS

In summary, we explored the possibility to synthesize ammonia from nitrogen using a 2D boron monolayer by performing DFT calculations at room temperature. N_2 adsorption is achieved through electron transfer from boron to N_2, requesting additional energy to achieve stable adsorption. After initial N_2 adsorption, the first reduction step has been identified as the rate-determining step. Among these active sites, site-2 of the α-sheet monolayer offers the best performance, with ΔG_{max} = 0.77 eV. Although site-2 of both sheets have the same coordination number, active site-2 of the α-sheet shows an overwhelming performance compared with the β_{12}-sheet. In addition, metal substrates can inject electrons to the boron sheet and promote its catalysis performance. Therefore, it is expected that a boron sheet as an NRR catalyst is highly promising with the substrate and boron sheets being further optimized.

ASSOCIATED CONTENT

ⓈSupporting Information

The Supporting Information is available free of charge on the ACS Publications website at DOI: 10.1021/acs.jpcc.8b10021.

Computational details; optimized structures (PDF)

AUTHOR INFORMATION

Corresponding Author

*E-mail: chenghuasun@swin.edu.au.

ORCID ⦿

Jie Zhang: 0000-0003-2493-5209

Chenghua Sun: 0000-0001-7654-669X

Notes

REFERENCES

(1) Montoya, J. H.; Tsai, C.; Vojvodic, A.; Nørskov, J. K. The Challenge of Electrochemical Ammonia Synthesis: A New Perspective on the Role of Nitrogen Scaling Relations. *ChemSusChem* **2015**, *8*, 2180−2186.

(2) Ertl, G. Surface Science and Catalysis—Studies on the Mechanism of Ammonia Synthesis: The P. H. Emmett Award Address. *Catal. Rev.* **1980**, *21*, 201−223.

(3) Liu, H. Ammonia Synthesis Catalyst 100 Years: Practice, Enlightenment and Challenge. *Chin. J. Catal.* **2014**, *35*, 1619−1640.

(4) Garagounis, I.; Kyriakou, V.; Skodra, A.; Vasileiou, E.; Stoukides, M. Electrochemical Synthesis of Ammonia in Solid Electrolyte Cells. *Front. Energy Res.* **2014**, *2*, No. 1.

(5) Kugler, K.; Ohs, B.; Scholz, M.; Wessling, M. Towards a Carbon Independent and CO_2-Free Electrochemical Membrane Process for NH_3 Synthesis. *Phys. Chem. Chem. Phys.* **2014**, *16*, 6129−6138.

(6) Abghoui, Y.; Garden, A. L.; Hlynsson, V. F.; Bjorgvinsdottir, S.; Olafsdottir, H.; Skulason, E. Enabling Electrochemical Reduction of Nitrogen to Ammonia at Ambient Conditions through Rational Catalyst Design. *Phys. Chem. Chem. Phys.* **2015**, *17*, 4909−4918.

(7) Studt, F.; Tuczek, F. Energetics and Mechanism of a Room-Temperature Catalytic Process for Ammonia Synthesis (Schrock Cycle): Comparison with Biological Nitrogen Fixation. *Angew. Chem., Int. Ed.* **2005**, *44*, 5639−5642.

(8) Amar, I. A.; Lan, R.; Petit, C. T. G.; Tao, S. Solid-State Electrochemical Synthesis of Ammonia: A Review. *J. Solid State Electrochem.* **2011**, *15*, 1845−1860.

(9) Amar, I. A.; Lan, R.; Humphreys, J.; Tao, S. Electrochemical Synthesis of Ammonia from Wet Nitrogen Via a Dual-Chamber Reactor Using $La_{0.6}Sr_{0.4}Co_{0.2}Fe_{0.8}O_{3−\Delta}$-$Ce_{0.8}gd_{0.18}Ca_{0.02}O_{2−\Delta}$ Composite Cathode. *Catal. Today* **2017**, *286*, 51−56.

(10) Chen, S.; Perathoner, S.; Ampelli, C.; Mebrahtu, C.; Su, D.; Centi, G. Electrocatalytic Synthesis of Ammonia at Room Temperature and Atmospheric Pressure from Water and Nitrogen on a Carbon-Nanotube-Based Electrocatalyst. *Angew. Chem., Int. Ed.* **2017**, *56*, 2699−2703.

(11) Greeley, J.; Mavrikakis, M. Alloy Catalysts Designed from First Principles. *Nat. Mater.* **2004**, *3*, 810−815.

(12) Freund, H.-J.; Pacchioni, G. Oxide Ultra-Thin Films on Metals: New Materials for the Design of Supported Metal Catalysts. *Chem. Soc. Rev.* **2008**, *37*, 2224−2242.

(13) Howalt, J. G.; Bligaard, T.; Rossmeisl, J.; Vegge, T. DFT Based Study of Transition Metal Nano-Clusters for Electrochemical NH_3 Production. *Phys. Chem. Chem. Phys.* **2013**, *15*, 7785−7795.

(14) Naguib, M.; Mashtalir, O.; Carle, J.; Presser, V.; Lu, J.; Hultman, L.; Gogotsi, Y.; Barsoum, M. W. Two-Dimensional Transition Metal Carbides. *ACS Nano* **2012**, *6*, 1322−1331.

(15) Naguib, M.; Halim, J.; Lu, J.; Cook, K. M.; Hultman, L.; Gogotsi, Y.; Barsoum, M. W. New Two-Dimensional Niobium and Vanadium Carbides as Promising Materials for Li-Ion Batteries. *J. Am. Chem. Soc.* **2013**, *135*, 15966−15969.

(16) Azofra, L. M.; Li, N.; MacFarlane, D. R.; Sun, C. Promising Prospects for 2D d^2-d^4 M_3C_2 Transition Metal Carbides (Mxenes) in N_2 Capture and Conversion into Ammonia. *Energy Environ. Sci.* **2016**, *9*, 2545−2549.

(17) Li, X.-F.; Li, Q.-K.; Cheng, J.; Liu, L.; Yan, Q.; Wu, Y.; Zhang, X.-H.; Wang, Z.-Y.; Qiu, Q.; Luo, Y. Conversion of Dinitrogen to

Ammonia by FeN$_3$-Embedded Graphene. *J. Am. Chem. Soc.* **2016**, *138*, 8706−8709.

(18) Zhao, J.; Chen, Z. Single Mo Atom Supported on Defective Boron Nitride Monolayer as an Efficient Electrocatalyst for Nitrogen Fixation: A Computational Study. *J. Am. Chem. Soc.* **2017**, *139*, 12480−12487.

(19) Tian, Y.-H.; Pierpont, A. W.; Batista, E. R. How Does Nishibayashi's Molybdenum Complex Catalyze Dinitrogen Reduction to Ammonia? *Inorg. Chem.* **2014**, *53*, 4177−4183.

(20) Tian, Y.-H.; Hu, S.; Sheng, X.; Duan, Y.; Jakowski, J.; Sumpter, B. G.; Huang, J. Non-Transition-Metal Catalytic System for N$_2$ Reduction to NH$_3$: A Density Functional Theory Study of Al-Doped Graphene. *J. Phys. Chem. Lett.* **2018**, *9*, 570−576.

(21) Miguel, A. L.; Chenghua, S.; Luigi, C.; Morse, R. Feasibility of N$_2$ Binding and Reduction to Ammonia on Fe-Deposited MoS$_2$ 2D Sheets: A DFT Study. *Chem. - Eur. J.* **2017**, *23*, 8275−8279.

(22) Li, Q.; He, L.; Sun, C.; Zhang, X. Computational Study of MoN$_2$ Monolayer as Electrochemical Catalysts for Nitrogen Reduction. *J. Phys. Chem. C* **2017**, *121*, 27563−27568.

(23) Légaré, M.-A.; Bélanger-Chabot, G.; Dewhurst, R. D.; Welz, E.; Krummenacher, I.; Engels, B.; Braunschweig, H. Nitrogen Fixation and Reduction at Boron. *Science* **2018**, *359*, 896−900.

(24) Légaré, M.-A.; Courtemanche, M.-A.; Rochette, É.; Fontaine, F.-G. Metal-Free Catalytic C-H Bond Activation and Borylation of Heteroarenes. *Science* **2015**, *349*, 513−516.

(25) Ma, F.; Jiao, Y.; Gao, G.; Gu, Y.; Bilic, A.; Chen, Z.; Du, A. Graphene-Like Two-Dimensional Ionic Boron with Double Dirac Cones at Ambient Condition. *Nano Lett.* **2016**, *16*, 3022−3028.

(26) Liu, Y.; Penev, E. S.; Yakobson, B. I. Probing the Synthesis of Two-Dimensional Boron by First-Principles Computations. *Angew. Chem.* **2013**, *125*, 3238−3241.

(27) Wu, X.; Dai, J.; Zhao, Y.; Zhuo, Z.; Yang, J.; Zeng, X. C. Two-Dimensional Boron Monolayer Sheets. *ACS Nano* **2012**, *6*, 7443−7453.

(28) Tang, H.; Ismail-Beigi, S. Novel Precursors for Boron Nanotubes: The Competition of Two-Center and Three-Center Bonding in Boron Sheets. *Phys. Rev. Lett.* **2007**, *99*, No. 115501.

(29) Gonzalez Szwacki, N.; Sadrzadeh, A.; Yakobson, B. I. B80 Fullerene: An Ab Initio Prediction of Geometry, Stability, and Electronic Structure. *Phys. Rev. Lett.* **2007**, *98*, No. 166804.

(30) Penev, E. S.; Bhowmick, S.; Sadrzadeh, A.; Yakobson, B. I. Polymorphism of Two-Dimensional Boron. *Nano Lett.* **2012**, *12*, 2441−2445.

(31) Oganov, A. R.; Chen, J.; Gatti, C.; Ma, Y.; Ma, Y.; Glass, C. W.; Liu, Z.; Yu, T.; Kurakevych, O. O.; Solozhenko, V. L. Ionic High-Pressure Form of Elemental Boron. *Nature* **2009**, *457*, 863−867.

(32) Feng, B.; Zhang, J.; Zhong, Q.; Li, W.; Li, S.; Li, H.; Cheng, P.; Meng, S.; Chen, L.; Wu, K. Experimental Realization of Two-Dimensional Boron Sheets. *Nat. Chem.* **2016**, *8*, 563−568.

(33) Hammer, B.; Hansen, L. B.; Nørskov, J. K. Improved Adsorption Energetics within Density-Functional Theory Using Revised Perdew-Burke-Ernzerhof Functionals. *Phys. Rev. B* **1999**, *59*, 7413−7421.

(34) Blöchl, P. E. Projector Augmented-Wave Method. *Phys. Rev. B* **1994**, *50*, 17953−17979.

(35) Kresse, G.; Hafner, J. Ab initio molecular dynamics for liquid metals. *Phys. Rev. B* **1993**, *47*, 558−561.

(36) Kresse, G.; Hafner, J. Ab initio molecular-dynamics simulation of the liquid-metal—amorphous-semiconductor transition in germanium. *Phys. Rev. B* **1994**, *49*, 14251−14269.

(37) Grimme, S.; Antony, J.; Ehrlich, S.; Krieg, H. A Consistent and Accurate Ab Initio Parametrization of Density Functional Dispersion Correction (DFT-D) for the 94 Elements H-Pu. *J. Chem. Phys.* **2010**, *132*, No. 154104.

(38) Liu, H.; Gao, J.; Zhao, J. From Boron Cluster to Two-Dimensional Boron Sheet on Cu(111) Surface: Growth Mechanism and Hole Formation. *Sci. Rep.* **2013**, *3*, No. 3238.

(39) Anderson, J. S.; Cutsail, G. E.; Rittle, J.; Connor, B. A.; Gunderson, W. A.; Zhang, L.; Hoffman, B. M.; Peters, J. C.

Characterization of an Fe≡N-NH$_2$ Intermediate Relevant to Catalytic N$_2$ Reduction to NH$_3$. *J. Am. Chem. Soc.* **2015**, *137*, 7803−7809.

25273

J. Phys. Chem. C 2018, 122, 25268−25273

150

3.2 Supporting Information

Theoretical Evaluation of Possible 2D Boron Monolayer in N$_2$ Electrochemical Conversion into Ammonia

Chuangwei Liu,[a,b] Qinye Li,[c] Jie Zhang,[a] Yonggang Jin,[d] Douglas R. MacFarlane,[a] Chenghua Sun[*,b,e]

[a] School of Chemistry, Faculty of Science, Monash University, Clayton, Victoria 3800, Australia

[b] Science & Technology Innovation Institute, Dongguan University of Technology, Dongguan, China

[c] School of Chemical Engineering, Monash University, Clayton, Victoria 3800, Australia

[d] CSIRO Energy, 1 Technology Court, Pullenvale, Queensland 4069, Australia

[e] Department of Chemistry and Biotechnology, Faculty of Science, Engineering & Technology, Swinburne University of Technology, Hawthorn, Victoria 3122, Australia

Email: chenghuasun@swin.edu.au

Table S1. The Adsorption Energies (eV), N-N and B-N bond length (Å) of the adsorbed N_2^* on the different active sites of two boron sheets.

Active site	N_2 Adsorption Energies (eV)	Distance of B-N (Å)	Distance of N-N (Å)
Site 1 of α sheet	1.17	1.52	1.12
Site 1 of α sheet	0.63	1.47	1.13
Tilt end-on of α sheet	2.89	1.45	1.45
Site 1 of $β_{12}$ sheet	1.03	1.51	1.12
Site 2 of $β_{12}$ sheet	0.54	3.49	1.10
Site 3 of $β_{12}$ sheet	0.91	1.49	1.12
Tilt end-on of $β_{12}$ sheet	3.29	1.51	1.50

Table S2. The N-N and B-N bond length (Å) of the adsorbed N_xH_y species on the site 1 of α sheet by two reaction pathways (distal and alternating pathways). 1 represents the adsorbed N_2^*.

Reaction Step		1	2	3	4	5	6
Distal	N-N	1.12	1.25	1.30	3.57		
	B-N	1.52	1.55	1.49	1.47	1.52	1.49
Alternating	N-N	1.12	1.25	1.31	1.43	1.49	3.59
	B-N	1.52	1.55	1.52	1.50	1.59	1.51

Table S3. The N-N and B-N bond length (Å) of the adsorbed N_xH_y species on the site 2 of α sheet by two reaction pathways (distal and alternating pathways). 1 represents the adsorbed N_2^*.

Reaction Step	Bond	1	2	3	4	5	6
Distal	N-N	1.13	1.26	1.31	3.63		
	B-N	1.47	1.50	1.46	1.51	1.47	1.45
Alternating	N-N	1.13	1.26	1.31	1.42	1.47	3.43
	B-N	1.47	1.50	1.50	1.45	1.64	1.46

Table S4. The N-N and B-N bond length (Å) of the adsorbed N_xH_y species on the site 1 of $β_{12}$ sheet by two reaction pathways (distal and alternating pathways). 1 represents the adsorbed N_2^*.

Reaction Step	Bond	1	2	3	4	5	6
Distal	N-N	1.12	1.25	1.29	3.42		
	B-N	1.51	1.56	1.5	1.49	1.50	1.57
Alternating	N-N	1.12	1.25	1.48	1.45	1.44	3.58
	B-N	1.51	1.56	1.45	1.51	1.55	1.61

Table S5. The N-N and B-N bond length (Å) of the adsorbed N_xH_y species on the site 3 of β_{12} sheet by two reaction pathways (distal and alternating pathways). 1 represents the adsorbed N_2^*.

Reaction Step	Bond	1	2	3	4	5	6
Distal	N-N	1.12	1.25	1.28	3.43		
	B-N	1.49	1.56	1.49	1.38	1.50	1.51
Alternating	N-N	1.12	1.25	1.28	1.41	1.45	3.61
	B-N	1.49	1.56	1.54	1.52	1.53	1.57

Table S6. The Gibes free energies (ΔG, eV) in each step of distal, alternating reaction pathway on two active sites of α sheet. 1 represents the adsorbed N_2^*.

Reaction Steps	1	2	3	4	5	6	7
Distal of site 1	1.17	0.88	-0.12	-0.86	-1.03	-0.38	-0.09
Alternating of site 1	1.17	0.88	-0.06	-0.42	-0.15	-1.75	-0.09
Distal of site 2	0.63	0.77	-0.16	-0.84	-0.23	-1.30	0.72
Alternating of site 1	0.63	0.77	0.01	-0.612	0.34	-2.27	0.72

Table S7. The Gibes free energies (ΔG, eV) in each step of distal, alternating reaction pathway on two active sites of β_{12} sheet. 1 represents the adsorbed N_2^*.

Reaction Steps	1	2	3	4	5	6	7
Distal of site 1	1.03	1.22	-0.19	-0.60	-1.39	-0.73	0.24
Alternating of site 1	1.03	1.22	-0.39	-0.74	0.31	-2.09	0.24
Distal of site 3	0.91	1.36	-0.36	-0.94	-0.89	-0.11	-0.39
Alternating of site 3	0.91	1.36	-0.55	0.04	0.31	-2.10	-0.39

Table S8. The atomic coordinates of all the optimized systems for electronic structure calculations on the site 2 of α sheet.

Clear α boron sheet

B1	0.334418	0.335085	0.507946
B2	0.166579	0.001397	0.499580
B3	0.000588	0.167689	0.492333
B4	0.167036	0.167672	0.492363
B5	0.334704	0.001409	0.499965
B6	0.000616	0.335070	0.508146
B7	0.334505	0.168973	0.482122
B8	0.166957	0.333942	0.515940
B9	0.834422	0.335145	0.508171
B10	0.666633	0.001377	0.499899
B11	0.500598	0.167654	0.492839
B12	0.667005	0.167673	0.492814
B13	0.834747	0.001371	0.499503
B14	0.500661	0.335159	0.507977
B15	0.834409	0.168967	0.482437
B16	0.666895	0.333881	0.517123
B17	0.334442	0.835119	0.490066
B18	0.166596	0.501397	0.498217
B19	0.000633	0.667686	0.505816
B20	0.167003	0.667633	0.505414
B21	0.334720	0.501398	0.497995
B22	0.000628	0.835062	0.490035
B23	0.334474	0.668956	0.516008
B24	0.166935	0.833919	0.481705
B25	0.834385	0.835074	0.489989
B26	0.666594	0.501326	0.498410
B27	0.500578	0.667619	0.505144
B28	0.666976	0.667671	0.505551
B29	0.834700	0.501330	0.498623
B30	0.500626	0.835133	0.490022
B31	0.834399	0.668898	0.515298
B32	0.666923	0.833912	0.479771

N$_2$*

B1	0.333895	0.335258	0.491193

B2	0.165997	0.000658	0.498279
B3	0.000650	0.167436	0.513948
B4	0.166041	0.166009	0.509567
B5	0.334733	0.999719	0.498635
B6	0.002950	0.335793	0.495104
B7	0.333257	0.166497	0.518111
B8	0.170585	0.335199	0.477198
B9	0.834502	0.333749	0.484122
B10	0.665599	0.999879	0.498596
B11	0.500201	0.167059	0.499970
B12	0.667304	0.167115	0.501007
B13	0.835304	0.000814	0.498928
B14	0.498904	0.333809	0.483525
B15	0.836442	0.169298	0.510189
B16	0.665854	0.332364	0.477852
B17	0.333456	0.833063	0.513391
B18	0.166860	0.500272	0.500703
B19	0.001050	0.666809	0.483409
B20	0.167426	0.664753	0.494484
B21	0.337220	0.500417	0.541148
B22	0.000488	0.833454	0.500338
B23	0.335679	0.665347	0.476710
B24	0.167368	0.831207	0.509953
B25	0.833342	0.833448	0.499538
B26	0.666558	0.500252	0.488743
B27	0.498878	0.665262	0.490630
B28	0.665319	0.666716	0.482999
B29	0.834992	0.500255	0.485254
B30	0.500304	0.834538	0.509289
B31	0.833708	0.668120	0.477798
B32	0.666949	0.833970	0.517959
N1	0.342978	0.501175	0.657728
N2	0.354166	0.502276	0.743704

N$_2$H*

B1	0.332802	0.332548	0.505141
B2	0.162993	0.996971	0.496271
B3	0.997011	0.163130	0.510811
B4	0.163890	0.163656	0.499999
B5	0.331859	0.995847	0.499718
B6	0.998140	0.332104	0.499545
B7	0.329065	0.161285	0.518853
B8	0.168278	0.334485	0.492078
B9	0.831346	0.329870	0.485027
B10	0.662526	0.996029	0.497750
B11	0.495663	0.161850	0.488263
B12	0.663030	0.162112	0.496294
B13	0.832364	0.996945	0.499180
B14	0.495457	0.330761	0.490495
B15	0.833059	0.163448	0.483784
B16	0.662689	0.328893	0.491694
B17	0.330287	0.828941	0.510439
B18	0.162214	0.496184	0.504902
B19	0.997623	0.662693	0.485128
B20	0.162480	0.660384	0.499146

B21	0.332591	0.497631	0.555815
B22	0.997194	0.830785	0.495663
B23	0.330706	0.657820	0.489993
B24	0.165562	0.828557	0.484885
B25	0.829919	0.830844	0.488252
B26	0.664039	0.496265	0.493614
B27	0.496627	0.660760	0.498522
B28	0.660841	0.661956	0.489858
B29	0.830729	0.496307	0.478929
B30	0.497162	0.830063	0.498341
B31	0.829505	0.663799	0.488035
B32	0.663150	0.830812	0.519162
N1	0.330310	0.491859	0.674619
N2	0.443027	0.591503	0.723627
H1	0.420210	0.568414	0.801021

N_2H_2*

B1	0.343490	0.167650	0.518788
B2	0.183004	0.339295	0.486735
B3	0.345828	0.337941	0.505946
B4	0.176377	0.001515	0.503080
B5	0.011020	0.169356	0.511565
B6	0.176479	0.167651	0.508317
B7	0.345611	0.000780	0.502488
B8	0.012732	0.337989	0.495646
B9	0.846530	0.169429	0.487960
B10	0.675844	0.334649	0.481899
B11	0.845189	0.335656	0.478409
B12	0.676368	0.001278	0.490934
B13	0.509535	0.167682	0.489023
B14	0.676986	0.167748	0.489648
B15	0.846317	0.002484	0.496228
B16	0.509021	0.335604	0.486957
B17	0.344510	0.663932	0.488917
B18	0.179885	0.834803	0.485796
B19	0.343575	0.834411	0.512891
B20	0.177307	0.501952	0.501189
B21	0.011250	0.667884	0.482257
B22	0.175793	0.665642	0.501345
B23	0.347726	0.502548	0.557818
B24	0.010992	0.835488	0.494827
B25	0.843570	0.668509	0.491168
B26	0.677926	0.836192	0.513696
B27	0.844118	0.836023	0.485439
B28	0.676517	0.501949	0.480855
B29	0.510239	0.665942	0.505012
B30	0.675467	0.667940	0.483587
B31	0.844739	0.501978	0.470470
B32	0.510469	0.835033	0.501425
N1	0.359098	0.496756	0.671889
N2	0.245169	0.483372	0.726709
H1	0.249264	0.473929	0.804685
H2	0.150234	0.479642	0.692295

158

N*

B1	0.336450	0.169175	0.512151
B2	0.157834	0.310667	0.467371
B3	0.330620	0.336293	0.502119
B4	0.167511	0.997551	0.504005
B5	0.000939	0.161014	0.516121
B6	0.165068	0.161007	0.516125
B7	0.337560	0.002542	0.504122
B8	0.010709	0.336311	0.502211
B9	0.837747	0.169185	0.512258
B10	0.669298	0.333606	0.475357
B11	0.840770	0.334341	0.475572
B12	0.669991	0.002568	0.504138
B13	0.501975	0.168315	0.491887
B14	0.671364	0.168306	0.491862
B15	0.835044	0.997575	0.504005
B16	0.498582	0.334316	0.475510
B17	0.347291	0.689564	0.467892
B18	0.168590	0.830908	0.512546
B19	0.339993	0.839139	0.516772
B20	0.148289	0.499896	0.568232
B21	0.006480	0.665758	0.475979
B22	0.174468	0.663817	0.502628
B23	0.356745	0.499876	0.568176
B24	0.003061	0.831739	0.492332
B25	0.835751	0.666503	0.475433
B26	0.667330	0.830920	0.512441
B27	0.833710	0.831745	0.492360
B28	0.666742	0.500074	0.469018
B29	0.494391	0.663844	0.502571
B30	0.664319	0.665772	0.475935
B31	0.838334	0.500064	0.469097
B32	0.504155	0.839125	0.516814
N1	0.252447	0.499663	0.636951

NH*

B1	0.329316	0.160573	0.501194
B2	0.161544	0.328612	0.511946
B3	0.328841	0.328402	0.500671
B4	0.162021	0.995927	0.473530
B5	0.993969	0.158674	0.518930
B6	0.162001	0.161732	0.489731
B7	0.331106	0.994976	0.473642
B8	0.994456	0.330064	0.514314
B9	0.830451	0.160361	0.484945
B10	0.661819	0.329002	0.490448
B11	0.829346	0.328885	0.492837
B12	0.660744	0.996412	0.514579
B13	0.495259	0.161344	0.470378
B14	0.661933	0.161477	0.492867
B15	0.832191	0.996949	0.519205
B16	0.494509	0.329679	0.480297
B17	0.331084	0.659800	0.498163
B18	0.162343	0.828478	0.475696

B19	0.330892	0.828447	0.497850
B20	0.159531	0.494366	0.519682
B21	0.995876	0.659740	0.473977
B22	0.162436	0.659970	0.497875
B23	0.328402	0.489306	0.556027
B24	0.994884	0.828791	0.473918
B25	0.830255	0.661537	0.501472
B26	0.662183	0.829311	0.512442
B27	0.829092	0.828864	0.490257
B28	0.661179	0.496376	0.480588
B29	0.501330	0.662319	0.556359
B30	0.662434	0.662012	0.501196
B31	0.829501	0.495624	0.470634
B32	0.496434	0.831316	0.519984
N1	0.426529	0.563571	0.650175
H1	0.382190	0.607224	0.700922

NH$_2$*

B1	0.331083	0.163693	0.514023
B2	0.171332	0.337653	0.490767
B3	0.335182	0.335562	0.506465
B4	0.165743	0.999593	0.489891
B5	0.999769	0.166013	0.505136
B6	0.166892	0.167020	0.494264
B7	0.334196	0.998517	0.495253
B8	0.000282	0.334938	0.496978
B9	0.835694	0.166580	0.477022
B10	0.665233	0.331828	0.491154
B11	0.833798	0.332896	0.481281
B12	0.665321	0.999373	0.493598
B13	0.498047	0.164900	0.483861
B14	0.665269	0.164829	0.490472
B15	0.835054	0.000080	0.494698
B16	0.497932	0.333925	0.489845
B17	0.332744	0.658728	0.493435
B18	0.168842	0.831346	0.476463
B19	0.332918	0.831880	0.505072
B20	0.165090	0.498509	0.502150
B21	0.000274	0.665272	0.482006
B22	0.164872	0.663153	0.495705
B23	0.331665	0.497970	0.564755
B24	0.000061	0.833985	0.488815
B25	0.832510	0.666725	0.486652
B26	0.666203	0.834262	0.512530
B27	0.832534	0.833558	0.482943
B28	0.666369	0.499079	0.490658
B29	0.499385	0.663291	0.505326
B30	0.663458	0.664510	0.490550
B31	0.833010	0.499133	0.475193
B32	0.499272	0.832269	0.495917
N1	0.329393	0.493658	0.679228
H1	0.418588	0.492944	0.715209
H2	0.300896	0.564376	0.715309

NHNH*

B1	0.337628	0.168452	0.514265
B2	0.175751	0.337789	0.475980
B3	0.338828	0.337262	0.490312
B4	0.170207	0.001585	0.499483
B5	0.005211	0.168956	0.505859
B6	0.170496	0.167240	0.505114
B7	0.339445	0.000698	0.498141
B8	0.007225	0.337182	0.485666
B9	0.840272	0.169788	0.499361
B10	0.669771	0.333339	0.472384
B11	0.838957	0.334593	0.473924
B12	0.670112	0.000806	0.487512
B13	0.503933	0.167609	0.491229
B14	0.671121	0.167435	0.488836
B15	0.839700	0.001996	0.490947
B16	0.502967	0.335098	0.479202
B17	0.338169	0.664390	0.480508
B18	0.172936	0.833364	0.500027
B19	0.338118	0.834107	0.512248
B20	0.171080	0.501297	0.498386
B21	0.005186	0.667593	0.483407
B22	0.170578	0.664981	0.496492
B23	0.339901	0.500371	0.544996
B24	0.004546	0.834444	0.498736
B25	0.838110	0.668917	0.478838
B26	0.671181	0.835022	0.511693
B27	0.838162	0.835428	0.492469
B28	0.670729	0.501210	0.482954
B29	0.503146	0.665281	0.494592
B30	0.669518	0.667478	0.481542
B31	0.839086	0.501274	0.477696
B32	0.504383	0.834988	0.502586
N1	0.350906	0.492400	0.661353
N2	0.245614	0.475056	0.726951
H1	0.448701	0.495682	0.687999
H2	0.282586	0.466629	0.798353

NHNH$_2$*

B1	0.343196	0.175989	0.511789
B2	0.185523	0.351549	0.489800
B3	0.347305	0.346804	0.500959
B4	0.177108	0.010697	0.494223
B5	0.012407	0.178566	0.501052
B6	0.177993	0.177592	0.494435
B7	0.346179	0.010057	0.493764
B8	0.013387	0.347304	0.489399
B9	0.848932	0.179052	0.473920
B10	0.676883	0.343402	0.481962
B11	0.846312	0.344988	0.478360
B12	0.677220	0.010374	0.485284
B13	0.510322	0.176594	0.482129
B14	0.677329	0.176282	0.486093
B15	0.846787	0.011632	0.491339

B16	0.510251	0.345767	0.488770
B17	0.344739	0.672474	0.485317
B18	0.180365	0.843778	0.475775
B19	0.344993	0.844089	0.502683
B20	0.178110	0.511946	0.495712
B21	0.012105	0.677557	0.480147
B22	0.176492	0.675276	0.494224
B23	0.345104	0.512881	0.558386
B24	0.011645	0.845359	0.490767
B25	0.844690	0.678523	0.489357
B26	0.678504	0.846724	0.511561
B27	0.844466	0.845416	0.481910
B28	0.678746	0.511143	0.489893
B29	0.510799	0.674505	0.501731
B30	0.675303	0.676348	0.486678
B31	0.845179	0.511162	0.474104
B32	0.511122	0.843364	0.490300
N1	0.348425	0.517656	0.673434
N2	0.214738	0.406297	0.726563
H1	0.448990	0.537771	0.706330
H2	0.205688	0.452998	0.794357
H3	0.222273	0.311053	0.742846

NH_2NH_2*

B1	0.319984	0.128601	0.488077
B2	0.154242	0.299692	0.469096
B3	0.320818	0.296902	0.490155
B4	0.153775	0.962715	0.504810
B5	0.987323	0.129505	0.463130
B6	0.152655	0.129061	0.486498
B7	0.320976	0.963454	0.522627
B8	0.987189	0.296849	0.485047
B9	0.820782	0.128504	0.498942
B10	0.652873	0.296959	0.519090
B11	0.821031	0.297285	0.495169
B12	0.653385	0.963233	0.487829
B13	0.486932	0.128296	0.516360
B14	0.652592	0.128356	0.496135
B15	0.820718	0.963010	0.465798
B16	0.486143	0.296754	0.503216
B17	0.338784	0.640012	0.549724
B18	0.155465	0.794424	0.500477
B19	0.324183	0.796379	0.498272
B20	0.158144	0.467841	0.481510
B21	0.987212	0.629297	0.522124
B22	0.157409	0.628328	0.500284
B23	0.323228	0.467062	0.467641
B24	0.986917	0.796566	0.506390
B25	0.821828	0.630443	0.487226
B26	0.651465	0.795889	0.468733
B27	0.820996	0.797504	0.489983
B28	0.652694	0.464064	0.504789
B29	0.484682	0.629115	0.461558
B30	0.652661	0.629510	0.492364
B31	0.821208	0.462824	0.515807

B32	0.483371	0.795094	0.476319
N1	0.391264	0.641294	0.671367
N2	0.415244	0.752944	0.753585
H1	0.494884	0.647314	0.665388
H2	0.318007	0.536963	0.705144
H3	0.492768	0.861989	0.725849
H4	0.315256	0.751917	0.763350

Chapter IV. Conversion of Dinitrogen to Ammonia on Ru Atoms Supported on Boron Sheets: A DFT Study

This Chapter demonstrates several transition metal atoms embedded on boron sheets as N_2 fixation electrocatalysts. Our results revealed that single ruthenium (Ru) atom doped boron sheets exhibited outstanding catalytic activity for ammonia synthesis at ambient conditions through the distal pathway with small activation barrier of 0.42 eV, which was less than half of that of the reported flat Ru (0001) catalysts (1.08 eV).
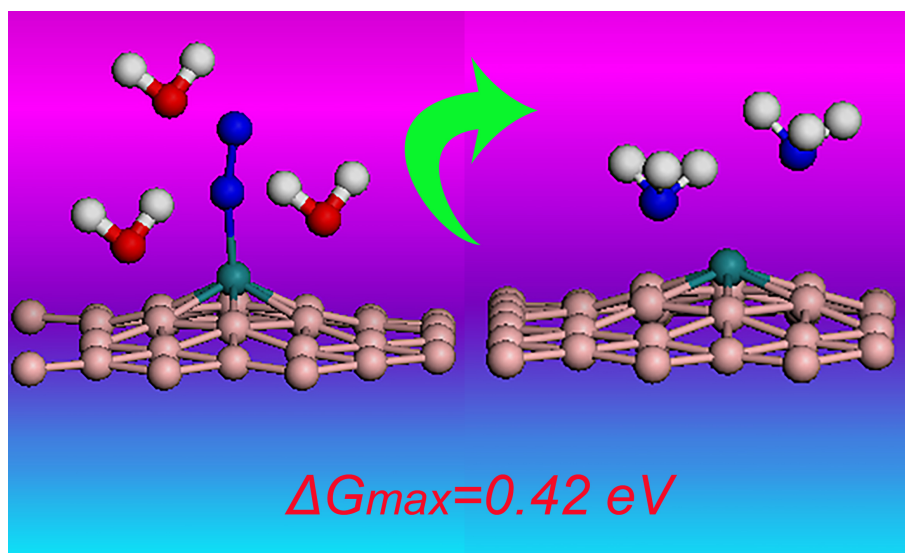
Scheme 4.1 Electrochemical nitrogen reduction reaction on 2D boron sheets.

This Chapter consists of two sections: (1) Published Paper, and (2) Supporting Information. The supporting information involves the computational details, the Gibbs free energies, geometries at different intermediates and cartesian coordinates.

4.1 Published Paper

PAPER

Check for updates

Conversion of dinitrogen to ammonia on Ru atoms supported on boron sheets: a DFT study†

Chuangwei Liu,[ab] Qinye Li,[c] Jie Zhang, [ID][b] Yonggang Jin,[d] Douglas R. MacFarlane [ID][b] and Chenghua Sun [ID] ⋆[ae]

The prevalent catalysts for natural and artificial N_2 fixation are transition-metal (TM) atoms. By using density functional theory computations, several TM atoms embedded on boron sheets as N_2 fixation electrocatalysts were investigated in this work. Our results revealed that single ruthenium (Ru) atom-doped boron sheets exhibited outstanding catalytic activity for ammonia synthesis at ambient conditions through the distal pathway with small activation barrier of 0.42 eV; this was less than half of that of the reported flat Ru (0001) catalysts (1.08 eV). These results highlight the value of boron as a substrate for the design of single-atom catalysts due to its unique electron-deficient features.

Introduction

Ammonia (NH_3) is one of the most important feedstocks in the modern chemical industry, where it is primarily used to produce fertilizers.[1] In addition, ammonia is also being considered as a significant green energy carrier due to its high energy density and carbon dioxide-free emission.[2] Many research studies have reported a number of catalytic systems for the conversion of dinitrogen (N_2) to NH_3.[3–5] At present, there are three typical ammonia synthesis methods: the Haber–Bosch process,[6] biological nitrogen fixation,[7,8] and electro/photo-electro chemical synthesis.[9,10] In the Haber–Bosch process, the bonds in N_2 and H_2 are often broken before reduction and passed over Fe or Mo-based catalysts to form ammonia.[11] As we know, the whole process is exothermic, but a significant energy input is required to achieve an acceptable reaction rate. Moreover, high pressure is also employed to shift the equilibrium in favor of ammonia synthesis.[12] After extensive efforts for decades, these drastic reaction conditions have improved remarkably, while the efficiency is still limited from 10% to 15%.[13]

Unlike the Haber–Bosch process, ammonia can be synthesized from solvated sequential protons and electrons and

atmospheric nitrogen on nitrogenases and molecular catalysts under ambient conditions.[7,14] Since the first transition metal-dinitrogen complex was discovered in 1965,[15] various transition metal-dinitrogen complexes have been successfully shown to be effective for ammonia production.[16–18] An understanding of biological N_2 fixation may further serve as the foundation for achieving a possible reaction pathway, but it remains an open challenge for scientists.[19] On the basis of many experimental and theoretical studies on the TM-cofactor,[20,21] three general pathways for ammonia synthesis from dinitrogen and hydrogen have been investigated: distal, alternating and enzyme mechanisms.[18,22] However, the poor stability and low yield of ammonia on the molecular catalysts greatly hamper the viability of large-scale industry application.

Greatly inspired by the proton and electron transfer in nitrogenases and molecular catalysts, a number of research groups have carried out studies on electrochemical technologies and catalysts.[23] For instance, ammonia was successfully synthesized in the solid electrolyte cell by the electrochemical method in 1998.[24] A great number of investigations have been devoted to the optimization of the electrochemical synthesis of ammonia.[25–27] When the solid-state proton conductor was employed, the yield of ammonia was as high as 78%.[24] Compared to the solid conductor, ionic liquids or molten salts have relatively better performance for ammonia synthesis under low current efficiencies at high temperatures.[28,29] Furthermore, numerous proton-conducting ceramic membranes have been studied and various materials have been tested as working electrodes in the past decades.[30,31] The synthesized ammonia can be easily separated from the mixture gas on the conductor membranes; therefore, the ceramic membranes have a considerably higher conversion rate of ammonia.[10] So far, most researchers have focused on improving the energy efficiency through smart design of novel catalysts, specifically reducing

[a]*Science & Technology Innovation Institute, Dongguan University of Technology, Dongguan, China*

[b]*School of Chemistry, Faculty of Science, Monash University, Clayton, Victoria 3800, Australia*

[c]*School of Chemical Engineering, Monash University, Clayton, Victoria 3800, Australia*

[d]*CSIRO Energy, 1 Technology Court, Pullenvale, Queensland 4069, Australia*

[e]*Department of Chemistry and Biotechnology, Faculty of Science, Engineering & Technology, Swinburne University of Technology, Hawthorn, Victoria 3122, Australia. E-mail: chenghuasun@swin.edu.au*

† Electronic supplementary information (ESI) available: Theoretical framework, analysis of other conceptual DFT properties, and additional figures. See DOI: 10.1039/c8ta08219g

This journal is © The Royal Society of Chemistry 2019

J. Mater. Chem. A, 2019, 7, 4771–4776 | **4771**

the overpotential and enhancing Faraday efficiency during the electrochemical process.

In recent years, single transition metal atoms doped on a substrate have been widely investigated in many works as ammonia synthesis electrocatalysts, and these include Fe–graphene,[32] Mo–BN,[22] Fe–TiO$_2$,[33] Fe–MoN$_2$,[34] and TiN$_4$–graphene.[35] In these heterogeneous catalysts, the single metal atoms can be distributed separately into the substrate, which can be viewed as single-atom catalysts.[36–39] The catalysts exhibit excellent activity performance due to the high ratio of low-coordinated metal atoms even with relatively low loading.[36,40] For high performance, both the catalyst (metal) and the substrate need to be optimized. In recent decades, a new 2D layered network structure, a boron sheet, was first predicted by Tang in 2007.[41] In the periodic table, boron is the neighbor of carbon with three valence electrons in the 2s and 2p orbitals; thus, it can exhibit sp^2 hybridization similar to carbon.[42] The structure of the boron sheet composed of a triangular and hexagonal motif has been identified to be more energetically stable than those of only triangular lattices or hexagonal lattices.[41,43,44] Therefore, it can be viewed as a hole-doped triangular lattice and may exhibit excellent chemistry applications. At present, more stable boron sheets were searched theoretically, leading to snub-sheet,[45] α-sheet,[41] β$_{12}$-sheet,[46] g$_{2/15}$-sheet,[47] struc-1/4, 1/8, 1/10, and 1/12-sheet structures.[48] Among these structures, α-sheet is confirmed to be the most stable one,[49] which can be viewed as being directly related to the synthesized boron nanotubes. Experimentally, the β$_{12}$ sheet is produced on a metal surface by direct evaporation of a pure boron source.[50] Until now, these boron sheets have been demonstrated as promising materials in superconductors,[51] hydrogen storage,[52] and oxygen evolution reaction.[53] Remarkably, the 2D sheets have the typically porous characteristic structure due to the "hexagonal hole", which can provide sufficient space to accept foreign atoms. The former work indicated that the adsorption of metal atoms is expected to occur more easily on a boron sheet than on graphene due to the electron deficiency of the boron structure.[54]

Herein, we reported a first-principles investigation of the work functions of transition metals anchored on boron sheets to find potential catalysts for N$_2$-to-NH$_3$ conversion under ambient conditions. From the primary density functional theory (DFT) search, Ru atoms supported on two boron sheets exhibited potential catalytic activity for N$_2$ reduction due to promising performance in N$_2$ adsorption, low energy barrier for N$_2$H* formation, and destabilization of NH$_2^*$ and NH$_3$ species. Thus, the mechanism of N$_2$ capture and electrochemical conversion into NH$_3$ catalysed by such Ru/B catalysts was studied in this work. The results indicated that the distal mechanism is the best reaction pathway for ammonia formation, for which the largest limiting energy barriers are only 0.42 and 0.44 eV on α-sheet and β$_{12}$-sheet, respectively.

Computational methods

In this study, all the computations of these structures and energies were based on the standard DFT by using Vienna ab initio Simulation Package (5.4.4 VASP).[55] The electron exchange correlation functional was treated through the generalized gradient approximation (GGA) with the revised Perdew–Burke–Ernzerhof (RPBE).[56] The 380 eV energy cut-off was adopted and the Brillouin zone was sampled with $3 \times 3 \times 1$ k-points using the Monkhorst–Pack scheme grid for geometry optimization and self-consistent calculations. The adatom-boron system is modelled using one transition metal adatom in a 2×2 boron supercell (alpha sheet contains 32 boron atoms) and 3×2 boron supercell (β$_{12}$-sheet contains 30 boron atoms). The atomic position was fully relaxed until the maximum force on each atom was less than -0.01 eV Å^{-1}. Thermal and zero point energy (ZPE) corrections were calculated over Γ points.[57] The van der Waals interaction has been considered using the DFT-D$_3$ scheme.[33]

Results and discussion

Initially, the geometrical configurations of the pristine α-sheet and β$_{12}$-sheet were designed following a previous method,[44] and the optimized atomic structures are shown in Fig. 1a and b. Both optimized structures maintained perfect monolayer structural characteristics, which was consistent with a previously reported result.[41] Boron atoms were aggregated and well-regulated to be triangular and hexagonal motifs by forming B–B bonds; the largest distances of boron and boron atoms of hexagonal holes were 3.36 Å and 2.92 Å in α-sheet and β$_{12}$-sheet, respectively.

Due to the special "hexagonal hole" structure and larger specific surface, the boron sheet as the substrate was expected to provide enough sites to accept extra metal atoms. In order to
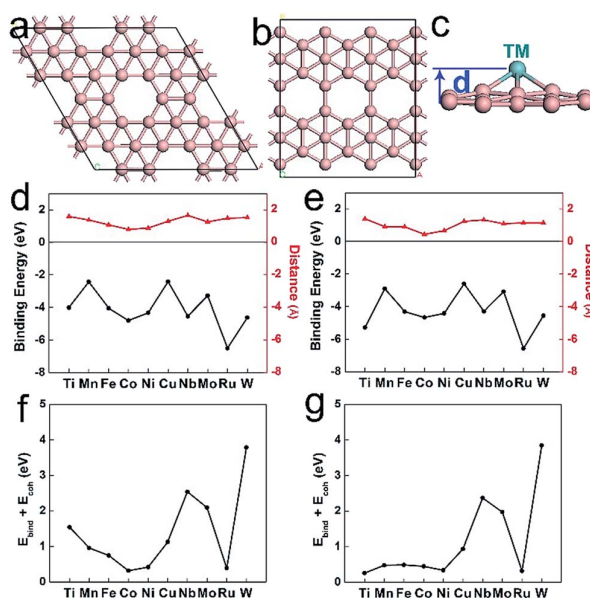

Fig. 1 DFT results of boron monolayer and TM adsorption: top view of (a) α-sheet and (b) β$_{12}$-sheet, (c) side view of TM-embedded boron sheet, binding energy and calculated distance of TM on the substrates (d) α-sheet and (e) β$_{12}$-sheet, calculated binding energy-cohesive energy ($E_b + E_c$) of two substrates (f) α-sheet and (g) β$_{12}$-sheet.

170

avoid the aggregation of doped atoms on the boron surface and provide enough activity during catalysis, the doped atoms should be separated far enough from each other. Therefore, the hexagon centers are excellent sites for adsorbing single metal atoms because the distances of the two holes are 5.04 Å and 2.92 Å, respectively. To investigate the interaction of the single metal and the boron sheet, a metal atom was placed on a boron hexagonal hole to construct computational models, and further optimizations were performed in this program. The stabilities and total energy of the single-atom were directly discussed in this study. To evaluate the relative stability of the metal–boron monolayer sheet, the binding energy (ΔE_b) was computed as follows:

$$\Delta E_b = E_{\text{metal-sheet}} - E_{\text{metal}} - E_{\text{sheet}}$$

E_{metal} and E_{sheet} are the energies of the pristine single metal atom and boron monolayer, respectively; $E_{\text{metal-sheet}}$ is the total energy of the single metal atom-adsorbed boron sheet. The binding energies and distance of TM and substrates of both sheets are plotted in Fig. 1d and e. According to the figures, the binding energy is always negative (Table S1 and S2†). The Cu atom is subject to the relatively weakest bonding energies with a short distance in both sheets, while the Ru atom experiences the strongest bonding with the relatively longest bond distance.

Numerous theoretical studies have shown that the electrochemical nitrogen reduction reaction (NRR) depends on the three key steps, namely N_2 capture, N_2H^* formation, and $deNH_2^*$ destabilization.[12,22] According to the above criterion, a series of TM atoms (Ti, Mn, Fe, Co, Ni, Cu, Nb, Mo, and Ru) doped on the two boron sheets were screened first. In the first step, the ΔG values for N_2 adsorption were employed as the indicator for N_2 capture. In Fig. 2a, the ΔG values of N_2 molecule chemisorption on anchored metals are negative except for Co, Ni, and Ru, but these values are very small (<0.1 eV), indicating that all these single-metals are good N_2-adsorbers (Fig. S1†). However, most of these anchored TM atoms were ruled out as NRR catalysts when we considered the formation of N_2H^* because a large energy input was required except for Ti, Nb, Mo and Ru (ΔG < 1.0 eV) (Fig. 2a). Finally, these four candidates were examined against the energy for the final release of NH_3 product. Our results indicated that Ti, Nb, and Mo anchored on α-sheet were not eligible for NRR because a large amount of energy is needed for this step: 1.17 eV, 1.31 eV, and 1.15 eV, respectively.

Following the above analytical method, the performance of TM atoms doped on a β_{12}-sheet was investigated, as shown in Fig. 2b (Fig. S2†). For N_2H^* formation, several metals (Ti, Mn, Fe, Co, Ni, Cu, and Nb) were eliminated because these need large amounts of energy (>1.0 eV). Mo and Ru exhibited appropriate catalytic performances for forming N_2H^* (0.97 and 0.44 eV, respectively); Mo was ruled out with a further consideration of NH_3 release (1.15 eV). Therefore, Ru was the only left species for NRR meeting the three screening criteria discussed above with a maximum energy requirement of ∼0.4 eV for these three steps; a full NRR process catalyzed by Ru-embedded boron sheets, labelled as Ru/B_α and Ru/B_β, will be further investigated below.

We started from the analysis of H-source for NRR process. In principle, a continuous H-source can be provided through two mechanisms in the electrochemical process: the first one is the Tafel-type mechanism, in which the solvated protons first combine with electrons on the catalyst surface. The hydrogen adatoms then react with the adsorbed N_2H_x or NH_x species. However, the Tafel-type mechanism is very slow because the activation barrier is often more than 1.0 eV.[58] The other mechanism is the Heyrovsky-type, in which the adsorbed intermediate species separately react with the protons and electrons. An applied bias can directly reduce the activation barrier in the Heyrovsky-type mechanism for the electrochemical process, while the barrier of Tafel-type mechanism can only be affected by varying the concentrations of the reactants.[59] Therefore, the Heyrovsky-type mechanism reaction was investigated here.

In order to explore whether aggregation will occur in the Ru/B_α and Ru/B_β systems, the (E_b) binding energy and (E_c) cohesive energy were calculated (Fig. 1). Generally, clustering on the surface is unfavourable if the value ($E_b + E_c$) is negative.[57] However, even if the value is positive, the single atom can be stable on the substrate when the aggregation barrier is high enough to prevent aggregation, which is the kinetic stability of SACs.[60–62] For example, $Pd/g-C_3N_4$ was synthesized experimentally in 2015, and even the value ($E_b + E_c$) was up to 2.4 eV.[62] In order to evaluate the kinetic stability of the two systems in our work, the nudged elastic band calculations were studied along the single atom migration paths (Fig. S3†).[63,64] The calculated aggregation barriers were 2.16 and 2.32 eV for Ru migration on the two boron sheets; these barrier energies were much larger than ($E_b + E_c$) of two Ru/boron systems (0.35 and 0.31 eV). Therefore, the migration of Ru atoms on the substrates was very difficult.

To estimate the NRR performance of the Ru/B catalyst, we investigated three possible reaction pathways including the distal, alternating, and enzymatic mechanisms.[32,65] Hydrogen atoms were added one by one to the adsorbed species and DFT calculations were used to find the minimum energy configurations, based on which ΔG for each step was derived. The schematic diagrams and optimized geometric structures of various intermediates of the three feasible reaction pathways are illustrated in Fig. 3. Each pathway is accompanied with six pairs of protons and electrons, which can be divided into 7 steps including N_2-adsorption (step 1) plus six reduction elementary reactions (steps 2–7). From the distal pathway, the consecutive
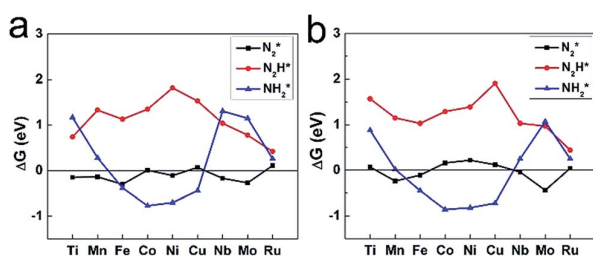

Fig. 2 Calculated Gibbs free energies of N_2 molecule, N_2H and NH_2 species adsorbed on various single TM atoms embedded on (a) α-sheet and (b) β_{12}-sheet.

171

protonation occurs first at the distal N and then at the proximal N. The following steps result in full scission of the N–N bond and the release of an NH_3 molecule in the fourth step, while second NH_3 is released in the subsequent parts, and the active center is regenerated in the 7th step. For both the alternating and enzymatic pathways, the protonation alternates between the two N atoms, due to which the first NH_3 molecule is released at the sixth step.

The DFT calculation results showed that the ΔG values for N_2-adsorption on Ru/Bα were only 0.11 and 0.22 eV for end-on and side-on configurations, respectively, as shown in Fig. 4. Such a small energy input indicates that N_2 can be effectively captured (Table S3†). With respect to side-on adsorption, the end-on module was slightly favorable, with Ru–N bond length of 1.97 Å, while the length of Ru–N bonds was 2.18 Å in the side-on condition. Moreover, the N–N distance increased from 1.10 Å in a free individual N_2 to 1.13 and 1.17 Å in two conditions, indicating that N_2 is activated. The difference between the two adsorption configurations originated from the subsequent protonation. With side-on adsorption, the $N_2^* \rightarrow N_2H^*$ conversion only required energy of 0.42 eV, with N–N bond further elongated to 1.23 Å (Fig. 4a). For the following steps, the reaction was divided into two paths: distal and alternating reactions. In the distal pathway, the second ($H^+ + e^-$), known as coupled proton and electron transfer (CPET), consecutively attacked the distal N atoms of N_2H^* species. The $N_2H_2^*$ intermediate was produced with $\Delta G = 0.17$ eV in the third step with length of 1.33 Å for N–N distance. In the following fourth step, first NH_3 could be released after the third CPET reacted with the $N_2H_2^*$ species with an exothermal reaction (0.94 eV). As a result, one N atom connected with the Ru atom with a length of 1.65 Å, followed by full hydrogenation of N* intermediate to release the second NH_3 with three CPET steps. The ΔG values for such three steps were −0.01, −0.42, and 0.26 eV. Overall, the maximum energy input associated with the distal path was 0.42 eV for the 1st hydrogenation ($N_2^* \rightarrow N_2H^*$).

When NRR followed the alternating pathway (Fig. 4b), it needed to adsorb energy of 0.66 eV for acquiring the second CPET in the third step with length of 1.30 Å of N–N bond. In the

Fig. 4 Calculated energy profiles for NRR catalysed by Ru/B$_\alpha$: (a) distal, (b) alternating, and (c) enzymatic mechanisms.

subsequent steps, the ΔG values for the four steps were −0.18, 0.07, −1.75 and 0.26 eV. In this pathway, the real challenge came from acquiring the second CPET ($\Delta G = 0.66$ eV) for the $N_2H^* \rightarrow NHNH^*$ step. Similarly, the profile for the enzymatic path has been presented in Fig. 4c, which shows a large energy demand (0.9 eV) for initial hydrogenation ($N_2^* \rightarrow N_2H^*$); it is remarkably higher than the required amount of the distal pathway (0.42 eV). Therefore, the distal pathway is energetically favorable among the three shown in Fig. 4.

Then, we turned to the discussion of NRR on Ru/B$_\beta$ (Table S4†). Similarly, the initial step of N_2 reduction is N_2-adsorption with ΔG values being 0.04 and 0.6 eV for end-on and side-on configurations, respectively, indicating that the side-on module should dominate. In the following ($N_2^* \rightarrow N_2H^*$) step, the reactions were slightly endothermic in the free energy profile by 0.44 and 0.64 eV, as shown in Fig. 5. In the side-on case, there was a distinctive energy difference of 0.58 eV for N_2H_2 formation between the distal and alternating pathways similar to that observed for the α-sheet. For the distal pathway, RDS for both Ru/B$_\alpha$ and Ru/B$_\beta$ comes from the second step ($N_2^* \rightarrow N_2H^*$), with $\Delta G = 0.42$ eV and 0.44 eV, respectively; however, for the alternating pathway, RDS is the third step ($N_2H^* \rightarrow NHNH^*$) and the fifth step ($NHNH_2^* \rightarrow NH_2NH_2^*$) for two boron sheets. For the enzymatic pathway, RDS is the $N_2H^* \rightarrow NHNH^*$ step, showing $\Delta G = 0.78$ eV, which is larger than that of the distal pathway (0.44 eV). Therefore, the distal mechanism is energetically favourable, which is the same as that observed in the case of Ru/B$_\alpha$.

To further understand the catalytic performance of the Ru/B concept catalyst, the charge population fluctuation along with the favourable distal pathway is illustrated in Fig. 6. In this part, each intermediate was divided into three moieties: boron sheet (moiety 1, substrate), Ru (moiety 2, catalyst centre), and the adsorbed N_xH_y species (moiety 3, intermediates). For the α-sheet (Fig. 6a), the N_2 molecule gained 0.29 electrons from the Ru/B catalyst in the N_2-adsorption step. For the following
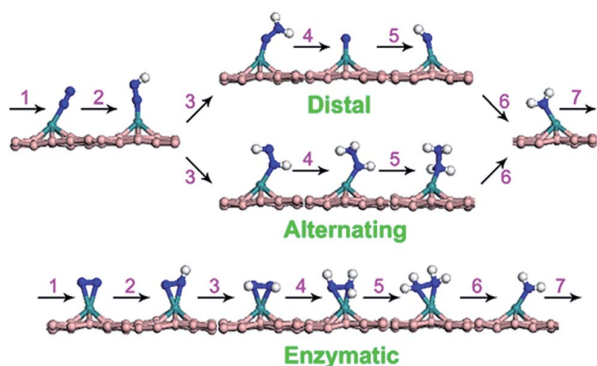

Fig. 3 Optimized structures of various intermediates along the three reaction paths of NRR proceeding on Ru-boron monolayer through distal, alternating and enzymatic pathways.
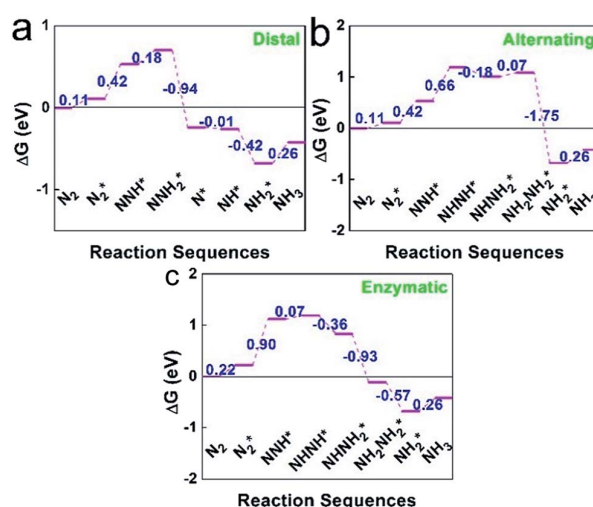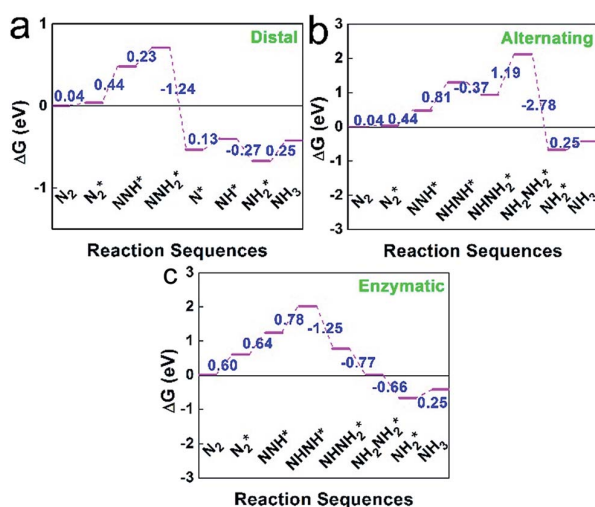
172

Fig. 5 Calculated energy profiles for NRR catalysed by Ru/B$_\beta$: (a) distal (b) alternating, and (c) enzymatic mechanisms.

hydrogenation steps, significant charge variation occurred for moiety 1 and moiety 2, while moiety 3 showed a relatively stable plot. Interestingly, the charge variation of boron sheet showed a reverse trend to the charge population of Ru atom. In the case of Ru/B$_\beta$, a much more complicated fluctuation curve was found, as shown in Fig. 6b. Initially, the sum of electron transfer from moieties 1 and 2 was 0.41 electrons to moiety 3. For the subsequent process, the formed N$_2$H* species gained about 0.51 electrons from the boron sheet and more for following steps. Therefore, the Ru/B catalyst served as an electron donor, with the boron sheet actively involved for both α and β boron sheets; this indicated space for further improvement, for example, through the optimization of ligands bonded to the metal centre.

From the above results, two features were observed: (1) a very small energy requirement for N$_2$ adsorption is achieved using an Ru/B catalyst (0.11 and 0.04 eV), which is almost equal to the performance of flat Ru (0001) catalysts (0.08 eV);[12] (2) NRR occurring on the Ru/B catalyst prefers the distal pathway due to the small limiting energy barriers (0.42 and 0.44 eV, respectively), which are less than half of that reported for the flat Ru (0001) catalysts (1.08 eV).[12] In the literature, several single-atom

catalysts have been investigated; to make valuable comparisons, the calculated data should be from the same method. In recent years, Fe–MoN$_2$ (0.47 eV) and TiN$_4$–graphene (0.69 eV) have been identified as excellent NRR catalysts using RPBE functional as we used in this work; both are close or slightly worse than Ru on boron monolayers. Therefore, the anchored Ru atom in the hexagonal hole of boron sheet is expected to be a very promising single-atom catalyst for NRR. Given that the boron monolayer has been experimentally synthesized on metal substrates, the proposed Ru/B concept catalyst is feasible.[40,48]

Conclusions

In summary, by performing first-principles calculations, we proposed a new single-atom catalyst for activating N$_2$ and converting it into NH$_3$ at ambient conditions. Our results indicated that the single Ru-atom-embedded boron monolayers possessed outstanding NRR catalytic activity, and the reaction pathway preferred distal mechanism with $\Delta G_{max} = 0.42$ eV, which is less than half of that reported for the flat Ru (0001) catalysts (1.08 eV). Therefore, our computations suggested that a suitable substrate offers large space for the optimization of transition metals for N$_2$ reduction at ambient conditions, which could encourage more experimental and theoretical studies on exploring the potential of 2D nanomaterials as substrates to design high-performance single-TM catalysts for electrochemical synthesis of ammonia.

Conflicts of interest

The authors declare no competing financial interest.

Acknowledgements

References

1 J. W. Erisman, M. A. Sutton, J. Galloway, Z. Klimont and W. Winiwarter, *Nat. Geosci.*, 2008, **1**, 636–639.

2 A. Klerke, C. H. Christensen, J. K. Norskov and T. Vegge, *J. Mater. Chem.*, 2008, **18**, 2304–2310.

3 C. H. Jacobsen, S. Dahl, B. S. Clausen, S. Bahn, A. Logadottir and J. K. Nørskov, *J. Am. Chem. Soc.*, 2001, **123**, 8404–8405.

4 B. A. MacKay and M. D. Fryzuk, *Chem. Rev.*, 2004, **104**, 385–402.

5 K. C. MacLeod and P. L. Holland, *Nat. Chem.*, 2013, **5**, 559–565.

6 F. Haber, *Naturwissenschaften*, 1923, **11**, 753–756.

7 D. V. Yandulov and R. R. Schrock, *Science*, 2003, **301**, 76–78.

8 M. M. Rodriguez, E. Bill, W. W. Brennessel and P. L. Holland, *Science*, 2011, **334**, 780–783.
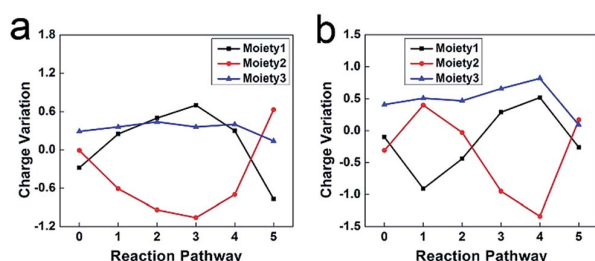
Fig. 6 Charge fluctuation of three moieties along the distal pathway steps (a) Ru/B$_\alpha$, (b) Ru/B$_\beta$. Step 0 represents the charge transferred during N$_2$ adsorption.

This journal is © The Royal Society of Chemistry 2019

J. Mater. Chem. A, 2019, **7**, 4771–4776 | **4775**

173

9 S. Giddey, S. P. S. Badwal and A. Kulkarni, *Int. J. Hydrogen Energy*, 2013, **38**, 14576–14594.

10 Y. Abghoui, A. L. Garden, V. F. Hlynsson, S. Bjorgvinsdottir, H. Olafsdottir and E. Skulason, *Phys. Chem. Chem. Phys.*, 2015, **17**, 4909–4918.

11 F. Haber, *Naturwissenschaften*, 1923, **11**, 339–340.

12 E. Skulason, T. Bligaard, S. Gudmundsdottir, F. Studt, J. Rossmeisl, F. Abild-Pedersen, T. Vegge, H. Jonsson and J. K. Norskov, *Phys. Chem. Chem. Phys.*, 2012, **14**, 1235–1245.

13 S. Robert, *Angew. Chem., Int. Ed.*, 2003, **42**, 2004–2008.

14 Y. Tanabe and Y. Nishibayashi, *Coord. Chem. Rev.*, 2013, **257**, 2551–2564.

15 A. D. Allen and C. V. Senoff, *Chem. Commun.*, 1965, 621–622.

16 J. S. Anderson, J. Rittle and J. C. Peters, *Nature*, 2013, **501**, 84–87.

17 B. M. Hoffman, D. Lukoyanov, Z. Y. Yang, D. R. Dean and L. C. Seefeldt, *Chem. Rev.*, 2014, **114**, 4041–4062.

18 G. Schwarz, R. R. Mendel and M. W. Ribbe, *Nature*, 2009, **460**, 839–847.

19 S. C. Lee and R. H. Holm, *Chem. Rev.*, 2004, **104**, 1135–1158.

20 T. Spatzal, M. Aksoyoglu, L. Zhang, S. L. A. Andrade, E. Schleicher, S. Weber, D. C. Rees and O. Einsle, *Science*, 2011, **334**, 940.

21 T. H. Rod and J. K. Nørskov, *J. Am. Chem. Soc.*, 2000, **122**, 12751–12763.

22 J. Zhao and Z. Chen, *J. Am. Chem. Soc.*, 2017, **139**, 12480–12487.

23 V. Rosca, M. Duca, M. T. de Groot and M. T. M. Koper, *Chem. Rev.*, 2009, **109**, 2209–2244.

24 G. Marnellos and M. Stoukides, *Science*, 1998, **282**, 98–100.

25 I. A. Amar, R. Lan, C. T. G. Petit and S. Tao, *J. Solid State Chem.*, 2011, **15**, 1845–1860.

26 V. Kyriakou, I. Garagounis, E. Vasileiou, A. Vourros and M. Stoukides, *Catal. Today*, 2017, **286**, 2–13.

27 J. H. Montoya, C. Tsai, A. Vojvodic and J. K. Nørskov, *ChemSusChem*, 2015, **8**, 2180–2186.

28 T. Murakami, T. Nishikiori, T. Nohira and Y. Ito, *J. Am. Chem. Soc.*, 2003, **125**, 334–335.

29 F. Zhou, L. M. Azofra, M. Ali, M. Kar, A. N. Simonov, C. McDonnell-Worth, C. Sun, X. Zhang and D. R. MacFarlane, *Energy Environ. Sci.*, 2017, **10**, 2516–2520.

30 Z. Li, R. Liu, Y. Xie, S. Feng and J. Wang, *Solid State Ionics*, 2005, **176**, 1063–1066.

31 V. Kordali, G. Kyriacou and C. Lambrou, *Chem. Commun.*, 2000, 1673–1674.

32 X. Li, Q. Li, J. Cheng, L. Liu, Q. Yan, Y. Wu, X. Zhang, Z. Wang, Q. Qiu and Y. Luo, *J. Am. Chem. Soc.*, 2016, **138**, 8706–8709.

33 W. Zhao, J. Zhang, X. Zhu, M. Zhang, J. Tang, M. Tan and Y. Wang, *Appl. Catal., B*, 2014, **144**, 468–477.

34 Q. Li, L. He, C. Sun and X. Zhang, *J. Phys. Chem. C*, 2017, **121**, 27563–27568.

35 C. Choi, S. Back, N. Y. Kim, J. Lim, Y. H. Kim and Y. Jung, *ACS Catal.*, 2018, **8**, 7517–7525.

36 B. Qiao, A. Wang, X. Yang, L. F. Allard, Z. Jiang, Y. Cui, J. Liu, J. Li and T. Zhang, *Nat. Chem.*, 2011, **3**, 634–641.

37 C. Ling, Y. Ouyang, Q. Li, X. Bai, X. Mao, A. Du and J. Wang, *Small Methods*, 2018, 1800376.

38 Z. Chen, J. Zhao, C. R. Cabrera and Z. Chen, *Small Methods*, 2018, 1800368.

39 X. Zhang, A. Chen, Z. Zhang and Z. Zhou, *J. Mater. Chem. A*, 2018, **6**, 18599–18604.

40 J. M. Thomas, *Nature*, 2015, **525**, 325–326.

41 H. Tang and S. Ismail-Beigi, *Phys. Rev. Lett.*, 2007, **99**, 115501.

42 H. Liu, J. Gao and J. Zhao, *Sci. Rep.*, 2013, **3**, 3238.

43 X. Wu, J. Dai, Y. Zhao, Z. Zhuo, J. Yang and X. Zeng, *ACS Nano*, 2012, **6**, 7443–7453.

44 F. Ma, Y. Jiao, G. Gao, Y. Gu, A. Bilic, Z. Chen and A. Du, *Nano Lett.*, 2016, **16**, 3022–3028.

45 R. R. Zope and T. Baruah, *Chem. Phys. Lett.*, 2011, **501**, 193–196.

46 H. Tang and S. Ismail-Beigi, *Phys. Rev. B*, 2009, **80**, 134113.

47 E. S. Penev, S. Bhowmick, A. Sadrzadeh and B. I. Yakobson, *Nano Lett.*, 2012, **12**, 2441–2445.

48 X. Yu, L. Li, X. Xu and C. Tang, *J. Phys. Chem. C*, 2012, **116**, 20075–20079.

49 A. R. Oganov, J. Chen, C. Gatti, Y. Ma, Y. Ma, C. W. Glass, Z. Liu, T. Yu, O. O. Kurakevych and V. L. Solozhenko, *Nature*, 2009, **457**, 863–867.

50 B. Feng, J. Zhang, Q. Zhong, W. Li, S. Li, H. Li, P. Cheng, S. Meng, L. Chen and K. Wu, *Nat. Chem.*, 2016, **8**, 563–568.

51 C. Wu, H. Wang, J. Zhang, G. Gou, B. Pan and J. Li, *ACS Appl. Mater. Interfaces*, 2016, **8**, 2526–2532.

52 J. Li, H. Zhang and G. Yang, *J. Phys. Chem. C*, 2015, **119**, 19681–19688.

53 S. H. Mir, S. Chakraborty, P. C. Jha, J. Wärnå, H. Soni, P. K. Jha and R. Ahuja, *Appl. Phys. Lett.*, 2016, **109**, 053903.

54 S. Er, G. A. de Wijs and G. Brocks, *J. Phys. Chem. C*, 2009, **113**, 18962–18967.

55 G. Kresse and D. Joubert, *Phys. Rev. B*, 1999, **59**, 1758.

56 J. P. Perdew, K. Burke and M. Ernzerhof, *Phys. Rev. Lett.*, 1996, **77**, 3865.

57 S. Grimme, J. Antony, S. Ehrlich and H. Kerieg, *Chem. Phys.*, 2010, **132**, 154104.

58 J. Heyrovsky, *Recl. Trav. Chim. Pays-Bas*, 1927, **46**, 582.

59 S. Wang, V. Petzold, V. Tripkovic, J. Kleis, J. G. Howalt, E. Skulason, E. M. Fernandez, B. Hvolbaek, G. Jones and A. Toftelund, *Phys. Chem. Chem. Phys.*, 2011, **13**, 20760–20765.

60 J. Liu, Y. Tang, Y. Wang, T. Zhang and J. Li, *Natl. Sci. Rev.*, 2018, **5**, 638–641.

61 R. Ouyang, J. Liu and W. Li, *J. Am. Chem. Soc.*, 2013, **135**, 1760–1771.

62 G. Vilé, D. Albani, M. Nachtegaal, Z. Chen, D. Dontsova, M. Antonietti, N. López and J. Pérez-Ramírez, *Angew. Chem., Int. Ed.*, 2015, **54**, 11265–11269.

63 S. Li, H. Yin, X. Kan, L. Gan, U. Schwingenschlögl and Y. Zhao, *Phys. Chem. Chem. Phys.*, 2017, **19**, 30069–30077.

64 B. Li, M. B. Katz, Q. Zhang, L. Chen, G. W. Graham and X. Pan, *J. Chem. Phys.*, 2013, **138**, 144705.

65 J. S. Anderson, G. E. Cutsail, J. Rittle, B. A. Connor, W. Gunderson, L. Zhang, B. M. Hoffman and J. C. Peters, *J. Am. Chem. Soc.*, 2015, **137**, 7803–7809.

4776 | *J. Mater. Chem. A*, 2019, **7**, 4771–4776

This journal is © The Royal Society of Chemistry 2019

174

4.2 Supporting Information

Supporting Information

Conversion of Dinitrogen to Ammonia on Ru Atom Supported on Boron Sheets: A DFT Study

Chuangwei Liu,[ab] Qinye Li,[c] Jie Zhang,[b] Yonggang Jin,[d] Douglas MacFarlane[b] Chenghua Sun[*ae]

[a] Science & Technology Innovation Institute, Dongguan University of Technology, Dongguan, China

[b] School of Chemistry, Faculty of Science, Monash University, Clayton, Victoria 3800, Australia

[c] School of Chemical Engineering, Monash University, Clayton, Victoria 3800, Australia

[d] CSIRO Energy, 1 Technology Court, Pullenvale, Queensland 4069, Australia

[e] Department of Chemistry and Biotechnology, Faculty of Science, Engineering & Technology, Swinburne University of Technology, Hawthorn, Victoria 3122, Australia

Email: chenghuasun@swin.edu.au

Contents — Pages

Thermochemistry

The fundamental thermodynamic relation states that

$$G^0 = H^0 - \mathrm{T}S \tag{1}$$

At constant pressure and ambient temperature, the enthalpy can be described as term of H^0 and the heat capacity, C_P:

$$H = H^0 + \int C_P\, \mathrm{dT} \tag{2}$$

Moreover, the entropy term can be presented to the sum of the translational, rotational, vibrational, and electronic contributions as to:

$$S = S_t + S_r + S_v + S_e \tag{3}$$

In the above equation, the approximations entropy can be expressed:

  (a) At the fundamental electronic level: $S_e = 0$.
  (b) For gases, translational, rotational, and vibrational entropy terms have contributions that might not be neglected: $S = S_t + S_r + S_v$.
  (c) For solids and adsorbates, both $S_t = 0$ and $S_r = 0$, and thus: $S = S_v$.
  (d) Because $\int C_P\, \mathrm{dT}$ is almost negligible and $\Delta \int C_P\, \mathrm{dT} = 0$, no thermal corrections for the enthalpy have been taken into the following calculate for Gibbs free energies (ΔG).

And also, intrinsic zero point energy (ZPE) and extrinsic dispersion (D) corrections can be obtained by the above analytical:

$$G = H^0 + \int C_P\, \mathrm{dT} - \mathrm{T}(S_t + S_r + S_v + S_e) + \mathrm{ZPE} + D \tag{4}$$

The neighboring intermediates can be named as 1 and 2, thus we can gain the Gibbs free energy of neighboring intermediates reaction:

$$\Delta G_{21} = G_2 - G_1 \tag{5}$$

Such as: in the reaction ($N_2^* \rightarrow N_2H^*$), the Gibbs free energy $\Delta G = G(N_2H^*) - G(N_2^*) - G(H^+/e^-)$

In such equation, the chemical potential of the H+/e- pair has the half value of the chemical potential of the dihydrogen molecule, under the standard hydrogen electrode conditions, the $G(H^+/e^-)$ equal to $\frac{1}{2} G(H_2)$.

Table S1. The system energy (eV), binding energy (eV) and cohesive energy (eV) of the TM-embedded α sheet and distance of transition single metal (TM) to monolayer (Å).

Metal Atoms	System Energy (eV)	Binding Energy (eV)	Cohesive Energy (eV)	Distance of TM to Substrates (Å)
Ti	-205.77	-4.01	5.54	1.60
Mn	-206.10	-2.43	3.39	1.38
Fe	-205.38	-4.04	4.79	1.08
Co	-203.76	-4.79	5.11	0.80
Ni	-202.38	-4.32	4.74	0.88
Cu	-201.42	-2.42	3.55	1.30
Nb	-209.04	-4.53	7.07	1.66
Mo	-210.37	-3.28	6.57	1.49
Ru	-206.93	-6.49	6.84	1.26
W	-213.21	-4.61	8.4	1.53

Table S2. The system energy (eV) and binding energy (eV) of the TM-embedded of β_{12} sheet and distance of TM to monolayer (Å).

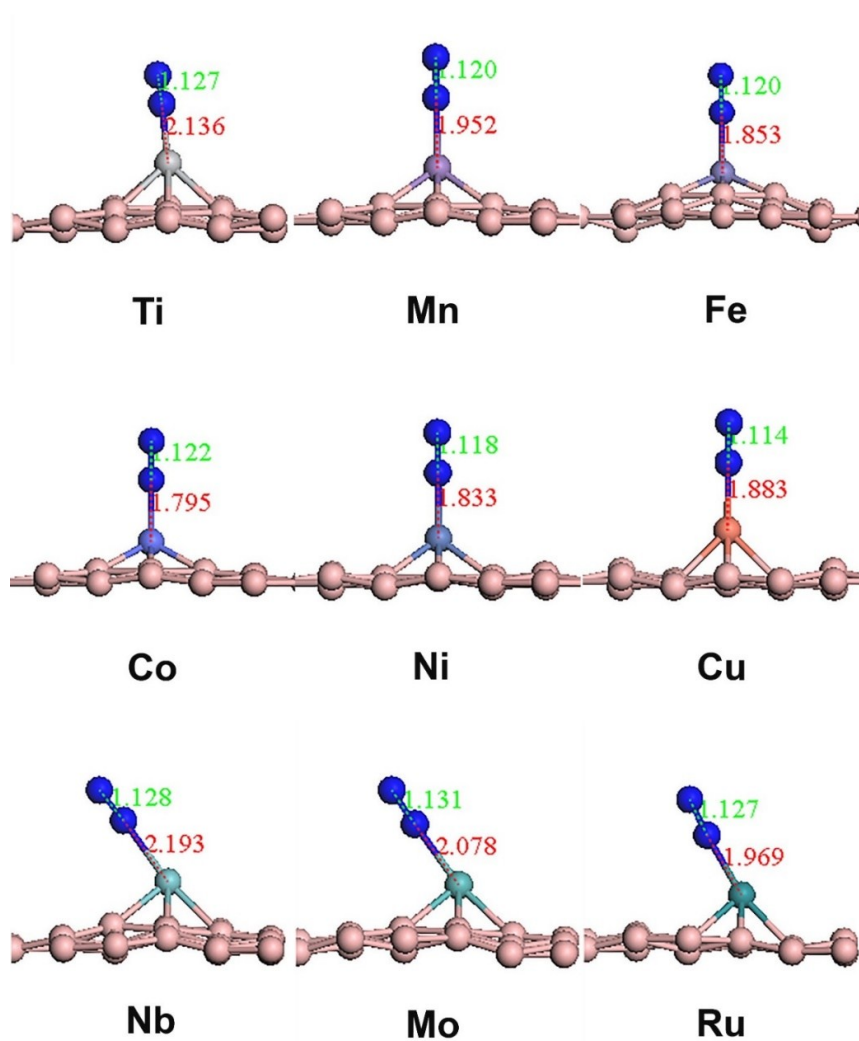| Metal Atoms	System Energy (eV)	Binding Energy (eV)	Distance of TM to Substrates (Å)
Ti	-191.08	-5.28	1.40
Mn	-192.19	-2.91	0.91
Fe	-191.69	-4.30	0.90
Co	-190.47	-4.66	0.44
Ni	-188.87	-4.41	0.66
Cu	-187.81	-2.61	1.24
Nb	-195.87	-4.30	1.33
Mo	-197.13	-3.09	1.15
Ru	-193.43	-6.53	1.09
W	-199.85	-4.55	1.15

Figure S1. Optimized structures of N_2 adsorption on single TM-embedded α sheet.
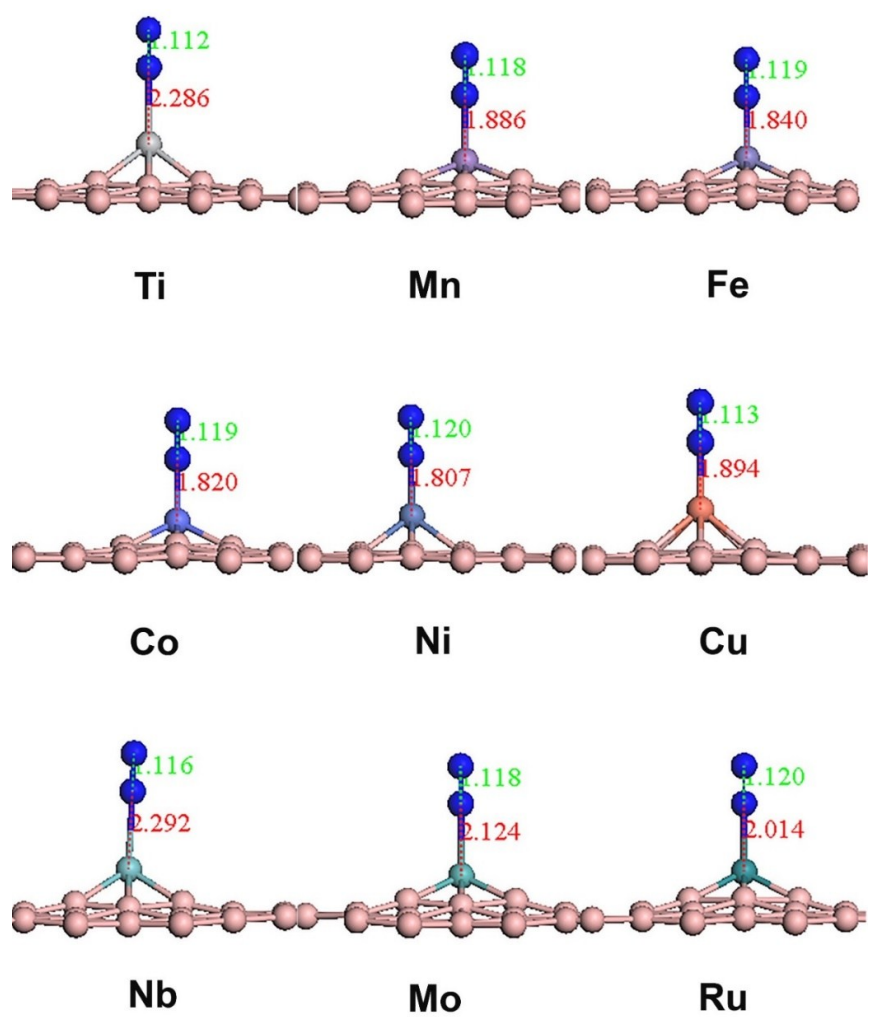
Figure S2. Optimized structures of N_2 adsorption on single TM-embedded β_{12} sheet.
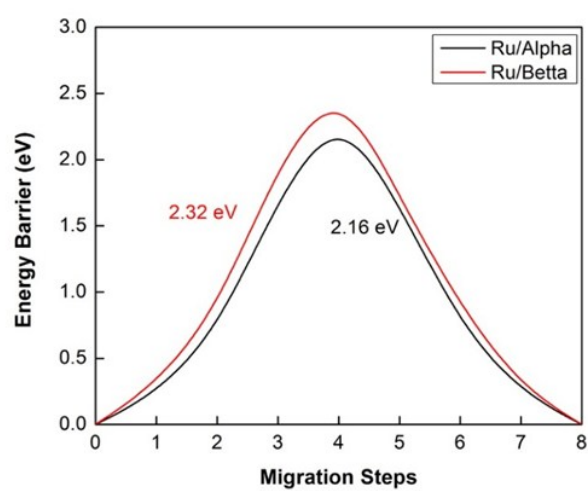
Figure S3. The energy barrier of a single Ru atom migration between two holes of two boron sheets.

182

Table S3. The N-N, B-N bond length (Å), and the Gibes free energies (ΔG, eV) of the adsorbed N_xH_y species on the Ru-embedded α sheet by two reaction pathways (distal and alternating pathways). 1 represents the adsorbed N_2^*.

Reaction Step		1	2	3	4	5	6	7
Distal	ΔG	0.11	0.42	0.18	-0.94	-0.01	-0.42	0.26
	N-N	1.13	1.23	1.33	3.52			
	B-N	1.97	1.81	1.80	1.65	1.77	1.94	
Alternating	ΔG	0.11	0.42	0.66	-0.18	0.07	-1.75	0.26
	N-N	1.13	1.23	1.29	1.42	1.78	3.60	
	B-N	1.97	1.81	1.99	1.93	1.76	1.94	

Table S4. The N-N, B-N bond length (Å), and the Gibes free energies (ΔG, eV) of the adsorbed N_xH_y species on the Ru-embedded $β_{12}$ sheet by two reaction pathways (distal and alternating pathways). 1 represents the adsorbed N_2^*.

Reaction Step		1	2	3	4	5	6	7
Distal	ΔG	0.04	0.44	0.23	-1.24	0.13	-0.27	0.25
	N-N	1.12	1.23	1.33	3.49			
	B-N	2.01	1.79	1.76	1.64	1.74	1.91	
Alternating	ΔG	0.04	0.44	0.81	-0.37	1.19	-2.78	0.25
	N-N	1.12	1.23	1.29	1.42	1.48	3.61	
	B-N	2.01	1.79	1.99	1.91	1.75	1.91	

Cartesian Coordinates

Clear Ru-embedded α boron sheet

B1	0.331952	0.163903	0.488469
B2	0.163905	0.331975	0.488513
B3	0.331893	0.331897	0.495623
B4	0.165066	0.999702	0.498890
B5	0.999698	0.165106	0.498926
B6	0.164885	0.164879	0.506187
B7	0.334628	0.999706	0.498877
B8	0.999690	0.334644	0.498916
B9	0.833345	0.166700	0.508396
B10	0.668079	0.331960	0.488468
B11	0.834948	0.334639	0.498889
B12	0.665390	0.000332	0.498959
B13	0.500017	0.164885	0.506147
B14	0.665402	0.165090	0.498875
B15	0.834944	0.000341	0.498963
B16	0.500009	0.331902	0.495575
B17	0.331961	0.668071	0.488558
B18	0.166680	0.833369	0.508397
B19	0.334639	0.834968	0.498961
B20	0.164877	0.500020	0.506273
B21	0.000326	0.665407	0.498933
B22	0.165078	0.665400	0.498963
B23	0.331879	0.500014	0.495749
B24	0.000322	0.834962	0.498920
B25	0.836113	0.668083	0.488516
B26	0.668053	0.836123	0.488560
B27	0.835148	0.835154	0.506278
B28	0.668129	0.500002	0.495626
B29	0.500014	0.668163	0.495781
B30	0.668146	0.668138	0.495754
B31	0.835147	0.500020	0.506192
B32	0.500006	0.835150	0.506336
Ru1	0.500012	0.499918	0.562974

N_2*

B1	0.326007	0.160578	0.489140
B2	0.155952	0.327814	0.487399
B3	0.325269	0.328627	0.493283
B4	0.158108	0.995541	0.490790
B5	0.993349	0.162164	0.503310
B6	0.158068	0.161440	0.502878
B7	0.327362	0.995551	0.489497
B8	0.993338	0.330790	0.503356
B9	0.825062	0.162357	0.512750
B10	0.661894	0.329127	0.490010
B11	0.827681	0.332055	0.507387
B12	0.658533	0.996293	0.507011
B13	0.492573	0.160255	0.504922
B14	0.658555	0.161883	0.507065
B15	0.827652	0.995230	0.507255
B16	0.492892	0.326997	0.499593
B17	0.325990	0.665082	0.489153
B18	0.159058	0.829334	0.503456
B19	0.327372	0.831462	0.489441
B20	0.158047	0.496254	0.502750

B21	0.993290	0.662021	0.493184
B22	0.158096	0.662231	0.490713
B23	0.325190	0.496275	0.493137
B24	0.993261	0.830896	0.493206
B25	0.827208	0.663425	0.494423
B26	0.661845	0.832411	0.489903
B27	0.828484	0.832012	0.509854
B28	0.660271	0.495458	0.504500
B29	0.492846	0.665457	0.499450
B30	0.660222	0.664369	0.504322
B31	0.828534	0.496115	0.509872
B32	0.492576	0.831942	0.504838
Ru1	0.488675	0.494352	0.569687
N1	0.599643	0.552263	0.655050
N2	0.655617	0.581438	0.705706

N$_2$H*

B1	0.333421	0.165398	0.492185
B2	0.166235	0.333139	0.491337
B3	0.328633	0.327741	0.512173
B4	0.166016	0.999928	0.492156
B5	0.000037	0.165388	0.492657
B6	0.163664	0.163707	0.504362
B7	0.334643	0.999584	0.492278
B8	0.000037	0.334688	0.492648
B9	0.834226	0.167132	0.500908
B10	0.667823	0.332576	0.492423
B11	0.835288	0.334614	0.491970
B12	0.666741	0.001139	0.492368
B13	0.500686	0.163099	0.503813
B14	0.666743	0.165640	0.492348
B15	0.835287	0.000711	0.491999
B16	0.500687	0.327290	0.512116
B17	0.333422	0.668061	0.492213
B18	0.167207	0.833624	0.501019
B19	0.334645	0.835096	0.492293
B20	0.163658	0.499994	0.504374
B21	0.001267	0.666049	0.492958
B22	0.166018	0.666129	0.492177
B23	0.328623	0.500929	0.512203
B24	0.001263	0.835256	0.492951
B25	0.835079	0.667559	0.491691
B26	0.667816	0.835277	0.492447
B27	0.837644	0.836940	0.504626
B28	0.672831	0.499791	0.513166
B29	0.500682	0.673443	0.512180
B30	0.672836	0.673077	0.513200
B31	0.837645	0.500742	0.504603
B32	0.500688	0.837628	0.503847
Ru1	0.499265	0.499618	0.575614
N1	0.489360	0.494542	0.665536
N2	0.465096	0.482327	0.726250
H1	0.562470	0.531135	0.754504

N$_2$H$_2$*

B1	0.316320	0.152708	0.493494
B2	0.148042	0.320964	0.490597
B3	0.313910	0.318684	0.506756

B4	0.148835	0.988049	0.491352
B5	0.983501	0.154123	0.499577
B6	0.148225	0.153048	0.505589
B7	0.317642	0.987646	0.490010
B8	0.983397	0.322830	0.498944
B9	0.816934	0.155230	0.510026
B10	0.652203	0.321774	0.492168
B11	0.818522	0.323769	0.502814
B12	0.649238	0.988606	0.504217
B13	0.483019	0.151550	0.507787
B14	0.649335	0.154194	0.503886
B15	0.818621	0.988222	0.503965
B16	0.483233	0.316707	0.509983
B17	0.316343	0.657163	0.493079
B18	0.150060	0.821855	0.503993
B19	0.317738	0.823569	0.490365
B20	0.147925	0.488601	0.505397
B21	0.983771	0.654274	0.495003
B22	0.148981	0.654502	0.491499
B23	0.313551	0.488808	0.506973
B24	0.983763	0.823205	0.495346
B25	0.818049	0.655793	0.495384
B26	0.651994	0.823798	0.492838
B27	0.820581	0.825479	0.513246
B28	0.654613	0.487971	0.513807
B29	0.482920	0.660042	0.510998
B30	0.654717	0.660010	0.514363
B31	0.820450	0.488473	0.512096
B32	0.483023	0.825123	0.508508
Ru1	0.485868	0.490050	0.576399
N1	0.540696	0.523481	0.662983
N2	0.656866	0.589484	0.705273
H1	0.630408	0.601418	0.753445
H2	0.757625	0.675897	0.686415

N*

B1	0.332208	0.164247	0.489554
B2	0.164334	0.332157	0.489619
B3	0.330210	0.330137	0.506023
B4	0.165267	0.999711	0.494053
B5	0.999783	0.165209	0.494083
B6	0.163960	0.163891	0.504599
B7	0.334608	0.999703	0.494020
B8	0.999787	0.334554	0.494088
B9	0.833439	0.166705	0.503872
B10	0.668015	0.332133	0.489490
B11	0.834951	0.334535	0.493978
B12	0.665604	0.000374	0.494059
B13	0.500104	0.163883	0.504482
B14	0.665611	0.165198	0.494000
B15	0.834943	0.000382	0.494032
B16	0.500116	0.330152	0.505905
B17	0.332220	0.667928	0.489620
B18	0.166772	0.833372	0.503872
B19	0.334615	0.834874	0.494078
B20	0.163957	0.500036	0.504656
B21	0.000459	0.665550	0.493992
B22	0.165275	0.665531	0.494102
B23	0.330204	0.500040	0.506090

B24	0.000454	0.834885	0.494002
B25	0.835925	0.667952	0.489495
B26	0.668002	0.835837	0.489560
B27	0.836268	0.836199	0.504491
B28	0.669995	0.500039	0.505855
B29	0.500115	0.669944	0.506039
B30	0.670001	0.669927	0.505923
B31	0.836267	0.500036	0.504429
B32	0.500103	0.836191	0.504601
Ru1	0.500291	0.500031	0.573693
N1	0.500735	0.500027	0.656055

NH*

B1	0.335545	0.166762	0.489941
B2	0.168468	0.334306	0.490756
B3	0.332450	0.330622	0.509664
B4	0.168767	0.001753	0.494489
B5	0.003501	0.167185	0.496134
B6	0.167101	0.165047	0.508537
B7	0.338224	0.001861	0.495759
B8	0.003520	0.336532	0.496202
B9	0.836774	0.168493	0.505087
B10	0.671030	0.333725	0.488291
B11	0.838300	0.336132	0.494020
B12	0.669026	0.002285	0.492643
B13	0.504209	0.166261	0.506357
B14	0.668998	0.166958	0.492794
B15	0.838313	0.002422	0.493796
B16	0.504183	0.331851	0.506716
B17	0.335523	0.668979	0.489782
B18	0.170202	0.835192	0.504874
B19	0.338203	0.836571	0.495649
B20	0.167192	0.502321	0.508415
B21	0.004355	0.667728	0.491753
B22	0.168759	0.667220	0.494310
B23	0.332542	0.502066	0.509486
B24	0.004364	0.836823	0.491818
B25	0.839656	0.669915	0.487926
B26	0.671091	0.837568	0.488198
B27	0.839348	0.837445	0.503162
B28	0.673996	0.502288	0.503315
B29	0.504200	0.672499	0.506364
B30	0.673965	0.671934	0.503115
B31	0.839384	0.502153	0.503342
B32	0.504191	0.838094	0.506082
Ru1	0.502064	0.501107	0.572556
N1	0.461934	0.479656	0.659069
H1	0.378713	0.435017	0.694740

NH$_2$*

B1	0.321125	0.158181	0.489555
B2	0.152231	0.326248	0.493665
B3	0.318546	0.324780	0.504876
B4	0.153739	0.994197	0.505256
B5	0.987307	0.159305	0.492926
B6	0.152216	0.158391	0.508820
B7	0.323746	0.995115	0.504258
B8	0.987284	0.328280	0.492958
B9	0.820002	0.160147	0.503572

B10	0.656847	0.327635	0.489725
B11	0.823200	0.329230	0.491920
B12	0.653437	0.994846	0.491326
B13	0.488273	0.158857	0.507209
B14	0.653439	0.158916	0.491307
B15	0.823208	0.994247	0.491887
B16	0.488495	0.326520	0.502792
B17	0.321007	0.663196	0.489594
B18	0.154516	0.827484	0.511913
B19	0.323683	0.828960	0.504185
B20	0.152233	0.494149	0.508721
B21	0.988299	0.659495	0.502654
B22	0.153745	0.659894	0.505181
B23	0.318550	0.494109	0.504746
B24	0.988329	0.829142	0.502614
B25	0.825296	0.662739	0.489088
B26	0.656838	0.829469	0.489658
B27	0.823749	0.830021	0.505118
B28	0.656550	0.494853	0.497438
B29	0.488412	0.662318	0.502801
B30	0.656489	0.661899	0.497552
B31	0.823805	0.494067	0.505149
B32	0.488298	0.829776	0.507169
Ru1	0.497010	0.498551	0.570080
N1	0.612310	0.553831	0.652427
H1	0.560523	0.529292	0.698348
H2	0.727573	0.608902	0.656990

Clear Ru-embedded β₁₂ sheet

B1	0.000000	0.418293	0.496789
B2	0.165355	0.330518	0.499728
B3	0.000000	0.080545	0.488857
B4	0.164672	0.161410	0.491428
B5	0.000000	0.248790	0.493815
B6	0.320430	0.400319	0.524018
B7	0.500000	0.315471	0.519369
B8	0.331985	0.079456	0.483644
B9	0.500000	0.157099	0.487158
B10	0.331126	0.236643	0.496771
B11	0.679570	0.400319	0.524018
B12	0.834644	0.330518	0.499728
B13	0.668015	0.079456	0.483644
B14	0.835328	0.161410	0.491428
B15	0.668874	0.236643	0.496771
B16	0.000000	0.919455	0.488857
B17	0.164672	0.838590	0.491428
B18	0.000000	0.581707	0.496789
B19	0.165355	0.669482	0.499728
B20	0.000000	0.751210	0.493815
B21	0.331985	0.920544	0.483644
B22	0.500000	0.842901	0.487158
B23	0.320430	0.599681	0.524018
B24	0.500000	0.684529	0.519369
B25	0.331126	0.763357	0.496771
B26	0.668015	0.920544	0.483644
B27	0.835328	0.838590	0.491428
B28	0.679570	0.599681	0.524018
B29	0.834644	0.669482	0.499728
B30	0.668874	0.763357	0.496771
Ru1	0.500000	0.500000	0.554671

N₂*

B1	0.999983	0.418297	0.497743
B2	0.164872	0.332658	0.498169
B3	0.000002	0.081302	0.489402
B4	0.165036	0.162775	0.490474
B5	0.999997	0.249060	0.491875
B6	0.320614	0.407756	0.518402
B7	0.499961	0.317390	0.519260
B8	0.331442	0.079837	0.485499
B9	0.500028	0.157440	0.491473
B10	0.331107	0.239872	0.497915
B11	0.679426	0.407921	0.518330
B12	0.835092	0.332633	0.498143
B13	0.668555	0.079847	0.485503
B14	0.834970	0.162780	0.490456
B15	0.668902	0.239918	0.497939
B16	0.000002	0.918765	0.489394
B17	0.165035	0.837289	0.490456
B18	0.999983	0.581758	0.497734
B19	0.164867	0.667402	0.498147
B20	0.999997	0.750999	0.491866
B21	0.331439	0.920233	0.485483
B22	0.500028	0.842631	0.491440
B23	0.320583	0.592282	0.518372
B24	0.499960	0.682682	0.519196

B25	0.331109	0.760183	0.497876
B26	0.668557	0.920223	0.485487
B27	0.834971	0.837283	0.490438
B28	0.679457	0.592116	0.518301
B29	0.835096	0.667427	0.498122
B30	0.668900	0.760137	0.497900
Ru1	0.499963	0.500069	0.561071
N1	0.499830	0.500559	0.661756
N2	0.499758	0.500917	0.717750

N$_2$H*

B1	0.000733	0.413338	0.505003
B2	0.166220	0.330065	0.502712
B3	0.000333	0.076423	0.493087
B4	0.166501	0.158442	0.494356
B5	0.000622	0.245736	0.496693
B6	0.328079	0.410765	0.507507
B7	0.500774	0.323310	0.510463
B8	0.332142	0.075849	0.493062
B9	0.500319	0.155316	0.497409
B10	0.332370	0.239778	0.498479
B11	0.673613	0.410404	0.507378
B12	0.835298	0.330133	0.502414
B13	0.668604	0.075822	0.493278
B14	0.834454	0.158291	0.494630
B15	0.668737	0.239915	0.498595
B16	0.000190	0.913560	0.493574
B17	0.166632	0.831722	0.495727
B18	0.000562	0.577087	0.504547
B19	0.165933	0.659908	0.501427
B20	0.000291	0.744186	0.497937
B21	0.332328	0.914394	0.496078
B22	0.500382	0.834366	0.500191
B23	0.330324	0.579174	0.500077
B24	0.500236	0.663380	0.499003
B25	0.332389	0.749365	0.496191
B26	0.668052	0.914451	0.496200
B27	0.833947	0.831581	0.495388
B28	0.670734	0.579198	0.500862
B29	0.834784	0.659862	0.501156
B30	0.668053	0.749571	0.496109
Ru1	0.500746	0.498645	0.568902
N1	0.495121	0.543594	0.655228
N2	0.509179	0.564038	0.715638
H1	0.410558	0.553849	0.741407

N$_2$H$_2$*

B1	0.999959	0.418304	0.503608
B2	0.165638	0.335845	0.502460
B3	0.999934	0.081752	0.493865
B4	0.166279	0.164132	0.495863
B5	0.999947	0.251278	0.497089
B6	0.329813	0.415809	0.504112
B7	0.499920	0.328455	0.506649
B8	0.331520	0.080600	0.494280
B9	0.499931	0.159853	0.500378
B10	0.332160	0.244795	0.497739
B11	0.670063	0.415797	0.504348

B12	0.834249	0.335860	0.502543
B13	0.668335	0.080609	0.494283
B14	0.833575	0.164155	0.495813
B15	0.667705	0.244775	0.497762
B16	0.999945	0.918803	0.493805
B17	0.166323	0.836362	0.495711
B18	0.999990	0.582150	0.503481
B19	0.165740	0.664589	0.502229
B20	0.999968	0.749231	0.496996
B21	0.331593	0.919845	0.494215
B22	0.499945	0.840587	0.500053
B23	0.330095	0.584700	0.503699
B24	0.499965	0.671693	0.505845
B25	0.332205	0.755580	0.497460
B26	0.668293	0.919847	0.494220
B27	0.833585	0.836366	0.495650
B28	0.669903	0.584763	0.503911
B29	0.834227	0.664578	0.502249
B30	0.667712	0.755611	0.497467
Ru1	0.499936	0.499821	0.568651
N1	0.500285	0.496059	0.656575
N2	0.502288	0.481931	0.722716
H1	0.407816	0.512074	0.746780
H2	0.599147	0.510133	0.744494

N*

B1	0.999993	0.418190	0.504026
B2	0.165624	0.335158	0.501257
B3	0.999993	0.081065	0.492920
B4	0.166487	0.163634	0.494699
B5	0.999993	0.251008	0.496518
B6	0.329538	0.416603	0.500529
B7	0.499993	0.331653	0.502246
B8	0.332306	0.080951	0.494427
B9	0.499993	0.161029	0.499345
B10	0.332200	0.245373	0.496143
B11	0.670447	0.416603	0.500533
B12	0.834361	0.335158	0.501259
B13	0.667679	0.080951	0.494428
B14	0.833498	0.163634	0.494699
B15	0.667785	0.245373	0.496145
B16	0.999993	0.919009	0.492912
B17	0.166488	0.836439	0.494685
B18	0.999993	0.581885	0.504017
B19	0.165624	0.664914	0.501242
B20	0.999993	0.749066	0.496507
B21	0.332306	0.919123	0.494420
B22	0.499993	0.839044	0.499329
B23	0.329539	0.583469	0.500517
B24	0.499993	0.668419	0.502222
B25	0.332200	0.754699	0.496127
B26	0.667679	0.919123	0.494420
B27	0.833497	0.836439	0.494685
B28	0.670446	0.583469	0.500520
B29	0.834361	0.664914	0.501244
B30	0.667785	0.754699	0.496128
Ru1	0.499989	0.500050	0.568827
N1	0.499984	0.500074	0.650725

NH*

B1	0.997683	0.418030	0.504728
B2	0.164159	0.335224	0.502435
B3	0.999248	0.081000	0.492059
B4	0.165517	0.163902	0.494311
B5	0.998906	0.250984	0.497128
B6	0.328517	0.416702	0.499879
B7	0.498382	0.332114	0.499962
B8	0.331599	0.081081	0.495050
B9	0.498729	0.161219	0.500119
B10	0.331280	0.245143	0.495228
B11	0.667888	0.417320	0.496572
B12	0.832857	0.334905	0.501540
B13	0.666937	0.081211	0.496085
B14	0.832200	0.163892	0.496019
B15	0.666667	0.245542	0.495419
B16	0.999249	0.919133	0.492055
B17	0.165520	0.836229	0.494311
B18	0.997684	0.582100	0.504726
B19	0.164162	0.664907	0.502433
B20	0.998908	0.749147	0.497121
B21	0.331604	0.919051	0.495051
B22	0.498732	0.838917	0.500119
B23	0.328521	0.583428	0.499870
B24	0.498387	0.668014	0.499948
B25	0.331286	0.754986	0.495227
B26	0.666937	0.918919	0.496083
B27	0.832200	0.836240	0.496009
B28	0.667887	0.582816	0.496562
B29	0.832857	0.665224	0.501531
B30	0.666667	0.754587	0.495408
Ru1	0.499802	0.500070	0.565246
N1	0.505098	0.500108	0.652421
H1	0.444901	0.500298	0.695343

NH$_2$*

B1	0.000065	0.418245	0.505975
B2	0.165695	0.334259	0.502700
B3	0.000017	0.080942	0.493472
B4	0.166715	0.164278	0.497269
B5	0.000054	0.250257	0.499312
B6	0.330273	0.418191	0.493903
B7	0.500062	0.333832	0.496597
B8	0.333190	0.081417	0.497935
B9	0.500055	0.162762	0.501471
B10	0.332324	0.246340	0.494762
B11	0.669911	0.418157	0.493858
B12	0.834419	0.334273	0.502599
B13	0.666891	0.081396	0.497889
B14	0.833389	0.164266	0.497233
B15	0.667749	0.246292	0.494695
B16	0.000017	0.919231	0.493488
B17	0.166717	0.835893	0.497297
B18	0.000065	0.581927	0.505990
B19	0.165696	0.665915	0.502727
B20	0.000054	0.749916	0.499340
B21	0.333190	0.918757	0.497950
B22	0.500055	0.837415	0.501498
B23	0.330273	0.581986	0.493912

Chapter V. Single-Boron Catalysts for Nitrogen Reduction Reaction

This Chapter demonstrates that the catalytic activity of boron is highly correlated with the degree of charge transfer between the boron atom and the substrate. Among the 21 concept-catalysts, single boron atoms supported on graphene and substituted into h-MoS$_2$ are identified as the most promising NRR catalysts, offering excellent energy efficiency and selectivity against hydrogen evolution reaction.
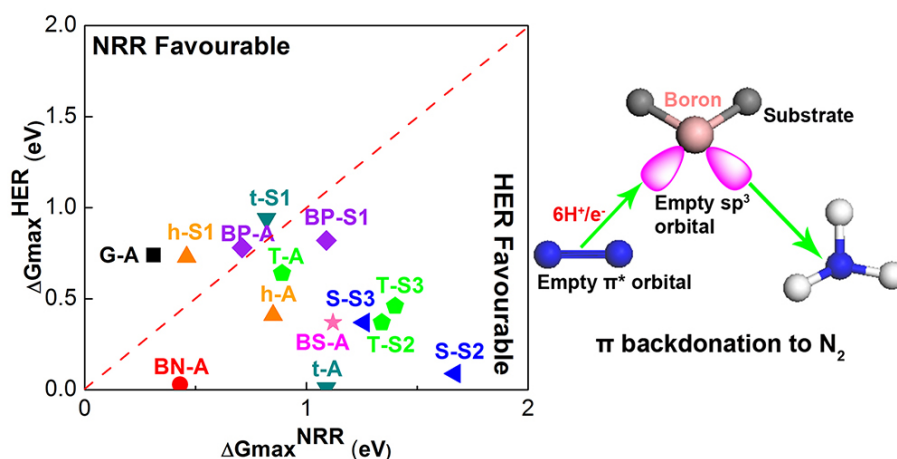
Scheme 5.1 Electrochemical nitrogen reduction reaction on single boron catalysts.

This Chapter consists of two sections: (1) Published Paper, and (2) Supporting Information. The supporting information involves the computational details, the Gibbs free energies, geometries at different intermediates, bader charges variation, and energy of transition states.

5.1 Published Paper

Single-Boron Catalysts for Nitrogen Reduction Reaction

Chuangwei Liu,[†] Qinye Li,[‡] Chengzhang Wu,[§] Jie Zhang,[†] Yonggang Jin,[∥] Douglas R. MacFarlane,[†] and Chenghua Sun*,[†,⊥]

[†]School of Chemistry, Faculty of Science, Monash University, Clayton, Victoria 3800, Australia

[‡]School of Chemical Engineering, Monash University, Clayton, Victoria 3800, Australia

[§]Key Laboratory of Advanced Special Steel, Shanghai Key Laboratory of Advanced Ferrometallurgy, School of Materials Science and Engineering, Shanghai University, Shanghai 200072, China

[∥]CSIRO Energy, 1 Technology Court, Pullenvale, Queensland 4069, Australia

[⊥]Department of Chemistry and Biotechnology, Faculty of Science, Engineering & Technology, Swinburne University of Technology, Hawthorn, Victoria 3122, Australia

S *Supporting Information*

ABSTRACT: Boron has been explored as p-block catalysts for nitrogen reduction reaction (NRR) by density functional theory. Unlike transition metals, on which the active centers need empty d orbitals to accept the lone-pair electrons of the nitrogen molecule, the sp^3 hybrid orbital of the boron atom can form B-to-N π-back bonding. This results in the population of the N−N π^* orbital and the concomitant decrease of the N−N bond order. We demonstrate that the catalytic activity of boron is highly correlated with the degree of charge transfer between the boron atom and the substrate. Among the 21 concept-catalysts, single boron atoms supported on graphene and substituted into h-MoS$_2$ are identified as the most promising NRR catalysts, offering excellent energy efficiency and selectivity against hydrogen evolution reaction.

In 2017, global ammonia (NH$_3$) production reached 172 million tons, overwhelmingly by the energy-intensive Haber−Bosch (H−B) process using methane-reformed hydrogen (H$_2$) to react with dinitrogen (N$_2$), to carry out the nitrogen reduction reaction (NRR).[1] As a result, globally significant energy consumption and carbon emission are involved.[1−3] Hence it is of paramount importance to develop green techniques to replace H−B production of ammonia.[4]

The key is a catalyst that could effectively activate and convert N$_2$ to NH$_3$ under mild conditions.[5] Inspired by the biological process one could envisage N$_2$ fixation to occur upon addition of protons and electrons to an appropriate catalyst at room temperature. Ammonia has been successfully synthesized in a solid electrolyte cell by electrochemical methods.[6] During this process, water is often the proton source, rather than H$_2$, and more importantly, solar electricity can be employed to drive the reaction at room temperature if NRR catalysts are active enough.[7−12] To achieve this, two challenges should be addressed, namely, high NRR over-potential and low Faraday efficiency (FE).[13,14] Ideally, the electrocatalyst should have a strong capacity to catalyze NRR while at the same time suppress the competing hydrogen

evolution reaction (HER). In this context, numerous electro-catalysts have been widely investigated, such as MXenes,[15] Fe-graphene,[16] Mo-BN,[17,18] Fe-MoN$_2$,[19] Mo-C$_2$N,[20] W-C$_3$N$_4$,[21] and more can be found in several excellent reviews.[5,22−24] In most cases, activation of N$_2$ relies on the catalytic center of transition metals (TMs), which are often active for HER, and thus high FE is difficult to achieve.[25,26]

In 2018, a pioneering work demonstrated that N$_2$ could be fixed and reduced by boron atoms,[27] providing a new pathway for NRR at ambient conditions. Boron has three valence electrons in the $2s^2 2p^1$ and an empty orbital that is similar to the d orbital of TMs.[28] In addition, B atoms can also prohibit the binding of Lewis acid H$^+$ under acidic conditions, which can promote NRR and suppress HER as expected.[29,30] So far, several B-based electrocatalyts have been reported in the past months, namely, B-graphene, B-g-C$_3$N$_4$, and 2D boron sheets.[30−32] Different from transition metals,[33,34] boron offers p-block catalysis; so far, however, the relationship between the states of boron and NRR performance is poorly known. Here we investigate the design principles that can be used for the rational design of boron-based NRR catalysts and reveal how the local bonding structure and boron−substrate charge transfer can affect the NRR catalysis and selectivity.

Following early studies of single-boron NRR catalysts,[29,31] we constructed 21 models through incorporating one boron atom on eight popular 2D materials, including graphene (**G**), boron nitride (**BN**), boron sulfide (**BS**), black phosphorus (**BP**), S-triazine-based g-C$_3$N$_4$ (**S**), tri-s-triazine-based g-C$_3$N$_4$ (**T**), h-MoS$_2$ (**h**), and T-MoS$_2$ (**t**). Specifically, three boron states have been studied, including adsorbed (A), substituted (S), and lattice boron (D), as shown in Figure 1. As a result, 21 boron-based catalysts are generated and labeled as "**2D substrate−B site**", such as **G-A**, indicating boron adsorbed on graphene. We start from the stability of these concept-catalysts using the adsorption energies of boron (E_{ads}), the cohesive energy of boron (E_{coh}), and formation energy as listed in Table S1. Negative ($E_{ads} + E_{coh}$) indicates high thermodynamic stability of such boron catalysts. Among
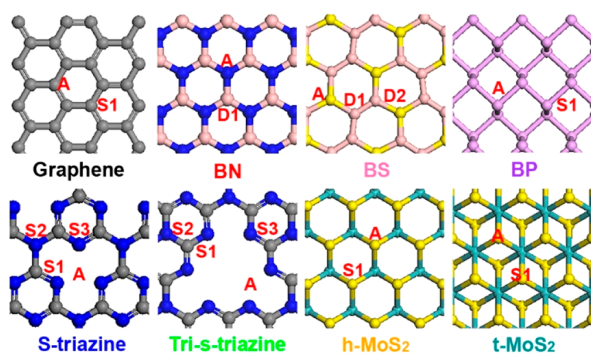
197

Figure 1. Proposed 2D materials and potential B-sites. The numbers indicate different bonding environments described in the text. Black, blue, rose, yellow, purple, and cyan spheres represent C, N. B, S, P, and Mo, respectively.

Figure 2. Volcano diagrams for the 14 catalysts for nitrogen reduction reaction.

these catalysts, only three are positive, including **BN**-A (0.28 eV), **BS**-A (1.35 eV), and **T**-A (0.48 eV), for which the diffusion barrier of boron is large, indicating that these single-boron catalysts are kinetically stable.[35−37] As indicated by formation energy, B-doped or B-adsorbed structures can be formed, indicating that these concept-catalysts can be synthesized readily, being line with recent experiments.[38−41]

Generally, three mechanisms were considered for NRR, being the distal, alternating, and enzymatic paths. According to our investigations, the enzymatic path is not feasible because enzymatic intermediates fail to form on these catalysts. Therefore, only the distal and alternating mechanisms have been investigated. Fully relaxed structures are shown in Figures S1−S8, according to which seven models (**G**-S1, **BN**-D1, **BS**-D1, **BS**-D2, **S**-A, **S**-S1, and **T**-S1) are not eligible for following NRR because N_2 cannot be fixed over these sites, as indicated by the large boron−nitrogen distance (>3.0 Å, see Table S1). Boron atoms terminated by three p-block atoms, such as **BS**-D1, **BS**-D2, **S**-A, **S**-S1, and **T**-S1, cannot adsorb extra nitrogen. As reflected by the Bader charge (δ), boron atoms contained by these seven catalysts lose more than two electrons. Clearly, the coexistence of partially occupied states and empty states is essential for B-based NRR catalysts; therefore, fully coordinated boron is not active for NRR.

To examine NRR performance, elementary steps associated with distal and alternating mechanisms have been studied.[16,42] The overall performance was evaluated based on calculated ΔG values for elementary steps, with the maximum, ΔG_{max}, representing an indicator of the overall energy input required; as a result, it is often employed to determine the limiting potential and overpotential required for NRR.[17] Figure 2 shows the calculated ΔG_{max} versus $E(N^*) − E(N^*)_{Ru}$, where $E(N^*)$ is the binding energy of a single N, which has been identified as an excellent indicator for NRR catalysts,[43] and N-adsorption on Ru has been employed as a reference. All intermediate states and energy profiles of two possible reaction pathways are shown in the Supporting Information (Figures S9−S22). Similar to early studies,[7,33] a volcano plot has been observed between ΔG_{max} and $E(N^*)$ for these catalysts, among which those with $E(N^*)$ being close to that on Ru(0001) often offer excellent NRR catalysis.[7,33] As confirmed in Figure 2, this rule is applicable to these boron-based catalysts. Specifically, $E(N^*)$ for **G**-A, **BN**-A, and **h**-S1 is −0.45, −0.52, and −0.54 eV, respectively, being close to the benchmark value for Ru
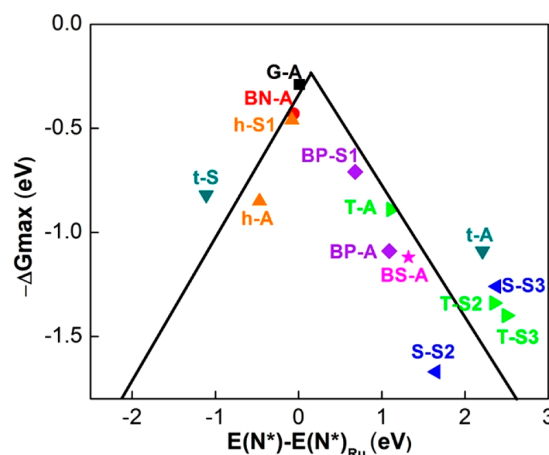
(0001) ($E(N^*) = −0.46$ eV).[7] These offer $\Delta G_{max} = 0.31, 0.45$, and 0.46 eV, respectively. Such performance is much better than most reported single-metal catalysts.[16,19]

HER is the key side reaction and directly consumes protons and electrons, leading to low FE.[13,32,44] The overall HER is often evaluated by a three-state diagram consisting of initial H^+ state, intermediate H^*, and $1/2$ H_2 as the final product.[45] An ideal HER catalyst has nearly zero free energy $\Delta G(H^*)$, indicating ultralow overpotential. As shown in Figure 3a, the studied catalysts perform remarkably differently, with **BN**-A and **S**-S2 offering superior HER performance with $\Delta G(H^*) <$ 0.1 eV, while **t**-S1 shows $\Delta G(H^*) \approx 0.9$ eV. Therefore, it is important to further clarify whether the relationship between HER performance and the state of boron is the same or similar to that for NRR, which can directly determine NRR selectivity.

Figure 3b compares the energy request for HER and NRR, as determined by the maximum ΔG, in which catalysts located above the red dashed line offer optimum NRR selectivity. Accordingly, NRR catalyzed by **G**-A, **h**-S1, **BP**-A, and **t**-S1 would be less hindered by H adsorption in the low energy barrier region. Combined NRR energy efficiency, as indicated by ΔG_{max} and selectivity, would indicate that **G**-A and **h**-S1 are particularly attractive for further experimental validations. This prediction has been partially supported by an early experiment, which demonstrated that boron-doped graphene offers an FE = 10.8% for NRR,[26] remarkably higher than most transition metals.[5,20,21]

It is worth understanding the relationship between NRR performance and boron chemical environment. As seen in Table S1, Bader charge, δ, has a direct impact on N_2 adsorption. To further understand the relationship between catalytic performance and the boron−substrate electron transfer, the ΔG_{max} for NRR and ΔG_{max} for HER versus the Bader charges are shown in Figure 4. The plot shows that small and even negative δ leads to small energy request for NRR but large $\Delta G(H^*)$. As B → N_2 electron transfer plays a key role for N_2 adsorption and activation,[27] more electrons in the boron site would increase the possibility for such electron injection and following reduction. In the case of HER, however, positively charged B is obviously favorable, as indicated by the orange line in Figure 4. It is well known that Bader population often gives larger charges than those by Hirshfeld and Mulliken
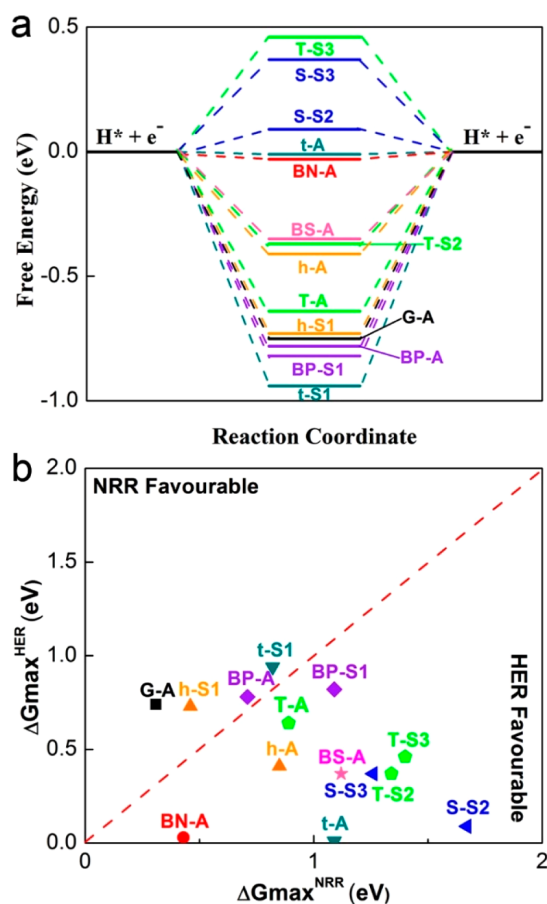
Figure 3. Computational screening of 14 catalyst combinations: (a) Hydrogen evolution reaction performance; (b) ΔG_{max}^{HER} vs ΔG_{max}^{NRR}.
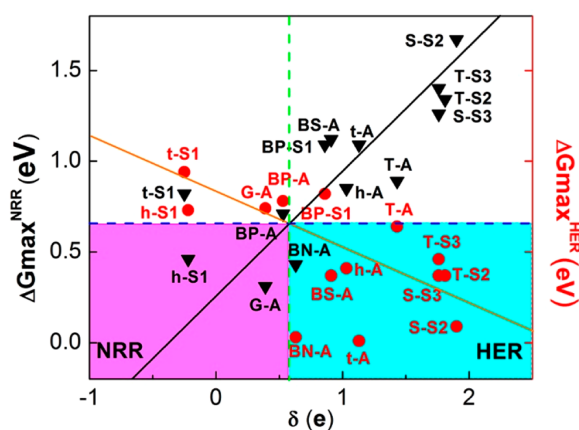

Figure 4. Computational screening of 14 catalyst combinations in terms of ΔG_{max}^{HER} and ΔG_{max}^{NRR} vs Bader charge (δ, in units of e) of single boron in or on a 2D substrate.

methods, but these populations follow an approximate linear relationship (Figure S24).[46] Therefore, a different method does not affect the conclusion. Overall, negatively charged boron sites seem to offer enhanced NRR performance in terms of energy efficiency and selectivity.

In terms of the kinetics, additional calculations have been performed to search the transition states for the promising NRR catalysts **G**-A and **h**-S1, as identified above (the pink area in Figure 4 is the NRR favorable zone, having a small energy requirement and high selectivity). Full reaction energies and transition states in the favorable pathway are presented in Figure S25). The largest reaction energies for the **G**-A and **h**-S1 materials are only 0.31 and 0.46 eV in the distal pathway, respectively. Moreover, the activation barrier for initial hydrogenation $N_2^* \rightarrow N_2H^*$ is 0.38 and 0.90 eV for **G**-A and **h**-S1, respectively. However, it is worth noting that the kinetic rate-determining step (RDS) for **G**-A and **h**-S1 are different, being the first hydrogenation step (TS1, 0.90 eV) for **h**-S1 and the fourth hydrogenation step for **G**-A (TS3, 0.81 eV, see Figure S25). All these activation barriers are even smaller than the reaction energy on flat Ru (1.08 eV),[7] indicating that an excellent kinetics can be expected from these two catalysts.

In summary, we have systematically studied 21 B-based concept NRR catalysts. We identify two promising catalysts, **h**-S1 and **G**-A, as offering appropriate thermodynamics, selectivity, and kinetics. By taking consideration of electron transfer of the boron dopant on charge redistribution over the 2D substrate surface, we have developed the design principles for enhancing B-catalyzed NRR, that negatively charged boron sites are promising for low overpotential and high selectivity, which can be hardly obtainable from TM catalysts. Our findings can be explained by competition between the ability to form covalent bonds with nitrogen and that to transfer electrons in the reaction, which not only reduces the energy barrier and stabilizes the adsorbates but also supports fast NRR kinetics. Importantly, N_2 becomes activated via the distal pathway on the **G**-A and **h**-S1 surfaces, exhibiting relatively low reaction energy barriers of 0.31 and 0.46 eV, respectively, with relatively small activation barriers.

■ ASSOCIATED CONTENT

ⓢ Supporting Information

The Supporting Information is available free of charge on the ACS Publications website at DOI: 10.1021/jacs.8b13165.

Computational details (PDF)

■ AUTHOR INFORMATION

Corresponding Author

*chenghuasun@swin.edu.au

ORCID ⓘ

Jie Zhang: 0000-0003-2493-5209
Douglas R. MacFarlane: 0000-0001-5963-9659
Chenghua Sun: 0000-0001-7654-669X

Notes

The authors declare no competing financial interest.

■ ACKNOWLEDGMENTS

199

■ REFERENCES

(1) Ham, C. J. M.; Koper, M. T. M.; Hetterscheid, D. G. H. Challenges in Reduction of Dinitrogen by Proton and Electron Transfer. *Chem. Soc. Rev.* **2014**, *43*, 5183−5191.

(2) Rod, T. H.; Logadottir, A.; Nørskov, J. K. Ammonia Synthesis at Low Temperatures. *J. Chem. Phys.* **2000**, *112*, 5343.

(3) Montoya, J. J.; Charlie, T.; Aleksandra, V.; Norskov, J. K. The Challenge of Electrochemical Ammonia Synthesis: A New Perspective on the Role of Nitrogen Scaling Relations. *ChemSusChem* **2015**, *8*, 2180−2186.

(4) Klerke, A.; Christensen, C. H.; Nørskov, J. K.; Vegge, T. Ammonia for Hydrogen Storage: Challenges and Opportunities. *J. Mater. Chem.* **2008**, *18*, 2304−2310.

(5) Guo, C.; Ran, J.; Vasileff, A.; Qiao, S. Rational Design of Electrocatalysts and Photo(electro)catalysts for Nitrogen Reduction to Ammonia (NH_3) under Ambient Conditions. *Energy Environ. Sci.* **2018**, *11*, 45−56.

(6) Marnellos, G.; Stoukides, M. Ammonia Synthesis at Atmospheric Pressure. *Science* **1998**, *282*, 98−100.

(7) Skúlason, E.; Bligaard, T.; Gudmundsdóttir, S.; Studt, F.; Rossmeisl, J.; Abild-Pedersen, F.; Vegge, T.; Jónsson, H.; Nørskov, J. K. A Theoretical Evaluation of Possible Transition Metal Electrocatalysts for N_2 Reduction. *Phys. Chem. Chem. Phys.* **2012**, *14*, 1235−1245.

(8) Abghoui, Y.; Garden, A. L.; Hlynsson, V. F.; Bjorgvinsdottir, S.; Olafsdottir, H.; Skulason, E. Enabling Electrochemical Reduction of Nitrogen to Ammonia at Ambient Conditions through Rational Catalyst Design. *Phys. Chem. Chem. Phys.* **2015**, *17*, 4909−4918.

(9) Studt, F.; Tuczek, F. Energetics and Mechanism of a Room-Temperature Catalytic Process for Ammonia Synthesis (Schrock Cycle): Comparison with Biological Nitrogen Fixation. *Angew. Chem., Int. Ed.* **2005**, *44*, 5639−5642.

(10) Amar, I. A.; Lan, R.; Petit, C. T. G.; Tao, S. Solid-state Electrochemical Synthesis of Ammonia: A Review. *J. Solid State Electrochem.* **2011**, *15*, 1845−1860.

(11) Amar, I. A.; Lan, R.; Humphreys, J.; Tao, S. Electrochemical Synthesis of Ammonia from Wet Nitrogen via a Dual-chamber Reactor Using $La_{0.6}Sr_{0.4}Co_{0.2}Fe_{0.8}O_{3−\Delta}$-$Ce_{0.8}Gd_{0.18}Ca_{0.02}O_{2−\Delta}$ Composite Cathode. *Catal. Today* **2017**, *286*, 51−56.

(12) Chen, S.; Perathoner, S.; Ampelli, C.; Mebrahtu, C.; Su, D.; Centi, G. Electrocatalytic Synthesis of Ammonia at Room Temperature and Atmospheric Pressure from Water and Nitrogen on a Carbon-Nanotube-Based Electrocatalyst. *Angew. Chem., Int. Ed.* **2017**, *56*, 2699−2703.

(13) Singh, A. R.; Rohr, B. A.; Schwalbe, J. A.; Cargnello, M.; Chan, K.; Jaramillo, T. F.; Chorkendorff, I.; Nørskov, J. K. Electrochemical Ammonia Synthesis—the Selectivity Challenge. *ACS Catal.* **2017**, *7*, 706−709.

(14) Lan, R.; Alkhazmi, K. A.; Amar, I. A.; Tao, S. Synthesis of Ammonia Directly from Wet Air Using New Perovskite Oxide $La_{0.8}Cs_{0.2}Fe_{0.8}Ni_{0.2}O_{3−\delta}$ as Catalyst. *Electrochim. Acta* **2014**, *123*, 582−587.

(15) Azofra, L. M.; Li, N.; MacFarlane, D. R.; Sun, C. Promising Prospects for 2D d^2−d^4 M_3C_2 Transition Metal Carbides (MXenes) in N_2 Capture and Conversion into Ammonia. *Energy Environ. Sci.* **2016**, *9*, 2545−2549.

(16) Li, X.; Li, Q.; Cheng, J.; Liu, L.; Yan, Q.; Wu, Y.; Zhang, X.; Wang, Z.; Qiu, Q.; Luo, Y. Conversion of Dinitrogen to Ammonia by FeN_3-Embedded Graphene. *J. Am. Chem. Soc.* **2016**, *138*, 8706−8709.

(17) Zhao, J.; Chen, Z. Single Mo Atom Supported on Defective Boron Nitride Monolayer as an Efficient Electrocatalyst for Nitrogen Fixation: A Computational Study. *J. Am. Chem. Soc.* **2017**, *139*, 12480−12487.

(18) Han, L.; Liu, X.; Chen, J.; Lin, R.; Liu, H.; Lu, F.; Bak, S.; Liang, Z.; Zhao, S.; Stavitski, E.; Luo, J.; Adzic, R. R.; Xin, H. Atomically Dispersed Mo Catalysts for High-efficiency Ambient N_2 Fixation. *Angew. Chem., Int. Ed.* DOI: 10.1002/anie.201811728.

(19) Li, Q.; He, L.; Sun, C.; Zhang, X. Computational Study of MoN_2 Monolayer as Electrochemical Catalysts for Nitrogen Reduction. *J. Phys. Chem. C* **2017**, *121*, 27563−27568.

(20) Wang, Z.; Yu, Z.; Zhao, J. Computational Screening of a Single Transition Metal Atom Supported on the C_2N Monolayer for Electrochemical Ammonia Synthesis. *Phys. Chem. Chem. Phys.* **2018**, *20*, 12835−12844.

(21) Chen, Z.; Zhao, J.; Cabrera, C. R.; Chen, Z. Computational Screening of Efficient Single-Atom Catalysts Based on Graphitic Carbon Nitride (g-C_3N_4) for Nitrogen Electroreduction. *Small Methods* **2018**, 1800368.

(22) Chen, X.; Li, N.; Kong, Z.; Ong, W.; Zhao, X. Photocatalytic Fixation of Nitrogen to Ammonia: State-of-the-art Advancements and Future Prospects. *Mater. Horiz.* **2018**, *5*, 9−27.

(23) Cui, X.; Tang, C.; Zhang, Q. A Review of Electrocatalytic Reduction of Dinitrogen to Ammonia under Ambient Conditions. *Adv. Energy Mater.* **2018**, *8*, 1800369.

(24) Jin, H.; Guo, C.; Liu, X.; Liu, J.; Vasileff, A.; Jiao, Y.; Zheng, Y.; Qiao, S. Emerging Two-Dimensional Nanomaterials for Electrocatalysis. *Chem. Rev.* **2018**, *118*, 6337−6408.

(25) Tian, Y.; Pierpont, A. W.; Batista, E. R. How Does Nishibayashi's Molybdenum Complex Catalyze Dinitrogen Reduction to Ammonia? *Inorg. Chem.* **2014**, *53*, 4177−4183.

(26) Jiao, Y.; Zheng, Y.; Davey, K.; Qiao, S. Activity Origin and Catalyst Design Principles for Electrocatalytic Hydrogen Evolution on Heteroatom-doped Graphene. *Nat. Energy* **2016**, *1*, 16130.

(27) Légaré, M. A.; Bélanger-Chabot, G.; Dewhurst, R. D.; Welz, E.; Krummenacher, I.; Engels, B.; Braunschweig, H. Nitrogen Fixation and Reduction at Boron. *Science* **2018**, *359*, 896−900.

(28) Ma, F.; Jiao, Y.; Gao, G.; Gu, Y.; Bilic, A.; Chen, Z.; Du, A. Graphene-like Two-Dimensional Ionic Boron with Double Dirac Cones at Ambient Condition. *Nano Lett.* **2016**, *16*, 3022−3028.

(29) Hering-Junghans, C. Metal-Free Nitrogen Fixation at Boron. *Angew. Chem., Int. Ed.* **2018**, *57*, 6738−6740.

(30) Yu, X.; Han, P.; Wei, Z.; Huang, L.; Gu, Z.; Peng, S.; Ma, J.; Zheng, G. Boron-Doped Graphene for Electrocatalytic N_2 Reduction. *Joule* **2018**, *2*, 1610−1622.

(31) Ling, C.; Niu, X.; Li, Q.; Du, A.; Wang, J. Metal-Free Single Atom Catalyst for N_2 Fixation Driven by Visible Light. *J. Am. Chem. Soc.* **2018**, *140*, 14161−14168.

(32) Liu, C.; Li, Q.; Zhang, J.; Jin, Y.; MacFarlane, D. R.; Sun, C. Theoretical Evaluation of Possible 2D Boron Monolayer in N_2 Electrochemical Conversion into Ammonia. *J. Phys. Chem. C* **2018**, *122*, 25268−25273.

(33) Vasileff, A.; Xu, C.; Ge, L.; Zheng, Y.; Qiao, S. Bronze Alloys with Tin Surface Sites for Selective Electrochemical Reduction of CO_2. *Chem. Commun.* **2018**, *54*, 13965−13968.

(34) Ling, C.; Ouyang, Y.; Li, Q.; Bai, X.; Mao, X.; Du, A.; Wang, J. A General Two-Step Strategy-Based High-Throughput Screening of Single Atom Catalysts for Nitrogen Fixation. *Small Methods* **2018**, 1800376.

(35) Liu, J.; Tang, Y.; Wang, Y.; Zhang, T.; Li, J. Theoretical Understanding of the Stability of Single-atom Catalysts. *Natl. Sci. Rev.* **2018**, *5*, 638−641.

(36) Ouyang, R.; Liu, J.; Li, W. Atomistic Theory of Ostwald Ripening and Disintegration of Supported Metal Particles under Reaction Conditions. *J. Am. Chem. Soc.* **2013**, *135*, 1760−1771.

(37) Vilé, G.; Albani, D.; Nachtegaal, M.; Chen, Z.; Dontsova, D.; Antonietti, M.; López, N.; Pérez-Ramírez, J. A Stable Single-Site Palladium Catalyst for Hydrogenations. *Angew. Chem., Int. Ed.* **2015**, *54*, 11265−11269.

(38) Usachov, D. Y.; Fedorov, A. V.; Petukhov, A. E.; Vilkov, O. Y.; Rybkin, A. G.; Otrokov, M. M.; Arnau, A.; Chulkov, E. V.; Yashina, L. V.; Farjam, M. Epitaxial B-Graphene: Large-Scale Growth and Atomic Structure. *ACS Nano* **2015**, *9*, 7314−7322.

(39) Agnoli, S.; Favaro, M. Doping Graphene with Boron: A Review of Synthesis Methods, Physicochemical Characterization, and Emerging Applications. *J. Mater. Chem. A* **2016**, *4*, 5002−5025.

200

(40) Rao, C. N. R.; Gopalakrishnan, K.; Govindaraj, A. Synthesis, Properties and Applications of Graphene Doped with Boron, Nitrogen and other Elements. *Nano Today* **2014**, *9*, 324−343.

(41) Gao, D.; Liu, Y.; Liu, P.; Si, M.; Xue, D. Atomically Thin B Doped G-C_3N_4 Nanosheets: High-Temperature Ferromagnetism and Calculated Half-Metallicity. *Sci. Rep.* **2016**, *6*, 35768.

(42) Anderson, J. S.; Cutsail, G. E.; Rittle, J.; Connor, B. A.; Gunderson, W. A.; Zhang, L.; Hoffman, B. M.; Peters, J. C. Characterization of an Fe≡N-NH_2 Intermediate Relevant to Catalytic N_2 Reduction to NH_3. *J. Am. Chem. Soc.* **2015**, *137*, 7803−7809.

(43) Jacobsen, C. J. H.; Dahl, S.; Clausen, B. S.; Bahn, S.; Logadottir, A.; Nørskov, J. K. Catalyst Design by Interpolation in the Periodic Table: Bimetallic Ammonia Synthesis Catalysts. *J. Am. Chem. Soc.* **2001**, *123*, 8404−8405.

(44) Choi, C.; Back, S.; Kim, N.; Lim, J.; Kim, Y.; Jung, Y. Suppression of Hydrogen Evolution Reaction in Electrochemical N_2 Reduction Using Single-Atom Catalysts: A Computational Guideline. *ACS Catal.* **2018**, *8*, 7517−7525.

(45) Tang, Q.; Jiang, D. Mechanism of Hydrogen Evolution Reaction on 1T-MoS_2 from First Principles. *ACS Catal.* **2016**, *6*, 4953−4961.

(46) De Proft, F.; Van Alsenoy, C.; Peeters, A.; Langenaeker, W.; Geerlings, P. Atomic Charges, Dipole Moments, and Fukui Functions Using the Hirshfeld Partitioning of the Electron Density. *J. Comput. Chem.* **2002**, *23*, 1198−1209.

201

5.2 Supporting Information

Single-Boron Catalysts for Nitrogen Reduction Reaction

Chuangwei Liu,[a] Qinye Li,[b] Chengzhang Wu,[c] Jie Zhang,[a] Yonggang Jin,[d] Douglas R. MacFarlane,[a] Chenghua Sun[*,e]

[a] School of Chemistry, Faculty of Science, Monash University, Clayton, Victoria 3800, Australia

[b] School of Chemical Engineering, Monash University, Clayton, Victoria 3800, Australia

[c] Key Laboratory of Advanced Special Steel, Shanghai Key Laboratory of Advanced Ferrometallurgy, School of Materials Science and Engineering, Shanghai University, Shanghai 200072, China

[d] CSIRO Energy, 1 Technology Court, Pullenvale, Queensland 4069, Australia

[e] Department of Chemistry and Biotechnology, Faculty of Science, Engineering & Technology, Swinburne University of Technology, Hawthorn, Victoria 3122, Australia

Email: chenghuasun@swin.edu.au

Contents

Contents	Pages
Computational Details	S2
Table 1	S3
Optimized Structures	S4
Calculated Reaction Free Energies	S8
Bader Charges Variation	S17
Hirshfeld charge vs. Bader charge	S18
Energy of Transition States	S19
References	S20

COMPUTATIONAL METHOD

In this study, all the computations about those structures and energies were based on the standard DFT by using Vienna ab initio Simulation Package (5.4.4 VASP).[1] The electron exchange correlation functional was treated through the generalized gradient approximation (GGA) with the revised Perdew-Burke-Ernzerhof.[2] The 380 eV energy cutoff was adopted and Brillouin zone was sampled with a $3\times3\times1$ k-points using the Monkhorst-Pack scheme grid for geometry optimization and self-consistent calculations. A vacuum space exceeds 20 Å was employed to avoid the interaction between two periodic units. The atomic position was fully relaxed until the maximum force on each atom was less than -0.01 eV/A and 10^{-5} eV. And thermal and zero point energy (ZPE) corrections were calculated over Γ points.[3] The van der Waals interaction has been considered using the DFT-D_3 scheme.[4]

Since the G-A and h-S1 surfaces are demonstrated to be the most promising catalysts for the N_2 conversion into NH_3, due to the low reaction energies the exhibit, the nudge elastic band (NEB) method has been applied to these materials to find the transition states (TS) through the minimum energy path.[5]

Table S1. Calculated free energy G(H*), E_{ads}, $E_{ads}+E_{coh}$, Formation energy (ForE), Bader charge (δ), B-N bond length, $\Delta G(N_2*)$, ΔG_{max} and $\Delta E(N*)$.

	HER (eV)	Eads (eV)	$E_{ads}+E_{coh}$ (eV)	ForE (eV)	δ (e)	B-N (Å)	$\Delta G(N_2*)$ (eV)	ΔG_{max} (eV)	$\Delta E(N*)$ (eV)
G-A	-0.74	-5.86	-0.05		0.39	1.32	0.09	0.31	-0.45
G-S1	0.41	-5.99	-0.18	1.16	2.03	3.51			
BN-A	-0.03	-5.53	0.28		0.63	1.38	0.20	0.43	-0.52
BN-D1	2.47				2.15	3.25			
BS-A	-0.37	-4.46	1.35		0.91	1.38	1.04	1.12	0.86
BS-D1	0.57				1.59	3.52			
BS-D2	0.13				1.67	3.58			
BP-A	-0.78	-6.21	-0.40		0.53	1.41	0.65	0.71	0.22
BP-S1	-0.82	-7.08	-1.27	2.08	0.86	1.50	0.38	1.09	0.63
S-A	-0.52	-7.87	-2.06		2.04	3.18			
S-S1	1.74	-6.35	-0.54	0.41	2.31	3.41			
S-S2	0.09	-6.84	-1.03	0.47	1.90	1.56	0.23	1.67	1.19
S-S3	0.37	-6.19	-0.38	0.38	1.76	1.47	1.00	1.26	1.92
T-A	-0.64	-5.33	0.48		1.43	1.42	-0.51	0.89	0.65
T-S1	1.81	-7.16	-1.35	0.27	2.16	3.49			
T-S2	-0.37	-7.05	-1.24	0.29	1.81	1.49	0.06	1.34	1.89
T-S3	0.46	-6.28	-0.47	0.33	1.76	1.44	0.64	1.40	2.04
h-A	-0.41	-6.18	-0.37		1.03	1.38	0.80	0.85	-0.93
h-S1	-0.73	-6.48	-0.67	0.65	-0.22	1.32	-0.39	0.46	-0.54
t-A	-0.01	-7.28	-1.47		1.13	1.33	0.52	1.09	1.75
t-S1	-0.94	-7.84	-2.03	1.23	-0.25	1.44	-0.45	1.62	-1.57
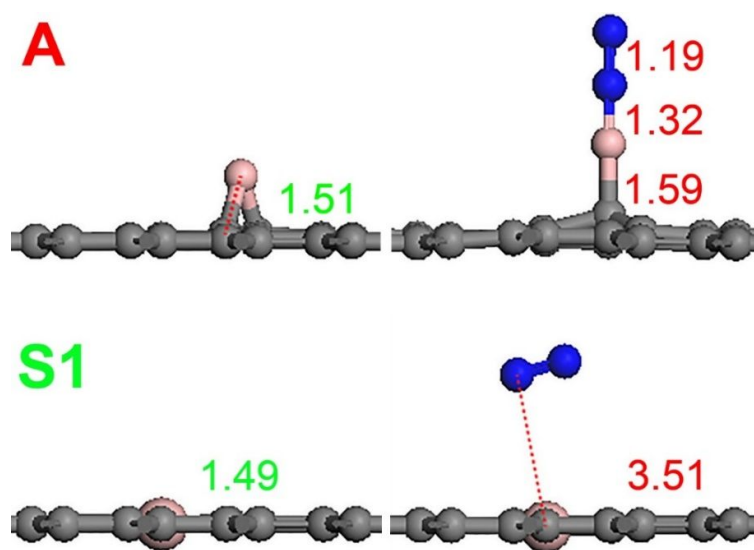
Figure S1. Optimized structures of N_2 adsorption on different boron (B) atom active sites of graphene. The key B-substrates, B-N, and N-N lengths (Å) are also given.
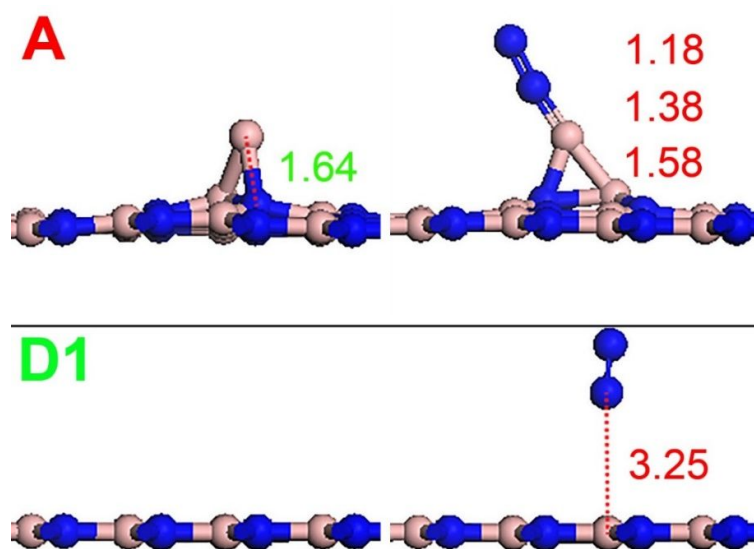
Figure S2. Optimized structures of N_2 adsorption on different boron (B) atom active sites of boron nitride (BN). The key B-substrates, B-N and N-N lengths (Å) are also given.
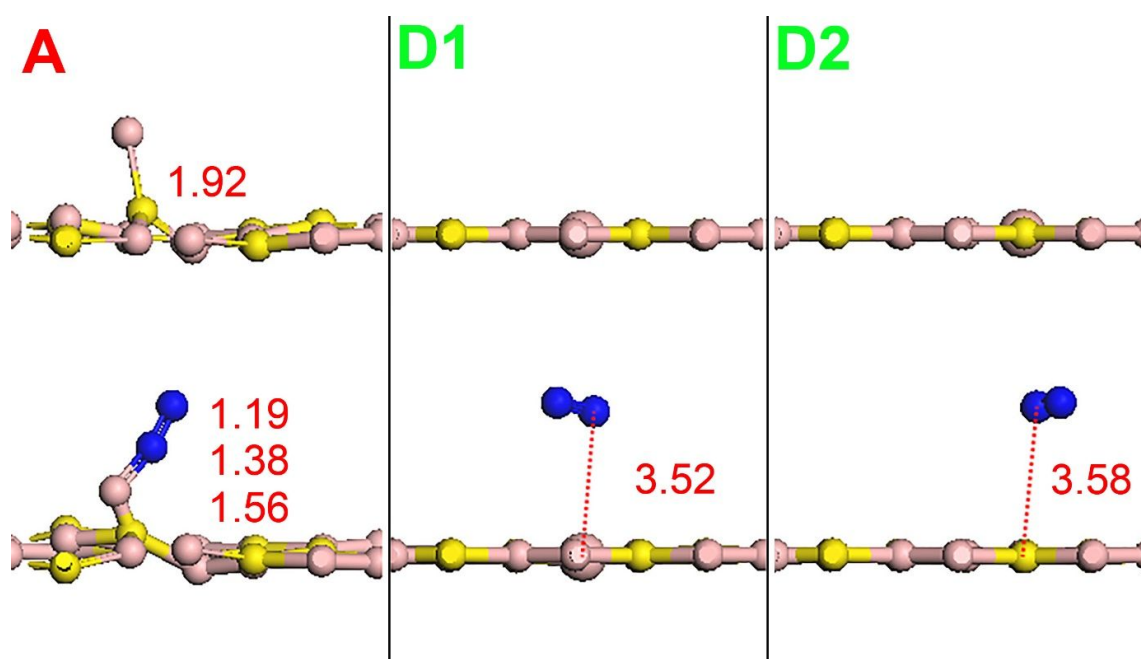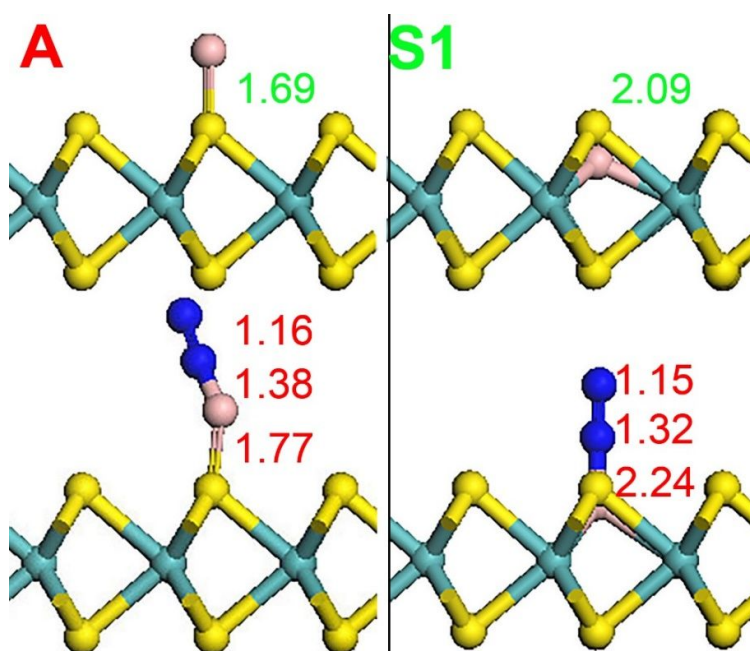
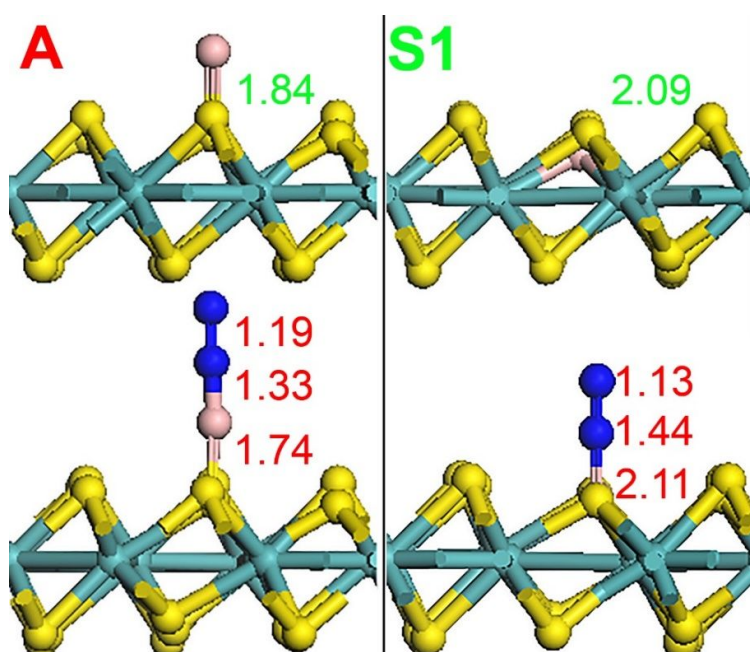**Figure S3.** Optimized structures of N_2 adsorption on different boron (B) atom active sites of boron sulfide (BS). The key B-substrates, B-N and N-N lengths (Å) are also given.
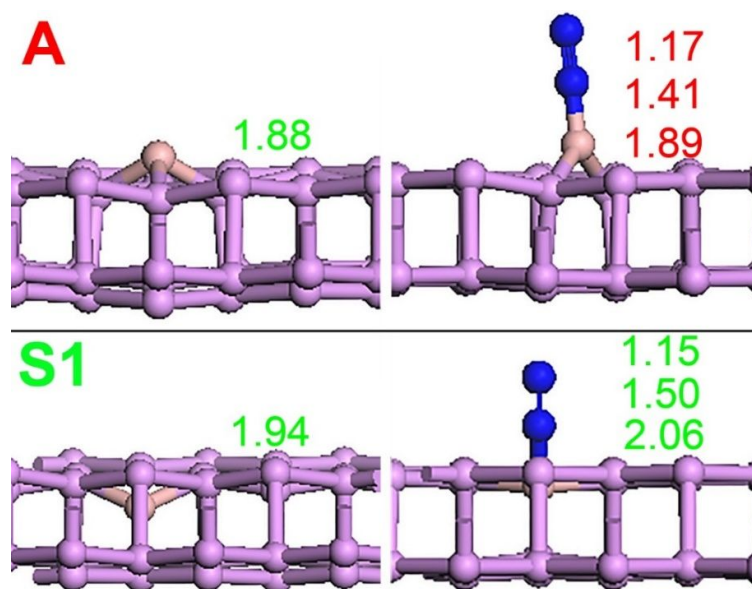
Figure S4. Optimized structures of N_2 adsorption on different boron (B) atom active sites of black phosphorus (BP). The key B-substrates, B-N and N-N lengths (Å) are also given.
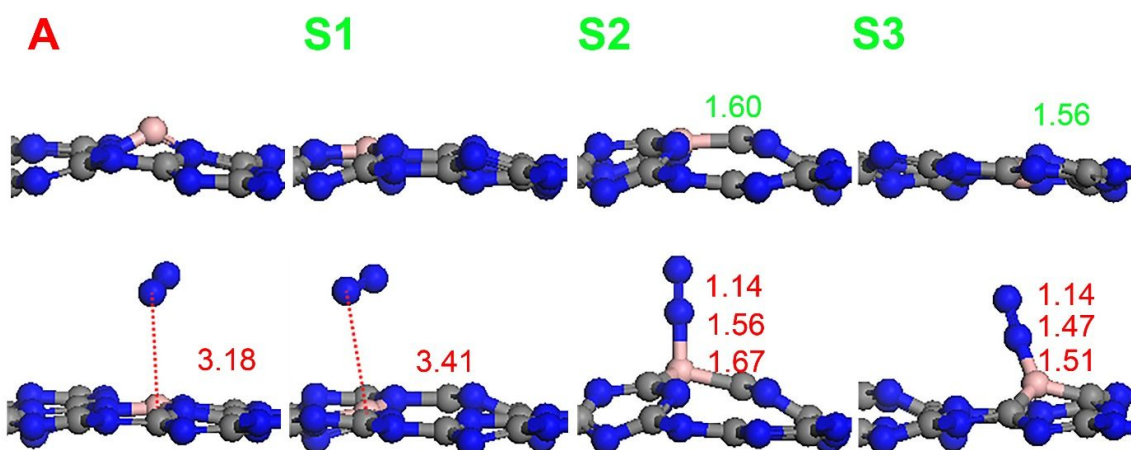
Figure S5. Optimized structures of N_2 adsorption on different boron (B) atom active sites of S-triazine (g-C_3N_4). The key B-substrates, B-N, and N-N lengths (Å) are also given.
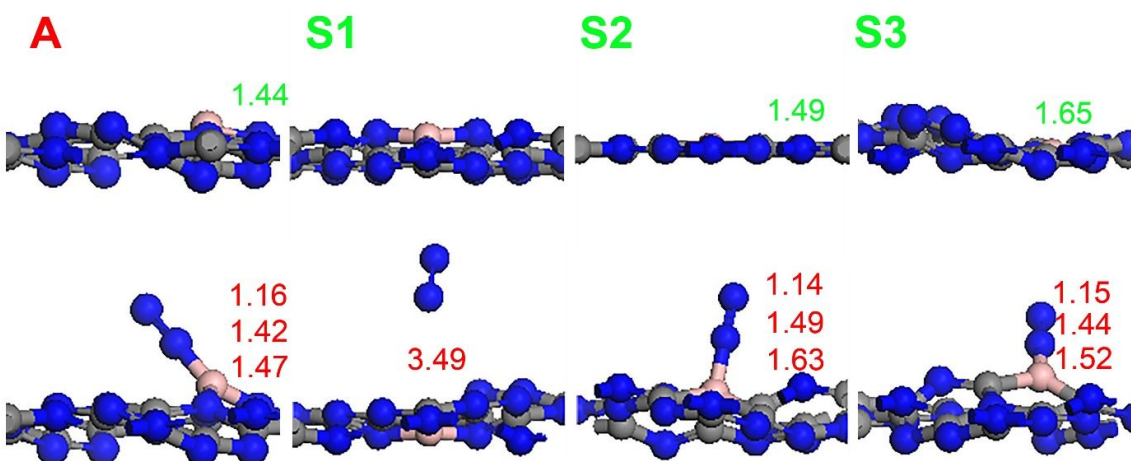
Figure S6. Optimized structures of N_2 adsorption on different boron (B) atom active sites of Tri-s-triazine (C_3N_4). The key B-substrates, B-N, and N-N lengths (Å) are also given.

210

Figure S7. Optimized structures of N_2 adsorption on different boron (B) atom active sites of molybdenum disulfide (h-MoS$_2$). The key B-substrates, B-N, and N-N lengths (Å) are also given.

Figure S8. Optimized structures of N_2 adsorption on different boron (B) atom active sites of molybdenum disulfide (t-MoS$_2$). The key B-substrates, B-N, and N-N lengths (Å) are also given.
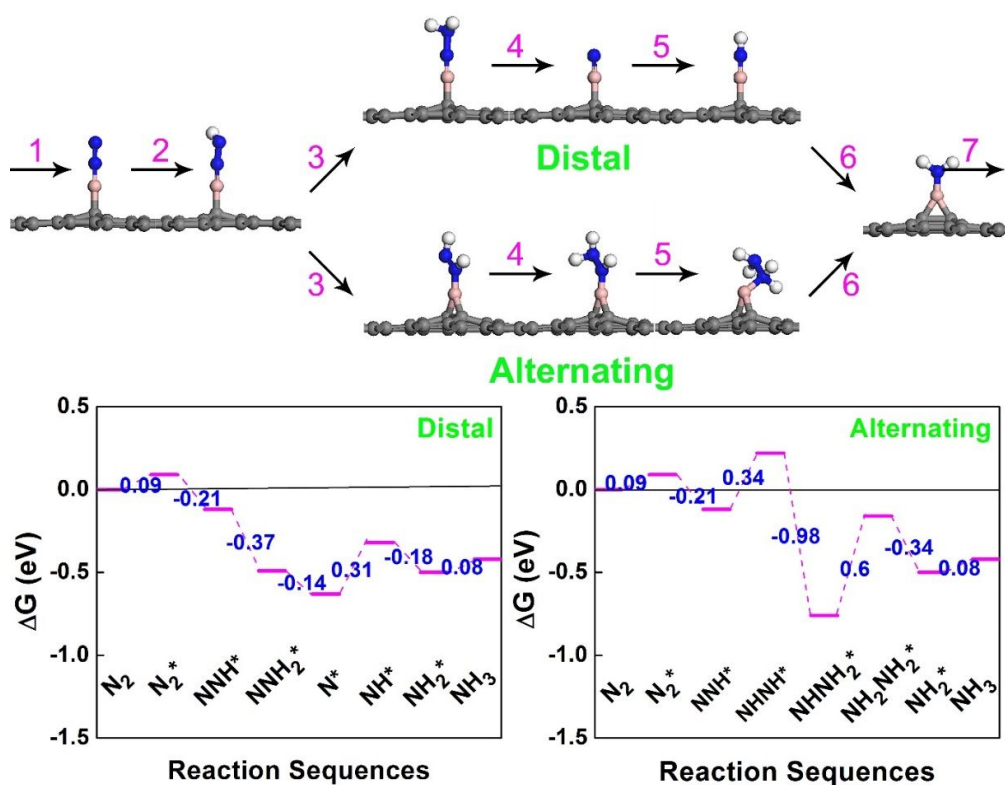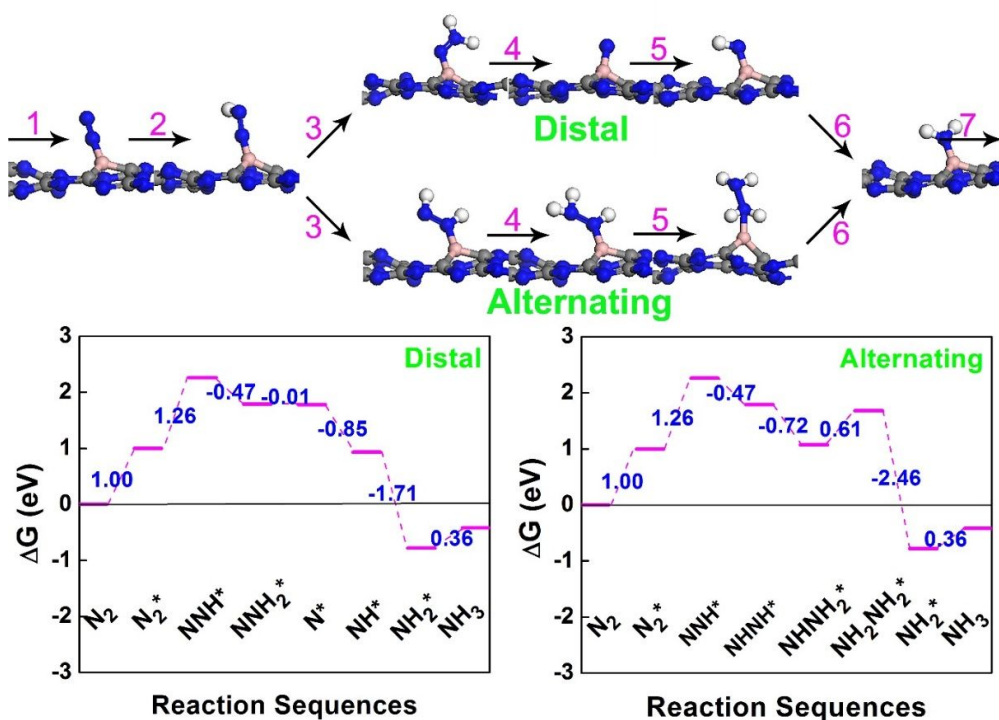
Figure S9. Optimized geometric structures of various intermediates along the distal and alternating paths of NRR on boron atom adsorbed on perfect graphene. And calculated reaction ΔG of two reaction pathways.
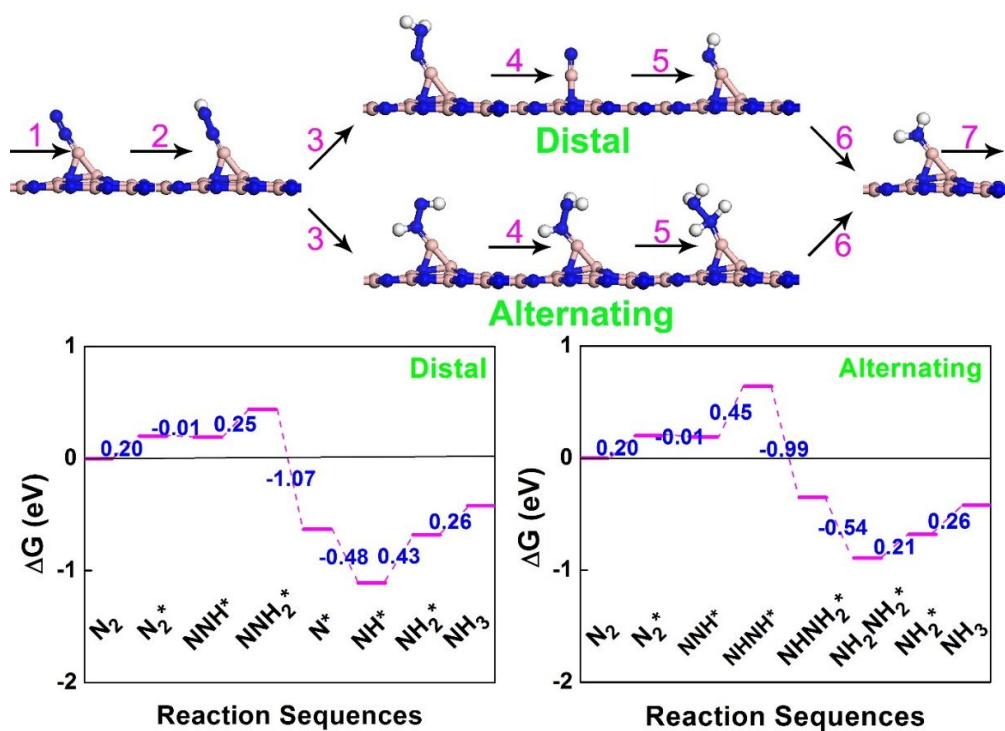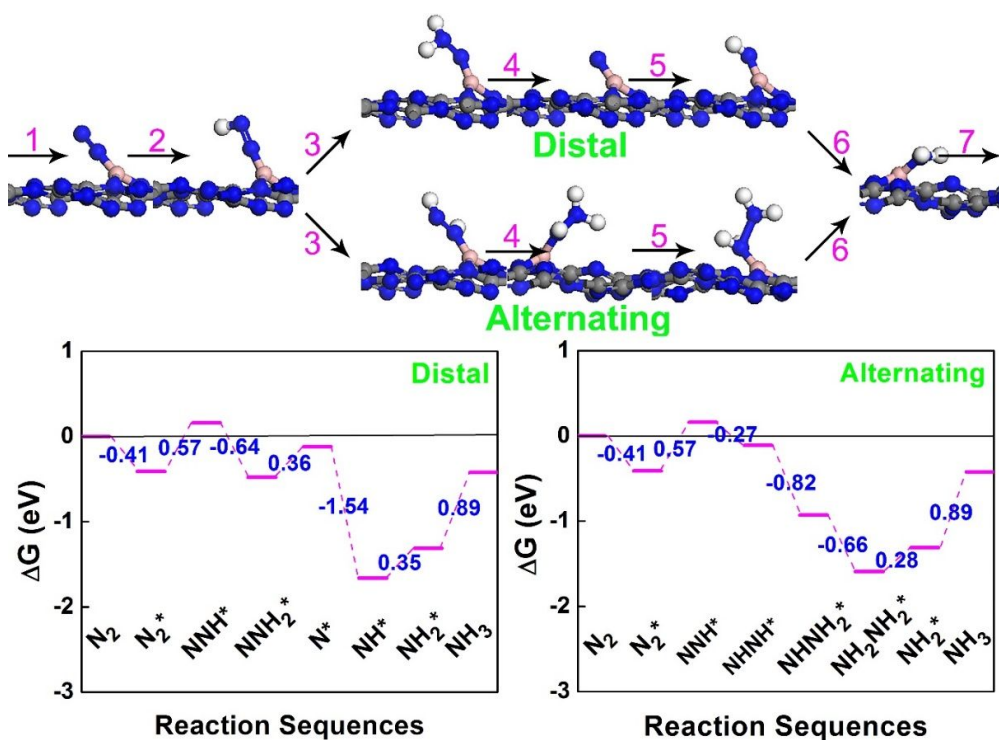

Figure S10. Optimized geometric structures of various intermediates along the distal and alternating paths of NRR on boron atom adsorbed on perfect BN. And calculated reaction ΔG of two reaction pathways.

212
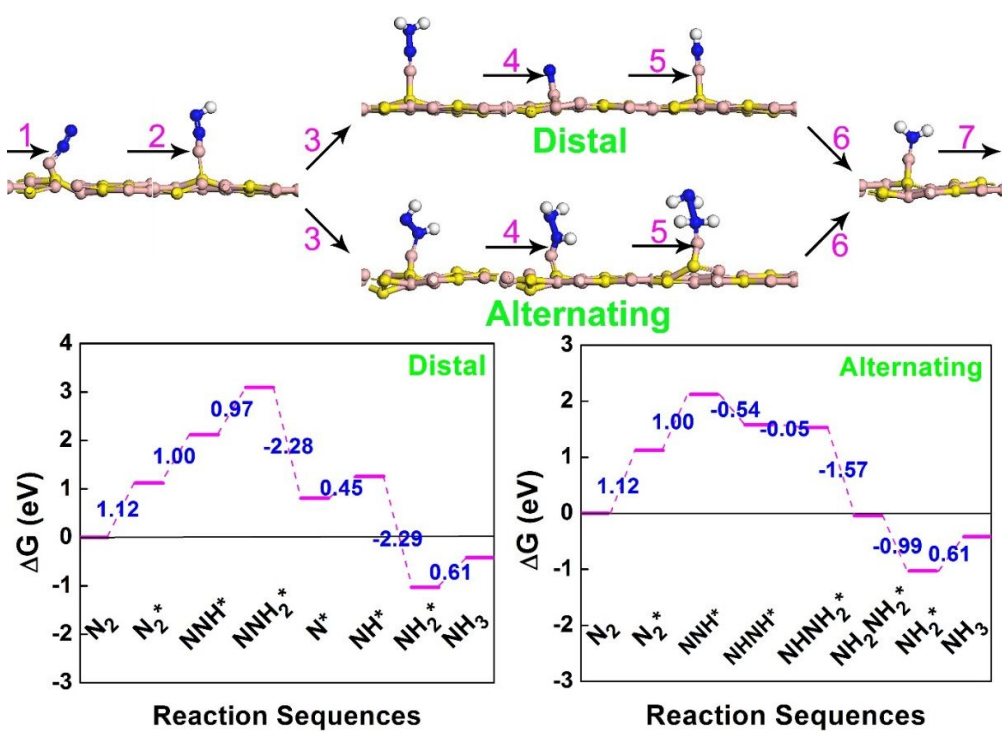
Figure S11. Optimized geometric structures of various intermediates along the distal and alternating paths of NRR on boron atom adsorbed on perfect B_2S. And calculated reaction ΔG of two reaction pathways.
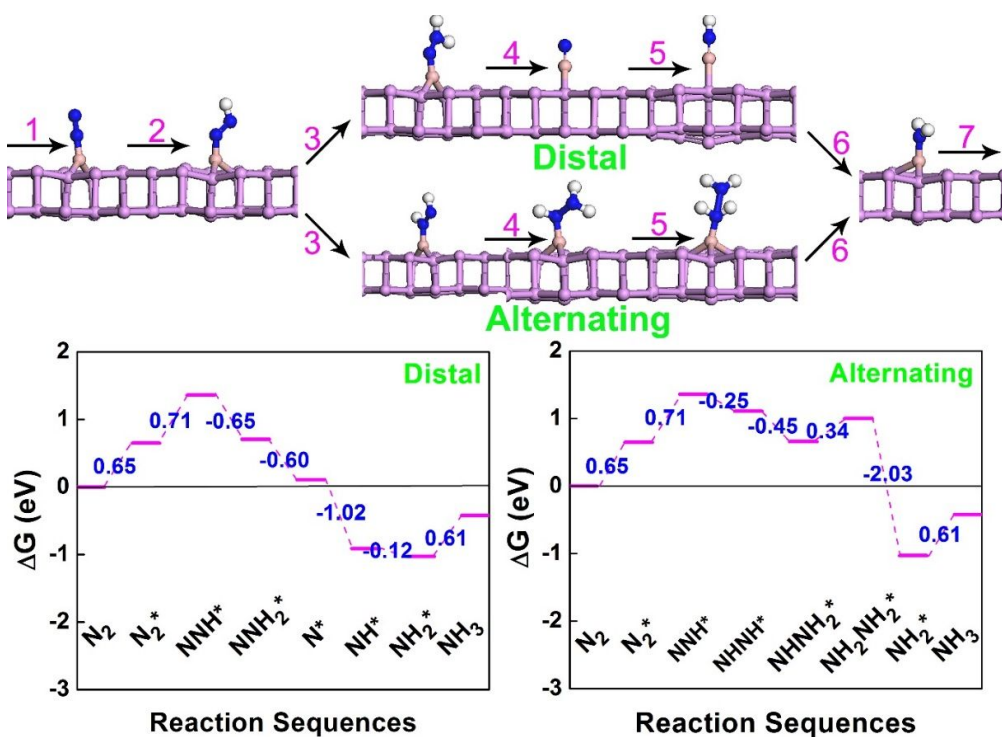
Figure S12. Optimized geometric structures of various intermediates along the distal and alternating paths of NRR on boron atom adsorbed on perfect BP. And calculated reaction ΔG of two reaction pathways.
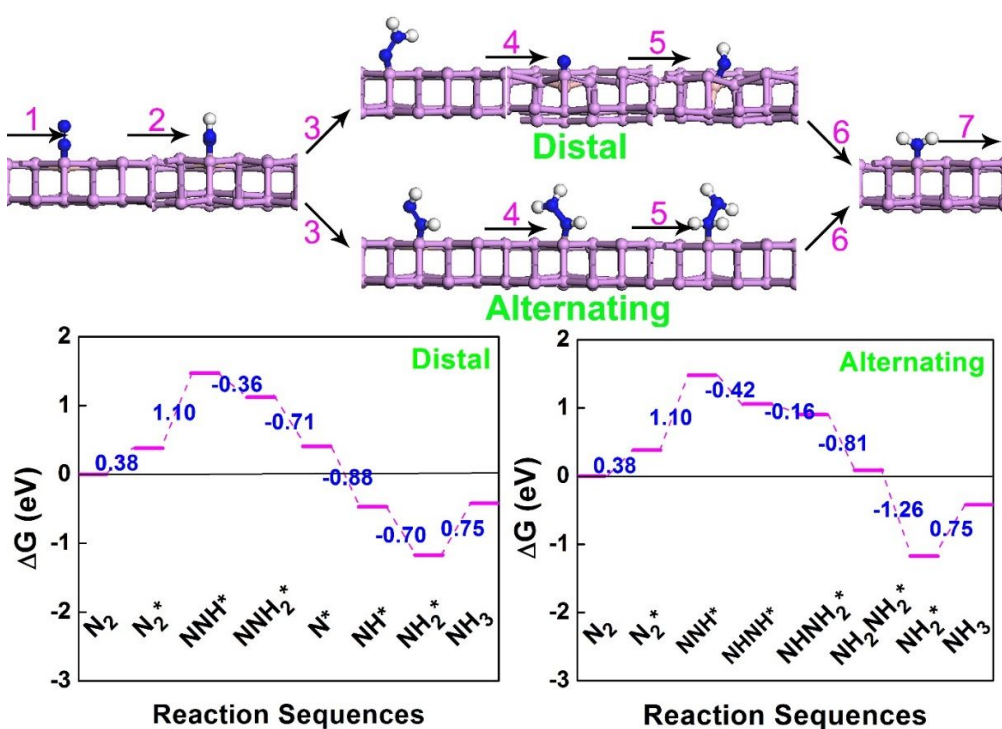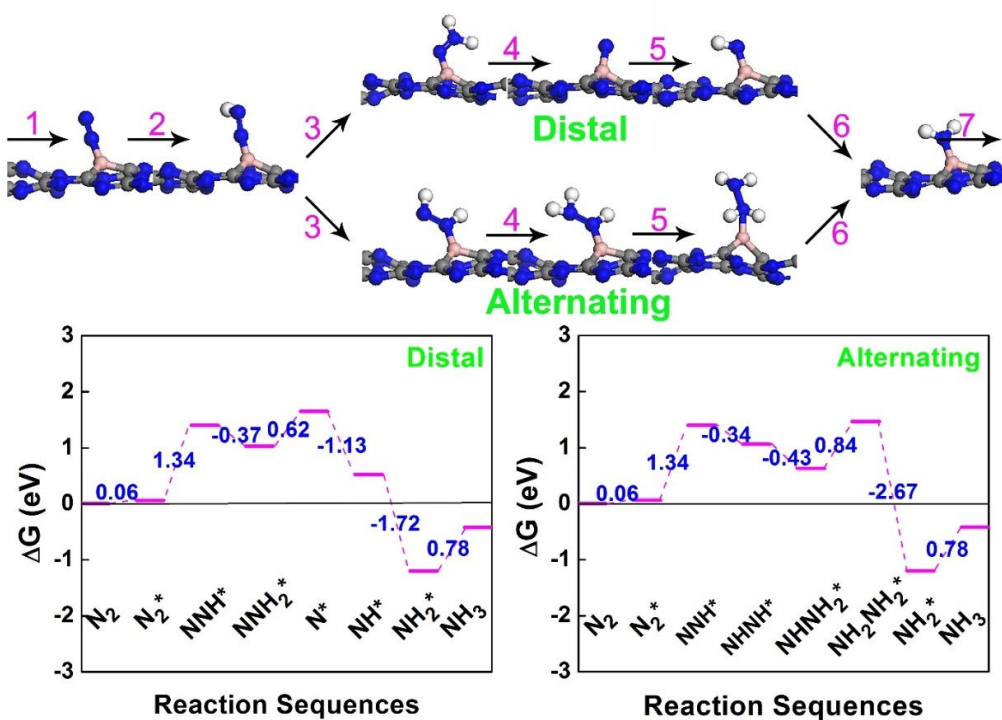
Figure S13. Optimized geometric structures of various intermediates along the distal and alternating paths of NRR on boron atom which substitution doping on the BP. And calculated reaction ΔG of two reaction pathways.
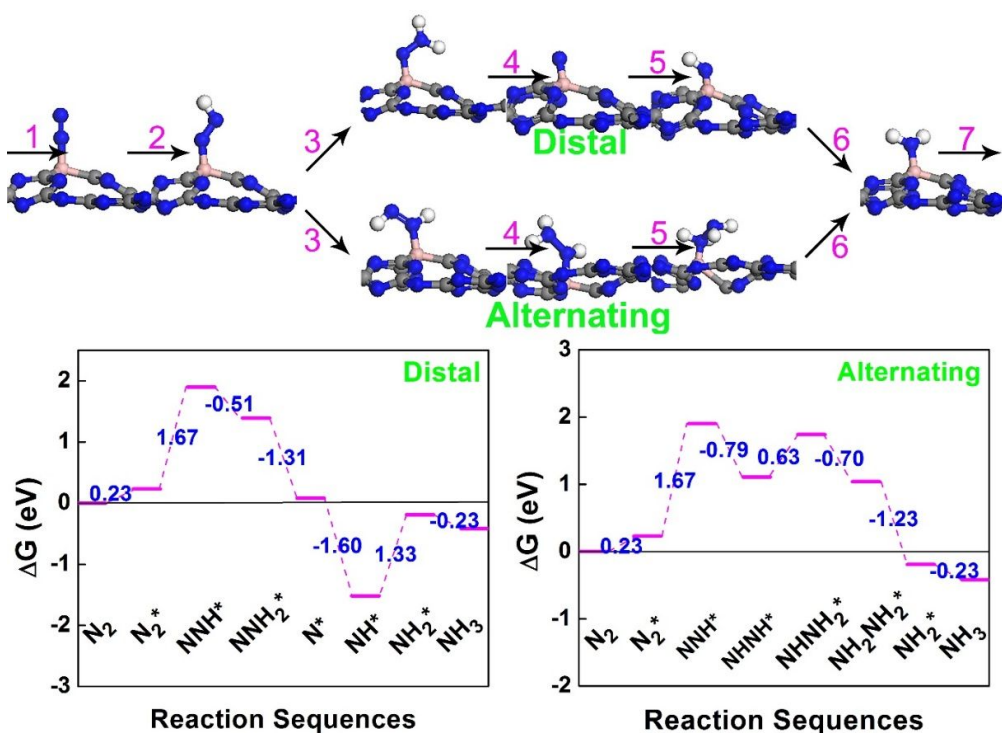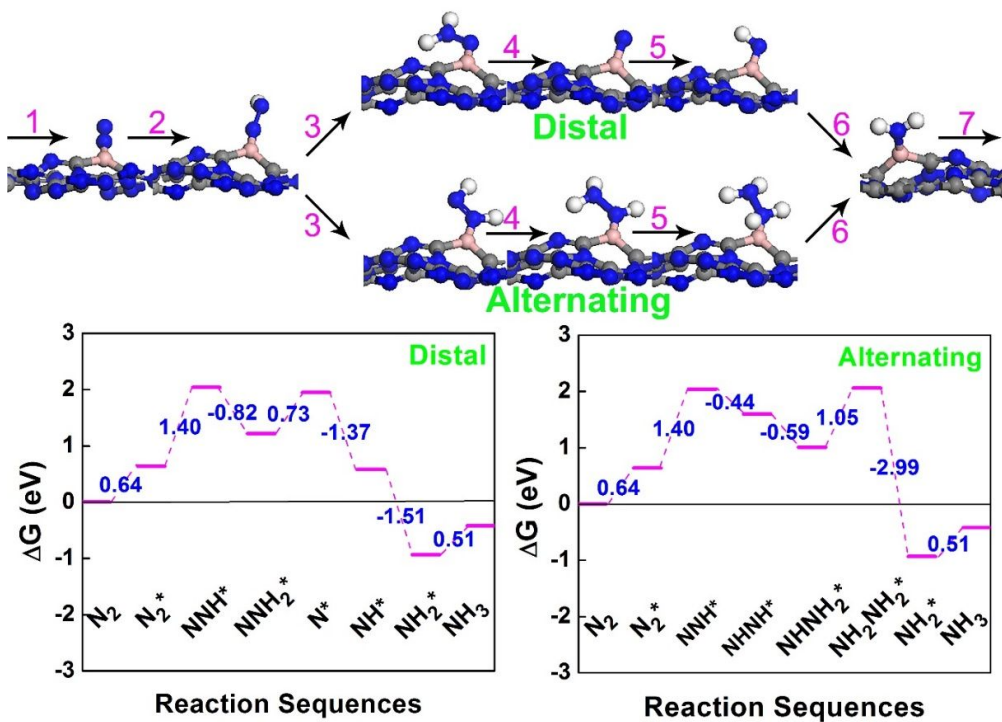

Figure S14. Optimized geometric structures of various intermediates along the distal and alternating paths of NRR on boron atom which substitution doping on the S-triazine C_3N_4 (site 2). And calculated reaction ΔG of two reaction pathways.
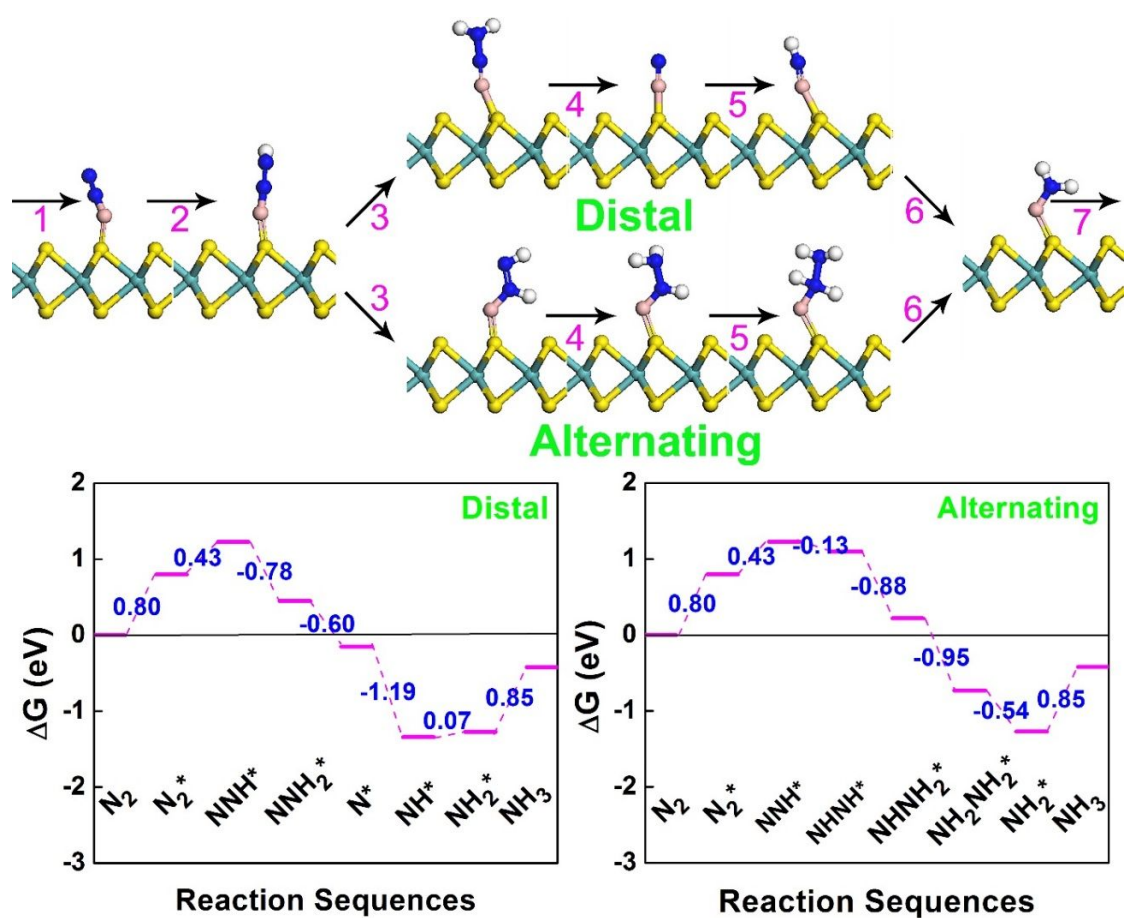
S10

214

Figure S15. Optimized geometric structures of various intermediates along the distal and alternating paths of NRR on boron atom which substitution doping on the S-triazine C_3N_4 (site 3). And calculated reaction ΔG of two reaction pathways.

Figure S16. Optimized geometric structures of various intermediates along the distal and alternating paths of NRR on boron atom adsorbed on the perfect Tri-s-triazine C_3N_4. And calculated reaction ΔG of two reaction pathways.
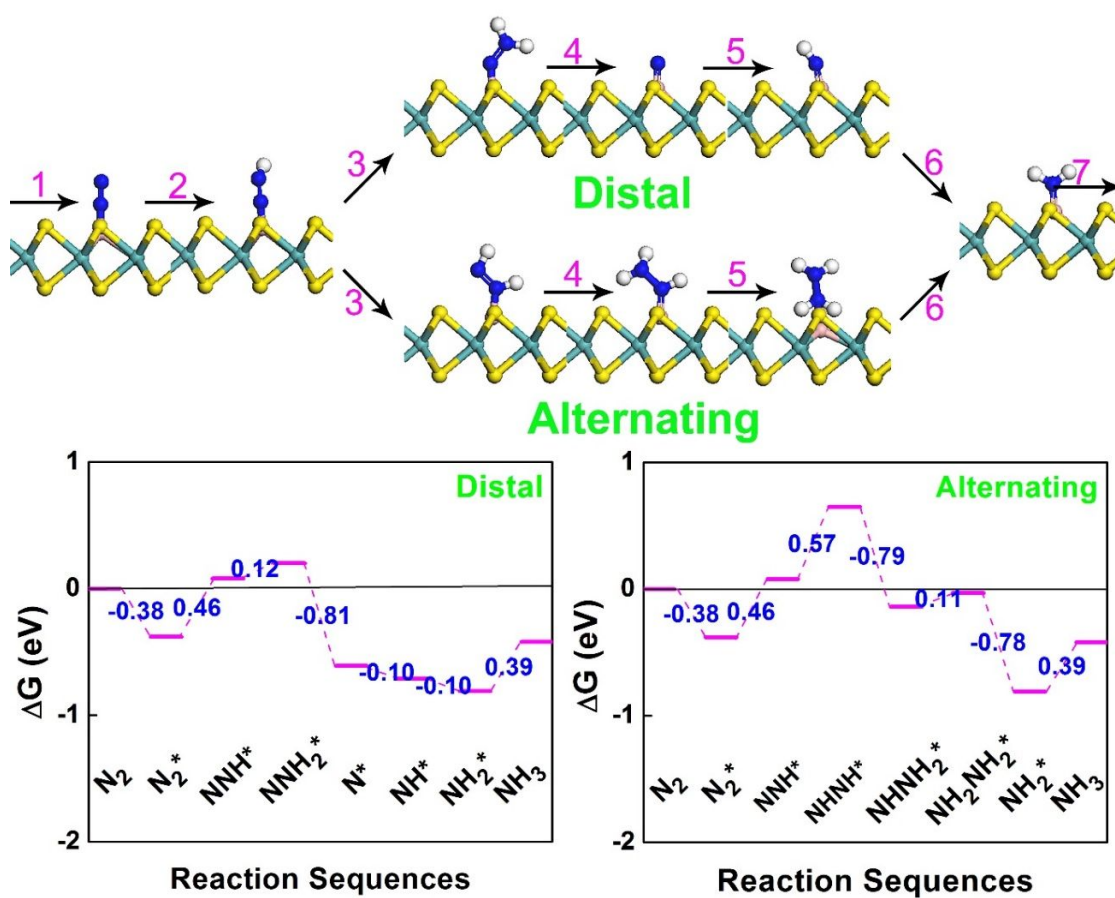
Figure S17. Optimized geometric structures of various intermediates along the distal and alternating paths of NRR on boron atom which substitution doping on the Tri-s-triazine C_3N_4 (site2). And calculated reaction ΔG of two reaction pathways.

Figure S18. Optimized geometric structures of various intermediates along the distal and alternating paths of NRR on boron atom which substitution doping on the Tri-s-triazine C_3N_4 (site3). And calculated reaction ΔG of two reaction pathways.
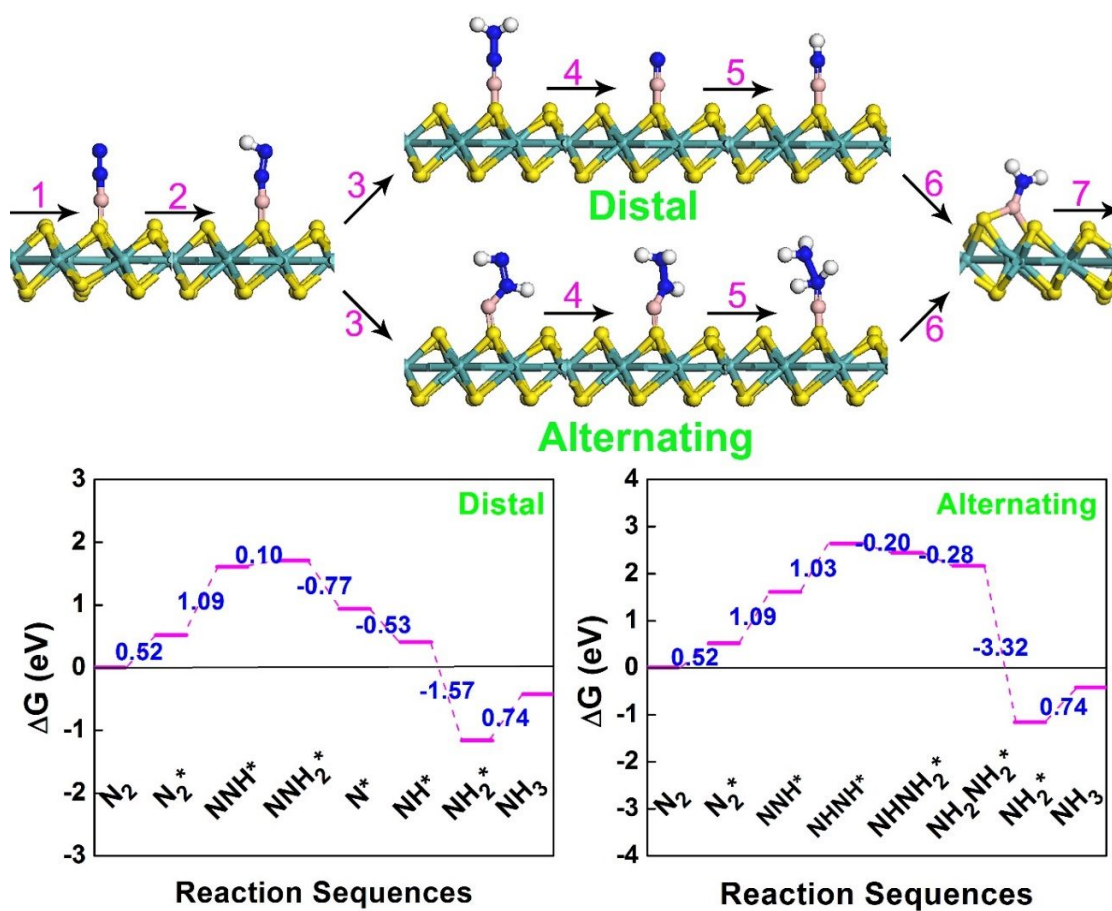
216

Figure S19. Optimized geometric structures of various intermediates along the distal and alternating paths of NRR on boron atom which adsorbed on the perfect h-MoS$_2$. And calculated reaction ΔG of two reaction pathways.
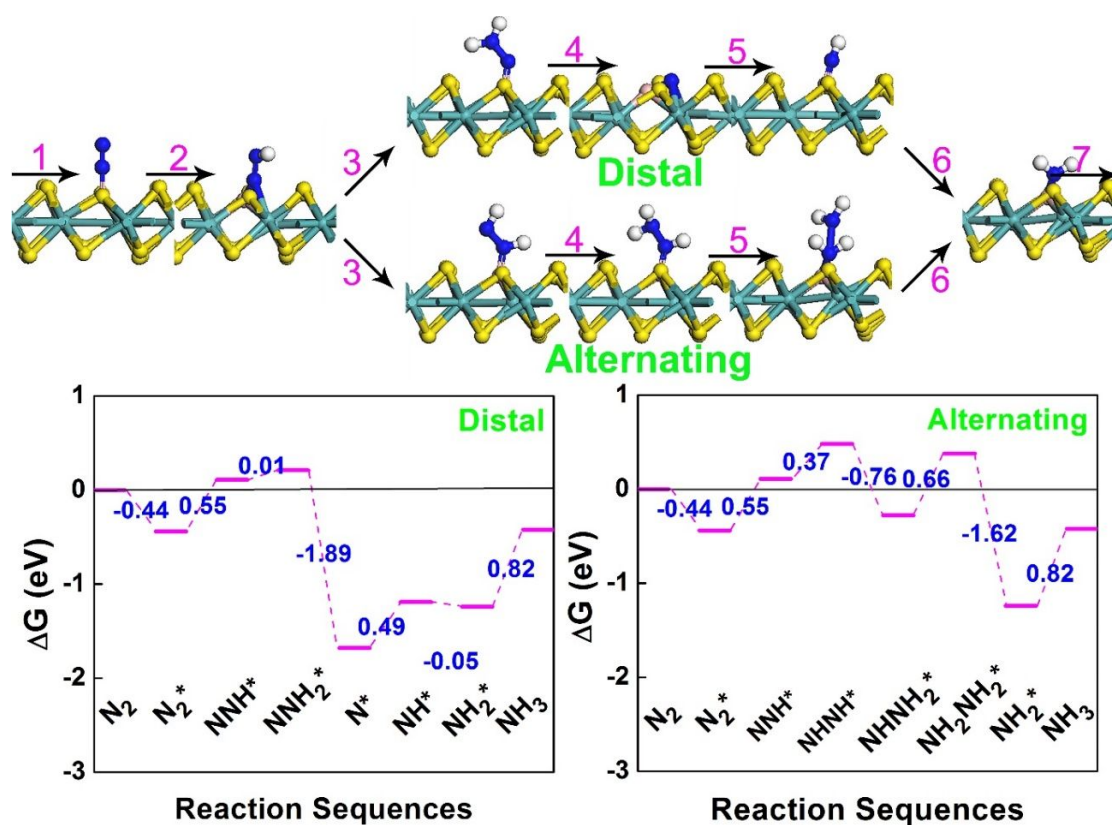
Figure S20. Optimized geometric structures of various intermediates along the distal and alternating paths of NRR on boron atom which substitution doping on the h-MoS$_2$. And calculated reaction ΔG of two reaction pathways.

Figure S21. Optimized geometric structures of various intermediates along the distal and alternating paths of NRR on boron atom which adsorbed on the perfect t-MoS$_2$. And calculated reaction ΔG of two reaction pathways.

Figure S22. Optimized geometric structures of various intermediates along the distal and alternating paths of NRR on boron atom which substitution doping on the t-MoS$_2$. And calculated reaction ΔG of two reaction pathways.
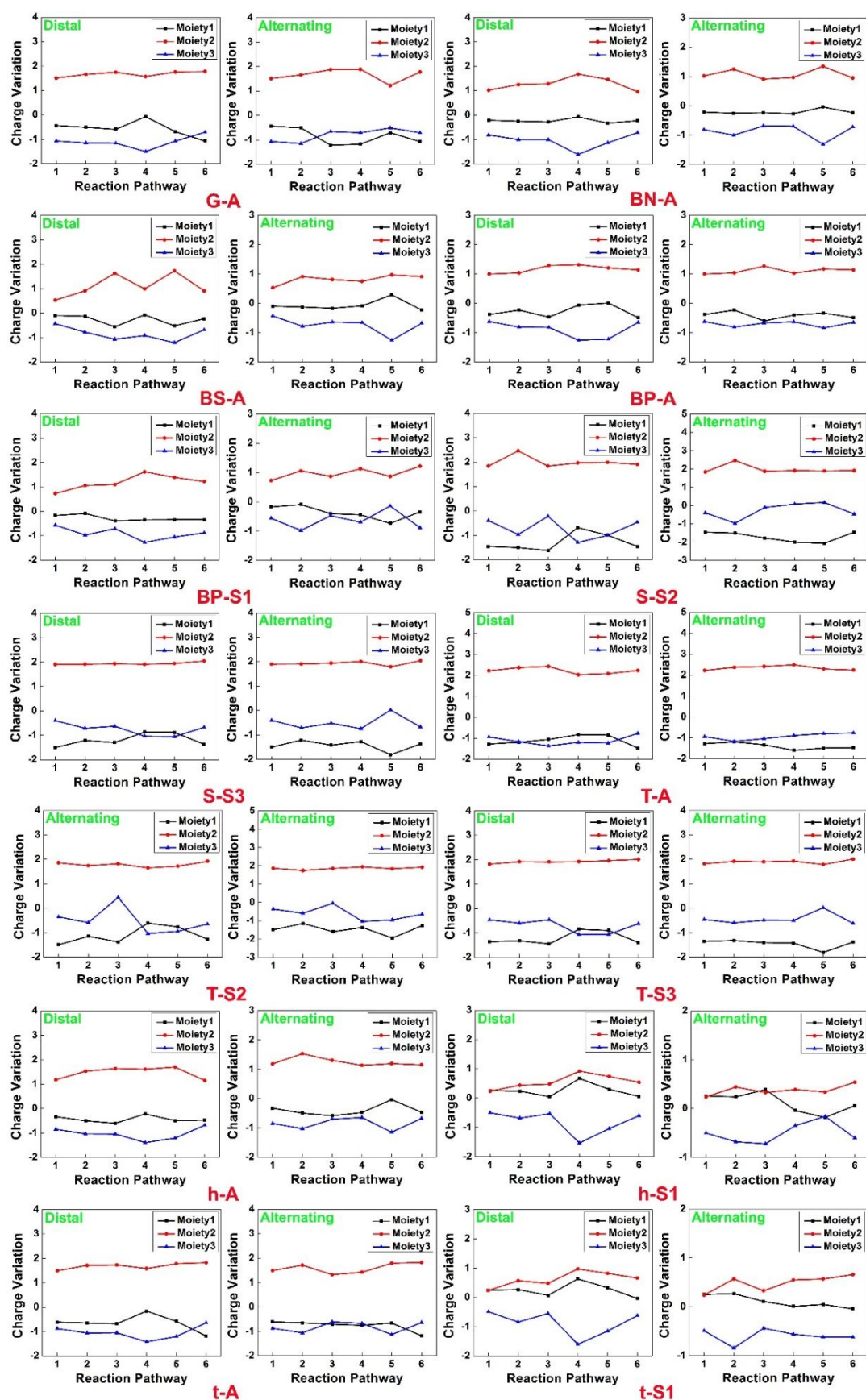
220

Figure S23. The Charges variation of the intermediate species for fourteen catalysts. Reaction sequence are defined by above figures. Moiety 1 (2D substrate). Moiety 2 (boron atom), and Moiety 3 (adsorbed N_xH_y).
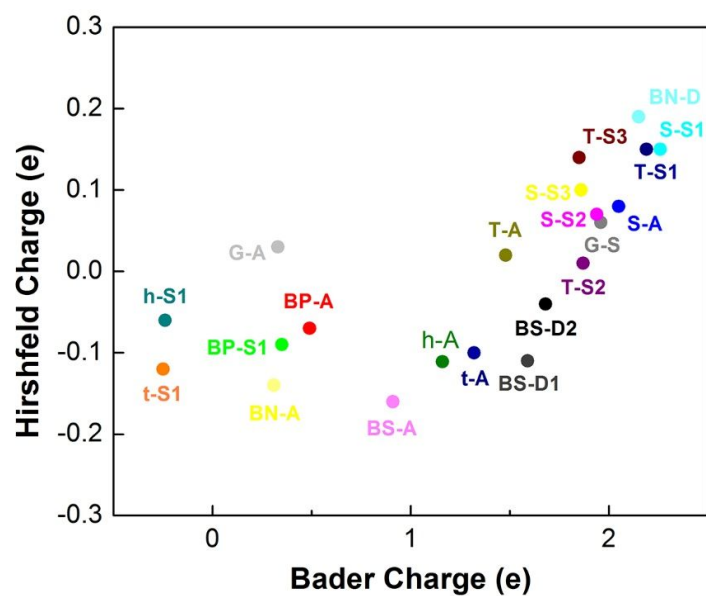
Figure 24. Hirshfeld charge vs. Bader charge of single boron atom in twenty-one substrates.
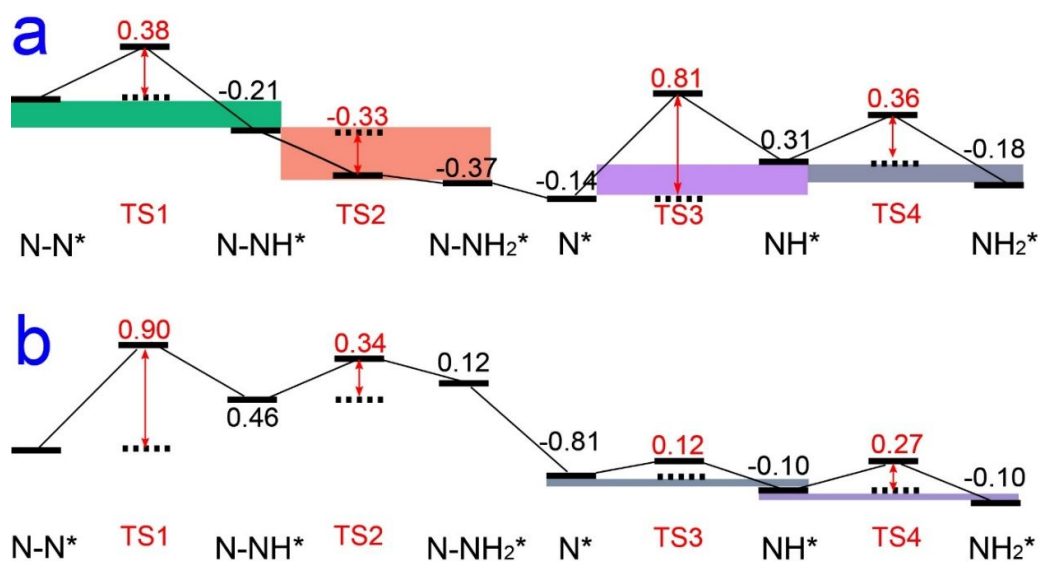
Figure S25. Minimum energy path for the N_2 conversion into NH_3 catalyzed by B-graphene (a) and B-h-MoS$_2$ (b), and energies of the intermediates and transition stats (TS) indicated.

References:

(1) Kresse, G.; Joubert, D., From Ultrasoft Pseudopotentials to the Projector Augmented-wave Method. *Phys. Rev. B* **1999**, *59*, 1758.

(2) Perdew, J. P.; Burke, K.; Ernzerhof, M., Generalized Gradient Approximation Made Simple. *Phys. Rev. Lett.* **1996**, *77*, 3865.

(3) Azofra, L. M.; Li, N.; MacFarlane, D. R.; Sun, C., Promising Prospects for 2D d^2–d^4 M_3C_2 Transition Metal Carbides (MXenes) in N_2 Capture and Conversion into Ammonia. *Energy Environ. Sci.* **2016**, *9*, 2545-2549.

(4) Zhao, W.; Zhang, J.; Zhu, X.; Zhang, M.; Tang, J.; Tan, M.; Wang, Y., Enhanced Nitrogen Photofixation on Fe-doped TiO_2 with Highly Exposed (1 0 1) Facets in the Presence of Ethanol as Scavenger. *Appl. Catal. B Environ.* **2014**, *144*, 468.

(5) Mills, G.; Jónsson, H.; Schenter, G. K., Reversible Work Transition State Theory: Application to Dissociative Adsorption of Hydrogen. *Surf. Sci.* **1995**, *324*, 305-337.

224

Chapter VI: Conclusions and Perspectives

6.1 Conclusions

The nitrogen reduction reaction catalytic performance of boron-based two-dimensional materials was performed by first-principles calculations under ambient condition in this thesis. Boron atom has three valence electrons in the $2s^2 2p^1$ and empty orbital, which is similar to the d orbital of transition metals. Transition metals active centers need empty d orbital to accept the lone-pair electrons of the nitrogen molecule, while the sp^2 hybrid orbital of the boron atom can form B-to-N pie back-bonding to weak the triple bond of nitrogen. As demonstrated in Chapter II to V, the electrocatalytic performance of pristine two 2D boron sheets, single metal atoms doped boron sheets, and single boron atom incorporated some 2D substrates were studied by using DFT, respectively.

The research of Chapter II represented the application of the hydrogen evolution reaction on the, metal-free, two boron sheets. As indicated by ΔG_{H*}, both α and β_{12} sheets offer ultralow overpotential for HER and such performance can keep well at different H-coverages. Due to the coexistence of unpaired electron and empty states, unsaturated boron atoms along the hexagon holes are the active sites, with loading as high as 3/4 and 4/5 in terms of atomic ratio.

In the Chapter III, we demonstrated the site-2, triangular boron atom, of α-sheet offers the best performance, with $\Delta G_{max} = 0.77$ eV. It also indicated that the first reduction step is the rate-determining step for the most active sites on both boron sheets.

In addition, the NRR performance was improved after the boron sheet was deposited on metal surface, indicating metal substrate can inject electrons to boron sheet and reduce the energy barrier.

In the Chapter IV, the catalytic performance of a series of single metal atoms supported on boron sheets for NRR is evaluated by means of DFT computations. Among all the candidates, the Ru atom supported on substrates exhibit potential catalytic activity for NRR due to promising performance in N_2 adsorption, low energy barrier for first protonation, and destabilizing NH_2* and NH_3 species. And the results indicated that the distal mechanism is the best reaction pathway for ammonia formation, for which the biggest limit energy barriers are only 0.42 and 0.44eV on α-sheet and β_{12}-sheet, respectively.

Inspired by the second work: the boron atoms present different NRR performance with different coordination numbers. So, we constructed 21 models through incorporating one boron atom on eight popular 2D materials in the Chapter V. The result identified two promising catalysts **h**-S1 and **G**-A, as offering appropriate thermodynamics, selectivity and kinetics. And we have developed the design principles for enhancing B-catalyzed NRR by taking the Bader charge, that negatively charged boron sites are promising for low overpotential and high selectivity, which can be hardly obtainable from TM catalysts. Our findings can be explained by competition between the ability to form covalent bonds with nitrogen and that to transfer electrons in the reaction, which not only reduces the energy barrier and stabilize the adsorbates, but also supports fast NRR kinetics.

6.2 Perspectives

Despite the efforts of over half a century, electrochemical nitrogen still faces significant challenges both scientifically and technically.

1. Ultralow ammonia yield. For electrochemical NRR, the production rate of ammonia per unit and area/mass is a direct parameter to evaluate the performance of catalysts. As so far, the most reported yield values mostly fall in the range of 0.1 to 100 $\mu g\ h^{-1}\ mg^{-1}$ (or $\mu g\ h^{-1}\ cm^{-2}$) in aqueous solution under ambient conditions, which much smaller than the H-B industrial methods. Some groups studied the molten eutectic electrolytes to enhance the ammonia formation under low-temperature and the yield reached about 300 $\mu g\ h^{-1}\ mg^{-1}$, which is comparable to the industrial level.

2. Stability. The stability of catalysts is a major concern for the NRR compared with other electrocatalytic processes. The catalyst surface can be poisoned by coverage with water, oxygen and hydrogen, blocking the active sites for N_2 adsorption. This poisoning effect may occur in the initial stage of electrolysis, leading to distinct catalytic behaviour with DFT predictions, exhibiting mainly HER or occurring during continuous electrolysis due to the accumulation of in situ electrochemically generated H adatoms, which gradually saturate the catalyst surface.

3. Ultralow selectivity. The ammonia production process is normally accompanied by the simultaneous generation of hydrogen and hydrazine, resulting in a very low selectivity towards NH_3. If hydrogen formation is really an inevitable concomitant process with nitrogen reduction, what need to do is not try to suppress the HER, but making efforts to maximize the overall performance considering both the NRR and

HER. Based on the experience from carbon dioxide electroreduction, where a catalyst with low CO selectivity but high current density can be considered a good candidate for the production of syngas with a tuneable composition, an NRR catalyst with high NH_3 yield but low Faraday efficiency may also be considered a good candidate for concurrent NH_3/H_2 production.

4. Verifying the nitrogen source. As a rapidly developing field, electrochemical NRR currently has no standard testing procedures, and thus researchers have proposed several different experimental protocols. Although different electro- chemical cells including single-chamber, H-typed double chamber, PEM-type and back-to-back-type cells were comprehensively reviewed by many works, a major issue is to verify the source of nitrogen, excluding labile nitrogen contamination commonly existing in the atmosphere, human breath, experimental equipment and gas feedstock. To verify the source of nitrogen and confirm the successful reduction of feeding nitrogen gas into ammonia, at least three types of control experiments must be performed: (i) blank or background controls, (ii) Ar-based electrolysis, and (iii) ^{15}N-isotopic labelling experiments.

More importantly, current understanding on the fundamental mechanisms of N_2 photo-reduction and electro-reduction is still very limited due to the considerably complicated reaction process. To promote the development of heterogeneous nitrogen fixation under ambient conditions, there are some perspectives to further improve the performance of electrocatalytic NRR systems.

Firstly, to rationally design a catalyst, it is critical to understand which intrinsic material characteristics, or descriptors, control catalysis. The development of design principles or descriptors that correlate tuned structures to the catalytic activity of heterogeneous catalysts will accelerate the search for highly active catalysts based on earth-abundant, cost-effective environment friendly and robust materials.

Secondly, to understand the obscure advanced knowledge regarding fundamental mechanisms of heterogeneous NRR processes is important. N_2 reduction is regarded as a considerably complicated multi-step reaction, and many details still remain unclear in the experiment. The DFT method has been utilized as a powerful tool to predict the possible active sites, the rate-determining step and the intermediates of the reaction. The effective combination of theoretical analysis and experimental results is advantageous to reveal the reaction mechanisms of NRR at molecular scale.